# DOCTORAL (PhD) DISSERTATION

Shoaib Mukhtar

University of Pannonia

2025

# Doctoral (PhD) Dissertation

# University of Pannonia

Doctoral School of Chemistry and Environmental Sciences

# Synthesis and characterization of UV- and visible-light-driven photocatalysts for the degradation of organic pollutants

Written by
**Shoaib Mukhtar**

DOI:10.18136/PE.2026.976

Supervisors
**Dr. Ottó Horváth, DSc**
Professor

**Dr. Erzsébet Szabó-Bárdos, PhD**
Associate Professor

**University of Pannonia, Center for Natural Sciences**
Research Group of Environmental and Inorganic Photochemistry
Veszprém, Hungary

# Synthesis and characterization of UV- and visible-light-driven photocatalyst for the degradation of organic pollutants

The thesis was prepared for the award of a doctoral degree (PhD) within the framework of the Doctoral School of Chemistry and Environmental Sciences at the University of Pannonia

in the discipline of chemistry

Written by Shoaib Mukhtar

Supervisor(s):
Dr. Ottó Horváth, DSc, Dr. Erzsébet Szabó-Bárdos, PhD

I recommend the dissertation for acceptance: yes / no.

……………………….
supervisor

I recommend the dissertation for acceptance: yes / no.

……………………….
supervisor

I recommend the dissertation for peer review.

……………………….
chair of the DDHC

The PhD-candidate has achieved.……. % at the public debate.
The composition of the Final Examination Committee:
chair:……………………………………………………………………
reviewers:.………………………………………………………………
members:………………………………………………………………..
Veszprém,

……………………….
chair of the committee

Qualification of degree: ….................................
Veszprém,

……………………….
chair of the UDHC

# Abbreviations

| | | |
|---|---|---|
| AOP | | Advanced oxidation processes |
| A | | Acceptor |
| BET | | Brunauer-Emmett-Teller |
| 1,4-BQ | | 1,4-Benzoquinone |
| CB | | Conduction band |
| DRS | | Diffuse reflectance spectra |
| D | | Donor |
| $D_{av}$ | | Average pore diameter |
| $E_g$ | | Band-gap energy |
| $e^-_{CB}$ | | Photo-generated electron |
| $E^0$ | | Standard redox potential |
| EDS | | Energy dispersive X-ray spectrometry |
| $\varepsilon$ | | Molar absorption coefficient |
| FFT | | Fast Fourier transform |
| FTIR | | Fourier Transform Infrared Spectroscopy |
| $h^+_{VB}$ | | Photo-generated hole |
| HPLC | | High-performance liquid chromatography |
| HAADF | | High-angle annular dark-field |
| 1,4-$H_2Q$ | | 1,4-hydroquinone |
| HRTEM | | High Resolution Transmission Electron Microscopy |
| ICP-OES | | Inductively Coupled Plasma Optical Emission Spectroscopy |
| k | | Rate constant |
| 7-OHC | | 7-hydroxycoumarin |
| $^{\bullet}OH$ | | Hydroxyl radical |
| OHC | | Hydroxylated coumarin or hydroxycoumarin |
| $O_2^{\bullet-}$ | | Superoxide anion radical |
| OP | | Organic pollutant |
| PN | | Para-nitrophenol |

|  |  |  |
|---|---|---|
| ROS |  | Reactive oxygen species |
| SEM |  | Scanning electron microscope |
| SPR |  | Surface plasmon resonance |
| TA |  | Terephthalic acid |
| TOC |  | Total organic carbon |
| TEM |  | Transmission electron microscope |
| UV |  | Ultraviolet |
| V |  | Pore volume |
| $v_0$ |  | Initial rate |
| VB |  | Valence band |
| XRD |  | X-ray diffraction |
| XPS |  | X-ray Photoelectron Spectroscopy |

# Abstract

Heterogeneous photocatalysis has been extensively studied for decades due to its potential in environmental and energy applications. Graphitic carbon nitride (g-$C_3N_4$), a metal-free photocatalyst with a bandgap of approximately 2.7 eV, suitable for visible-light-driven photocatalysis, has garnered significant attention in recent years. The photocatalytic performance of g-$C_3N_4$ is closely linked to its composition, morphology, and microstructure. Consequently, optimizing these properties through morphology control, heterojunction construction, and property enhancement is essential to improve its effectiveness.

However, pristine g-$C_3N_4$ suffers from rapid electron-hole recombination and low quantum efficiency, limiting its photocatalytic efficiency. To address these limitations, modifications with metals and non-metals have been widely explored to enhance charge separation, increase light absorption, and provide more reactive sites.

This study aimed to synthesize g-$C_3N_4$ using various precursors and temperatures and to identify the optimal g-$C_3N_4$ for photocatalytic applications. g-$C_3N_4$ nanosheets with controlled composition and enhanced photocatalytic properties were prepared via a one-step thermal polymerization process. The selected g-$C_3N_4$ was further modified with silver nanoparticles, $Bi_2S_3/Bi_2O_3$ nanoparticles and ZnS/ZnO nanoparticles using bio-inspired and starch-assisted methods.

The modifications involved varying nanoparticle concentrations, synthesis temperatures, and calcination conditions to optimize the photocatalytic activity. The catalysts were evaluated using colorless para-nitrophenol as a model pollutant, coumarin as a hydroxyl radical scavenger, and 1,4-hydroquinone as a superoxide radical scavenger. Results revealed that the morphology and specific surface area of the catalysts significantly influenced their photocatalytic performance. The incorporation of metal and metal sulfide nanoparticles enhanced charge separation, resulting in superior photocatalytic activity compared to pristine g-$C_3N_4$.

Furthermore, different amounts of Ag, $Bi_2S_3/Bi_2O_3$ and ZnS/ZnO were successfully deposited on g-$C_3N_4$ surfaces using bio-inspired, adsorption-impregnation, and starch-assisted techniques. The modified catalysts, including Ag-g-$C_3N_4$, g-$C_3N_4$-$Bi_2S_3/Bi_2O_3$, and g-$C_3N_4$-ZnS/ZnO, exhibited enhanced visible-light absorption due to localized surface plasmon resonance effects. These modifications facilitated charge transfer,

suppressed electron-hole recombination, and improved the generation of reactive oxygen species, such as hydroxyl radicals and superoxide anions.

The modified g-$C_3N_4$ photocatalysts effectively degraded colorless organic pollutants, mineralizing them into harmless products like $CO_2$ and $H_2O$. This work underscores the potential of modified g-$C_3N_4$ as an eco-friendly and cost-effective solution for addressing water pollution challenges.

# Table of contents

**1. Introduction** .......... 1

**2. Objective** .......... 3

**3. Literature review** .......... 4

3.1. Water pollution .......... 4

3.2. Wastewater treatment .......... 5

3.3. Advanced oxidation processes .......... 7

3.4. Photocatalysis .......... 8

*3.4.1. Homogeneous Photocatalysis* .......... 9

*3.4.2. Heterogeneous photocatalysis* .......... 11

3.5. History of g-$C_3N_4$ .......... 15

3.6. Methods for the Preparation of g-$C_3N_4$ .......... 19

*3.6.1. Sol-gel method* .......... 19

*3.6.2. Hydrothermal method* .......... 19

*3.6.3. Solvothermal method* .......... 20

*3.6.4. Chemical vapor deposition (CVD)* .......... 21

*3.6.5. Template-assisted synthesis* .......... 22

*3.6.6. Doping and co-doping strategies* .......... 23

*3.6.7. Thermal polymerization* .......... 24

3.7. Role of g-$C_3N_4$ as photocatalyst .......... 26

3.8. Photocatalytic assessment .......... 33

*3.8.1. Coumarin as a hydroxyl radical scavenger* .......... 33

*3.8.2. 1,4-hydroquinone as a superoxide radical scavenger* .......... 35

**4. Experimental** .......... 38

4.1. Chemicals and reagents .......... 38

4.2. Synthesis of catalyst .......... 39

*4.2.1. Synthesis of g-$C_3N_4$* .......... 39

*4.2.2. Synthesis of Ag-g-$C_3N_4$ nanocomposites* .......... 39

*4.2.3. Synthesis of bismuth and zinc-sulfide-modified g-$C_3N_4$* .......... 40

*4.2.4. Determination of silver concentration on the surface of g-$C_3N_4$* .......... 43

*4.2.5. Determination of bismuth sulfide and zinc sulfide concentration on the catalyst* .......... 44

4.3. Physicochemical characterization of the photocatalyst .......... 46

4.4. Photocatalytic experiments .......... 50

*4.4.1. Reactor* .......... 50

*4.4.2. Preparation of solution* ........ 51
*4.4.3. Analytical measurements (model compound)* ........ 52
**5. Results and discussion** ........ 54
5.1. Catalyst g-$C_3N_4$ ........ 54
*5.1.2. Photocatalytic reactions with coumarin* ........ 58
*5.1.4. Effect of temperature and time of preparation on the photocatalytic activity…* ........ 63
5.2. Ag-g-$C_3N_4$ catalyst ........ 64
*5.2.1. Photocatalytic degradation of coumarin* ........ 65
*5.2.2. Photocatalytic degradation of para-nitrophenol* ........ 68
*5.2.3. Reusability* ........ 71
*5.2.4. Mineralization of para-nitrophenol* ........ 72
*5.2.5. Characterization of Ag-g-$C_3N_4$* ........ 74
*5.2.6. Conclusion* ........ 81
5.3. Catalyst g-$C_3N_4$-Bi and g-$C_3N_4$-Zn ........ 82
*5.3.1. Characterizations of g-$C_3N_4$-Bi and g-$C_3N_4$-Zn catalysts* ........ 82
*5.3.2. Comparison of atomic content by XPS and EDX analysis* ........ 99
*5.3.3. Photoactivity of g-$C_3N_4$-Bi and g-$C_3N_4$-Zn* ........ 101
*5.3.4. Photoactivity of combined nanocomposites* ........ 111
*5.3.5. Reusability* ........ 114
*5.3.6. Conclusions* ........ 114
**6. Summary** ........ 116
**7. Thesis points of PhD dissertation** ........ 119
**8. References** ........ 123
**9. Attachment figures** ........ 148
**10. Attachment tables** ........ 159
**11. Acknowledgement** ........ 161

# 1. Introduction

Heterogeneous photocatalysis has emerged as a transformative approach for environmental remediation, garnering significant attention for its ability to degrade a wide range of organic pollutants in water and air. The advanced oxidation process (AOP) employs photocatalysts, typically photoactive semiconductors that utilize solar radiation, a renewable and abundant energy source, to drive chemical reactions. Among the notable benefits of photocatalysis are its cost-effectiveness, environmental friendliness, and potential for large-scale applications. However, many conventional photocatalysts, such as $TiO_2$, ZnO, and $SnO_2$, exhibit limitations, including excitation restricted to ultraviolet light, which constitutes only 5 % of solar radiation. This limitation has driven the search for visible-light-responsive materials to better utilize the solar spectrum.

Graphitic carbon nitride has emerged as a highly promising photocatalyst due to its unique properties. As a conjugated polymer composed of carbon, nitrogen, and trace amounts of hydrogen, g-$C_3N_4$ is metal-free, environmentally benign, and sustainable. Its graphite-like layered structure, formed by $sp^2$ hybridization of carbon and nitrogen atoms and held together by van der Waals forces, enhances its stability and durability. The semiconductor's narrow bandgap of 2.7-2.8 eV enables visible-light absorption and renders it suitable for a wide range of photocatalytic applications. However, pristine g-$C_3N_4$ suffers from drawbacks such as limited visible-light absorption (up to ~450 nm) and rapid recombination of photogenerated electron-hole pairs, which significantly limits its photocatalytic efficiency.

To address these challenges, extensive research has focused on modifying g-$C_3N_4$ through doping, heterojunction formation, and hybridization with other materials. Among the most effective strategies is the incorporation of metal and metal sulfide nanoparticles, which enhance light absorption, suppress electron-hole recombination, and introduce additional reactive sites.

This research aligns closely with the ongoing activities of the laboratory, which emphasizes the development of advanced materials for sustainable environmental technologies. The laboratory's expertise in semiconductor synthesis, nanomaterial modification, and photocatalytic processes provides the necessary methodological and analytical foundation for this work. By focusing on bio-inspired and starch-assisted green synthesis, metal and metal sulfide nanoparticle incorporation into g-$C_3N_4$, this project contributes to the department’s goals of creating cost-effective, eco-friendly photocatalysts for practical applications such as wastewater treatment and pollutant degradation under UV and visible light. The systematic investigation of photocatalyst stability, reusability, and mechanisms under realistic conditions further supports the laboratory's mission to bridge fundamental science with real-world environmental solutions.

## 2. Objective

The primary goal of this study is to investigate the enhancement of photocatalytic activity in graphitic carbon nitride through modification with silver, bismuth sulphide, and zinc sulphide nanoparticles. These modifications are aimed at improving the photocatalytic degradation of para-nitrophenol (PN), a common and persistent organic pollutant found in industrial wastewater. The study will focus on understanding how varying concentrations of Ag, $Bi_2S_3$, and ZnS nanoparticles affect the photocatalytic performance of g-$C_3N_4$, specifically under UV and visible light irradiation.

Several strategies have been employed in this study to modify g-$C_3N_4$, including bio-inspired, starch-assisted, and impregnation methods, which are crucial in controlling the concentration of nanoparticles and optimizing the synthesis conditions. Silver nanoparticles are incorporated to act as electron traps and plasmonic enhancers, extending the material's ability to absorb light through localized surface plasmon resonance effects. Similarly, $Bi_2S_3$ nanoparticles are expected to enhance charge separation due to their narrow bandgap and appropriate conduction band position, while ZnS nanoparticles contribute to improved light absorption and stability under reaction conditions.

The photocatalytic performance of the modified g-$C_3N_4$ photocatalysts is assessed through the degradation of para-nitrophenol, a model organic compound commonly used in photocatalysis studies due to its environmental persistence. The study also explores the role of reactive species, such as hydroxyl radicals ($^{\bullet}OH$) and superoxide anion radicals ($O_2^{\bullet-}$), in the degradation of para-nitrophenol into non-toxic by-products like $CO_2$ and $H_2O$.

Finding optimal compositions for maximum photocatalytic efficiency through systematic variation in the concentrations of silver nanoparticles, bismuth sulfide and zinc sulfide nanoparticles was aimed at. These modifications were designed to enhance not only light absorption and charge-carrier dynamics but also the surface area and catalytic activity of the photocatalysts, particularly under visible-light conditions.

# 3. Literature review

## 3.1. Water pollution

Water is essential for supporting life on Earth and is a critical resource necessary for human survival [1, 2, 3, 4, 5]. It is universally acknowledged as the most valuable natural asset, indispensable not only for drinking but also for sustaining ecosystems and supporting diverse life forms [6]. However, the rapid expansion of the global population [7], coupled with accelerated industrial growth [8], has led to an alarming increase in energy consumption and the discharge of harmful substances into the environment. Water bodies, including lakes, rivers, oceans, and groundwater, are particularly vulnerable to this pollution, posing a significant threat to both human and environmental health [9, 10].

Industrial sectors such as chemicals [11, 12], pesticides [13, 14], oil refining [15, 16], petrochemicals [17, 18], and pharmaceuticals [19, 20] are among the largest contributors to water pollution. These industries often release untreated effluents containing a myriad of hazardous organic pollutants directly into nearby water sources. This practice significantly exacerbates pollution levels and introduces persistent organic contaminants into the environment. Among these contaminants are toxic chemicals and pharmaceutical compounds, which contain organic pollutants, which are not only harmful to aquatic ecosystems but can also infiltrate food chains, ultimately affecting human populations even at significant distances from the initial pollution source [21].

These organic pollutants are particularly concerning due to their resilience in natural environments. They can persist for extended periods, leading to bioaccumulation and biomagnification within aquatic and terrestrial ecosystems [22]. Such pollutants pose grave risks to biodiversity and disrupt ecological balance. Moreover, exposure to these pollutants has been linked to severe health issues in humans, including endocrine disruption, carcinogenic effects [23], and other chronic conditions [24].

The significance of addressing pharmaceutical pollutants and water-soluble dyes cannot be overstated. The pharmaceutical industry has witnessed exponential growth, leading to an increase in the prevalence of pharmaceutical residues in water bodies [25]. Many pharmaceutical compounds resist conventional treatment methods, retaining their toxicity and posing long-term environmental and health risks. Similarly, water-soluble dyes, commonly used in industries such as textiles, leather tanning, and paper production, are notorious for their stability and environmental persistence. These dyes often impart coloration to water bodies, reducing light penetration and affecting photosynthetic aquatic organisms, thereby disrupting the ecological balance [26]. The schematic diagram of different water pollution sources with their causes and effects have been shown below in Figure 3.1.

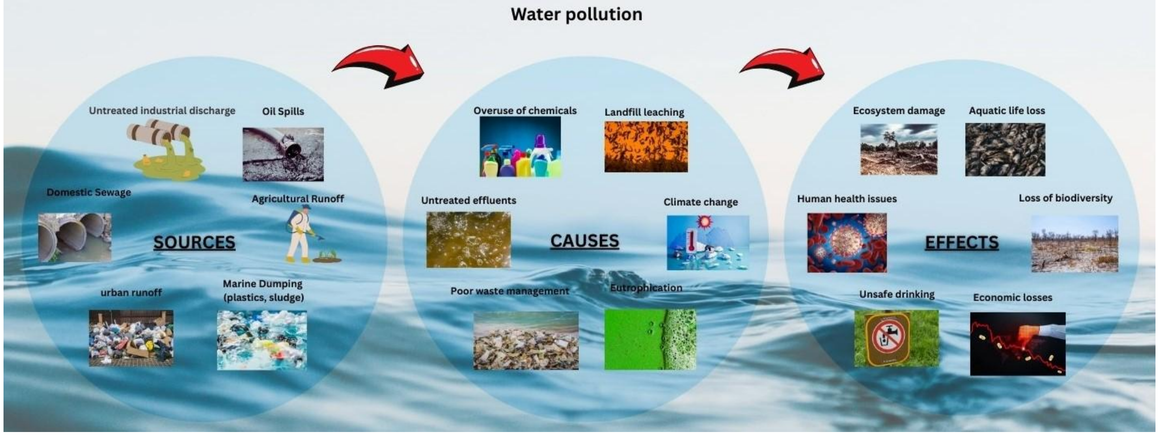

**Figure 3.1.** Environmental water pollution source, cause, and effect [27].

## 3.2. Wastewater treatment

Conventional wastewater treatment relies on a sequence of physical, chemical, and biological processes, including coagulation, oxidation, adsorption, membrane filtration, and biological degradation [28, 29, 30, 31, 32, 33, 34]. Technologies such as ozonation, sonochemical decomposition, and nanofiltration have improved removal efficiencies for various contaminants. Coagulation-flocculation and advanced filtration methods, including those utilizing activated carbon and membranes, are widely employed alongside chemical and electrochemical approaches for challenging pollutants. Despite these advances, conventional techniques often struggle to fully remove persistent organic pollutants and newly emerging micropollutants, which are increasingly detected in treated effluents. This limitation underscores the need for next-generation, sustainable water treatment solutions.

An optimal wastewater treatment process must possess the ability to fully mineralize all toxic organic components, ensuring that no harmful by-products remain [35]. Typically, various treatments such as biological, mechanical, thermal, chemical, or physical methods, or a combination of these, can be utilized to address contaminated water [36, 37, 38]. The selection of a wastewater treatment method is contingent upon the characteristics of the pollutants found in the water and the permissible contamination threshold in the treated effluent [39]. The cost-effectiveness of wastewater treatment significantly influences the selection of the specific process [40]. A variety of wastewater management methods are presently employed, each demonstrating different levels of effectiveness, and every process exhibits certain limitations [41, 42]. Wastewater treatment is often categorized into three principal stages: primary, secondary, and tertiary treatment [43, 44, 45] as shown in Figure 3.2 below. This research emphasizes the tertiary treatment step, when highly advanced substances like photocatalysts are crucial for decomposing persistent organic pollutants [46].

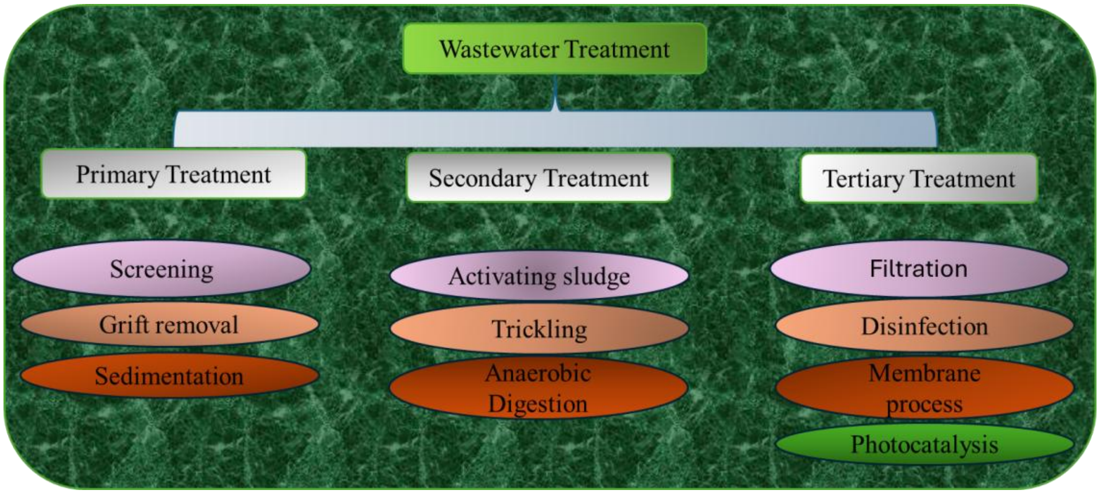

**Figure 3.2.** Wastewater treatment [47].

During the initial treatment phase, physical techniques including screening, grit removal, and sedimentation are employed to remove large solids and suspended substances. This phase diminishes the total burden on ensuing biological therapy systems [48, 49]. The secondary treatment entails the biological breakdown of dissolved and colloidal organic substances, predominantly via aerobic methods such as the activated sludge system, trickling filters, or anaerobic digestion. These approaches utilize microorganisms to transform organic contaminants into stable byproducts, including carbon dioxide and water [50, 51]. Tertiary treatment aims to eliminate residual contaminants, including nutrients (nitrogen and phosphorus), pathogens, and refractory organic compounds. Methods include sand filtering, UV or chlorine disinfection, membrane technology, and advanced oxidation processes such as photocatalysis, which are routinely utilized in this phase to generate high-quality effluent appropriate for disposal or reuse [52, 53, 54, 55, 56]. This multi-phase strategy guarantees thorough pollutant elimination while providing adaptability for technological incorporation customized to the required water quality needs.

## 3.3. Advanced oxidation processes

AOPs leverage the production of highly reactive oxygen species, such as hydroxyl radicals, to degrade and mineralize organic pollutants into less harmful or harmless substances. The advancement of AOPs is crucial for overcoming the drawbacks of traditional water and wastewater treatment methods [57, 58]. In AOPs, reactive oxygen species (ROS) are produced by commencing a secondary reaction with water. Its functioning under ambient circumstances can generate a diverse array of reactive oxygen species, including hydroxyl radical ($^{\bullet}OH$), hydrogen peroxide ($H_2O_2$), ozone ($O_3$), superoxide anion radicals ($O_2^{\bullet-}$), and singlet oxygen ($^1O_2$). Each AOP produces distinct species for the breakdown of organic contaminants [59]. Advanced oxidation processes (Figure 3.3) have emerged as a promising class of solutions for water treatment [60].

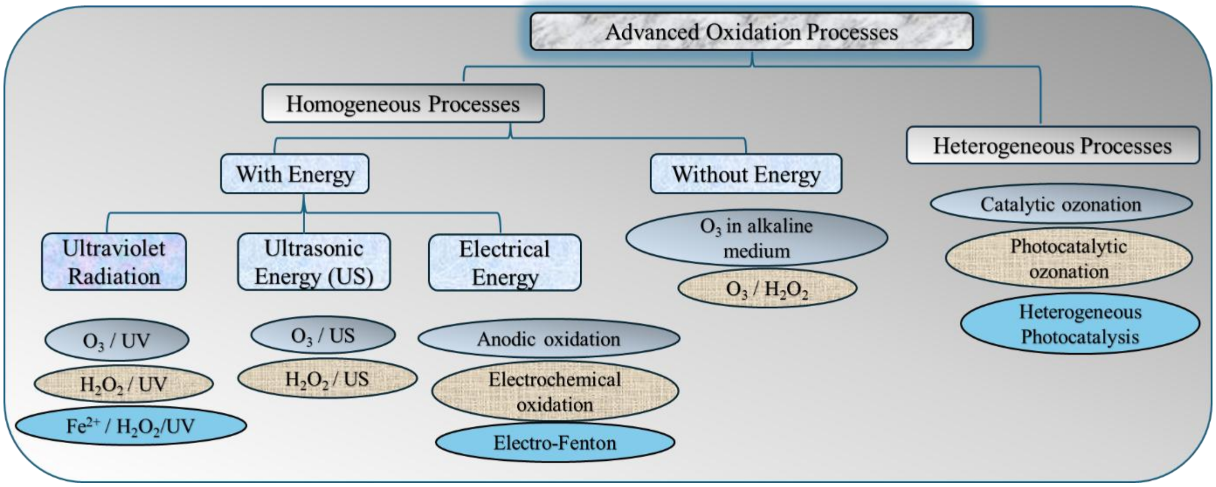

**Figure 3.3.** Types of advanced oxidation processes [61].

Water pollutants undergo chemical changes when exposed to reactive oxygen species. Most of these changes include contaminant oxidation and fragmentation, which can mineralize chemicals or produce more hazardous byproducts [62, 63]. Since ROS and pollutants respond in complicated contexts, understanding how they react is vital yet restricted. Even with the same AOP, pollutant type affects ROS interaction, and degradation pathways vary. Not all pollutants respond the same to ROS. In high oxidant concentrations, some contaminants may remain unharmed. AOP pollutant degradation is regulated by several environmental factors [64]. Most AOPs run in ambient conditions; however, regional temperatures might vary greatly. Temperature impacts gas solubility, chemical reaction kinetics, and several reaction equilibrium constants. Ozonation and UV/$H_2O_2$ oxidation, well-investigated AOPs, depend on oxidant concentration. Water pH varies widely based on location and other natural circumstances [65].

AOPs typically target a certain organic pollutant family. However, combinatorial usage of two or more AOPs increases treatment versatility, making them suited for customized therapies [66]. Recent studies have examined the technological and economic potential of AOPs for degrading dyes [67], insecticides [68], phenols [69], medicines [70], aromatic chemicals [71], and industrial waste [72]. The kinetics, reaction routes, and toxicity progression of radical degradation of organic contaminants have been intensively researched. Several successful case studies show that AOPs can manage organic-polluted wastewater from textile [73], pharmaceuticals, pesticide [74], and agricultural waste sectors [75].

Despite the rapid developments in the field, there remain several critical knowledge gaps that need to be addressed to promote the wider adoption of AOPs in mainstream water treatment practices. These include the unavailability of cost-effective AOP technologies, unknown radical generation mechanisms for certain processes, and a lack of fundamental understanding of the radical degradation pathways of various organic pollutants.

### 3.4. Photocatalysis

Photocatalysis has long been taken as a promising oxidation technique for water decontamination and disinfection over the past few decades. Photocatalytic degradation represents a method that harnesses light energy to decompose detrimental organic pollutants. Since *Carey et al.* discovered the photo-dichlorination of polychlorobiphenyls in aqueous $TiO_2$ suspension [76], photocatalytic water treatment has rapidly derived a tremendous amount of research on material synthesis, mechanism elucidation, and microreactor design, etc. The mild reaction conditions, low energy consumption, and high mineralization potential of photocatalysis are advantageous in cost-restricted scenarios [77]. One key benefit of photocatalytic water treatment is that only water and oxygen are required as the substrates for the oxidation process to proceed [78]. Despite substantial theoretical research on photocatalytic water treatment, many roadblocks are preventing the pace of photocatalysis from theoretical research to practical application. First, the yield of oxidative species (such as photogenerated holes and reactive oxygen species) is severely restricted by the inherent photogenerated electron-hole recombination inside the photocatalyst. Besides, owing to the short lifetime and non-selectivity, ROS are readily quenched by complex background constituents, such as anions, cations, and natural organic matter [79]. *Xie, Z. H. et al.* stated that only a minority of photogenerated ROS contributed to the eventual degradation of target pollutants [80]. So, the low yield and the poor effectiveness of photogenerated reactive species lead to the unsatisfactory oxidation efficiency of the single photocatalytic oxidation process, which greatly limits its practical application.

There are two forms of photocatalysis that are often employed in a variety of applications: homogeneous and heterogeneous. In homogeneous photocatalysis, the catalyst and reactants are in the same phase, whereas in heterogeneous photocatalysis, the catalyst and reactants are in distinct phases. To initiate chemical reactions, both depend on the catalyst's contact with light energy. Grasping the fundamentals of these processes is essential for creating effective photocatalytic systems aimed at eliminating organic pollutants [81].

### *3.4.1. Homogeneous Photocatalysis*

In homogeneous photocatalytic systems, both the photocatalyst and reactants coexist within the same phase, typically an aqueous solution where light-driven reactions occur at the molecular level. This configuration offers distinct advantages over heterogeneous systems, as it ensures intimate contact between catalytic species and target substrates, often resulting in enhanced reaction kinetics and improved selectivity. The homogeneous approach is particularly valuable for environmental remediation, synthetic chemistry, and biomedical applications due to its ability to generate highly reactive oxidizing species under relatively mild operating conditions**.**

Common homogeneous photocatalysts include organic dyes [82], transition metal complexes [83], and specific metal ions such as iron in Fenton-type systems [84]. Upon light absorption, these catalysts undergo electronic excitation, which initiates redox processes capable of degrading environmental contaminants or facilitating desired chemical transformations. The photo-Fenton process, in particular, has gained significant attention as it combines the efficiency of Fenton chemistry with photocatalytic activation, producing hydroxyl radicals through the interaction of iron species, hydrogen peroxide, and light irradiation**.**

Despite the high efficiency and mechanistic simplicity of homogeneous photocatalytic systems, practical implementation faces challenges related to catalyst recovery, separation from treated solutions, and long-term stability factors that remain critical considerations for industrial-scale applications.

*Saber et al.* conducted an extensive study optimizing the homogeneous photo-Fenton oxidation of organic dyes, targeting wastewater treatment [85]. Under carefully controlled conditions, they observed over 85 % removal of chemical oxygen demand and nearly 80 % reduction in total organic carbon after 180 minutes of treatment. Their research not only confirmed the process's high efficiency but also integrated predictive statistical modeling to establish optimum operating parameters for maximum contaminant removal, demonstrating clear paths for industrial application.

These studies underscore the significant role of homogeneous photocatalysis and the photo-Fenton process in environmental remediation, with ongoing efforts to optimize operational conditions, expand the range of light sources, and address practical challenges like catalyst recovery and recyclability [85].

### 3.4.2. *Heterogeneous photocatalysis*

Heterogeneous photocatalysis has emerged as a highly promising and sustainable approach for wastewater treatment due to its ease of implementation, cost-effectiveness, and ability to harness abundant solar energy [86, 87].

Photocatalysis occurs when a semiconductor absorbs light, triggering redox reactions that generate an oxidative environment in aqueous solutions. Semiconductors act as light-sensitive catalysts because of their unique electronic structure, which includes a filled valence band and an empty conduction band separated by a defined bandgap (Figure 3.4).

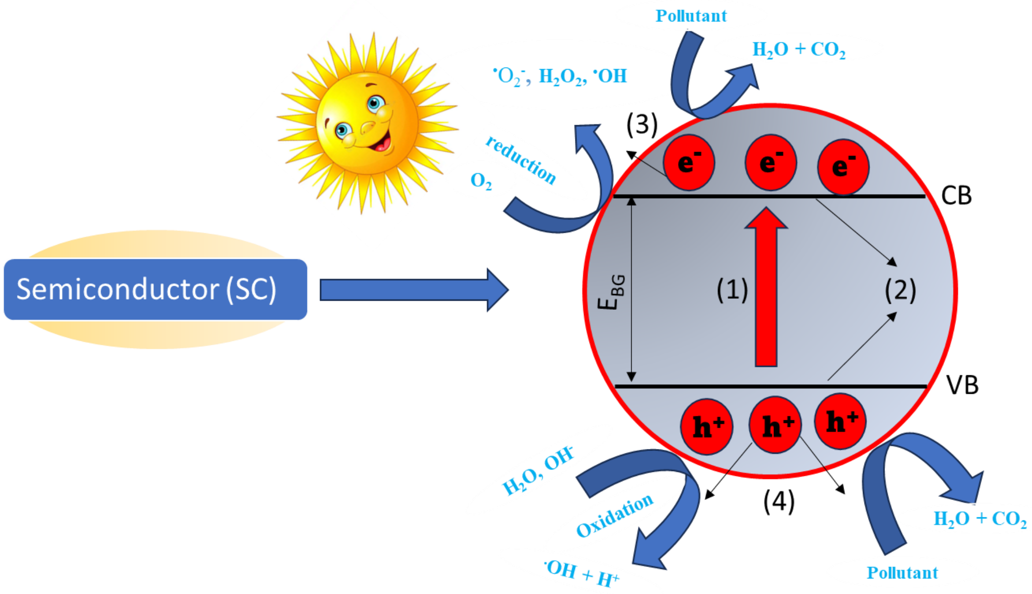

**Figure 3.4.** Semiconductor-based photocatalytic mechanism [88].

When the semiconductor (SC) absorbs photons with energy equal to or greater than this bandgap energy ($E_{BG}$), electrons are excited from the valence band to the conduction band, leaving behind electronic vacancies known as holes in the valence band [89].

$$SC + h\nu \rightarrow e^-_{CB} + h^+_{VB} \tag{3.1}$$

These photogenerated electrons and holes may migrate to the surface of the semiconductor, where they participate in oxidation and reduction reactions with adsorbed molecules, donor (D) and acceptor (A). To maximize photocatalytic efficiency, it is crucial to prevent the recombination of these charge carriers, which would otherwise dissipate the absorbed energy as heat and deactivate the catalyst.

$e^-_{CB} + h^+_{VB} \rightarrow SC + heat$ (3.2)

$e^-_{CB} + A_{ads} \rightarrow A^{\bullet-}_{ads}$ (3.3)

$h^+_{VB} + D_{ads} \rightarrow D^{\bullet+}_{ads}$ (3.4)

The electron-hole recombination can take place in multiple ways, which may be both radiative and non-radiative. Auger recombination, for instance, is a non-radiative, multi-particle process, transferring the released energy to a third carrier (either an electron or a hole) [90]. The Shockley-Read-Hall recombination is also a non-radiative process through an intermediate defect or trap state within the band gap, involving the electron transitioning from the conduction band to the trap level, and then to the valence band, releasing its energy as heat (a phonon) [91]. In a radiative recombination, the annihilation of an electron-hole pair takes place, in which the released energy is emitted in the form of a photon [92]. The emitted photon's energy is typically close to the semiconductor's bandgap energy.

During photocatalysis, the holes oxidize water or hydroxide ions to form highly reactive hydroxyl radicals, while excited electrons can reduce dissolved oxygen to produce superoxide anion radicals and ultimately hydrogen peroxide [93].

$h^+_{VB} + H_2O \rightarrow {}^{\bullet}OH + H^+$ (3.5)

$h^+_{VB} + OH^- \rightarrow {}^{\bullet}OH$ (3.6)

$e^-_{CB} + O_2 \rightarrow O_2^{\bullet-}$ (3.7)

$O_2^{\bullet-} + H^+ \rightarrow HO_2^{\bullet}$ (3.8)

$2HO_2^{\bullet} \rightarrow H_2O_2 + O_2$ (3.9)

$H_2O_2 + e^-_{CB} \rightarrow {}^{\bullet}OH + OH^-$ (3.10)

Through this sequence, advanced oxidation species such as hydroxyl and superoxide radicals play a central role in decomposing harmful organic pollutants (OP), making semiconductor-based photocatalysis an effective method for environmental remediation.

$h^+_{VB} + OP \rightarrow$ Degraded Products (3.11)

$e^-_{CB} + OP \rightarrow$ Degraded Products (3.12)

$OP + {}^{\bullet}OH/\ O_2^{\bullet-}\ /H_2O_2 \rightarrow$ Degraded Products (3.13)

Over the past few decades, various photocatalysts, including g-$C_3N_4$, $Bi_2O_3$, $WO_3$, and traditional $TiO_2$, have been extensively investigated for the photocatalytic removal of organic contaminants. However, the photocatalytic activity of pristine semiconductors is often limited by rapid charge-carrier recombination and inappropriate redox potential. To overcome these limitations, numerous modification strategies have been developed, including: (i) incorporation of transition metals such as nickel, copper, cobalt, zinc, and cerium; (ii) decoration with plasmonic metals like gold, platinum, and silver; (iii) utilization of sensitizers such as organic dyes; (iv) formation of heterojunctions with other semiconductors in binary and ternary systems; and (v) integration with carbon supports including graphene, carbon nanotubes, and activated carbon [94].

*Issaka et al.* conducted comprehensive research on heterogeneous photocatalytic processes for degrading pharmaceutical pollutants in wastewater [95]. Their work demonstrates that pharmaceutical contaminants, even at low concentrations, can act as endocrine disruptors affecting ecosystems. The research highlights the effectiveness of heterogeneous photocatalysis under light irradiation for treating these persistent pollutants, establishing it as a viable technology for pharmaceutical wastewater treatment.

*Ahmed and co-workers* published an influential review discussing various photocatalytic nanomaterials, both metal-based and metal-free, for water and wastewater purification [87]. Their work systematically presents the design and performance of photocatalytic reactors, recent advancements in visible-light photocatalysis, and the effects of fundamental parameters such as temperature, pH, catalyst loading, and reaction time. This comprehensive study has been widely cited and provides crucial insights into enhancing photocatalytic efficiency and recyclability.

*Teng and colleagues* developed heterostructured α-$Bi_2O_3$/BiOCl nanosheets for enhanced photocatalytic performance [96]. Their research demonstrates that coupling $Bi_2O_3$ (narrow band gap) with layered BiOCl (rapid photoelectron transmission) creates effective heterojunctions. The $Bi_2O_3$/BiOCl composite achieved 99.9 % removal of Rhodamine B under visible-light irradiation, significantly outperforming pristine $Bi_2O_3$ (36.0 %) and BiOCl (74.4 %). Their work contributes to understanding charge-separation mechanisms in bismuth-based photocatalysts.

*Rengifo-Herrera et al.* provide a comprehensive critical review covering five decades of research on $TiO_2$-based heterogeneous photocatalysis, especially in water disinfection and detoxification [97]. They pinpoint several significant challenges limiting the practical application of $TiO_2$ photocatalysts. Key drawbacks include the wide bandgap of $TiO_2$ (~3.2 eV) restricting activation to UV light, which constitutes only a small fraction of the solar spectrum, rapid recombination of photogenerated electron-hole pairs reducing quantum efficiency, insufficient adsorption of pollutants on the catalyst surface and photo-corrosion affecting catalyst stability.

To address these issues, the review discusses a range of strategies: doping $TiO_2$ with metals and non-metals to narrow its bandgap and enhance visible-light absorption, synthesizing heterojunction composites with other semiconductors to improve charge separation, surface modifications to increase pollutant adsorption, and fabrication of nanostructured forms to boost surface area and reaction sites. Additional approaches include noble metal loading for plasmonic enhancement and optimizing synthesis and reaction conditions to improve stability.

These insights highlight the fundamental limitations of pristine $TiO_2$ and pave the way toward more efficient photocatalysts through engineered modifications, guiding future research for environmental remediation applications.

*Yuan and colleagues* developed highly efficient Z-scheme $Ag_2CO_3/Ag/WO_3$ photocatalysts for organic pollutant degradation under visible light [98]. Their innovative work demonstrates enhanced photocatalytic activity through extended visible-light absorption via surface plasmon resonance effects and effective charge separation through Z-scheme mechanisms. The photocatalyst showed superior performance in degrading various organic pollutants, including rhodamine B, methyl orange, ciprofloxacin, and tetracycline hydrochloride, while maintaining high stability and reusability.

*Dong et al.* published an extensive review on photocatalytic Fenton-like processes for environmental remediation [99]. Their work systematically examined the synergistic effects of combining photocatalysis with Fenton chemistry, demonstrating how photo-generated electrons can enhance iron ion recycling efficiency. The researchers highlighted that the $Fe^{2+}/TiO_2/H_2O_2$/UV system showed superior performance compared to standalone $TiO_2$ photocatalysis, with degradation efficiencies reaching 99 % for methylene blue and

83 % for total organic carbon removal. Their mechanistic studies revealed that photo-induced electrons facilitate the crucial $Fe^{3+}/Fe^{2+}$ cycle, while simultaneously preventing electron-hole recombination, thereby maximizing hydroxyl radical generation.

*Khan et al.* conducted a comprehensive comparison between heterogeneous and homogeneous photo-Fenton systems for Rhodamine B degradation [100]. Their investigation employed iron(II) doped copper ferrite nanoparticles in heterogeneous systems while examining homogeneous $Fe^{2+}/H_2O_2$ processes. The study demonstrated that the heterogeneous photo-Fenton system achieved optimal performance at neutral pH conditions, overcoming the traditional limitation of requiring acidic conditions. Their work showed that the $Cu^{II}_{0.4}Fe^{II}_{0.6}Fe^{III}_{2}O_4$ catalyst maintained high activity across a broader pH range, making it more practically viable for real wastewater treatment applications.

These research examples demonstrate the evolution of heterogeneous photocatalysis from traditional $TiO_2$-based systems to advanced heterojunctions, Z-scheme mechanisms, and specialized applications for pharmaceutical and industrial wastewater treatment. The field continues to advance through innovative material design, mechanistic understanding, and practical applications for environmental remediation.

## 3.5. History of g-$C_3N_4$

The first scientific investigation into carbon nitrides began during the early nineteenth century due to researchers' interest in compound structures and possible properties. In the early 19th century, *Berzelius and Liebig* investigated cyanogen compounds as well as their derivatives before others took an interest in carbon-nitrogen frameworks [101]. Science did not genuinely explore the idea of a stable graphite-like carbon nitride polymeric structure until significant later advancements took place. Predictions developed in the late 20th century about carbon nitrides led to renewed research interest, thanks to their anticipated mechanical properties combined with high chemical stability and electronic characteristics [102].

The theoretical investigation of carbon nitrides received one of its important milestones when *Liu and Cohen et al.* postulated the existence of exceptionally mechanically strong carbon nitride compounds. Their findings generated substantial interest among researchers because they showed that β-$C_3N_4$ might match diamond's hardness level [103]. The theoretical discovery of β-$C_3N_4$ crystalline forms motivated researchers to conduct multiple experiments in synthesizing them. Intensive research could not achieve the direct synthesis of β-$C_3N_4$ because kinetic barriers, alongside the high energy needed to form crystalline phases at ambient conditions, represent major synthesis obstacles [104].

The research community started exploring polymeric carbon nitride structures, specifically the graphitic carbon nitride, despite the initial focus on crystalline carbon nitride. Research efforts by *Wang et al.* and others at the start of the 1990s achieved g-$C_3N_4$ synthesis through basic thermal polycondensation of urea, melamine, and cyanamide precursors [105]. Synthesis through these methods generated graphite-like carbon nitride materials with excellent electron-sharing properties alongside proper crystal patterns and strong chemical stability. Synthesizing graphitic carbon nitride proved possible through precursor heating between 500 °C to 600 °C under inert atmosphere or atmosphere-controlled conditions.

The crystal structure of g-$C_3N_4$ adopts graphite configurations through planar linkages, which use tri-s-triazine (heptazine) units linked by tertiary amines, as shown in Figure 3.5 below. The g-$C_3N_4$ structure provides both chemical resistance and thermal stability, thus making it suitable for different applications. The initial research about g-$C_3N_4$ concentrated on analyzing fundamental properties such as thermal decomposition patterns and mechanical strength, and band gap measurements. Research studies discovered that g-$C_3N_4$ possesses a band gap energy of about 2.7 eV, which makes it suitable for semiconductor usage [106].

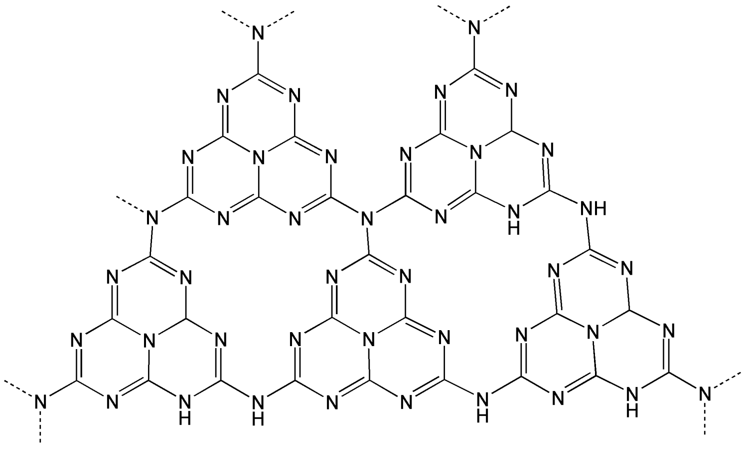

**Figure 3.5.** Tri-s-triazine (heptazine) g-$C_3N_4$ [107].

Research concerning g-$C_3N_4$ took a significant trajectory when scientists discovered its ability to function as a photocatalyst. The research by *Wang et al.* showed that g-$C_3N_4$ behaves as a powerful metal-free photocatalyst that produces hydrogen from water using visible light [105]. These findings were significant because scientists primarily used metal-containing materials such as $TiO_2$ for photocatalysis, where UV light activation was necessary [108]. By its ability to absorb visible light and enable photocatalytic activities g-$C_3N_4$ enabled sustainable energy applications, particularly for water splitting and the reduction of $CO_2$ and environmental clean-up operations [109].

The g-$C_3N_4$ research exhibited accelerated development after this breakthrough occurred. Researchers started changing the g-$C_3N_4$ structure and surface properties for better photocatalytic productivity. Scientists improved g-$C_3N_4$ photocatalysis by incorporating sulfur [110], phosphorus [111], and oxygen dopants [112] and implementing porous structure fabrication and heterogeneous semiconductor formation, and metal or carbon-based material composite development. The researchers applied structural changes to g-$C_3N_4$ because they wanted to improve its photogenerated electron-hole pair separation capability, together with light absorption, along with reaction rate, although pristine g-$C_3N_4$ exhibited limited surface area and fast electron-hole pair recombination rates.

The application range of g-$C_3N_4$ extends beyond photocatalysis. Scientists have examined g-$C_3N_4$ for various applications, such as photodetectors [113] and sensors [114] and energy storage devices like lithium-ion batteries and supercapacitors, and electrocatalysis [115]. For these technologies, their metal-free character, tuned electrical structure, and simplicity of synthesis appeal. For adsorption and catalysis, for example, the nitrogen-rich surface of g-$C_3N_4$ provides active sites; its two-dimensional form facilitates effective electron flow.

The 2D structure provides a high degree of crystallinity and an extended conjugated planar network, which enables efficient charge delocalization and mobility within the plane. This facilitates the rapid transport of photoexcited electrons across the layers, reducing the probability of electron-hole recombination [116].

The high surface-to-volume ratio typical of 2D materials increases the availability of active sites and shortens the diffusion length for charge carriers. Additionally, the anisotropic electronic band structure in the layered material promotes directional charge transport, enhancing the separation of photogenerated electron-hole pairs. As a result, 2D g-$C_3N_4$-based photocatalysts exhibit improved charge carrier dynamics, which are crucial for effective photocatalytic processes such as pollutant degradation.

These photophysical characteristics distinguish 2D materials from their bulk counterparts and underpin their growing importance in photocatalysis.

Recent years have witnessed the advancement of innovative synthesis procedures for g-$C_3N_4$, focused on enhancing control over its shape, porosity, and crystallinity. Template-assisted synthesis techniques have been utilized to produce mesoporous g-$C_3N_4$, resulting in increased surface areas and enhanced accessibility of active sites [117]. Likewise, thermal exfoliation [118] and liquid-phase exfoliation [119] methods have been employed to generate ultrathin g-$C_3N_4$ nanosheets exhibiting improved electrical characteristics and heightened reactivity.

Present-day scientists choose bio-inspired and green synthesis methods to manufacture g-$C_3N_4$. Scientists develop g-$C_3N_4$-based materials for sustainable materials science through their combination of natural polymers and plant extracts, and low-toxicity preparation techniques [120]. These production techniques simultaneously decrease the environmental impact while introducing distinctive structural features capable of enhancing performance in photocatalysis and sensing applications.

Notwithstanding the considerable advancements achieved in recent decades, obstacles persist in the domain of g-$C_3N_4$ research. A significant concern is the comparatively low quantum efficiency of g-$C_3N_4$ in photocatalytic processes compared to certain metal-based systems. Furthermore, its absorption of visible light is confined to wavelengths below roughly 460 nm, limiting its exploitation of the entire solar spectrum. Researchers persist in exploring methods to surmount these constraints, including the fabrication of advanced heterostructures, doping techniques, and the integration of g-$C_3N_4$ with plasmonic materials to enhance light absorption and optimize charge carrier dynamics [121].

Many researchers in materials science focus on developing sustainable multifunctional metal-free materials after studying the historical development of graphitic carbon nitride. After its theoretical origin in the 1990s followed by its first synthesis, g-$C_3N_4$ became adaptable for electrical applications and environmental uses, emerging as a dominant photocatalyst in the 2000s. Beyond its current applications, g-$C_3N_4$ shows promise for future breakthroughs in green energy and catalysis through the continuous advancements in fabrication methods and structural innovations, and composite designs.

## 3.6. Methods for the Preparation of g-$C_3N_4$

Researchers now possess a flexible framework for the advancements of graphitic carbon nitride synthesis, thanks to substantial progress made over time. The sections ahead detail multiple vital synthesis techniques that offer specific advantages and drawbacks.

### *3.6.1. Sol-gel method*

The sol-gel process functions as an intricate method to produce various ceramic materials through its synthesis routes. The bottom-up synthesis approach provided effective control over purity, homogeneity, and dimensions through adaptable synthesis methodology (Figure 3.6). A sol represents a colloidal solution which develops when precursors undergo hydrolysis followed by polymerisation. Inorganic metal salts, together with metal-organic complexes and metal alkoxides, form the precursors during this procedure. The process of polymerization completion, together with solvent evaporation, led to the development of a liquid sol into a solid gel phase [122].

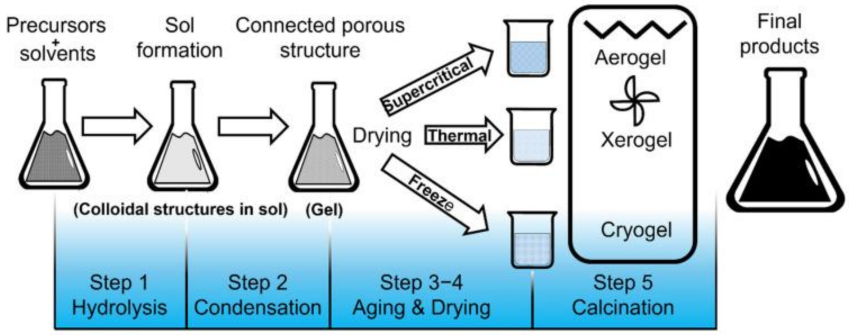

**Figure 3.6.** Sol-gel synthesis methodology [122].

### *3.6.2. Hydrothermal method*

Hydrothermal synthesis takes place inside steel pressure containers (autoclaves), which may or may not have a teflon lining during reaction conditions that require temperature control and pressure management while using an aqueous solution [123]. In the hydrothermal method, starting materials are usually solid or powder precursors (often metal salts, oxides, or other inorganic compounds) or even gel precursors, all dissolved or suspended in water for reaction under elevated temperature and pressure. The thermal conditions reach beyond the water boiling point and result in vapour pressure saturation. Autoclave internal pressure derives mainly from solution temperature alongside the amount of fluid added to the chamber. The ceramics industry makes extensive use of this method for preparing fine particles.

### *3.6.3. Solvothermal method*

The solvothermal method performs similarly to hydrothermal synthesis and only uses non-aqueous solvents as its main distinction. The elevated temperature requirement is needed since the process uses organic solvents whose boiling points are higher than those used in hydrothermal reactions [124]. The core starting materials are generally the same (e.g., melamine or related nitrogen-rich precursors), but the solvent system and synthesis conditions differ significantly between sol-gel, hydrothermal, and solvothermal methods, affecting the final material structure and properties. Solvothermal chemistry surpasses the hydrothermal procedure for controlling the size and shape characteristics in g-$C_3N_4$ synthesis. Reaction control helps to establish specific shapes and structures when using these fabrication methods with g-$C_3N_4$. The chosen solvent controls the final properties of the produced material, as shown in Table 3.1 below. The solvothermal technique enables the production of hierarchical g-$C_3N_4$ structures with improved photocatalytic performances (Figure 3.7). The recent use of these techniques has proven efficient in making g-$C_3N_4$ usable for applications.

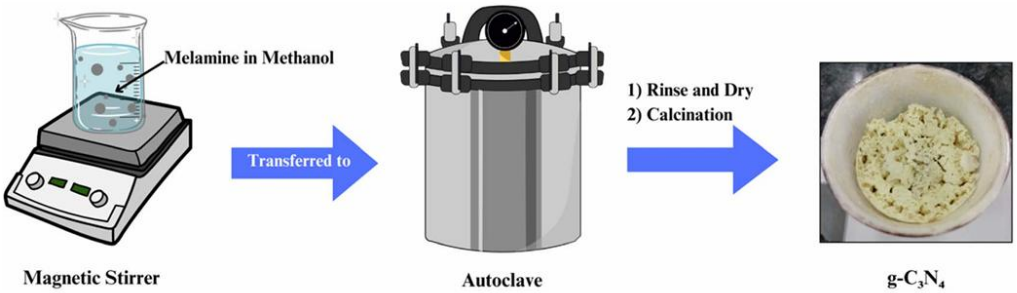

**Figure 3.7.** Solvothermal synthesis scheme [123].

**Table 3.1.** Solvent effects in solvothermal synthesis of g-$C_3N_4$.

| Solvent | Boiling Point (°C) | Type | Morphology | Photo Effect | Reference |
|---|---|---|---|---|---|
| Ethanol | 78 | Protic | Nanoporous | High | [125] |
| DMF | 153 | Aprotic | Thin layer | Moderate | [126] |
| Acetonitrile | 82 | Aprotic | Thick layer | Moderate-high | [127] |
| Ethylene glycol | 197 | Protic | Nanosheet | Moderate-high | [128] |
| DMSO | 189 | Aprotic | Nanoporous | High | [129] |

### *3.6.4. Chemical vapor deposition (CVD)*

Synthesis of g-$C_3N_4$ through CVD (Figure 3.8) provides researchers with total command over forming materials with determined dimensions and thickness levels. CVD techniques use cyanamide along with volatile precursors that enter high-temperature reactors to generate g-$C_3N_4$ on substrates. The CVD technique enables the production of thin films as well as nanostructures, which have direct implications for photovoltaic and optoelectronic technologies. Manufacturing costs rise at the same time as the requirement for sophisticated equipment during production using the CVD method [130].

**Figure 3.8.** CVD synthesis methodology [131].

### 3.6.5. Template-assisted synthesis

Template-assisted synthesis (Figure 3.9) of g-$C_3N_4$ commonly employs hard templates such as silica (e.g., SBA-15, MCM-41, or $SiO_2$ nanospheres) and soft templates like block copolymers or surfactants to dictate the pore size, structure, and morphology of the resulting photocatalyst [132, 133].

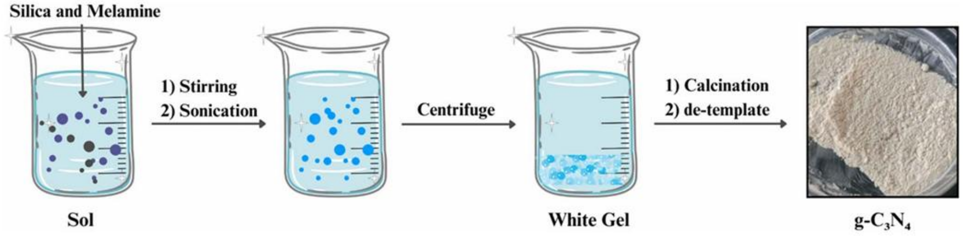

**Figure 3.9.** Template-assisted synthesis [123].

Hard templates create ordered mesoporous structures with tunable pore sizes (typically 3-50 nm) and significantly increased surface area, which facilitate enhanced mass transfer, more exposed active sites, and superior charge carrier separation. For example, using SBA-15 silica as a template forms g-$C_3N_4$ with uniform mesopores (~7-30 nm) and surface areas reaching several hundred $m^2/g$, substantially boosting its photocatalytic efficiency for water purification and solar-driven applications. Soft templates can also direct the formation of layered, nanosheet, or other complex architectures, impacting light absorption and electron mobility. The resulting characteristics influenced by template choice include surface area, pore size distribution, pore connectivity, crystallinity, charge-transport pathways, and ultimately the material’s overall photocatalytic performance.

**Mechanism of Template-Assisted Synthesis:** In the template-assisted synthesis method, a porous material, such as carbon-based substances or silica with well-defined pore sizes and shapes, is used as a scaffold. When nitrogen-rich precursors (e.g., melamine, dicyandiamide) undergo thermal polymerization in the presence of this template, the growing g-$C_3N_4$ network forms along the surfaces and within the pores of the template. The template physically restricts the structure, directing the formation of g-$C_3N_4$ with controlled porosity and surface area. After the polymerization step, the template is removed, typically by chemical etching or calcination, resulting in a porous g-$C_3N_4$ material whose morphology mirrors that of the original template [134].

**Chemistry Behind Template-Assisted Synthesis:** Chemically, the synthesis involves thermal condensation of nitrogen-rich precursors, which polymerize through successive condensation reactions to form the layered, conjugated polymeric network of g-$C_3N_4$. This process includes the formation of tri-s-triazine rings linked via planar amino groups. The template influences these reactions primarily by spatially confining the polymer growth, ensuring the resulting g-$C_3N_4$ has increased surface area and pore volume. The chemical stability of g-$C_3N_4$ enables it to maintain its structure even after the removal of the template, retaining a porous architecture beneficial for enhanced photocatalytic activity in applications such as solar energy conversion and pollutant degradation [135].

### *3.6.6. Doping and co-doping strategies*

Research efforts aimed at enhancing the photocatalytic activity of graphitic carbon nitride widely employ doping and co-doping strategies involving elements such as sulfur, boron, and various metals (Figure 3.10).

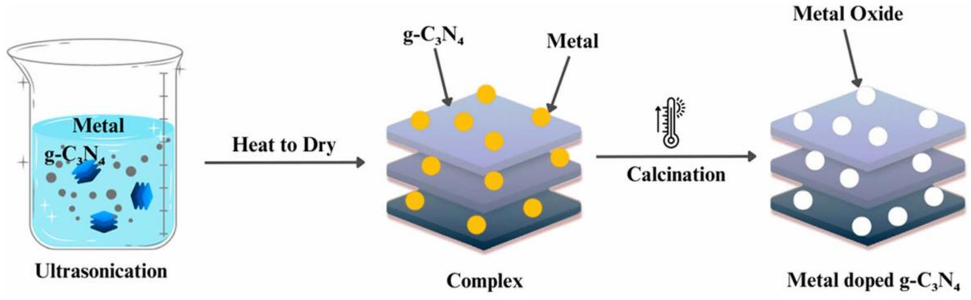

**Figure 3.10.** Doping and co-doping [123].

These doping agents alter the electronic structure of g-$C_3N_4$ by substituting or introducing defect sites within the lattice, which expands the range of active sites available for photocatalytic reactions. Specifically, non-metal dopants like sulfur and boron [136] can narrow the bandgap by shifting the conduction and valence bands, thereby improving visible-light absorption and facilitating more efficient separation and transport of photogenerated charge carriers. Metal dopants, such as iron or copper [137], often introduce mid-gap states that act as electron traps or catalytic centers, further enhancing redox capabilities. Co-doping, which involves the simultaneous incorporation of two or more dopants, can produce synergistic effects that enhance photocatalytic performance beyond the sum of individual dopants. This is achieved through improved charge-carrier dynamics, augmented surface area, and better structural stability. Such modifications are central to tuning g-$C_3N_4$ photocatalysts for applications in pollutant degradation, hydrogen evolution, and selective oxidation reactions.

### *3.6.7. Thermal polymerization*

Among modern production methods for g-$C_3N_4$ material, thermal polymerization stands out due to its economical use of precursors such as urea and cyanamide, as well as additional precursors as dicyanamide, thiourea, cyanuric acid, and melamine (Figure 3.11). The thermal precursor heating takes place between 500-600 °C in unreactive gas environments. Through the thermal polymerization process, an extensive layered g-$C_3N_4$ structure with a large surface area can be achieved, so the material works well across multiple photocatalytic applications. The high popularity of this method stems from its inexpensive nature as well as user-friendly characteristics [123].

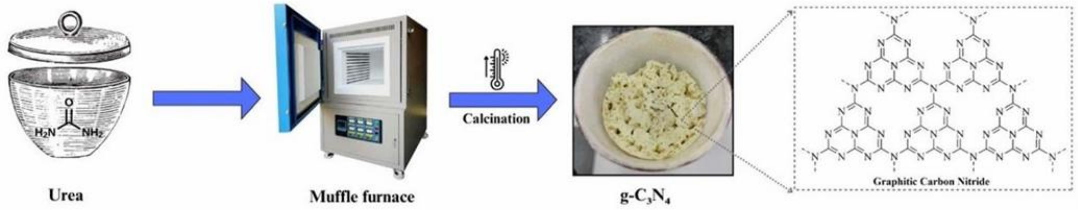

**Figure 3.11.** Thermal polymerization [123].

The chemistry of graphitic carbon nitride (g-$C_3N_4$) is defined by its unique polymeric structure, consisting of heptazine (tri-s-triazine) units linked through planar, aromatic nitrogen-rich frameworks. The formation of g-$C_3N_4$ typically involves the thermal polymerization of organic precursors such as melamine, thiourea, or urea under controlled heating. During synthesis, these precursors undergo sequential condensation reactions and molecular rearrangement at increasing temperatures, producing intermediate compounds like melam and melem, which facilitate the transition from small molecular building blocks to extended networks (Figure 3.12). The final structure is established at around 550 °C, where melem units condense further to form the robust, graphitic layers characteristic of g-$C_3N_4$.

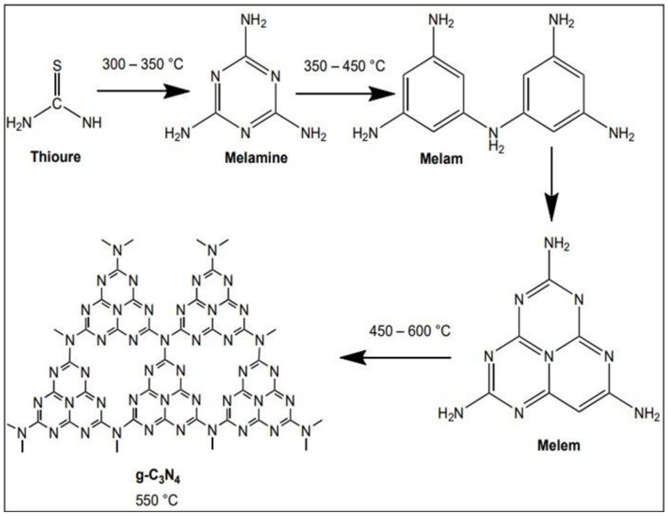

**Figure 3.12.** Schematic representation of g-$C_3N_4$ synthesis, illustrating potential intermediate phases generated at various temperature intervals [138].

Chemically, g-$C_3N_4$ is composed entirely of carbon and nitrogen atoms arranged in a conjugated polymer network, with trace hydrogen commonly retained in terminal amino groups. This framework imparts high thermal and oxidative stability, strong π-conjugation, and a moderate band gap, making it an effective visible-light-activated semiconductor for photocatalytic applications. The synthesis chemistry, particularly the selection of precursors, heating profile, and control over intermediate phases, influences the crystallinity, surface area, defect density, and thus the photocatalytic efficiency of the final material. Detailed understanding and regulation of these chemical aspects are fundamental for designing g-$C_3N_4$ with optimized properties suited to water treatment, solar energy conversion, and related fields.

Graphitic carbon nitride demonstrates significant growth, enabling multiple operational approaches that have different advantages alongside limitations. The thermal polymerization of melamine precursors through affordable processing methods produces layered g-$C_3N_4$ materials suitable for extensive applications. Reported production expenses, together with unique processing devices, make chemical vapor deposition a precise method for creating dimensions and shapes. Solvothermal and hydrothermal processes use intense pressure combined with high-temperature arrangements to obtain precise morphological control, which has made them prominent for modifying g-$C_3N_4$ characteristics. The use of templates enables special structures by modifying both surface area requirements and pore formation, which determines photocatalytic performance. The photocatalytic activity can be enhanced by electronic structure modifications together with doping and multi-element doping methods. Different methods provide different performance outcomes through yield and cost, and complexity factors. The relatively easy and cost-effective thermal polymerization process does not deliver exact precision. CVD offers better control than its higher price point. Solvothermal and hydrothermal methods allow controlling morphological results yet require particular reaction conditions. The synthesis process using templates enables researchers to create customized structures, even though it requires more complex procedures. Techniques that use doping enable better performance, though they make processes more complicated. The selection process is based on performance requirements, which define expense implications and operational efficiency.

The selection of synthesis methods for g-$C_3N_4$ relies on its intended applications alongside required performance characteristics. The different synthesis methods available allow researchers and engineers to develop suitable g-$C_3N_4$ materials that fulfill distinct requirements for sustainable environmental applications.

## 3.7. Role of g-$C_3N_4$ as photocatalyst

Graphitic carbon nitride has gained significant attention as an exceptionally promising photocatalytic material, thanks to its distinctive characteristics and environmental advantages. This conjugated polymer, primarily composed of carbon and nitrogen with minimal hydrogen content, stands out as a metal-free, eco-friendly, and sustainable photocatalyst.

The photocatalytic activity of g-$C_3N_4$ is fundamentally attributed to its capacity to generate electron-hole pairs upon light absorption (see Eq. 3.1 in Section 3.4.2). These photogenerated charge carriers are transported to the material surface, where holes participate in the formation of hydroxyl radicals (Eq. 3.5-3.6), while electrons reduce dissolved oxygen, yielding superoxide radicals (see Eq. 3.7). Both reactive species play significant and complementary roles in the oxidative degradation of organic pollutants, as illustrated in the reaction pathways detailed in Section 3.4.2.

Despite these promising characteristics, pure g-$C_3N_4$ encounters several limitations that restrict its practical effectiveness. The material can only absorb a limited portion of the visible-light spectrum (up to approximately 450 nm), which constrains its ability to utilize the full range of solar energy. Additionally, the photogenerated electron-hole pairs tend to recombine rapidly, which significantly reduces the overall photocatalytic efficiency by limiting the availability of reactive species for pollutant degradation. These challenges have motivated extensive research into modification strategies to enhance g-$C_3N_4$ performance and broaden its practical applicability.

Incorporating silver into g-$C_3N_4$ matrices has proven to be a powerful approach for improving photocatalytic performance. The catalyst g-$C_3N_4$ is commonly produced by thermal polymerization, and Ag nanoparticles are introduced via calcination, impregnation, green synthesis, and in situ reduction (Table 3.2).

**Table 3.2.** Literature for Ag-g-$C_3N_4$ preparation method.

| SN | Light source | Silver modification | Pollutant | Reference |
|---|---|---|---|---|
| 1. | Vis | urea+ silver nitrate pyrolysis | Indocyanine green | [139] |
| 2. | UV-Vis | impregnation method with ethanol on the surface | Acid orange 7 | [140] |
| 3. | Vis | single-strain biofilm fabrication | Methylene blue | [141] |
| 4. | Vis | purple leaf extract | Rhodamine B | [142] |
| 5. | Vis | dicyanamide + silver nitrate polycondensation | Ciprofloxacin | [143] |
| 6. | UV | reduction of silver nitrate with $NaBH_4$ | Rhodamine B | [144] |
| 7. | UV | reduction of silver nitrate with $NaBH_4$ | Methyl orange | [145] |

The synergy between Ag NP's surface plasmon resonance and the semiconductor properties of g-$C_3N_4$ results in enhanced interfacial charge transfer and visible-light utilization. This leads to efficient degradation of various pollutants, including dyes, antibiotics, and colourless organics, positioning Ag-modified g-$C_3N_4$ as a promising candidate for environmental remediation under UV and visible light.

The integration of bismuth-based materials, such as $Bi_2S_3$ and $Bi_2O_3$, with graphitic carbon nitride has emerged as an effective strategy to boost photocatalytic activity. Typically, g-$C_3N_4$ is synthesized through thermal polymerization, while bismuth nanoparticles are formed using different techniques before or after being combined with g-$C_3N_4$ (Table 3.3). These hybrid structures create heterojunctions that enhance charge separation and light absorption, leading to high degradation efficiencies for pollutants like methylene blue, tetracycline, ciprofloxacin, and para-nitrophenol. The resulting composites show strong potential for practical applications in water purification due to their stability and reusability.

**Table 3.3.** Literature for the g-$C_3N_4$-$Bi_2S_3$/$Bi_2O_3$ preparation method.

| SN | Light source | $Bi_2S_3$/$Bi_2O_3$ modification | Pollutant | Reference |
|---|---|---|---|---|
| 1. | UV | hydrothermal deposition | Reactive Black 5 | [146] |
| 2. | UV | hydrothermal deposition | Rhodamine B | [147] |
| 3. | Vis | one-step hydrothermal | Malachite green | [148] |
| 4. | UV | peroxymonosulfate activation | Methylene blue | [149] |
| 5. | Vis | ball milling | Methylene blue | [150] |
| 6. | Vis | impregnation method with ethanol on the surface | Tetracycline hydrochloride | [151] |
| 7. | UV | impregnation method with ethylene glycol on the surface | Toluene | [152] |
| 8. | UV | thermal treatment | Tetracycline | [153] |

Recent research has demonstrated that modifying g-$C_3N_4$ with zinc sulfide or zinc oxide nanoparticles significantly enhances its photocatalytic activity for the degradation of various organic pollutants, including dyes (Azo dye, rhodamine B, methylene blue), antibiotics (tetracycline), and endocrine disruptors (bisphenol A) under visible light irradiation. The g-$C_3N_4$ is typically synthesized via thermal polymerization of nitrogen-rich precursors, while ZnS and ZnO nanoparticles are prepared by impregnation, hydrothermal, mechanochemical, or wet-chemical methods, and then integrated into the g-$C_3N_4$ matrix to form heterojunctions (Table 3.4). These composites improve charge separation, extend visible-light absorption, and boost degradation efficiency, making them promising candidates for advanced oxidation processes in water treatment applications.

**Table 3.4.** Literature for the g-$C_3N_4$-ZnS/ZnO preparation method.

| SN | Light source | ZnS/ZnO modification | Pollutant | Reference |
|---|---|---|---|---|
| 1. | Sun light | thermal polymerization of thiourea and zinc acetate | Azo dye | [154] |
| 2. | Vis | impregnation | Rhodamine B | [155] |
| 3. | UV | thermal impregnation | Methylene blue | [156] |
| 4. | UV-Vis | thermal impregnation | Reactive black 5 | [157] |
| 5. | Vis | thermal polymerization of urea and zinc acetate | Bisphenol A | [158] |
| 6. | Solar | in situ mechanochemical method | Methylene blue | [159] |
| 7. | Vis | solvothermal reaction of g-$C_3N_4$, thiourea and zinc acetate | Rhodamine B | [160] |
| 8. | Vis | hydrothermal method | Tetracycline | [161] |

While many photocatalysis studies (as shown above in Tables 3.2, 3.3, and 3.4) employ colored dyes such as methylene blue, rhodamine B, or methyl orange for facile spectrophotometric monitoring, these dyes may not truly represent pollutant degradation in real-world water treatment. Colored dyes can undergo photosensitization and have different reactivity than non-chromophoric organic contaminants. We focused on colorless pollutants such as para-nitrophenol, which addresses this gap and enables a more representative assessment of a photocatalyst's efficiency in degrading relevant, real-world pollutants.

Recent years have witnessed substantial progress in the development of modified g-$C_3N_4$-based photocatalysts specifically targeting the degradation of para-nitrophenol, a challenging persistent water pollutant. Researchers have pursued both metal and non-metal modifications to overcome the shortcomings of pristine g-$C_3N_4$, including rapid electron-hole recombination and limited visible-light absorption (Table 3.5).

**Table 3.5.** Literature comparison for para-nitrophenol degradation under visible light.

| Catalyst | Degradation Efficiency | Key Strengths | Reference |
|---|---|---|---|
| g-$C_3N_4$-MCy | High | Improved microstructure and charge mobility, no metal sulfide heterojunction | Abbasi et al. [162] |
| $ZrO_2$/g-$C_3N_4$ | High | Increased surface area, defect-mediated charge separation | Zarei et al. [163] |
| Ag/g-$C_3N_4$ | 100% | Plasmonic enhancement, rapid electron transfer, costly precious metal | Yang et al. [164] |
| NiO/g-$C_3N_4$ | High | p-n junction, enhanced charge separation, multiple oxidation states | Ismael et al. [165] |
| g-$C_3N_4$/CdS | ~99% | S-scheme heterojunction for strong redox potential; stability | Saad et al. [166] |
| Cu/g-$C_3N_4$ | Significant (7× increase) | Photo-Fenton synergism, radical overproduction | Xuan et al. [167] |

*Abbasi et al.* pioneered an innovative synthesis approach by utilizing melamine and cyanuric acid as dual precursors for g-$C_3N_4$ fabrication [162]. This method deviates from conventional single precursor approaches and creates a more structured polymeric network. The melamine-cyanuric acid combination forms hydrogen-bonded supramolecular assemblies during the thermal condensation process, resulting in a more ordered and crystalline g-$C_3N_4$ structure. This enhanced organization leads to improved π-conjugated systems with better electron delocalization, facilitating superior charge carrier mobility. The melamine and cyanuric acid-derived g-$C_3N_4$ exhibits increased surface area due to the controlled thermal decomposition of the precursor complex, creating more accessible active sites for para-nitrophenol adsorption and subsequent photocatalytic degradation. The improved microstructure also enhances light-harvesting efficiency across the visible spectrum, making it particularly effective for solar-driven applications.

*Zarei and colleagues'* work on zirconia-modified g-$C_3N_4$ showcases the role of high-surface-area supports in photocatalyst enhancement [163]. $ZrO_2$, with its amphoteric nature and high chemical stability, serves multiple functions in the composite system. Its high surface area (often >100 $m^2/g$) provides numerous anchoring sites for g-$C_3N_4$ sheets, preventing restacking and maintaining accessible active sites. The $ZrO_2$ incorporation creates oxygen vacancies and defect states that can trap photogenerated electrons, reducing recombination rates. Additionally, the oxide-nitride interface generates built-in electric fields that facilitate charge carrier separation. The bandgap narrowing observed in this system results from the formation of Zr-N bonds at the interface, creating intermediate energy levels that enable more efficient visible light utilization. The enhanced charge mobility stems from the formation of percolation pathways through the $ZrO_2$ network, allowing rapid electron transport to surface active sites.

*Yang et al.* silver-modified g-$C_3N_4$ represents one of the most effective metal-enhanced photocatalytic systems, achieving complete para-nitrophenol removal with an exceptionally high rate constant of 0.497 $min^{-1}$ [164]. The outstanding performance results from multiple enhancement mechanisms operating simultaneously. Silver nanoparticles function as electron sinks, capturing photogenerated electrons from g-$C_3N_4$ conduction band and preventing electron-hole recombination. The Ag nanoparticles also exhibit localized surface plasmon resonance (LSPR) effects under visible light, creating hot electrons that can be injected into the g-$C_3N_4$ conduction band, effectively extending the photocatalyst spectral response. The metallic nature of silver provides excellent electrical conductivity, facilitating rapid electron transport to surface reaction sites. Furthermore, silver catalytic properties enable direct reduction of para-nitrophenol through electron transfer processes, creating a dual-pathway degradation mechanism combining photocatalytic oxidation with catalytic reduction.

*Ismael et al.* reported that the NiO/g-$C_3N_4$ photocatalyst efficiently degrades para-nitrophenol under visible light due to the formation of a p–n heterojunction between p-type NiO and n-type g-$C_3N_4$ [165]. This interface generates a built-in electric field that enhances electron–hole separation, with electrons migrating to g-$C_3N_4$ and holes to NiO, thereby reducing recombination and accelerating redox reactions. The multiple oxidation states of Ni ($Ni^{2+}/Ni^{3+}$) provide additional pathways for hole transfer and generation of reactive oxygen species, while visible-light absorption of NiO enables energetic electron injection into the conduction band of g-$C_3N_4$. Together, these effects significantly improve photocatalytic performance, achieving much higher para-nitrophenol degradation efficiency than pristine g-$C_3N_4$.

*Saad et al.'s* work represents a significant advancement in heterojunction design through the S-scheme mechanism [166]. Unlike conventional Type-II heterojunctions, the S-scheme promotes the recombination of electrons and holes with weaker redox potential while preserving those with stronger oxidizing and reducing capabilities. In the g-$C_3N_4$/CdS system, electrons from CdS conduction band recombine with holes in g-$C_3N_4$ valence band, leaving highly energetic electrons in g-$C_3N_4$ conduction band and strongly oxidizing holes in CdS valence band. This mechanism achieves the remarkable ~99 % para-nitrophenol removal by maximizing the utilization of photogenerated charge carriers with optimal redox potentials. The 2D-2D interface provides an extensive contact area, ensuring efficient charge transfer kinetics. The system stability results from the thermodynamically favorable charge transfer pathway that reduces interfacial defect formation and photo corrosion.

*Xuan et al.'s* innovative approach combines photocatalysis with Fenton-like chemistry to achieve a sevenfold enhancement in degradation rates [167]. The copper modification serves multiple functions: $Cu^{2+}/Cu^{+}$ redox cycling facilitates $H_2O_2$ decomposition to generate hydroxyl radicals, while copper nanoparticles act as electron sinks to prevent recombination. The system operates through synergistic mechanisms where photogenerated electrons reduce $Cu^{2+}$ to $Cu^{+}$, which then reacts with $H_2O_2$ to produce $^{\bullet}OH$ radicals and regenerate $Cu^{2+}$. Simultaneously, photogenerated holes directly oxidize para-nitrophenol or react with water molecules to form additional hydroxyl radicals. This dual-pathway approach dramatically increases the concentration of reactive species compared to pure photocatalytic systems. The copper modification also enhances visible-light absorption through ligand-to-metal charge-transfer transitions, broadening the photocatalyst spectral response and improving solar energy utilization efficiency.

## 3.8. Photocatalytic assessment

The accurate assessment of photocatalytic materials fundamentally relies on understanding the generation and mechanistic roles of reactive oxygen species (ROS) during pollutant degradation processes. The comprehensive literature below examines the extensive research on coumarin and 1,4-hydroquinone as molecular probes for detecting hydroxyl radicals and superoxide radicals, respectively, with particular emphasis on their applications in photocatalytic systems.

### *3.8.1. Coumarin as a hydroxyl radical scavenger*

To evaluate how well these catalysts perform, we measured their ability to produce two important types of reactive species: hydroxyl radicals and superoxide radicals. when exposed to both UV and visible light. The formation of these radicals is considered a hallmark of effective photocatalytic activity because they act like molecular attackers that break down organic pollutants, leading to their complete degradation. To track hydroxyl radical production, we used coumarin as a chemical probe that reacts specifically with these radicals. We monitored the formation of a fluorescent compound called 7-OHC by measuring its light emission at 453 nanometers, then calculated how quickly these radicals were being generated by analyzing how 7-OHC concentrations changed over time. The amount of 7-OHC produced directly corresponded to the quantity of hydroxyl radicals created.

The reported work by *Leandri et al.* established coumarin as a quantitative probe for hydroxyl radical formation in heterogeneous photocatalysis [168]. Their systematic investigation revealed that coumarin produces multiple hydroxylated products upon reaction with $^{\bullet}$OH radicals, with 7-hydroxycoumarin being the primary fluorescent product. The study identified critical experimental challenges, particularly the inner-filtering effect caused by competing absorption between coumarin and 7-OHC, necessitating careful calibration procedures for accurate quantification.

*Nosaka et al.* provided important methodological commentary, emphasizing that coumarin reaction with hydroxyl radicals produces several hydroxylated isomers beyond 7-OHC [169]. This observation highlighted the need for comprehensive analytical approaches that account for all hydroxylated products rather than relying solely on 7-OHC fluorescence measurements.

A significant methodological breakthrough was achieved by *McCormick et al.,* who developed an electrochemical screening method capable of in situ monitoring of all main mono-hydroxylated coumarin products [170]. Their HPLC analysis revealed that 7-OHC accounts for approximately 38.5 % ± 2.9 % of total hydroxylated products, with 5-OHC, 6-OHC, and 8-OHC contributing 39 % ± 3.5 %, 15 % ± 2.4 %, and 7.5 % ± 1.8 %, respectively. This comprehensive approach provides a more accurate representation of total hydroxyl radical production compared to traditional fluorescence-based methods.

*Ducrozet et al.* further advanced the methodology by combining spectrophotometry and fluorimetry for hydroxyl radical quantification in low-temperature plasma systems [171]. Their study demonstrated that approximately 90 % of hydroxyl radicals react with coumarin under specific conditions, with 7-OHC formation representing only 3.3 % of total hydroxyl radical generation. This work emphasized the critical importance of pH control during coumarin-based assays for accurate quantification.

Recent applications of coumarin probing in photocatalytic systems have revealed significant insights into ROS generation mechanisms. *Wafi et al.* demonstrated coumarin's effectiveness in assessing photocatalytic hydroxyl radical formation, confirming its role as an adequate probe for evaluating photocatalytic oxidation processes [172]. The study highlighted coumarin selectivity and sensitivity for hydroxyl radical detection in complex photocatalytic environments.

*Geng et al.* developed an innovative online chemiluminescence method using coumarin for real-time hydroxyl radical determination in photocatalytic processes and Fenton reactions [173]. This advancement enabled continuous monitoring of hydroxyl radical generation, providing dynamic insights into photocatalytic mechanisms under various operational conditions.

The article "Revisiting terephthalic acid (TA) and coumarin as probes for photoluminescent determination of hydroxyl radical formation rate in heterogeneous photocatalysis" systematically investigates the effectiveness of terephthalic acid and coumarin as fluorescence-based probe molecules for detecting and quantifying hydroxyl radical generation during heterogeneous photocatalytic reactions [174]. The study highlights not only the direct oxidation reactions between these probes and $^{\bullet}OH$ radicals but also examines the influence of factors such as pH, catalyst surface adsorption, and the formation of potential side products or intermediates that can interfere with accurate measurement. The authors demonstrate that while both TA and coumarin can be used to monitor $^{\bullet}OH$ production, their selectivity, efficiency, and the reliability of quantification can vary, depending on the reaction environment and interfering species, emphasizing the importance of careful optimization and interpretation when using these probes in photocatalysis research.

### *3.8.2. 1,4-hydroquinone as a superoxide radical scavenger*

For detecting superoxide radicals, we employed a different approach using hydroquinone degradation experiments. This method works on the principle that superoxide radicals will break down 1,4-hydroquinone, so by monitoring this degradation process, we could confirm that superoxide radicals were indeed being produced during the photocatalytic reactions. The successful breakdown of hydroquinone validated that the catalysts were generating these important reactive species, proving this technique to be a reliable way to detect superoxide radical formation in photocatalytic systems.

*Fónagy et al.* conducted an extensive investigation of 1,4-benzoquinone and 1,4-hydroquinone for determining electrons and superoxide radicals in heterogeneous photocatalytic systems [175]. Their research demonstrated that 1,4-$H_2Q$ serves as a superior $O_2^{\bullet-}$ radical scavenger compared to 1,4-BQ, providing more accurate assessments of superoxide radical concentrations. The study revealed that 1,4-BQ tends to overestimate superoxide radical amounts, while 1,4-$H_2Q$ offers more reliable quantification. The oxidation mechanism involves superoxide radicals attacking 1,4-$H_2Q$ to form semiquinone radicals, subsequently producing 1,4-benzoquinone and other intermediates before complete mineralization to $CO_2$ and $H_2O$. This multi-step process involves collaboration with hydroxyl radicals and photogenerated holes, enhancing overall pollutant mineralization effectiveness.

*Hosseini et al.* employed 1,4-$H_2Q$ probing in ZnO/GO/CuO nanocomposite systems, demonstrating efficient photocatalytic activity with significant superoxide radical involvement [176]. Their work confirmed the effectiveness of 1,4-$H_2Q$ as a probe for superoxide radical detection in complex multi-component photocatalytic systems.

The application of 1,4-$H_2Q$ probing has been particularly valuable in understanding charge-transfer mechanisms in heterojunction photocatalysts. *McMichael et al.* utilized 1,4-$H_2Q$-based determination methods to investigate photo-electrocatalytic disinfection processes, revealing the crucial role of superoxide radicals in antimicrobial activity [177].

Recent advances in g-$C_3N_4$-based photocatalytic systems have benefited significantly from coumarin and 1,4-$H_2Q$ probing methodologies. The metal-free photocatalyst work involving reduced graphene oxide-doped g-$C_3N_4$ homojunctions demonstrated enhanced ROS generation under visible-light irradiation. These studies revealed that RGO doping effectively improves charge separation efficiency, leading to increased production of both hydroxyl and superoxide radicals [178].

A study of boron-functionalized g-$C_3N_4$ materials has shown promising results for enhanced photocatalytic performance [179]. This research indicates that B-functionalization creates favorable conditions for ROS generation, with coumarin and 1,4-$H_2Q$ probing confirming increased hydroxyl and superoxide radical production in B-doped systems compared to pristine g-$C_3N_4$.

The application of g-$C_3N_4$ photocatalysts for tetracycline degradation has been extensively studied using EPR and scavenging tests. This investigation confirmed that photogenerated holes and $O_2^{\bullet -}$ radicals are the primary species responsible for tetracycline degradation, with complete mineralization achieved within 90 minutes under optimal conditions [180]. The degradation mechanism involves the formation of intermediate organic molecules before complete mineralization.

The extensive literature on coumarin and 1,4-hydroquinone as ROS probes demonstrates their fundamental importance in photocatalytic research. The evolution of coumarin-based methods from simple fluorescence-based detection to comprehensive electrochemical analysis represents a significant advancement in the accuracy of hydroxyl radical quantification. Similarly, the superiority of 1,4-hydroquinone over 1,4-benzoquinone for superoxide radical detection has been firmly established through systematic comparative studies.

The integration of these probe molecules in advanced photocatalytic systems, particularly g-$C_3N_4$-based materials, has revealed complex ROS generation mechanisms and enabled rational catalyst design. The comprehensive understanding of ROS generation and detection methodologies provided by the above-reported researcher serves as a foundation for advancing photocatalytic technology toward more efficient and sustainable environmental remediation applications [181].

# 4. Experimental

## 4.1. Chemicals and reagents

All reagents were of analytical grade and were used as received, without additional purification; the full list is provided in Table 4.1 below.

**Table 4.1.** Chemicals and reagents.

| Company | Chemicals and reagents | Formula | Purity (%) |
|---|---|---|---|
| Carlo Erba Reagents | Coumarin | $C_9H_6O_2$ | 99 |
| | 4-Nitrophenol | $C_6H_5NO_3$ | 99 |
| Forr-Lab Kft. | Bismuth nitrate pentahydrate | $Bi(NO_3)_3 \cdot 5H_2O$ | 98 |
| | Silver nitrate | $AgNO_3$ | 99.9 |
| | Zinc nitrate hexahydrate | $Zn(NO_3)_2 \cdot 6H_2O$ | 96 |
| Merck Millipore | Milli-Q water | $H_2O$ | - |
| Sigma Aldrich Kft. | 1,4-Benzoquinone | $C_6H_4O_2$ | 98 |
| | 1,4-Hydroquinone | $C_6H_6O_2$ | 99 |
| | 7-OH coumarin | $C_9H_6O_3$ | 99 |
| Reanal Ltd. | Potassium chromate | $K_2CrO_4$ | 99 |
| | Starch | $C_6H_{10}O_5$ | 95 |
| Scharlab Hungary Kft. | Melamine | $C_3H_6N_6$ | 99 |
| VWR Ltd. | Urea | $CO(NH_2)_2$ | 99.9 |
| Honeywell Ltd. | Sodium sulfide | $Na_2S$ | 98 |

## 4.2. Synthesis of catalyst

### *4.2.1. Synthesis of g-$C_3N_4$*

Ten grams of precursor melamine and urea were poured into a ceramic crucible of 85 $cm^3$ volume. The crucible remained covered and at room temperature until it was heated using an air environment muffle furnace (a Nabertherm P330 furnace from Bartherm GmbH, Germany). The heater was turned on at 5 °C per minute up to 500 °C (550 °C), reaching that temperature in different times (0.5, 1, 2, 3, 4 h). As soon as the temperature in the crucible dropped to normal room temperature, the powdered product was meticulously analyzed using different instrument methods. (Results have been discussed in detail in Section 5.1.4).

### *4.2.2. Synthesis of Ag-g-$C_3N_4$ nanocomposites*

The Ag modified nanocomposites from g-$C_3N_4$ obtained at 550 °C (4 h) from melamine precursors were synthesized utilizing two methods: one incorporating seed extract and the other excluding it. The technique is detailed below.

a) Using a bio-inspired method

Cardamom seed extract plays a significant role in nanoparticle synthesis by acting as both a natural reducing and stabilizing agent. The phytochemicals present in the extract, such as flavonoids, tannins, terpenoids, and phenolic compounds, facilitate the reduction of metal ions to their respective nanoparticles, while also capping and stabilizing the formed particles to prevent aggregation [182]. This green synthesis approach offers an eco-friendly, efficient, and cost-effective method for producing nanoparticles with controlled size and morphology. Additionally, cardamom extracts impart bioactivity and biocompatibility to the nanoparticles, enhancing their suitability for various photocatalytic and environmental applications [183, 184].

1 gram of cardamom seeds was taken out and then cleaned, washing them and allowing them to dry. After that, 150 $cm^3$ of Milli-Q water was added, and the mixture was left to heat at 90 °C for two hours. Once totally cooled, the serum was filtered with Whatman

paper and put in the fridge to be used later. A representation of the absorbance spectrum of cardamom extract is shown in Figure A4.1 in the Attachment.

200 mg of g-$C_3N_4$ with optimized conditions (550 °C, 4 h) was mixed with 30 $cm^3$ of Milli-Q water, and the suspension was sonicated for 30 minutes and then kept on stirring for two hours. Then, 1 mL of cardamom seed extract was placed in 10 $cm^3$ of $AgNO_3$ (0.25, 0.5, and 1 mol $dm^{-3}$) solution and both were gently shaken for twenty-four hours at a temperature of 25 °C. Then, the solution of silver nanoparticles, which had been prepared beforehand, was mixed with the g-$C_3N_4$ suspension and the mixture was agitated at room temperature. It took two hours for the reaction to take place and then it was filtered. The dried sample was then tested by several analytical techniques.

### b) Adsorption impregnation method

In addition, it was possible to synthesize Ag-g-$C_3N_4$ nanocomposites without using cardamom seed extract. g-$C_3N_4$ with optimized conditions (550 °C, 4 h) was dissolved in 30 $cm^3$ of Milli-Q water to make a suspension, then the suspension was sonicated continuously for 30 minutes. After that, 10 $cm^3$ of the 0.5 (mol $dm^{-3}$) $AgNO_3$ solution was added to the mixture previously obtained. After two hours of stirring, the solution was then filtered. The Ag-g-$C_3N_4$ nanocomposite was then allowed to dry at normal temperature and examined through many separate investigations.

### *4.2.3. Synthesis of bismuth and zinc-sulfide-modified g-$C_3N_4$*

The role of starch in nanoparticle synthesis primarily involves functioning as a stabilizing and capping agent that prevents particle aggregation, thereby controlling particle size and dispersion. Mechanistically, starch molecules, rich in hydroxyl functional groups, adsorb onto the surface of forming nanoparticles through hydrogen bonding and electrostatic interactions. This adsorption creates a steric barrier around each particle, reducing surface energy and inhibiting further particle growth and agglomeration. Additionally, starch can act as a mild reducing agent, facilitating the conversion of metal ions into nanoparticles under appropriate reaction conditions. Its biodegradable, non-toxic nature makes it a favorable component in green synthesis routes, promoting environmentally friendly processes with enhanced control over nanoparticle morphology and stability [185].

To follow the standard protocol, 0.5 g of starch was put into 100 mL of MQ water and heated to 60-70 °C with stirring for 20 minutes to produce a clear starch solution. The solution with bismuth nitrate (10 mmol $dm^{-3}$) in starch was brought up to 60 °C and stirred for 10 minutes. Sodium sulfide (0.05 mol $dm^{-3}$) was separately mixed into 50 $cm^3$ of heated starch solution and maintained at 60 °C for 10 minutes during stirring. Sodium sulfide was added carefully to the bismuth nitrate solution with constant heat and shaking. The reaction mixture was set at 50 °C and then kept stirring continuously for about 10 minutes. Then, the reaction was simply allowed to return to ambient temperature. Afterwards, a dark-brown colloidal solution showed that $Bi_2S_3$ nanoparticles were produced.

g-$C_3N_4$ (300 mg) with optimized condition (500 °C, 4h) was individually mixed with 25 $cm^3$, 45 $cm^3$, and 65 $cm^3$ of the ascertained $Bi_2S_3$ nanoparticle solution and stirred overnight. The resulting compounds were then dried in an oven at 60 °C overnight and used in photocatalytic applications. They were denoted as g-$C_3N_4$-Bi(1), g-$C_3N_4$-Bi(2), and g-$C_3N_4$-Bi(3). The same procedure was repeated in the synthesis of ZnS nanoparticles, which resulted in a milky white colloidal solution that is a sign of the formation of zinc sulfide. The synthesis of g-$C_3N_4$-ZnS, namely g-$C_3N_4$-Zn(1), g-$C_3N_4$-Zn(2), and g-$C_3N_4$-Zn(3) followed a procedure similar to that of g-$C_3N_4$-Bi.

Pure solid $Bi_2S_3$ and ZnS were likewise prepared by simply adding sodium sulfide (0.05 mol $dm^{-3}$) to the metal nitrate solution without starch.

A summary of tables of all the photocatalyst produced has been shown in Table 4.2 below.

**Table 4.2.** List of photo-catalysts prepared using different methods.

| **Gas atmosphere of preparation (air or nitrogen)** | | |
|---|---|---|
| g-$C_3N_4$-melamine air | **500 °C** | **2 hours** |
| g-$C_3N_4$-melamine $N_2$ | | |
| g-$C_3N_4$-urea air | | |
| g-$C_3N_4$-urea $N_2$ | | |
| **Variation of time** | | |
| g-$C_3N_4$-melamine air | **500 °C** | **0.5, 1, 2, 4 hours** |
| g-$C_3N_4$-melamine air | **550 °C** | **4 hours** |
| **Catalyst used for modification** | | |
| g-$C_3N_4$-melamine air 550 °C 4h | | |
| **Modified Catalyst** | | **Method** |
| Ag modified g-$C_3N_4$ | Ag(1)-g-$C_3N_4$<br>Ag(2)-g-$C_3N_4$<br>Ag(3)-g-$C_3N_4$ | Bio-inspired |
| | Ag(4)-g-$C_3N_4$ | Adsorption impregnation |
| $Bi_2S_3$ modified g-$C_3N_4$ | g-$C_3N_4$-Bi(1)<br>g-$C_3N_4$-Bi(2)<br>g-$C_3N_4$-Bi(3) | Starch-assisted |
| ZnS modified g-$C_3N_4$ | g-$C_3N_4$-Zn(1)<br>g-$C_3N_4$-Zn(2)<br>g-$C_3N_4$-Zn(3) | |

### *4.2.4. Determination of silver concentration on the surface of g-$C_3N_4$*

Stock solutions were prepared at three different silver ion concentrations (0.25, 0.5, and 1 mol $dm^{-3}$). In addition, a potassium chromate solution (5 g $dm^{-3}$), a 0.05 mol $dm^{-3}$ silver nitrate solution, and sodium chloride solutions at concentrations of 0.25, 0.5, and 1 mol $dm^{-3}$ were also prepared. For each test, 1 $cm^3$ of $AgNO_3$ solution (at 0.25, 0.5, or 1mol $dm^{-3}$) was combined with 2 $cm^3$ of NaCl solution (matching concentrations), leading to the immediate appearance of a white precipitate of silver chloride, as described by Equation 4.1. Next, 10 $cm^3$ of distilled water and 1 $cm^3$ of $K_2CrO_4$ were introduced to the mixture, resulting in a yellow coloration. The titration process was carried out using a burette filled with 0.05 mol $dm^{-3}$ $AgNO_3$. Titration continued until the mixture developed a characteristic reddish-brown hue, signifying the formation of silver chromate (as described by Equation 4.2). This approach allows for the stepwise observation of precipitation and color changes associated with the key reactions, providing a clear indication of each stage in the analytical procedure.

$$AgNO_3 + NaCl \rightarrow AgCl + NaNO_3 \quad (4.1)$$

$$K_2CrO_4 + 2\,AgNO_3 \rightarrow Ag_2CrO_4 + 2KNO_3 \quad (4.2)$$

In the next phase of the synthesis, 200 mg of g-$C_3N_4$ was dispersed in 30 $cm^3$ of MQ water, to which 10 $cm^3$ of a silver nitrate solution was added by following the same methodology previously established for preparing Ag-g-$C_3N_4$ using cardamom extract. A portion of the resulting suspension was then filtered through a Millipore membrane. For the titration step, 1 $cm^3$ of this filtrate was analyzed, and the difference in silver concentration between the original solution and the filtrate was used to determine the amount of silver actually deposited onto the g-$C_3N_4$ surface. Calculations for this deposition, reflecting varying silver nitrate concentrations of 0.25, 0.5, and 1 mol $dm^{-3}$ in the presence of cardamom extract, are comprehensively summarized in Table 4.3.

For comparison, an identical titration was performed using a 0.5 mol $dm^{-3}$ $AgNO_3$ solution with g-$C_3N_4$ but without cardamom extract, and the resulting silver deposition data are also presented in Table 4.3.

**Table 4.3.** Preparation conditions and surface concentration of $Ag^+$ of different silver-modified catalysts.

| **Catalyst** | **Concentration of $AgNO_3$ solution ($mol\ dm^{-3}$)** | **Cardamom extract** | **$Ag^+$ concentration on the surface ($mol\ g^{-1}$)** |
|---|---|---|---|
| g-$C_3N_4$ | 0 | + | 0 |
| Ag(1)-g-$C_3N_4$ | 0.25 | + | $3.4\times10^{-3}$ |
| Ag(2)-g-$C_3N_4$ | 0.5 | + | $9.1\times10^{-3}$ |
| Ag(3)-g-$C_3N_4$ | 1 | + | $2.0\times10^{-2}$ |
| Ag(4)-g-$C_3N_4$ | 0.5 | − | $4.2\times10^{-3}$ |

The observed discrepancy, that noticeably less silver is deposited onto g-$C_3N_4$ when cardamom extract is absent, can be corroborated by transmission electron microscopy (TEM) results, which reveal a sparser distribution of silver nanoparticles following both UV and visible light irradiation in the absence of cardamom. These findings suggest that cardamom extract facilitates more effective reduction and deposition of silver onto the g-$C_3N_4$ surface, likely acting as both a reducing and stabilizing agent, thereby enhancing nanoparticle loading efficacy in the composite system.

### *4.2.5. Determination of bismuth sulfide and zinc sulfide concentration on the catalyst*

To prepare samples for elemental analysis, we used microwave-assisted acid digestion in sealed vessels. The process was carried out using an Anton Paar Multiwave 3000 system operating at 600 W microwave power.

For each sample, approximately 0.13 g of material was carefully weighed into a fluorocarbon polymer digestion vessel (HF100). We then added 6 mL of freshly prepared aqua regia solution, which consisted of 4.5 mL concentrated hydrochloric acid (HCl) mixed with 1.5 mL concentrated nitric acid ($HNO_3$). This powerful acid mixture is particularly effective at dissolving metal-containing samples.

Once the sample and acid were combined, the vessel was tightly sealed and placed in the microwave digestion unit, which features built-in pressure and temperature monitoring for safety and control. The heating program involved gradually raising the temperature to 175 °C over 30 minutes, then maintaining this temperature for an additional 30 minutes to ensure complete sample dissolution.

After the digestion cycle was complete, the vessels were allowed to cool down naturally before being carefully vented and opened. The clear, fully dissolved sample solution was then quantitatively transferred and diluted with deionized water to a final volume of 25 mL in a volumetric flask. These diluted solutions were then ready for elemental analysis using the ICP-OES technique. This standardized digestion procedure ensures complete sample dissolution while maintaining reproducible conditions for accurate quantitative analysis.

The elemental composition of the digested samples was determined using inductively coupled plasma optical emission spectrometry (ICP-OES) on a PerkinElmer Avio Max 550 instrument (PerkinElmer Inc., MA, USA). This technique works by exciting atoms in a high-temperature plasma, causing them to emit characteristic light at specific wavelengths that can be used to identify and quantify different elements.

For accurate quantification, we prepared calibration curves using certified reference standards. Bismuth and zinc standards were prepared from a Supelco multi-element standard solution (1000 mg $dm^{-3}$), while sulfur standards came from a TruQ standard solution (100 mg $dm^{-3}$). These stock solutions were systematically diluted with deionized water to create a series of calibration standards at concentrations of 0, 0.05, 0.1, and 1 mg $dm^{-3}$ for each target element.

The instrument was optimized to monitor specific emission lines for each element: bismuth at 223.065 nm, zinc at 206.200 nm, and sulfur at 181.975 nm. These wavelengths were selected because they provide the best sensitivity and minimal spectral interference for each element.

To ensure reliable results, each sample was analyzed in triplicate, and the relative standard deviation between measurements was consistently less than 5 %, indicating excellent analytical precision. This level of reproducibility confirms the reliability of the quantitative elemental data obtained for all the nanocomposite samples. The Bi and Zn contents of the composite catalysts are summarized below in Table 4.4. These data show that the nanoparticles exist in both sulfide and oxide forms on the surface of the graphitic carbon nitride.

**Table 4.4.** Bi and Zn contents of the composite catalysts.

| **Catalyst** | **g-$C_3N_4$-Bi(1)** | **g-$C_3N_4$-Bi(2)** | **g-$C_3N_4$-Bi(3)** |
|---|---|---|---|
| **Bi (w%)** | 1.87 | 3.41 | 4.13 |
| **S (w%)** | 0.10 | 0.18 | 0.20 |
| **$Bi_2S_3$ (w%)** | 0.54 | 0.96 | 1.07 |
| **$Bi_2O_3$ (w%)** | 1.75 | 3.20 | 3.98 |
| **Bi in sulfide form (mol%)** | 23.2 | 22.98 | 21.08 |
| | | | |
| **Catalyst** | **g-$C_3N_4$-Zn(1)** | **g-$C_3N_4$-Zn(2)** | **g-$C_3N_4$-Zn(3)** |
| **Zn (w%)** | 3.99 | 5.01 | 6.40 |
| **S (w%)** | 0.55 | 0.60 | 0.90 |
| **ZnS (w%)** | 1.76 | 1.82 | 2.74 |
| **ZnO (w%)** | 3.57 | 4.71 | 6.67 |
| **Zn in sulfide form (mol%)** | 28.17 | 24.47 | 28.74 |

## 4.3. Physicochemical characterization of the photocatalyst

**X-ray diffraction (XRD):** This method was performed for the crystal structure analysis using a Philips PW 3710 powder diffractometer manufactured by Philips Analytical in Almelo, Netherlands. The instrument uses copper K-alpha X-rays with a wavelength of 1.5405 Å as the radiation source.

This technique works by directing X-rays at the powdered samples, where they interact with the ordered crystal planes within the materials. When the X-rays hit these planes at specific angles, they create characteristic diffraction patterns that act like fingerprints for different crystalline phases. By analyzing these patterns, we can identify which crystal structures are present in our nanocomposite materials and determine how well-ordered they are. The use of copper K-alpha radiation is standard in powder diffraction because it provides good penetration depth and produces sharp, well-resolved peaks that make it easier to identify and distinguish between different crystalline phases present in the samples.

**Scanning electron microscopy (SEM):** To examine the surface structure and composition of samples, we employed two different scanning electron microscopes, each chosen for its specific strengths. The first was a Philips/FEI XL 30 environmental scanning electron microscope, which allowed us to observe samples under various atmospheric conditions without extensive preparation.

For more detailed imaging and elemental mapping, we used a ThermoFisher Apreo S scanning electron microscope fitted with an AMETEK Octane Elect Plus energy-dispersive X-ray spectroscopy (EDS) detector. This setup gave us the ability to not only see the surface features in great detail but also identify which elements were present and where they were located.

We used two different voltage settings depending on what we wanted to achieve: 5.0 kV for general imaging, which provides excellent surface detail while being gentle on the samples, and 25.0 kV for elemental analysis, which generates stronger X-ray signals needed to accurately identify and quantify the different elements present in our nanocomposite materials. This combination of instruments and techniques allowed us to get a comprehensive picture of both the physical structure and chemical composition of our samples at the microscopic level.

**Transmission electron microscopy:** Transmission electron microscopy (TEM) and related techniques were used to visualize the structure and composition of nanocomposites. A dilute suspension of each nanocomposite was dropped onto copper grids coated with a thin, lacey amorphous-carbon film. The grids were left to dry at room temperature, allowing the particles to settle naturally on the support. The dried grids were examined on an FEI Talos F200X G2 operated in TEM mode at 200 kV with an ~80 pA beam current. Bright-field (BF) images captured the overall two-dimensional morphology of the g-$C_3N_4$ sheets and the distribution of nanoparticles. Selected-area electron diffraction (SAED) patterns provided crystallographic information. High-resolution TEM (HRTEM) micrographs revealed fine lattice details within the nanocomposites. Elemental maps were acquired in STEM spectrum-imaging mode. Energy-dispersive X-ray (EDX) spectra were recorded pixel-by-pixel using a four-detector SuperX silicon-drift system while the beam current was increased to ~200 pA for optimal signal. All images, diffraction patterns, and EDX datasets were processed and analyzed with Velox 2.14 software, yielding detailed insights into particle size, shape, and elemental distribution across the composite materials.

**Low-temperature $N_2$ physisorption:** The surface area, pore volume, and pore size distribution of the materials were characterized using adsorption–desorption measurements at liquid nitrogen temperature (-196 °C), covering pores ranging from 1.7 to 100 nm in diameter. Before analysis, samples underwent thorough degassing to remove any adsorbed moisture or gases: first, they were heated at 160 °C for 2 hours under static conditions using a Micromeritics FlowPrep 060 degassing unit, then transferred to a Micromeritics 3Flex 3500 analyzer (USA) and maintained under vacuum for an additional 4 hours.

The specific surface area was determined using the well-established Brunauer-Emmett-Teller (BET) method, which analyzes how nitrogen molecules adsorb onto the material surface. To understand the microporous characteristics, we employed t-plot analysis, which provided both the micropore surface area ($S_{micro}$) and micropore volume ($V_{micro}$). For the mesoporous features, the Barrett-Joyner-Halenda (BJH) method was applied to the nitrogen desorption branch of the isotherms, allowing us to calculate the mesopore size distribution, total pore volume (V), and average pore diameter (Dav).

This comprehensive approach provides a detailed picture of the material's textural properties, which are crucial for understanding how the catalyst will perform in photocatalytic applications, since surface area and pore structure directly influence how reactant molecules can access active sites.

**X-ray photoelectron spectroscopy:** The surface chemistry and elemental composition of the samples were analyzed using X-ray photoelectron spectroscopy (XPS) on a Thermo Scientific ESCALAB $Xi^+$ instrument manufactured in Brno, Czech Republic. The system employed a monochromatic aluminum K-alpha X-ray source operating at 1486.6 eV with a focused beam spot diameter of 650 μm. Before analysis, the sample chamber was evacuated to ultra-high vacuum conditions (below $10^{-9}$ mbar) to ensure clean measurement conditions.

Initial survey scans were performed at 80 eV analyzer pass energy to identify all elements present on the sample surfaces. For detailed chemical state analysis, high-resolution spectra were acquired at 40 eV pass energy for specific photoelectron lines including C 1s, N 1s, O 1s, Ag 3d, Bi 4f, S 2p, S 2s, and Zn 2p.

To address sample charging effects commonly encountered in XPS analysis of insulating materials, the instrument's built-in automatic charge compensation system was utilized. Energy calibration was performed using the sp²-bonded carbon peak in the $N{=}C(-N)_2$ environment as an internal standard, with its binding energy fixed at 288.2 eV. This calibration approach ensured accurate determination of binding energies for all other elements and their chemical states.

XPS characterization provided detailed information about the surface composition and chemical bonding environments within the nanocomposite materials (g-$C_3N_4$ and g-$C_3N_4$-$Bi_2S_3$g-$C_3N_4$, and g-$C_3N_4$-ZnS, which is essential for understanding their photocatalytic behavior and structure-activity relationships.

**Fourier-transform infrared spectroscopy:** Infrared spectroscopy measurements were performed using a Bruker Vertex 70 Fourier-transform infrared (FTIR) spectrometer from Bruker GmbH (Rosenheim, Germany). The instrument was equipped with a Diamond ATR (Attenuated total reflectance) sampling accessory, which allows for direct analysis of solid samples without extensive preparation. The sample is simply pressed against the diamond crystal surface.

The spectrometer operated at a spectral resolution of 2 $cm^{-1}$ using a room-temperature DTGS (Deuterated triglycine sulfate) detector, providing good sensitivity across the mid-infrared range. To ensure high-quality, noise-free spectra, each measurement involved collecting and averaging 512 individual scans. Additionally, atmospheric correction was applied to compensate for interference from water vapor and carbon dioxide in the surrounding air, ensuring that only the sample characteristic absorption bands were observed.

This FTIR setup provided detailed information about the molecular vibrations and chemical bonding within the nanocomposite materials, helping to confirm successful synthesis and identify functional groups present on the surface and throughout the bulk material.

**UV-Vis Diffuse Reflectance Analysis:** To understand how well our materials can absorb light, which is crucial for photocatalytic performance. UV-visible diffuse reflectance spectroscopy (DRS) was performed to examine the optical properties of all the catalysts.

The results were quite promising; both the bismuth sulfide and zinc sulfide-modified materials showed strong light absorption across a wide range of visible wavelengths. This is important because it means these nanocomposites can potentially harness more of the solar energy for photocatalytic reactions. Compared to the pure g-$C_3N_4$, the modified versions demonstrated noticeably improved light absorption in the visible spectrum, which is exactly what we hoped to achieve.

To quantify how much energy is needed to excite electrons in these materials (known as the band gap energy), we applied the well-established Tauc relation shown in Equation 4.3 [186]. This mathematical approach allows us to calculate the band gap values for pure g-$C_3N_4$ and both types of nanocomposites, giving us insight into their electronic properties and potential photocatalytic behavior.

$$(\alpha h\nu)^{1/n} = A(h\nu - Eg) \tag{4.3}$$

In the Tauc relation, the variables represent the following physical quantities: $\alpha$-absorption coefficient, $h$-Planck's constant, $\nu$-frequency of light, $n$-Tauc exponent (n=2 for g-$C_3N_4$, for indirect allowed transition), $A$-proportionality constant, $Eg$-band gap energy. These parameters are used to determine the optical band gap of a material, which is essential for understanding its ability to absorb and utilize light energy in photocatalytic applications.

A list of tables of the sample for physicochemical characterization has been provided (in the Attachment) Table AT4.1.

## 4.4. Photocatalytic experiments

### *4.4.1. Reactor*

The photocatalytic activity of the nanocomposites was evaluated based on the degradation of a colorless organic compound in an aqueous solution. It was done by examining the changes in the absorbance of the solution upon exposure to UV and visible

LEDs with the setups (A) when exposing to UV and (B) when exposing to Vis LEDs, as shown in Figure A4.2 in the Attachment.

In brief, photocatalytic tests were conducted using a quartz reactor (lab-scale, 50 $cm^3$). As light sources, UV LED with the maximum wavelength of 374 nm and the power of 50 W (I (UV LED $\lambda_{max}$=374 nm): $2.34\cdot10^{-4}$ mol photon $dm^{-3}$ $min^{-1}$), two Vis LEDs with the maximum wavelength of 453 nm and the power of 14 W (2×7 W) (I (Vis LED $\lambda_{max}$=453 nm): $5.54\cdot10^{-4}$ mol photon $dm^{-3}$ $min^{-1}$), were used. Figure A4.3 in the Attachment shows their emission spectrum.

The light sources were placed on the left and right sides of the reactor with about 10 cm distance between them. In all the experimental runs, stirring of the reaction mixture was done by injecting air bubbles with a flow rate of 10 $dm^3$ $h^{-1}$. The reaction mixture temperature did not change appreciably upon illumination, even though there was a slight increase of 2-3 °C, which is insignificant to adsorption, desorption, and the photochemical process.

### *4.4.2. Preparation of solution*

To prepare the solutions for our photocatalytic experiments, we dissolved the appropriate amounts of each reagent in deionized water to achieve the desired concentrations. Specifically, we prepared a coumarin solution with a concentration of $9\times10^{-5}$ M, a para-nitrophenol solution at $4.5\times10^{-4}$ M, and a 1,4-hydroquinone solution at $2.25\times10^{-4}$ M. Each solution was freshly prepared before use to ensure accuracy and maintain consistency throughout the experimental process.

In the experiment method, a quantity of 50 mg of catalyst was taken and dispersed in 5 $cm^3$ Milli-Q water, and this was sonicated in a 10-minute procedure. This step was carried out to achieve particle homogenization; 45 $cm^3$ suspension of model compounds was introduced, and the suspension (catalyst concentration of 1 g $dm^{-3}$) was kept in the dark at room temperature with constant agitation to allow adsorption-desorption equilibrium to be established. Thereafter, the visible or UV LEDs were turned on, a 4-$cm^3$ syringe was used to take samples at various time points, and a Millipore Millex-LCR PTFE 0.45 μm membrane filter was used in filtration.

### *4.4.3. Analytical measurements (model compound)*

The experiment utilized coumarin as a molecular probe to detect hydroxyl radicals generated during photocatalytic processes, starting with an initial coumarin concentration of $9\times10^{-5}$ mol dm$^{-3}$ that underwent chemical transformation to form fluorescent 7-hydroxycoumarin, when exposed to hydroxyl radicals produced by photocatalyst irradiation. UV-vis spectrophotometer (Scinco S-3100) to monitor coumarin concentration changes by measuring light absorption at 277 nm, where coumarin exhibits a strong molar absorption coefficient of 11308 M$^{-1}$ cm$^{-1}$, while the fluorescent product 7-OHC demonstrated significantly weaker absorption with a coefficient of only 3209 M$^{-1}$ cm$^{-1}$, meaning that at low concentrations, the newly formed 7-OHC had minimal interference with overall light absorption measurements.

A spectrofluorometer (PerkinElmer LS50B) was utilized to measure fluorescent emission from 7-hydroxycoumarin using optimal wavelength conditions of 332 nm excitation and 453 nm emission, with quantitative determination of both compounds achieved through carefully constructed calibration curves that plotted UV-Vis absorbance at 277 nm against known coumarin concentrations (Figure A4.4/a in the Attachment) and fluorescence emission intensity at 453 nm against known 7-OHC concentrations (Figure A4.4/b in the Attachment). This dual-measurement approach offers high sensitivity and good selectivity for hydroxyl radical detection, with the relatively low molar absorption coefficient of 7-OHC at 277 nm helping to minimize inner filtering effects where coumarin might absorb excitation light intended for 7-OHC detection, making this experimental design a well-established approach for monitoring photocatalytic hydroxyl radical generation by combining the chemical specificity of coumarin as a hydroxyl radical trap with the sensitivity of fluorescence detection methods.

We employed 1,4-hydroquinone as another model compound at a concentration of $2.25\times10^{-4}$ mol dm$^{-3}$, utilizing its fluorescent properties with an excitation wavelength of 288 nm and emission wavelength of 330 nm, where the relationship between emission intensity and 1,4-$H_2Q$ concentration demonstrated linearity within the range of 0 to $4\times10^{-5}$ mol dm$^{-3}$ (Figure A4.5 in the Attachment). To accurately measure 1,4-$H_2Q$ concentrations exceeding $4\times10^{-5}$ mol dm$^{-3}$ and avoid self-absorption effects that could interfere with fluorescence measurements, the samples were diluted tenfold before analysis. Additionally, incorporation of para-nitrophenol as a third model compound at a concentration of $5\times10^{-4}$ mol dm$^{-3}$, characterized by its distinctive UV-Vis absorption spectrum with a maximum absorbance peak at 318 nm, with all optical property studies conducted using UV-Vis absorption spectroscopy in a specialized cuvette with a volume of 0.2 cm$^3$ to ensure precise spectroscopic measurements and maintain consistent experimental conditions across all compound analyses. The variation in para-nitrophenol concentration was determined based on the calibration curve presented in Figure A4.6 in the Attachment, considering the intermediate formed during irradiation.

The degradation efficiency of coumarin and para-nitrophenol (D(t), %) was determined using Equation 4.4.:

$$\text{Degradation efficacy} = (C_0 - C_t / C_0) \times 100 \qquad (4.4)$$

where $C_0$ is the initial concentration and $C_t$ is the concentration at time $t$. To describe the reaction kinetics, a pseudo-first-order kinetic model was applied based on Equation 4.5:

$$-\ln (C_t / C_0) = kt \qquad (4.5)$$

$k$ (min$^{-1}$) represents the rate constant.

For HPLC analysis of para-nitrophenol, samples were injected (0.02 cm$^3$) into a Shimadzu UFLC system equipped with a Phenomenex Kinetex C18 column (100×3 mm, 2.6 µm particle size), maintained at 30 °C. The mobile phase was 95:5 (v/v) mixture of water and methanol, and photometric detection was performed at 246 nm and 288 nm.

Mineralization was tracked by measuring total organic carbon (TOC) levels with a Shimadzu TOC-L CPN analyzer.

# 5. Results and discussion

## 5.1. Catalyst g-$C_3N_4$

The primary goal of this research is to develop catalysts that can work effectively when exposed to visible light. As a first step, we focused on determining the best temperature and heating duration for preparing g-$C_3N_4$, aiming to maximize its photocatalytic performance. Table 5.1 presents the product masses obtained from 10-gramm quantities of both melamine and urea precursors, synthesized at 500 °C for 2 hours under air or nitrogen atmospheres. The results demonstrate that melamine produces approximately ten times more product compared to urea under identical conditions. To ensure data reliability, the synthesis procedures were replicated multiple times, confirming consistent reproducibility across experiments. Based on these comparative results, melamine was selected as the optimal precursor for photocatalytic applications due to its superior product yield, enhanced photoactivity performance, and reduced environmental impact through lower air pollution generation during synthesis.

**Table 5.1.** Product masses obtained from 10 g of precursor melamine or urea under different atmospheric conditions.

| **melamine-air** | **melamine-$N_2$** | **urea-air** | **urea-$N_2$** |
|---|---|---|---|
| 4.87 ± 0.3 g | 4.89 ± 0.3 g | 0.40 ± 0.2 g | 0.34± 0.2 g |
| 4.80 ± 0.3 g | 4.91 ± 0.3 g | 0.35 ± 0.2 g | 0.31 ± 0.2 g |

### *5.1.1. Characterization*

To analyse the crystalline structure and interlayer spacing of graphitic carbon nitride (g-$C_3N_4$) nanosheets produced from melamine and urea, powder X-ray diffraction (XRD) was performed on samples calcined under both air and nitrogen atmospheres. g-$C_3N_4$ typically displays two characteristic diffraction peaks corresponding to the (100) and (002) crystallographic planes. The (100) peak reflects the in-plane structural order and the two-dimensional arrangement of the material, while the (002) peak is associated with the periodic stacking of g-$C_3N_4$ conjugated aromatic layers along the c-axis direction

[187, 188, 189]. In the XRD patterns (Figure 5.1), curves 1 and 2 represent the products obtained from melamine calcined at 500 °C for 2 hours in air and nitrogen, respectively, while curves 3 and 4 correspond to the products from urea calcined under the same conditions in air and nitrogen, respectively. This analysis allows the determination of both the crystal phase and the spacing between graphitic carbon nitride layers.

The observed shift of the (002) XRD peak at approximately 27° for sample 3 is most likely attributable to structural modifications in the g-$C_3N_4$ framework resulting from the use of urea as a precursor and calcination in air. This synthetic combination can promote the formation of additional defects or alter the interlayer stacking order, thereby affecting the interlayer distance and causing a displacement of the diffraction peak. In contrast, the other samples exhibit more uniform structural characteristics, resulting in closely overlapping peak positions.

All XRD patterns contain the reference lines of the identified PDF cards from the ICDD PDF-2 2021 reference database. The identified phase for g-$C_3N_4$ is shown, corresponding to the PDF card 00-066-0813, ensuring accurate phase identification.

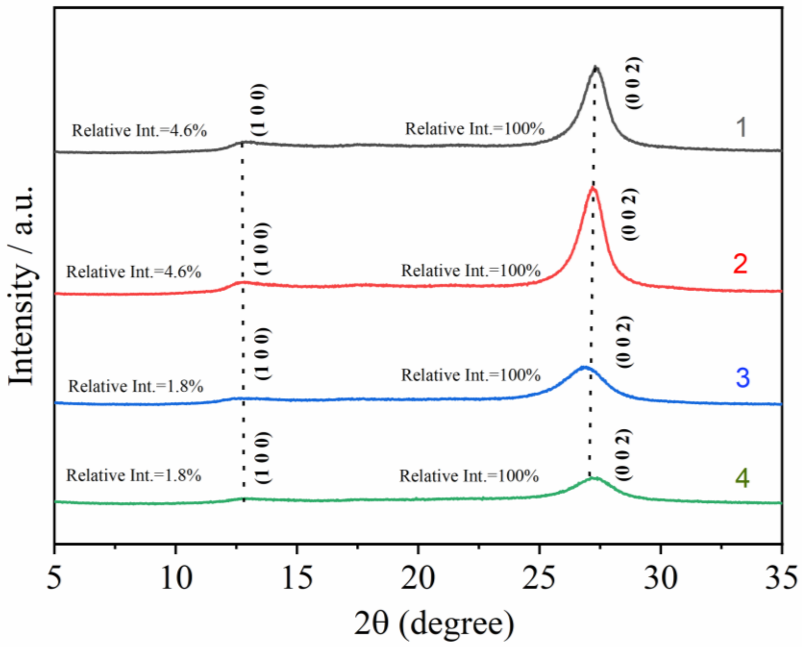

**Figure. 5.1.** XRD of g-$C_3N_4$ from melamine and urea (air and nitrogen atmosphere 500 °C-2h), curves 1 and 2; melamine (air and nitrogen), curves 3 and 4; urea (air and nitrogen).

We conducted scanning electron microscopy (SEM) analysis to investigate the microstructural characteristics and morphological features of g-$C_3N_4$ samples prepared from different nitrogen-rich precursors. The SEM images presented in Figure 5.2 reveal distinct morphological differences that are directly attributed to the choice of precursor material used during synthesis.

The g-$C_3N_4$ sample derived from melamine precursor Figure 5.2/A, B exhibits characteristic granular morphology with irregular, aggregated particles forming a two-dimensional sheet-like architecture. These structures appear as interconnected granules with varying sizes, creating a porous network that could facilitate enhanced surface accessibility for photocatalytic reactions. The granular nature suggests that during the thermal polycondensation process, melamine undergoes fragmentation and reassembly, resulting in these discrete but interconnected particle formations.

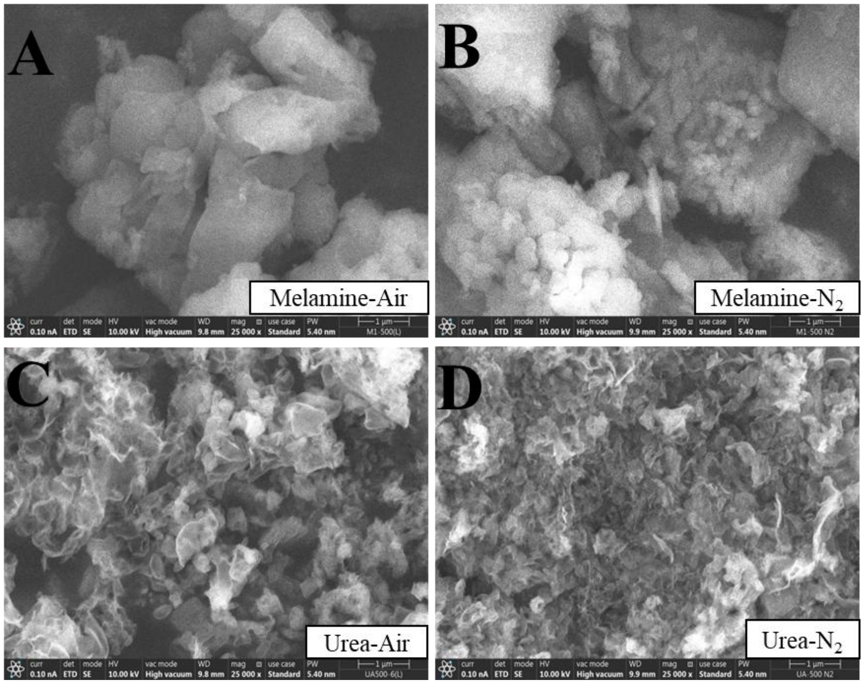

**Figure 5.2.** SEM images of g-$C_3N_4$ from melamine (A, B) and urea (C, D) (air and nitrogen atmosphere, 500 °C-2h).

In contrast, the urea-derived g-$C_3N_4$ sample, Figure 5.2/C, D displays a markedly different morphological structure, characterized by well-defined layered architectures with a more pronounced one-dimensional orientation. These structures exhibit smoother, more continuous surfaces with distinct layered stacking, resembling flake-like or platelet morphologies. The layered arrangement suggests a more ordered polycondensation pathway where urea serves as the precursor, leading to the formation of extended sheet structures with better structural integrity.

These morphological variations between melamine and urea-derived g-$C_3N_4$ can be attributed to the different thermal decomposition pathways and intermediate species formed during the synthesis process. The distinct morphologies likely influence the materials' surface area, active site accessibility, and ultimately their photocatalytic performance, making precursor selection a critical parameter in optimizing g-$C_3N_4$ properties for specific applications.

Energy-dispersive X-ray spectroscopy (EDS) (Figure 5.3) confirmed that pristine g-$C_3N_4$ contains approximately 42.9 % carbon and 57.1 % nitrogen.

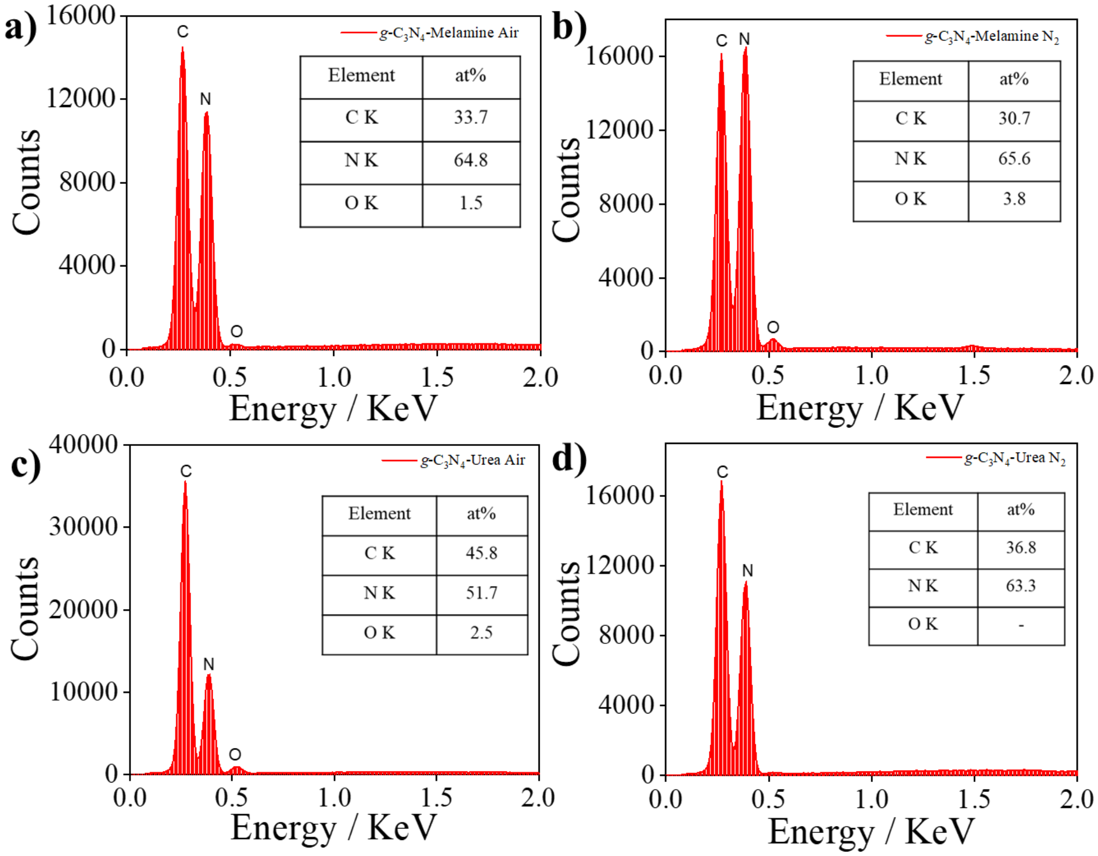

| Element | at% |
|---|---|
| C K | 33.7 |
| N K | 64.8 |
| O K | 1.5 |

| Element | at% |
|---|---|
| C K | 30.7 |
| N K | 65.6 |
| O K | 3.8 |

| Element | at% |
|---|---|
| C K | 45.8 |
| N K | 51.7 |
| O K | 2.5 |

| Element | at% |
|---|---|
| C K | 36.8 |
| N K | 63.3 |
| O K | - |

**Figure 5.3.** EDS spectra of g-$C_3N_4$ from melamine (a, b) and urea (c, d) (air and nitrogen atmosphere at 500 °C-2h).

For the urea precursor, nitrogen content varied markedly between samples calcined in air versus nitrogen, reflecting greater nitrogen loss during air calcination and partial compensation in a nitrogen atmosphere. In contrast, melamine-derived materials showed negligible differences in nitrogen content under both atmospheres, indicating fewer nitrogen vacancies. Trace oxygen detected by EDS likely originated from ambient exposure. Overall, the measured C/N ratios closely match the expected composition of g-$C_3N_4$, confirming successful synthesis.

### *5.1.2. Photocatalytic reactions with coumarin*

The main goal was to evaluate the photocatalytic performance of g-$C_3N_4$ by monitoring the behavior of coumarin under both UV and visible light. For this purpose, g-$C_3N_4$ samples were prepared by calcination at 500 °C with precursor urea and melamine in both air and nitrogen atmospheres. Coumarin acts as a selective trap for hydroxyl radicals, resulting in the formation of several hydroxylated derivatives. Among these, 7-hydroxycoumarin stands out for its strong fluorescence [190]. Throughout the experiments, the reaction mixtures were kept saturated with air to maintain consistent atmospheric conditions. When exposed to UV irradiation, the measurements revealed notable changes in the system, while visible-light irradiation led to minimal observable effects. The rates of photocatalytic reactions involving coumarin under UV light are illustrated in Figure 5.4/a, b providing quantitative insight into the effectiveness of g-$C_3N_4$ as a catalyst in these conditions.

For the g-$C_3N_4$ photocatalysts prepared from melamine and urea, the initial formation rates of 7-OHC under air and nitrogen were $1.69\times10^{-10}$ M min$^{-1}$ and $3.18\times10^{-11}$ M min$^{-1}$, $1.26\times10^{-10}$ M min$^{-1}$ and $1.83\times10^{-10}$ M min$^{-1}$, respectively, in 120 min of irradiation. The extent of coumarin degradation was evaluated from its concentration profile during photocatalysis. Correspondingly, the initial degradation rates of coumarin for melamine- and urea-derived g-$C_3N_4$ in air and nitrogen were $1.69\times10^{-7}$ M min$^{-1}$, $3.77\times10^{-8}$ M min$^{-1}$ and $1.25\times10^{-7}$ M min$^{-1}$, $1.57\times10^{-7}$ M min$^{-1}$, respectively, highlighting the influence of both precursor and atmosphere on the overall photocatalytic performance (Figure 5.4).

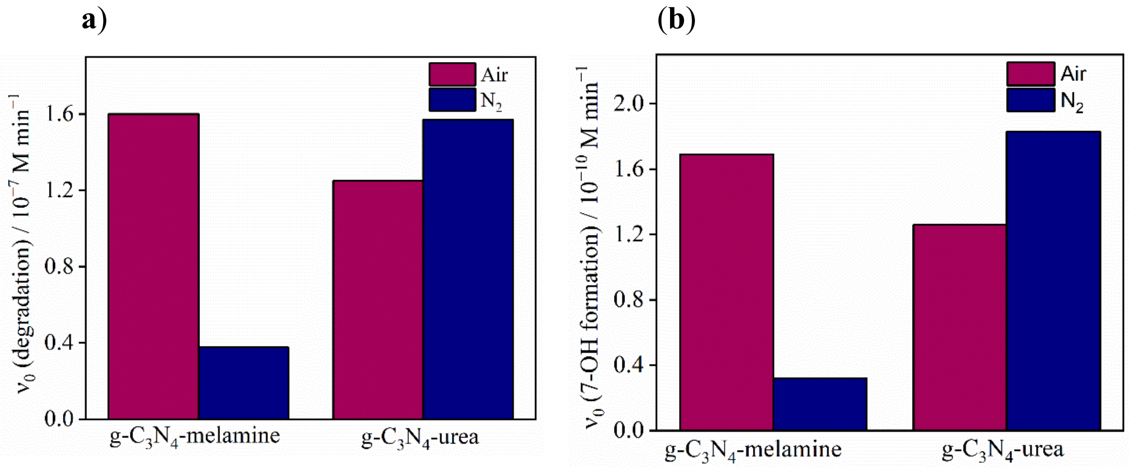

**Figure 5.4.** Rates of photocatalytic (a) degradation of coumarin and (b) formation of 7-OH coumarin.

Coumarin can participate in chemical reactions with three types of reactive species: electrons, superoxide radicals [191], and hydroxyl radicals [192]. When coumarin interacts with electrons ($k = 1.6\times10^{10}$ $M^{-1}$ $s^{-1}$, [193]) and superoxide radicals, it yields products that lack fluorescent properties, as outlined in equation 5.1. In contrast, the reaction between coumarin and hydroxyl radicals ($k = 2.0\times10^{9}$ $M^{-1}$ $s^{-1}$, [193]) generates fluorescent 7-hydroxycoumarin, along with additional hydroxylated compounds, as demonstrated in Equation 5.2.

$$\text{coumarin} + e^{-}_{CB} / O_2^{\bullet-} \rightarrow \text{non-fluorescent products} \qquad (5.1)$$

$$\text{coumarin} + {}^{\bullet}OH \rightarrow \text{fluorescent 7-OHC} + \text{other OHC} \qquad (5.2)$$

The total hydroxylated coumarin (OHC) concentration was calculated using the measured 7-OHC concentration, since 7-OHC represents approximately 29 % of all hydroxylated coumarin products formed [194]. Using this total OHC concentration, the amount of hydroxyl radicals generated in the system was subsequently determined. The efficiency of hydroxylated coumarin formation through hydroxyl radical capture by coumarin was found to be 6.42 % of the total hydroxyl radical production. Under aerobic conditions, the stoichiometry requires 2 hydroxyl radical molecules and 1 coumarin molecule to produce a single hydroxylated coumarin molecule [195]. Taking these stoichiometric relationships and efficiency factors into account, the hydroxyl radical concentration in the system was calculated using the Equations below:

$$[\mathrm{OHC}] = (100/\ 29) \times\ [\text{7-OHC}] \qquad (5.3)$$

$$[^{\bullet}\mathrm{OH}] = (2\ \mathrm{mol}/1\ \mathrm{mol}) \times (100/6.42) \times [\mathrm{OHC}] \qquad (5.4)$$

To examine the underlying mechanisms behind the photocatalytic breakdown of coumarin, we evaluated both the formation of all hydroxylated coumarin species and the overall degradation of coumarin. We calculated the total coumarin degradation by determining the difference between the initial and remaining coumarin concentrations after the reaction. The OHC concentration represents the amount of coumarin that was degraded specifically through reactions with hydroxyl radicals. The difference between the total coumarin degradation and the measured OHC concentration suggests that coumarin degradation also occurs through reactions with other highly reactive species beyond hydroxyl radicals. Figure 5.5 displays the formation rates of hydroxyl radicals, OHC, and 7-hydroxycoumarin for the melamine-air catalyst system, while Table 5.2 provides a comprehensive comparison of these rates across all catalyst systems tested.

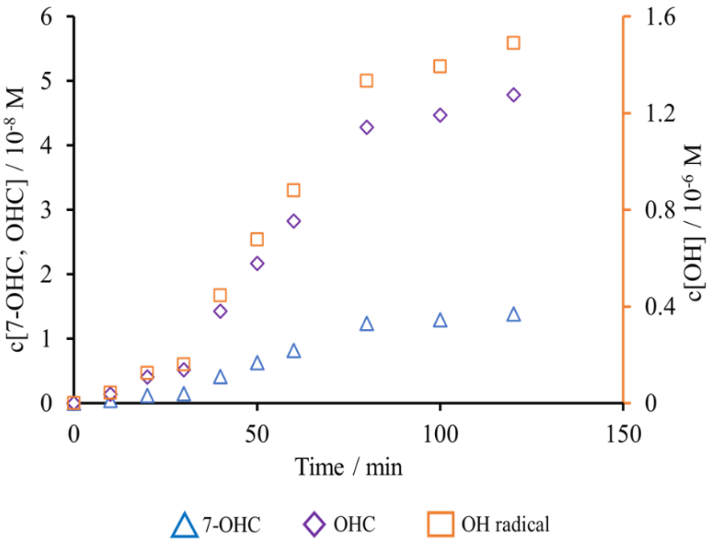

**Figure 5.5.** Change of concentration of 7-OH coumarin, OHC, hydroxyl radical.

**Table 5.2.** Formation rate of hydroxyl radicals**.**

| **Catalyst** | **$v_0$ (OH radical) ($M\ min^{-1}$)** |
|---|---|
| melamine-air | $1.11\times10^{-8}$ |
| melamine-$N_2$ | $9.40\times10^{-10}$ |
| urea-air | $3.41\times10^{-9}$ |
| urea-$N_2$ | $2.99\times10^{-7}$ |

Although catalyst urea-$N_2$ exhibited the highest $^{\bullet}OH$ generation rate, catalyst melamine-air was selected due to its tenfold greater overall yield; we then calculated the percentage of coumarin degraded by hydroxyl radicals after 120 minutes acknowledging that, over extended storage, coumarin may also react with electrons and superoxide radicals and summarized these results in Table 5.3.

**Table 5.3.** Percent degradation of coumarin by $^{\bullet}OH$ radicals after 40 min irradiation.

| **Catalyst** | **Percent degradation by $^{\bullet}OH$ radicals (after 40 min)** |
|---|---|
| melamine-air | 0.71 % |
| melamine-$N_2$ | 1.02 % |
| urea-air | 0.3 % |
| urea-$N_2$ | 1.39 % |

### 5.1.3. Photocatalytic reactions with 1,4-hydroquinone

Following *Fónagy's* methodology [175], we performed hydroquinone degradation experiments to detect superoxide radicals generated during photocatalytic reactions. The results successfully validated the production of superoxide radicals by confirming the degradation of 1,4-hydroquinone, thereby establishing this approach as an effective method for superoxide radical detection in photocatalytic systems.

For the g-$C_3N_4$ catalysts prepared from melamine, the degradation rates of 1,4-hydroquinone measured in air and nitrogen atmospheres were $1.69\times10^{-7}$ and $1.24\times10^{-7}$ M min$^{-1}$, respectively. When g-$C_3N_4$ was synthesized from urea, the corresponding degradation rates in air and nitrogen environments were $1.26\times10^{-7}$ and $1.38\times10^{-7}$ M min$^{-1}$, as illustrated in Figure 5.6. These results indicate that both the precursor material and the synthesis atmosphere influence catalytic performance in the degradation of 1,4-hydroquinone.

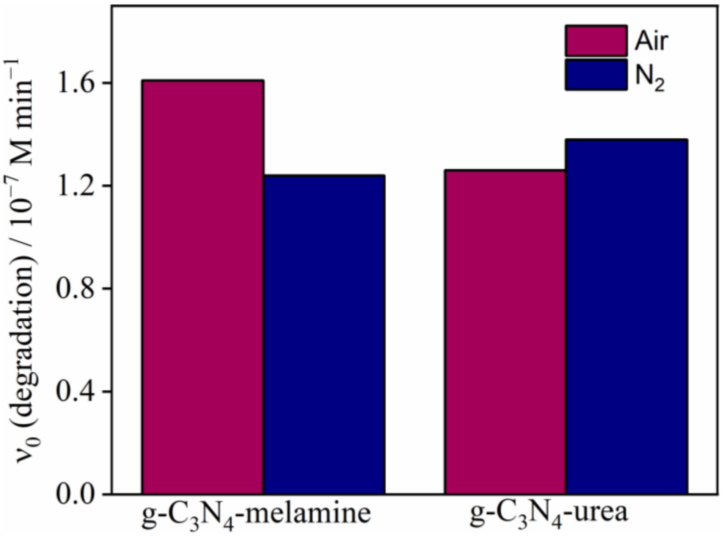

**Figure 5.6.** Photocatalytic reactions with 1,4-hydroquinone.

Based on experimental data, the catalyst performance is highly dependent on both the precursor material and the synthesis atmosphere. As illustrated in Figure 5.4, the catalyst synthesized from melamine in an air environment shows a significantly higher production rate of 7-OH coumarin and a faster degradation rate of coumarin compared to the same catalyst prepared under a nitrogen atmosphere.

In contrast, the catalyst derived from urea exhibits an increased rate of coumarin degradation and 7-OH coumarin formation when synthesized in a nitrogen atmosphere. This improvement is attributed to the external nitrogen environment compensating for the lost nitrogen from urea decomposition during the synthesis, a conclusion that is supported by the EDS data presented in Figure 5.3. Furthermore, the data in Figure 5.6 indicate that the g-$C_3N_4$ synthesized from melamine is more effective at degrading 1,4-hydroquinone than the g-$C_3N_4$ produced from urea in a nitrogen atmosphere.

### *5.1.4. Effect of temperature and time of preparation on the photocatalytic activity*

To further evaluate the impact of synthesis conditions on catalyst performance, experiments were conducted using melamine in an air atmosphere as the optimal precursor. The g-$C_3N_4$ catalyst was synthesized at 500 °C for durations of 0.5, 1, 2, and 4 hours, using a heating rate of 5 °C per minute. In addition, we carried out the synthesis at a higher temperature of 550 °C for 4 hours, with a ramp rate of 8 °C per minute.

To identify the optimal calcination conditions for preparing g-$C_3N_4$, we systematically varied both the calcination time and temperature and evaluated the resulting photocatalytic activity using coumarin degradation and 7-hydroxycoumarin formation as indicators. Initially, we investigated whether reducing the calcination time at 500 °C could enhance performance. However, as shown in Table 5.4 below, shorter times resulted in noticeably lower rates for both coumarin degradation and 7-OH coumarin formation (for example, at time 0.5 h, the degradation rate was $1.0\times10^{-7}$ M min$^{-1}$ compared to $2.7\times10^{-7}$ M min$^{-1}$ at time 4 h). This suggested that insufficient calcination time at this temperature adversely affected the development of photocatalytic properties.

**Table 5.4.** Comparison of various catalysts synthesized using melamine as precursor in an air atmosphere at different times and temperatures.

| **Calcination** | | **Degradation $v_0$ (coumarin) (M min$^{-1}$)** | **Formation $v_0$ (7-OH coumarin) (M min$^{-1}$)** |
|---|---|---|---|
| **Temperature (°C)** | **Time (h)** | | |
| 500 | 0.5 | $1.0\times10^{-7}$ | $2.7\times10^{-11}$ |
| | 1 | $1.4\times10^{-7}$ | $3.9\times10^{-11}$ |
| | 2 | $1.7\times10^{-7}$ | $6.3\times10^{-11}$ |
| | 4 | $2.7\times10^{-7}$ | $6.2\times10^{-11}$ |
| 550 | 4 | $5.9\times10^{-7}$ | $4.5\times10^{-9}$ |

Seeking further improvement, we then increased the calcination temperature to 550 °C with a 4-hour duration. This adjustment led to a substantial increase in photocatalytic performance, as evidenced by the higher degradation ($5.9\times10^{-7}$ M min$^{-1}$) and formation rates ($4.5\times10^{-7}$ M min$^{-1}$) observed. Based on these findings, we selected 550 °C for 4 hours as the optimal calcination condition, as it produced g-$C_3N_4$ with the most favorable photoactivity among the tested parameters, as shown in Table 5.4.

Graphitic carbon nitride exhibits thermal stability up to approximately 600 °C in inert atmospheres, beyond which significant thermal decomposition occurs. At temperatures exceeding 600-650 °C, g-$C_3N_4$ undergoes progressive degradation through the cleavage of C-N bonds and the release of volatile nitrogen species such as ammonia and nitrogen gas, ultimately leading to the collapse of the polymeric framework.

Additionally, excessive calcination temperatures result in reduced surface area, loss of structural porosity, and decreased photocatalytic activity due to over-condensation and reduced active site availability. The literature consistently reports that the optimal synthesis temperature range for g-$C_3N_4$ lies between 500-600 °C, with higher temperatures yielding materials with inferior photocatalytic performance. Therefore, the decision not to increase the temperature beyond 550 °C was based on these documented thermal stability constraints and the risk of material degradation, which would compromise both structural integrity and catalytic efficiency.

Accordingly, the synthesis temperature was not increased beyond 550 °C in order to avoid surpassing the thermal stability threshold of g-$C_3N_4$ and prevent its structural degradation, which would negatively affect both its integrity and photocatalytic performance.

## 5.2. Ag-g-$C_3N_4$ catalyst

First, the preparation conditions were optimized, then g-$C_3N_4$ was produced by heating melamine at 550 °C for 4 hours in air. Two Ag-g-$C_3N_4$ composites were synthesized: one using a green, bio-inspired route (Ag(1)-g-$C_3N_4$, Ag(2)-g-$C_3N_4$, and Ag(3)-g-$C_3N_4$) where cardamom seed extract served as a mild reducing agent to deposit silver nanoparticles, and another by a straightforward adsorption method without any extract (Ag(4)-g-$C_3N_4$). These eco-friendly modifications extended the catalyst's activity into the visible-light region, in line with our goal of harnessing solar irradiation.

The photocatalytic degradation of the model compounds, coumarin and para-nitrophenol, was thoroughly examined using the Ag-modified g-$C_3N_4$ catalyst, as detailed in the following sections.

### *5.2.1. Photocatalytic degradation of coumarin*

The photocatalytic performance of pure g-$C_3N_4$ and three different silver-modified catalysts with varying silver concentrations, Ag(1)-g-$C_3N_4$ ($3.4\times10^{-3}$ mol $g^{-1}$), Ag(2)-g-$C_3N_4$ ($9.1\times10^{-3}$ mol $g^{-1}$), and Ag(3)-g-$C_3N_4$ ($2.0\times10^{-2}$ mol $g^{-1}$), were evaluated. To test their effectiveness, it was studied how well each catalyst could break down a colorless coumarin solution in water when exposed to both UV and Vis LED. The degradation rates were calculated by analyzing the $C/C_0$ curves, which show how the coumarin concentration changes over time, and these results are presented in Figure 5.7 for both UV and visible light irradiation conditions.

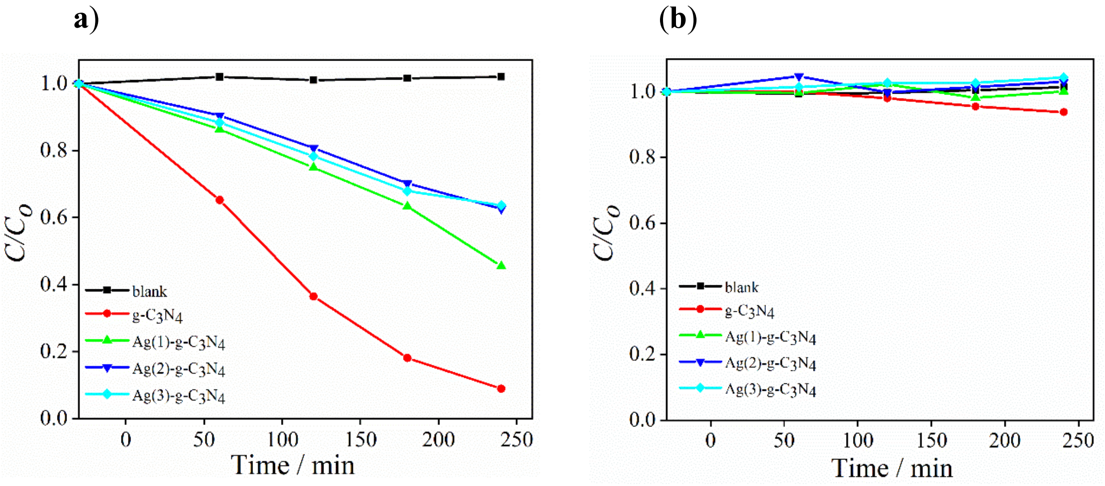

**Figure 5.7.** $C/C_0$ curves for coumarin degradation by irradiation with (a) UV and (b) Vis LEDs.

In a blank control experiment, the coumarin did not break down on its own under light exposure, confirming that it is quite stable without any catalyst. However, once the catalysts were introduced, the efficiency of coumarin photodegradation changed, depending on the amount of silver incorporated. Interestingly, all three silver-modified catalysts, Ag(1)-g-$C_3N_4$, Ag(2)-g-$C_3N_4$, and Ag(3)-g-$C_3N_4$, were actually less effective under UV light than the pure g-$C_3N_4$. When unmodified g-$C_3N_4$ was exposed to UV light for 240 minutes, coumarin degraded significantly, and there was also a considerable formation of 7-OH coumarin. But with the highest silver loading, Ag(3)-g-$C_3N_4$, the degradation rate dropped from 91 % down to just 36 %, and no 7-OH coumarin was produced, quite different from what we observed with pure g-$C_3N_4$.

When cardamom extract was used for synthesis, it was found that the catalyst with $9.1\times10^{-3}$ mol $g^{-1}$ of silver on its surface, labeled as Ag(1)-g-$C_3N_4$, gave the best performance for degradation of coumarin. To see how synthesis would work without the extract, we also tried making a silver-modified catalyst Ag(4)-g-$C_3N_4$ through a simple adsorption impregnation method.

The silver content on its surface was measured and a value of $4.2\times10^{-3}$ mol $g^{-1}$ was obtained. The difference is clear: using cardamom extract helps deposit more silver on the catalyst, while skipping the extract results in less silver on the surface.

The g-$C_3N_4$ catalyst was able to degrade 91 % of coumarin within 4 hours under UV light, with a degradation rate of $5.9\times10^{-7}$ M $min^{-1}$. It also produced 7-OH coumarin at a rate of $4.5\times10^{-10}$ M $min^{-1}$. However, under Vis LED light, g-$C_3N_4$ showed no coumarin degradation and no formation of 7-OH coumarin. On the other hand, the silver-modified catalyst Ag(4)-g-$C_3N_4$ achieved 55 % degradation of coumarin under UV light in 240 minutes (Figure 5.8), which is better than Ag(2)-g-$C_3N_4$, which showed only 37 % degradation. Still, neither of the silver-modified catalysts produced any 7-OH coumarin, nor did they degrade coumarin under visible light. This suggests that after silver modification regardless of the method used the catalysts no longer generate hydroxyl radicals.

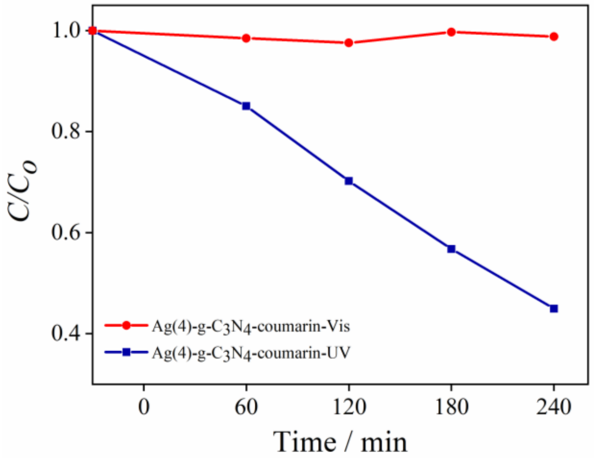

**Figure 5.8.** $C/C_0$ curves for photocatalytic degradation of coumarin under UV and visible light using Ag(4)-g-$C_3N_4$.

This suggests that with increasing silver content, the catalyst becomes less effective for coumarin degradation and does not generate hydroxyl radicals; instead, the breakdown might be happening via electrons or superoxide radicals. When performance was compared under visible light, there was no major difference between g-$C_3N_4$ and the silver-modified catalysts, regardless of the silver concentration. Table 5.5 below summarizes the degradation rate, amount of 7-OH coumarin formed, percentage of coumarin broken down, and the rate constants for both UV and visible light cases.

**Table 5.5.** Comparison of the results regarding the degradation and transformation of coumarin at different conditions.

| **Catalyst** | **Degradation $v_0$ (COU) (M min$^{-1}$)** | **Formation $v_0$ (7-OHC) (M min$^{-1}$)** | **% Degrad. (240 min)** | | **k (min$^{-1}$)** |
|---|---|---|---|---|---|
| | | | UV | Vis | UV |
| **g-$C_3N_4$** | $5.9\times10^{-7}$ | $4.5\times10^{-10}$ | 91 | 0 | $10.2\times10^{-3}$ |
| **Ag(1)-g-$C_3N_4$** | $2.6\times10^{-7}$ | 0 | 54 | 0 | $3.1\times10^{-3}$ |
| **Ag(2)-g-$C_3N_4$** | $2.4\times10^{-7}$ | 0 | 37 | 0 | $2.1\times10^{-3}$ |
| **Ag(3)-g-$C_3N_4$** | $2.3\times10^{-7}$ | 0 | 36 | 0 | $1.9\times10^{-3}$ |
| **Ag(4)-g-$C_3N_4$** | $2.26\times10^{-7}$ | 0 | 55 | 0 | $3.1\times10^{-3}$ |

The reduced photocatalytic efficiency of Ag-loaded g-$C_3N_4$ samples compared to the pristine material is likely attributable to several factors associated with the incorporation of silver. Loading metal nanoparticles onto a semiconductor can disrupt optimal charge-carrier mobility and promote local recombination at the metal-semiconductor boundary. In these Ag-modified samples, the silver may act as electron sinks at low concentrations, aiding charge separation; however, excessive Ag loading can introduce additional recombination sites, hinder carrier transport across interfaces, and block active areas on the g-$C_3N_4$ surface. This is reflected by the observation that no hydroxyl radicals were detected in the presence of Ag-loaded catalysts, indicating an altered primary degradation pathway, possibly dominated by superoxide radicals rather than hydroxyl species.

Carrier mobility and interfacial transport limitations at higher Ag loading are plausible explanations for this decreased performance. Overloading Ag may impede electron transfer by creating unfavorable energy barriers or by physically masking reactive g-$C_3N_4$ sites. As a result, the electron-hole pair separation efficiency is diminished, negatively affecting the overall photodegradation rates.

Regarding the similar performance of Ag(4)-g-$C_3N_4$ and Ag(1)-g-$C_3N_4$ under UV irradiation for coumarin degradation, both have relatively similar silver concentrations; $4.2\times10^{-3}$ mol $g^{-1}$ and $3.4\times10^{-3}$ mol $g^{-1}$, respectively. The small difference between these loadings means their influence on the catalyst's electronic properties, surface coverage, and the number of active sites is likely quite similar.

As a result, both samples demonstrate comparable photocatalytic activity under UV irradiation. This reflects the phenomenon where, at low to moderate Ag loadings, further increases in silver content do not substantially enhance, nor diminish the degradation efficiency, as the electronic and site-blocking effects are balanced. This supports the observed similar performance of Ag(4)-g-$C_3N_4$ and Ag(1)-g-$C_3N_4$ for coumarin degradation.

### *5.2.2. Photocatalytic degradation of para-nitrophenol*

During the experiment, it was found that the degradation of para-nitrophenol was minimal, with a breakdown rate of less than 3 %, indicating that it remains largely unaffected by direct light exposure. This confirmed that para-nitrophenol does not undergo direct photolysis, as shown in Figure 5.9. To evaluate the photocatalytic performance of the materials, we tested pure g-$C_3N_4$ along with three silver-modified versions Ag(1)-g-$C_3N_4$, Ag(2)-g-$C_3N_4$, Ag(3)-g-$C_3N_4$, and Ag(4)-g-$C_3N_4$ by examining how well they degraded para-nitrophenol in water under both UV and Vis LED light, with the results presented in Figure 5.9/a, b.

Among the bio-inspired modified catalysts, Ag(2)-g-$C_3N_4$ showed the best performance, achieving up to 82 % degradation under UV light and 27 % under visible light over a 360-minute period (Figure A5.1/a in the Attachment). Under UV light, g-$C_3N_4$ was able to degrade about 50 % of para-nitrophenol in 6 hours, but it showed no activity under visible light (Table 5.6). Interestingly, the silver-modified catalyst Ag(4)-g-$C_3N_4$ improved the degradation even further, achieving a 14 % increase (from 82 % to 96 %) under UV light compared to the Ag(2)-g-$C_3N_4$ catalyst synthesized using cardamom extract.

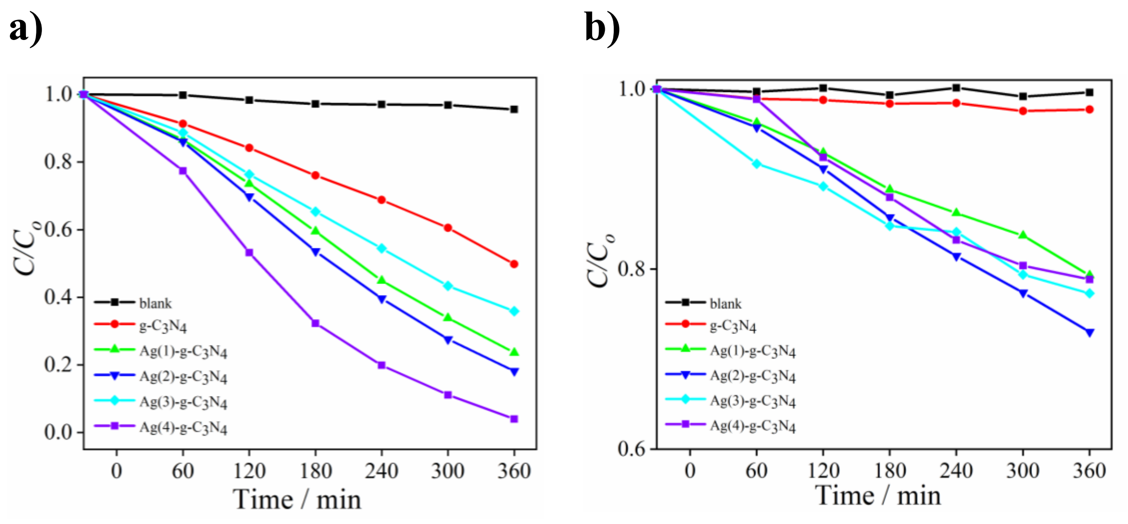

**Figure 5.9.** $C/C_0$ curves for para-nitrophenol degradation by irradiation with (a) UV LED and (b) Vis LEDs

Figure A5.2 in the Attachment shows the photocatalytic degradation of para-nitrophenol over Ag-g-$C_3N_4$, monitored by the absorption peak at 318 nm. The absorption intensity steadily decreased with irradiation time, indicating progressive pollutant degradation and reaching nearly complete removal after 360 minutes, confirming the high efficiency of the silver-modified g-$C_3N_4$ catalyst.

Out of the different silver concentrations tested, the catalyst (synthesized using cardamom extract containing) $9.1\times10^{-3}$ mol $g^{-1}$ of silver on its surface (Ag(2)-g-$C_3N_4$) demonstrated the best photocatalytic performance in both UV and visible light when compared to pure g-$C_3N_4$. Both higher ($2.0\times10^{-2}$ mol $g^{-1}$) and lower ($3.4\times10^{-3}$ mol $g^{-1}$) amounts of silver resulted in reduced activity, suggesting that $9.1\times10^{-3}$ mol $g^{-1}$ is the optimal silver loading for this catalyst. Apart from that, the catalyst synthesized without the use of extract Ag(4)-g-$C_3N_4$, demonstrated even superior degradation efficiency in UV compared to (Ag(2)-g-$C_3N_4$) and vice versa in the case of visible light.

As shown in Figure A5.3/a in the Attachment, over a 360-minute photocatalytic process, the Ag(4)-g-$C_3N_4$ catalyst performed well, achieving 96 % degradation of para-nitrophenol under UV light and 21 % under visible light. When we compared this to the unmodified g-$C_3N_4$, the silver-modified version was clearly much more effective at breaking down para-nitrophenol.

Overall, the silver-modified catalysts clearly outperformed the unmodified g-$C_3N_4$ for breaking down para-nitrophenol. To better understand and confirm these results, we used a pseudo-first-order kinetic model commonly applied in the Langmuir-Hinshelwood framework to analyze the steady reaction rates observed in Figure A5.1/b and Figure A5.3/b in the Attachment. This model helps describe the photocatalytic degradation process more accurately, using Equation 4.5.

Both catalysts, one prepared with cardamom extract and the other without, showed strong performance in breaking down para-nitrophenol. The catalyst synthesized using cardamom extract and silver nanoparticles was more effective under visible light, achieving up to 27 % degradation. The enhanced catalytic performance of Ag(2)-g-$C_3N_4$ over Ag(4)-g-$C_3N_4$ can be elucidated by analyzing the TEM images (Figure 5.14 and 5.15). During irradiation, silver nanoparticles were deposited on the support surface, owing to the support provided by the cardamom seed extract. This support acts as a trap for the photogenerated electrons, thereby significantly delaying electron-hole recombination. The presence of such supported silver nanoparticles effectively prolongs the charge-carrier lifetime, facilitating more efficient redox reactions on the catalyst surface, which in turn contributes to the higher degradation efficiency observed for Ag(2)-g-$C_3N_4$.

The catalyst made with just silver ions performed better under ultraviolet light, with an impressive 96 % degradation. Reusing the catalysts in repeated reactions will help determine which method produces a more stable catalyst over time. Importantly, both approaches are not only productive but also environmentally friendly. The values for the degradation rate, degradation percentage, and rate constant for para-nitrophenol under UV and visible light are summarized in Table 5.6.

**Table 5.6.** Comparison of the results regarding the degradation of para-nitrophenol under different conditions.

| **Catalyst** | **$v_0$ (PN) ($M\ min^{-1}$)** | **% Degradation (360 min)** | | **k ($min^{-1}$)** | |
|---|---|---|---|---|---|
| | | UV | Vis | UV | Vis |
| **g-$C_3N_4$** | $5.2\times10^{-7}$ | 50 | 0 | $1.8\times10^{-3}$ | 0 |
| **Ag(1)-g-$C_3N_4$** | $11.6\times10^{-7}$ | 76 | 21 | $3.9\times10^{-3}$ | $6.2\times10^{-4}$ |
| **Ag(2)-g-$C_3N_4$** | $12.6\times10^{-7}$ | 82 | 27 | $4.7\times10^{-3}$ | $8.8\times10^{-4}$ |
| **Ag(3)-g-$C_3N_4$** | $9.9\times10^{-7}$ | 64 | 23 | $2.8\times10^{-3}$ | $6.6\times10^{-4}$ |
| **Ag(4)-g-$C_3N_4$** | $2.2\times10^{-7}$ | 96 | 21 | $8.8\times10^{-3}$ | $7.1\times10^{-4}$ |

### *5.2.3. Reusability*

The long-term performance of photocatalysts depends on their stability and reusability. To evaluate this, Ag(2)-g-$C_3N_4$ and Ag(4)-g-$C_3N_4$ were subjected to repeated para-nitrophenol degradation tests, as shown in Figure 5.10/a, b. After each run, the catalysts were recovered by centrifugation, rinsed with Milli-Q water, and dried overnight, during which a small amount of material was unavoidably lost. Despite this, both nanocomposites maintained nearly constant photocatalytic activity, with only a slight decline attributable to the loss of catalyst during recovery. The efficiency remained largely stable over five cycles, lasting approximately 30 hours, confirming the excellent durability and recyclability of the materials without any significant reduction in performance.

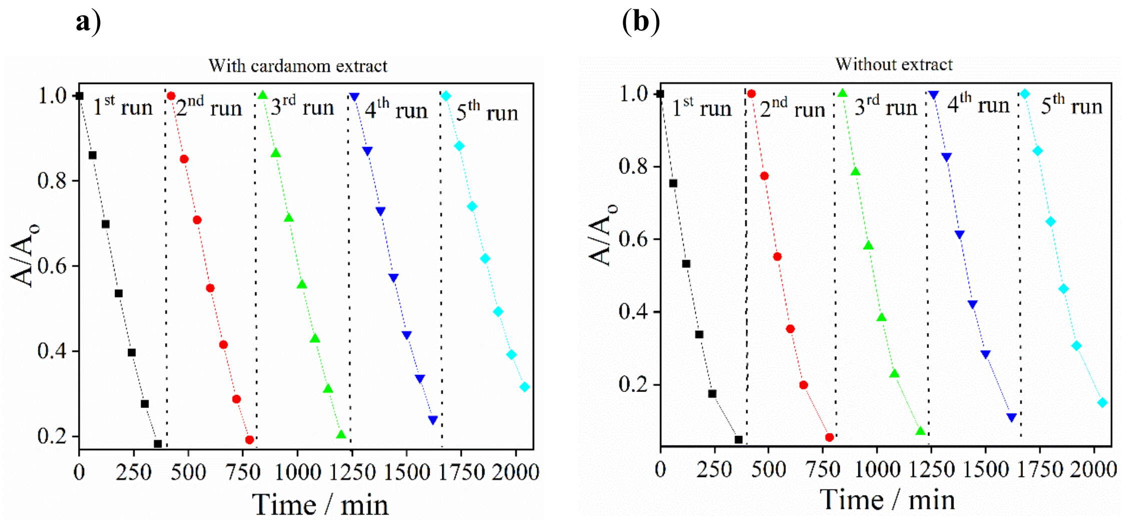

**Figure 5.10.** Reusability of the catalysts in repeated para-nitrophenol degradation tests

a) Catalyst synthesized using cardamom Ag(2)-g-$C_3N_4$ ($9.1\times10^{-3}$ mol $g^{-1}$)

b) Catalyst synthesized without using plant extract Ag(4)-g-$C_3N_4$ ($4.2\times10^{-3}$ mol $g^{-1}$)

### *5.2.4. Mineralization of para-nitrophenol*

To better understand the mineralization process, we measured the total organic carbon using the most effective catalyst, Ag(2)-g-$C_3N_4$. we determined the TOC content of the intermediates by subtracting the TOC value of unreacted para-nitrophenol from the total TOC in the reaction mixture. Over the course of the photodegradation, it was noticed that there is a gradual increase in TOC from the intermediate products, suggesting that the breakdown of para-nitrophenol leads to the formation of new organic compounds as the reaction progresses.

When the reaction mixture was exposed to UV light, the total organic carbon steadily dropped from 30.07 to 11.35 mg $dm^{-3}$ over 6 hours, decreasing at a rate of 3.14 mg $dm^{-3}$ $h^{-1}$. Meanwhile, intermediates formed at a rate of 1.42 mg $dm^{-3}$ $h^{-1}$. After 21 hours of UV exposure, the TOC further declined to 5.7 mg $dm^{-3}$. Under visible light, TOC also decreased but more gradually, going from 30.44 to 24.6 mg $dm^{-3}$ within 6 hours, at a rate of 0.94 mg $dm^{-3}$ $h^{-1}$, with intermediates forming at 0.29 mg $dm^{-3}$ $h^{-1}$. After 32 hours under visible light, TOC dropped to 9.83 mg $dm^{-3}$ (Figure 5.11).

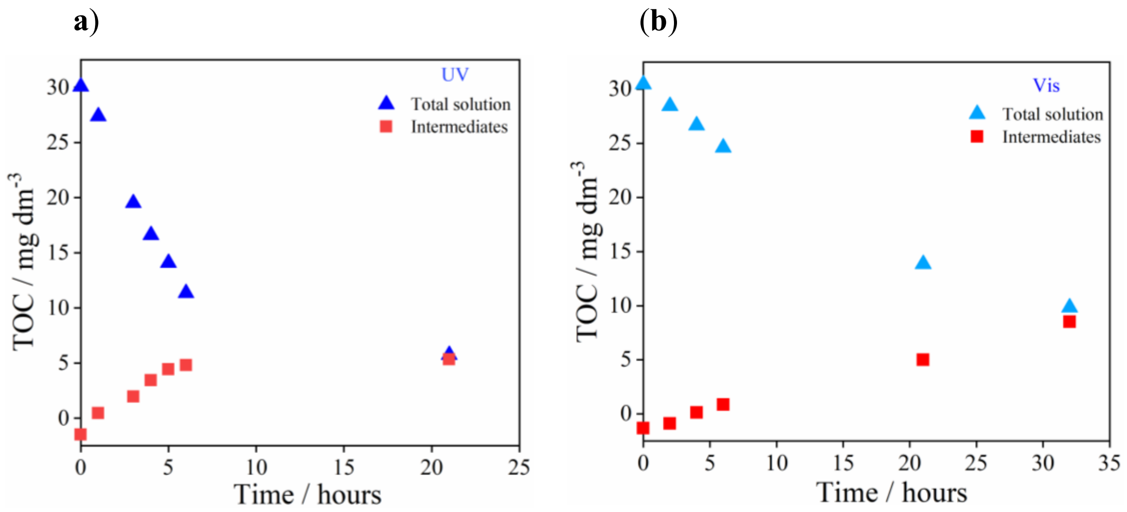

**Figure 5.11.** The change of total organic carbon (TOC) values during the photocatalytic degradation of para-nitrophenol.

Following extended exposure to both UV and visible light, only intermediates remained in the solution; complete degradation of para-nitrophenol was achieved. Continued irradiation beyond this point is expected to break down these intermediates as well. This pattern suggests that a large part of the intermediates is mineralized, producing harmless end products like carbon dioxide and water.

Using the most effective catalyst, Ag(2)-g-$C_3N_4$, HPLC measurements provided valuable insights into the intermediates formed during the reaction. Para-nitrophenol showed a retention time of 6.2 minutes, confirming its presence in the mixture, while an intermediate appeared at 7.6 minutes, indicating it was produced as the reaction progressed. The mass-to-charge ratio (m/z) for para-nitrophenol was measured at 139.1 (M= 139.1g mol$^{-1}$), further verifying its identity. The intermediate had an m/z value of 182.94, which differs from that of typical hydroxylated para-nitrophenol derivatives (theoretical m/z of 155 and 171), suggesting a unique molecular structure. Additionally, a less intense peak with an m/z of 388.97 hints at the formation of a dimerized compound. These HPLC results, along with the mass spectrometry data, offer a clearer understanding of the reaction pathway and intermediates involved. Figure 5.12 presents the HPLC traces for intermediate formation under (a) UV LEDs and (b) visible LEDs, while the mass spectrum for the intermediate is shown in Figure A5.4 in the Attachment.

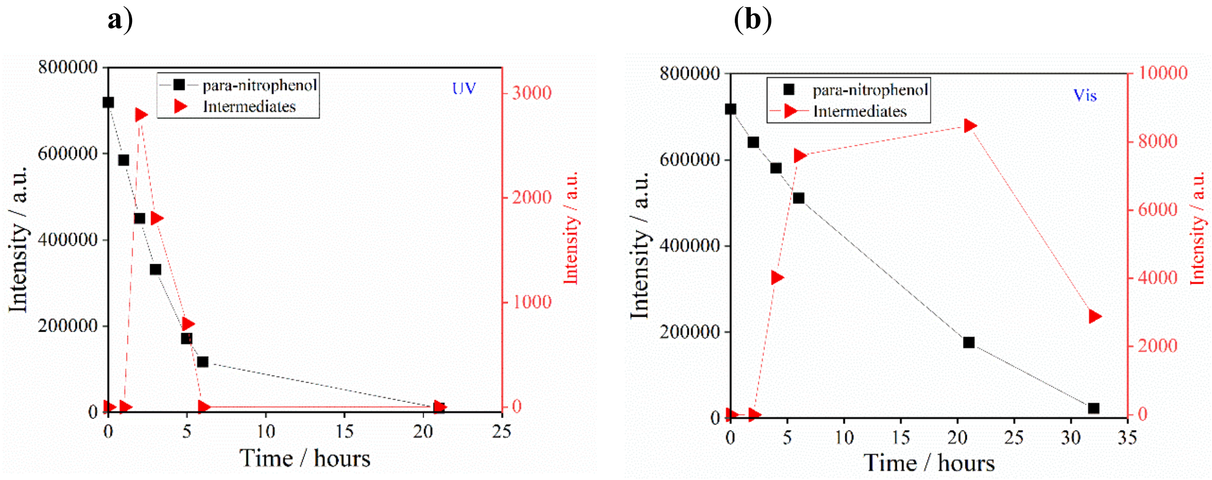

**Figure 5.12.** The change in intermediate concentration during the photocatalytic degradation of para-nitrophenol.

### 5.2.5. *Characterization of Ag-g-$C_3N_4$*

The microstructure of both pure g-$C_3N_4$ and the silver-modified catalysts was examined, with and without cardamom extract, before any irradiation and after exposure to UV and visible light, using TEM imaging combined with elemental mapping (Figure 5.13).

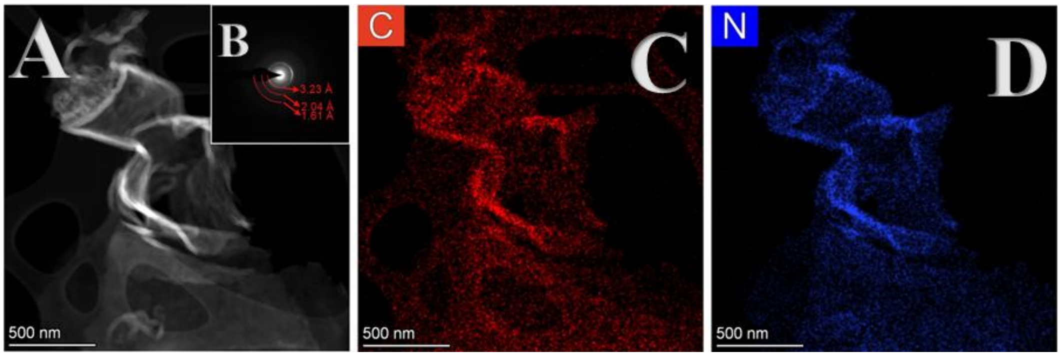

**Figure 5.13.** TEM image of g-$C_3N_4$.

Figure 5.13 clearly reveals the detailed morphology: the samples typically appeared as flake-like layers, giving them a distinct layered look across all variations (A-D). Elemental mapping highlighted that both carbon and nitrogen were evenly distributed throughout the material, confirming uniform makeup, and particularly, the nitrogen was spread out homogeneously across the entire structure. To get a better understanding of the actual molecular composition, the samples were analyzed using EDS spectra, focusing on the proportions of carbon, nitrogen, and oxygen (as described earlier in Figure 5.3). These analyses provided the specific percentages of carbon and nitrogen in each sample, confirming the expected composition for g-$C_3N_4$. Overall, the TEM images, especially those in Figure 5.13/A), made it clear that the g-$C_3N_4$ nanosheets display a structure and arrangement that resemble ultra-thin layers or sheets.

Upon examination of Ag(2)-g-$C_3N_4$ catalyst synthesized by use of cardamom seed extract, a gentle reducing agent for the silver ions, under TEM (Figure 5.14) well-defined silver nanoparticles, averaging approximately 20 nanometers in size, were observed to be sparsely distributed across the surface.

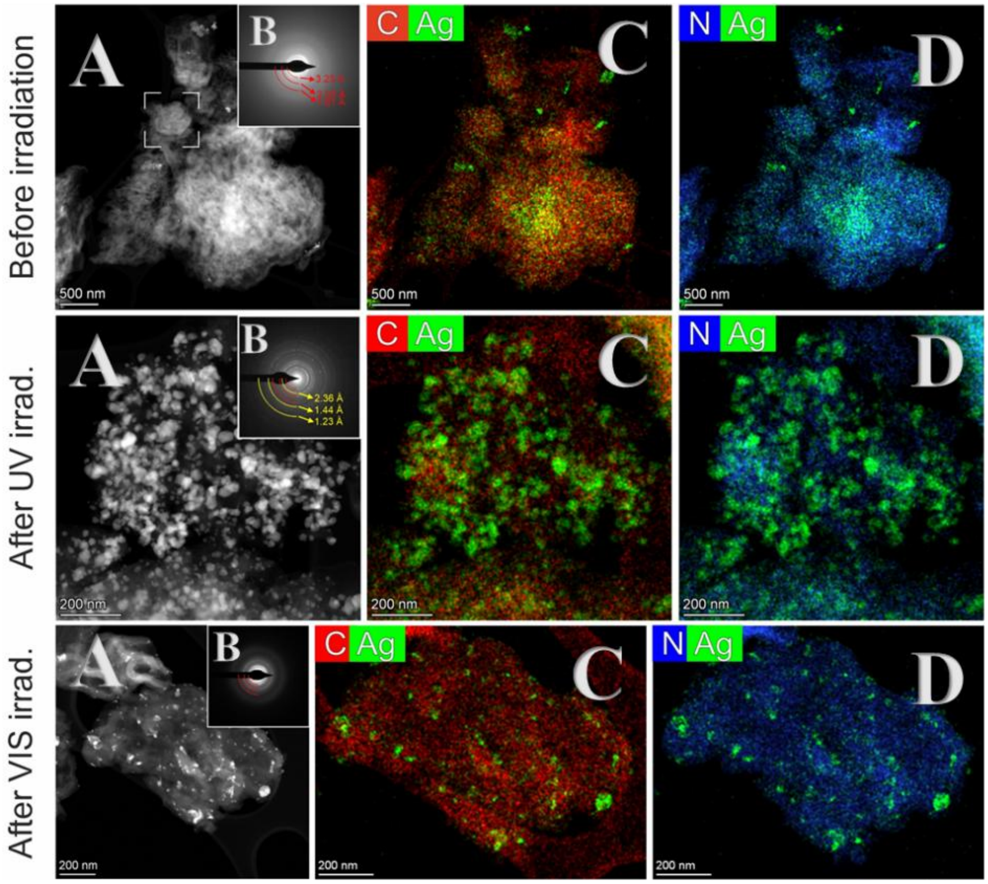

**Figure 5.14.** TEM image of Ag(2)-g-$C_3N_4$ before irradiation, after UV and Vis irradiation.

(In Fig. B (after UV irradiation), the yellow color of the arc corresponds to the crystalline silver, and the red color indicates the presence of graphite).

The corresponding diffraction pattern (Figure 5.14/B) displayed diffuse rings very similar to those seen in the unmodified g-$C_3N_4$ (Figure 5.13/B). This indicates that the primary crystal structure of the g-$C_3N_4$ support was largely preserved following silver incorporation, ensuring that its original properties remained substantially intact.

Following UV irradiation, a pronounced formation of nanocrystals is evident in the TEM micrographs (Figure 5.14), with particles densely populating the g-$C_3N_4$ surface. In contrast, visible light exposure yields fewer and smaller nanocrystals on the surface (Figure 5.14 after visible irradiation), indicating that UV light more effectively promotes the nucleation and growth of crystalline silver particles.

Contrary, Ag(4)-g-$C_3N_4$ catalyst was produced via a simple adsorption impregnation technique, omitting any use of plant extracts. As shown in Figure 5.15, transmission electron microscopy reveals that, before light treatment, silver ions have clustered together and deposited unevenly across the g-$C_3N_4$ surface.

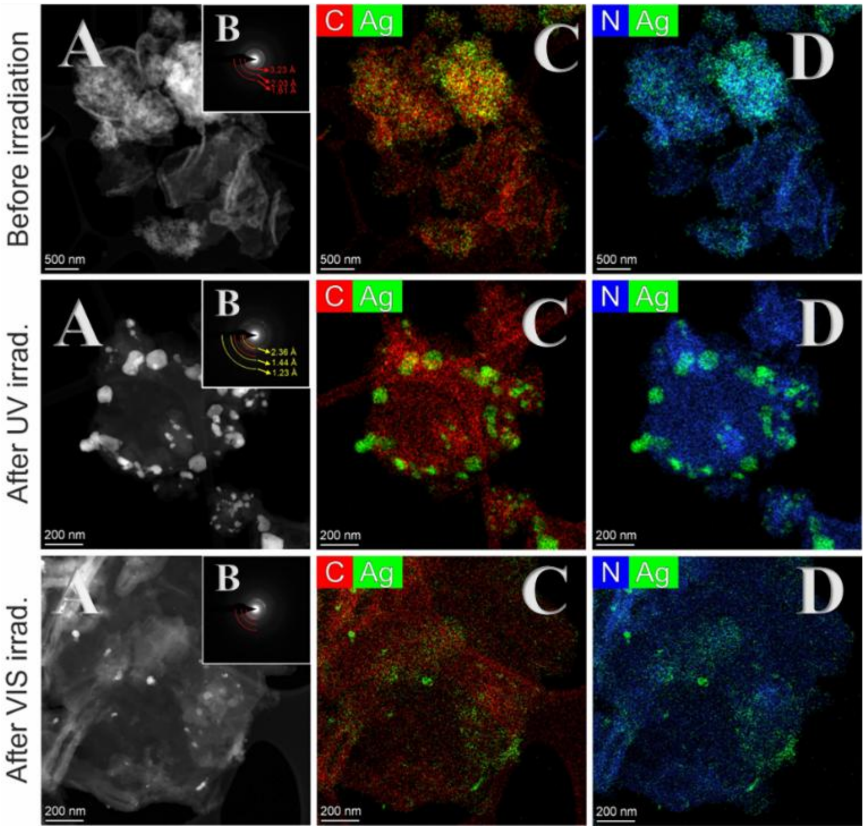

**Figure 5.15.** TEM image of Ag(4)-g-$C_3N_4$ without cardamom extract before irradiation, after UV and Vis irradiation.

Even though the silver ions initially clumped together on the surface, they transformed into nanocrystals after UV light exposure by capturing the electrons generated during photocatalysis, as shown in Figure 5.15. This behavior is very similar to what was observed with the Ag(2)-g-$C_3N_4$ catalyst made using cardamom extract (Figure 5.14). When exposed to visible light, nanoparticles also formed on the surface, but they were comparatively smaller, as illustrated in Figure 5. 15. The TEM results clearly highlight the differences between the two synthesis approaches and show how the morphology of both nanocrystals and ions varies depending on the method used.

The combined TEM-EDX and mapping results indicate that oxygen does not form a distinct silver-oxygen phase on either catalyst, and that silver remains predominantly metallic on g-$C_3N_4$. For both Ag(2)-g-$C_3N_4$ (bio-inspired route) and Ag(4)-g-$C_3N_4$ (impregnation route), the O/Ag elemental maps (Figure A5.5 in the Attachment) show a broadly distributed, low-intensity oxygen signal over the entire g-$C_3N_4$ flakes, while Ag appears as localized bright spots that evolve into nanocrystals after irradiation. The absence of preferential oxygen enrichment around these Ag-rich regions suggests that oxygen mainly arises from the support, adsorbed water, and surface functional groups of g-$C_3N_4$ rather than from silver oxide domains.

This interpretation is further supported quantitatively by the EDX spectra (Figure A5.6 in the Attachment) collected for Ag(4)-g-$C_3N_4$.

Using Digital Micrograph software, we analyzed each particle's shape and size by tracing its outline. In every sample except for Ag(4)-g-$C_3N_4$ without cardamom after visible light exposure, which only yielded about 100 particles. we counted over 200 particles. After visible light irradiation, the Ag(2)-g-$C_3N_4$ made with cardamom extract showed slightly smaller particles but a noticeably higher particle density than the Ag(4)-g-$C_3N_4$ prepared without extract. Under UV light, however, both Ag(2)-g-$C_3N_4$ and Ag(4)-g-$C_3N_4$ samples displayed very similar particle-size distributions (Figure 5. 16).

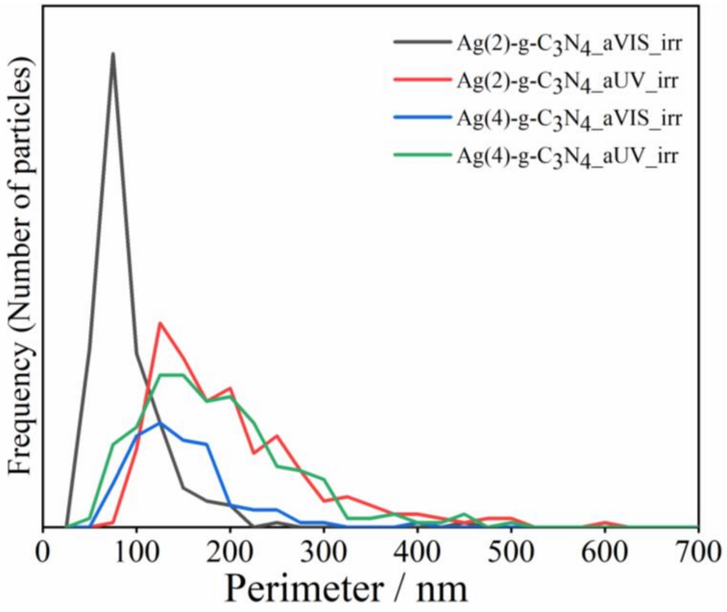

**Figure 5. 16.** Distribution of perimeter of the nanoparticles after irradiation.

The results of low-temperature $N_2$ adsorption measurements are summarized in Table 5.7. When exposed to light, the catalyst changes color from yellow to black due to the reduction of silver ions by electrons, resulting in silver nanoparticles being deposited on the g-$C_3N_4$ surface. The initial surface area of g-$C_3N_4$ was measured at 24 $m^2$ $g^{-1}$ (Table 5.7).

**Table 5.7.** Surface area and pore data of the catalyst samples.
(Abbreviations: b_irr: before irradiation, a_irr: after irradiation.)

| SN | Catalyst | $S_{BET}$ ($m^2$/g) | $S_{micro}$ ($m^2$/g) | $D_{av}$ (nm) |
|---|---|---|---|---|
| 1 | g-$C_3N_4$ | 24 | 4.5 | 28.3 |
| 2 | Ag(2)- g-$C_3N_4$_b_irr | 18 | 5.5 | 42.2 |
| 3 | Ag-(2)-g-$C_3N_4$_aUV_irr | 22 | 7.9 | 34.3 |
| 4 | Ag(2)-g-$C_3N_4$ _aVIS_irr | 22 | 9.5 | 36.4 |
| 5 | Ag(4)-g-$C_3N_4$ _b_irr | 21 | 7.5 | 31.7 |
| 6 | Ag(4)-g-$C_3N_4$ _aUV_irr | 23 | 5.5 | 34.5 |
| 7 | Ag(4)-g-$C_3N_4$ _aVIS_irr | 20 | 5.2 | 33.6 |

The addition of silver resulted in a reduction in the surface area of Ag(2)-g-$C_3N_4$ and Ag(4)-g-$C_3N_4$, which decreased to 18 $m^2$ $g^{-1}$ and 21 $m^2$ $g^{-1}$. This drop can be attributed to the silver ions covering the active surface. After exposure to UV radiation, the surface area exhibited an increase to 22 $m^2$ $g^{-1}$ and 23 $m^2$ $g^{-1}$. However, following Vis irradiation, the surface area was 22 $m^2$ $g^{-1}$ and 20 $m^2$ $g^{-1}$. The nanoscale silver deposits help trap and accumulate electrons, extending the lifetime of both electrons and holes. These accumulated electrons can then readily react with adsorbed oxygen molecules to form superoxide radicals, which are essential for the degradation of para-nitrophenol. The total pore volume (V) and micropore volume ($V_{micro}$) have been shown in Table AT5.1 in the Attachment.

XPS was employed to probe the surface chemistry of both pure g-$C_3N_4$ and its silver decorated counterpart (Figure 5.17).

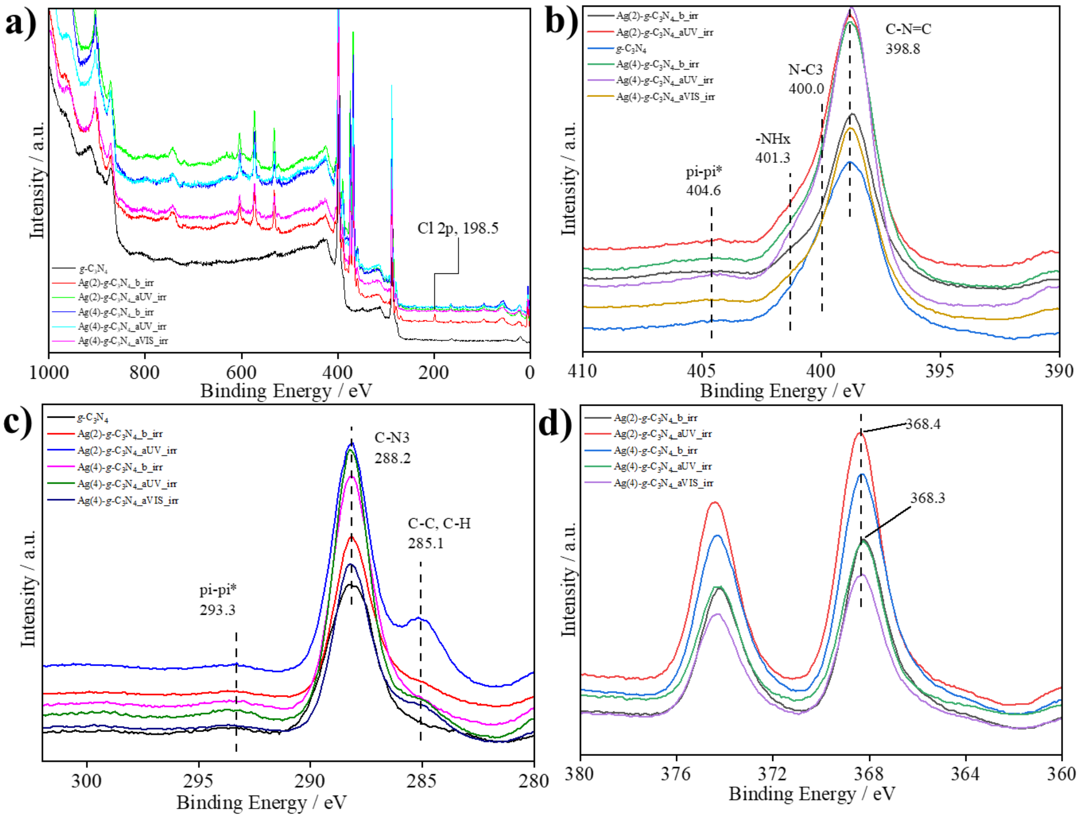

**Figure 5.17.** XPS: (a) survey spectra, (b) N 1s, (c) C 1s, and (d) Ag 3d.

In the survey scan (Figure 5.17/a), peaks for carbon (285.1 eV), silver (368.4 eV), nitrogen (400.0 eV), and oxygen (533 eV) are evident in every spectrum except in the pure g-$C_3N_4$ trace, which naturally lacks the silver signal. The carbon and nitrogen binding energies in the unmodified g-$C_3N_4$ closely match their expected values, confirming its identity. In the silver-modified samples, the clear Ag 3d peaks demonstrate that silver nanoparticles are indeed interacting with the g-$C_3N_4$ surface. Notably, the peak positions for all elements remain unchanged after UV and visible light treatment, underscoring the catalyst's chemical purity and structural stability under irradiation.

The N 1s XPS spectra (Figure 5.17/b) can be resolved into three distinct chemical states with binding energies at 398.8, 400.0, and 401.4 eV. The lowest-energy peak (398.8 eV) is attributed to C–N=C linkages, the middle peak (400.0 eV) to tertiary N–$C_3$ sites, and the highest-energy feature (401.4 eV) to protonated amine groups. A $\pi$-$\pi^*$ transition also appears in every spectrum, confirming the conjugated nature of the system.

In the C 1s region (Figure 5.17/c), two main peaks emerge at 285.1 and 288.0 eV. The lower-energy component (285.1 eV) arises from C–C and C–H bonds within the graphitic network, while the higher-energy peak reflects carbon-nitrogen species. Just like in the N 1s spectra, a $\pi$-$\pi^*$ transition is observed across all curves, indicating preserved aromatic character throughout the samples [196].

Finally, the Ag 3d spectrum (Figure 5.17/d) shows two spin-orbit split peaks at 368.3 and 368.4 eV, corresponding to the Ag $3d_{5/2}$ and $3d_{3/2}$ levels of metallic silver, as reported in the literature [197]. Throughout all these measurements, the consistent peak positions confirm that the chemical environments remain stable under exposure to both UV and visible light.

Based on the Tauc-plot analysis shown in Figure A5.7 in the Attachment, the band-gap energies for g-$C_3N_4$ synthesized from melamine (in air at 550 °C), along with various Ag-g-$C_3N_4$ nanocomposites, were determined and are summarized in Table 5.8. The precision of the band-gap measurements is high, with an uncertainty of approximately 0.01 to 0.02 eV, making the observed subtle differences significant.

**Table 5.8.** Band-gap energies of photocatalysts.

| **Catalyst** | **Band gap energy (eV)** |
|---|---|
| g-$C_3N_4$ | 2.87 |
| Ag(1)-g-$C_3N_4$ | 2.81 |
| Ag(2)-g-$C_3N_4$ | 2.79 |
| Ag(3)-g-$C_3N_4$ | 2.86 |
| Ag(4)-g-$C_3N_4$ | 2.88 |

Reducing the band gap in semiconductors generally broadens photon absorption, potentially improving photocatalytic activity, but the effect is modest, about a 5-10 % increase for every 0.1 eV reduction. Thus, band-gap narrowing alone doesn't fully explain performance gains. Interestingly, two different behaviors were seen among Ag-g-$C_3N_4$ composites: Ag(4)-g-$C_3N_4$ showed minimal influence of band-gap changes on activity, indicating other factors like surface properties or charge carrier dynamics are more critical, while Ag(2)-g-$C_3N_4$ had a stronger shift toward visible light absorption, correlating with better pollutant degradation, showing band-gap tuning can enhance efficiency.

### *5.2.6. Conclusion*

In conclusion, this work highlights the strong promise of g-$C_3N_4$ silver nanocomposites, whether featuring silver nanoparticles or silver ions for environmental cleanup. We found that photocatalytic activity depends critically on the amount of silver present: using cardamom extract leads to greater silver deposition than the simple adsorption method, but loading beyond the optimal level actually reduces silver uptake. Silver ions boost superoxide radical formation, which in turn drives much more efficient degradation of para-nitrophenol, a stubborn pollutant. Uniformly embedded silver nanoparticles within the g-$C_3N_4$ network, together with dispersed silver ions, enhance light absorption and promote effective separation of electron-hole pairs, resulting in superior photocatalytic performance. Notably, these nanocomposites perform exceptionally well under visible light, making them ideal for sun-rich regions. Overall, our study offers a thorough look at how silver species contribute to reactive-oxygen-species generation and contaminant breakdown, deepening our understanding of the mechanisms that enable g-$C_3N_4$-based materials to harness light for green chemistry applications. These findings underscore the potential of silver-modified g-$C_3N_4$ photocatalysts for tackling environmental pollution.

## 5.3. Catalyst g-$C_3N_4$-Bi and g-$C_3N_4$-Zn

Graphitic carbon nitride (g-$C_3N_4$) underwent modification through the incorporation of varying quantities of $Bi_2S_3$ and ZnS, following the synthetic procedures outlined in Section 4.2.3 of the experimental methodology. The synthesized photocatalysts with optimized properties were systematically designated as g-$C_3N_4$-Bi(1), g-$C_3N_4$-Bi(2), g-$C_3N_4$-Bi(3), g-$C_3N_4$-Zn(1), g-$C_3N_4$-Zn(2), and g-$C_3N_4$-Zn(3) to reflect their respective compositional variations. Inductively coupled plasma (ICP-OES) analysis was employed to quantify the bismuth, zinc, sulfur, and oxygen concentrations within the composite materials (Table 4.4). The analytical findings revealed that a substantial fraction of bismuth and a minor proportion of zinc existed predominantly in their oxidized forms rather than as the intended sulfide phases. This deviation from the target sulfide composition can be attributed to the implementation of an aerobic synthesis protocol, which facilitated the oxidation of metal species during the preparation process.

### *5.3.1. Characterizations of g-$C_3N_4$-Bi and g-$C_3N_4$-Zn catalysts*

The FTIR spectrum of pure g-$C_3N_4$ (Figure 5.18/a and b, black curve) displays several characteristic peaks that reveal the vibrational modes of its triazine ($C_3N_3$) ring structure.

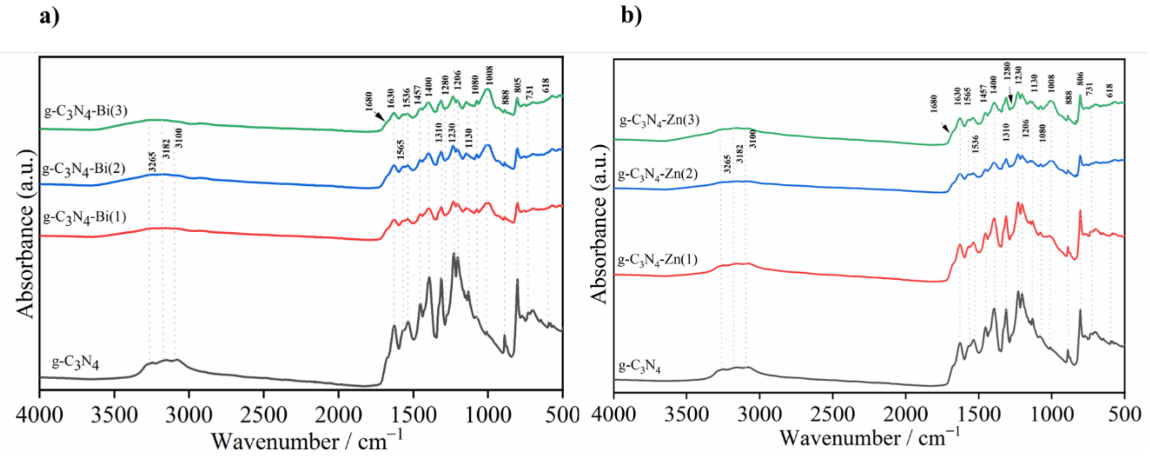

**Figure 5.18.** FTIR spectra of (a) g-$C_3N_4$ and g-$C_3N_4$-Bi (b) g-$C_3N_4$, and g-$C_3N_4$-Zn.

The FTIR spectra shown in Figure 5.18 reveal noticeable changes in g-$C_3N_4$ after the addition of $Bi_2S_3/Bi_2O_3$ and ZnS/ZnO nanoparticles, as represented by the green (g-$C_3N_4$-Bi(3) and g-$C_3N_4$-Zn(3)), blue (g-$C_3N_4$-Bi(2) and g-$C_3N_4$-Zn(2)), and red (g-$C_3N_4$-Bi(1) and g-$C_3N_4$-Zn(1)) curves. The most striking difference, especially at higher concentrations, is the broadening of the peak at 1008 $cm^{-1}$. This peak is connected to C-N stretching vibrations within the g-$C_3N_4$ framework. This broadening likely results from local strains or defects introduced into the g-$C_3N_4$ structure due to the physical interaction between $Bi_2S_3/Bi_2O_3$, ZnS/ZnO and the surface. In addition, changes in electron density around the C-N bonds, possibly from charge transfer between g-$C_3N_4$ and the added semiconductors, may contribute to the wider range of vibrational frequencies seen. Similar broadening of peaks is observed in the 1206-1310 $cm^{-1}$ region, indicating that $Bi_2S_3/Bi_2O_3$ and ZnS/ZnO alter the immediate vibrational environment, even though the main g-$C_3N_4$ framework stays largely intact.

Despite these modifications, the core structure of g-$C_3N_4$ remains largely unchanged following the addition of both sulfides. This is evidenced by the retention of the 805 $cm^{-1}$ peak, which stays sharp and at the same position. The broadening of other peaks and slight intensity reduction suggest that the interaction between g-$C_3N_4$ and both $Bi_2S_3/Bi_2O_3$ and ZnS/ZnO is primarily physical or governed by weak van der Waals forces, rather than forming strong covalent bonds. This interpretation is supported by the absence of new peaks in the spectra, which would indicate the formation of new chemical bonds between the components.

The reduction in the intensity of the FTIR bands characteristic of $Bi_2S_3/Bi_2O_3$ in the composite is mainly due to strong interfacial contact and charge transfer between g-$C_3N_4$ and $Bi_2S_3/Bi_2O_3$. These interactions modify the local bonding environment and vibrational dynamics of $Bi_2S_3/Bi_2O_3$, which leads to peak suppression. Such changes are typical for well-integrated semiconductor composites, indicating effective heterojunction formation and enhanced photocatalytic behavior.

The incorporation of $Bi_2S_3/Bi_2O_3$ and ZnS/ZnO appears to create surface heterogeneity and modify the electronic environment around the g-$C_3N_4$ surface, leading to subtle changes in the FTIR spectrum while maintaining the essential chemical framework.

(Reference FTIR spectra of pure $Bi_2S_3/Bi_2O_3$ and ZnS/ZnO are shown in Figure A5.8 in the Attachment for comparison).

The addition of starch likely introduces extra hydroxyl or other functional groups that subtly alter hydrogen bonding and other weak interactions between g-$C_3N_4$ and the metal sulfides. This helps explain why some FTIR peaks broaden slightly without any major shifts in their positions. The unchanged 805 $cm^{-1}$ band confirms that the triazine framework of g-$C_3N_4$ remains intact despite the modification [198]. Additionally, the broad O-H stretching region around 3000-3500 $cm^{-1}$ can be attributed, at least in part, to the starch hydroxyl groups, supporting the idea that starch is modifying the surface chemistry of the composite [199]. Overall, incorporating starch enhances the dispersion and stability of the metal sulfide particles on g-$C_3N_4$, thereby improving interfacial interactions and resulting in the observed spectral changes.

The XRD patterns shown in Figure 5.19/a and b give valuable insights into the crystal structures of pure g-$C_3N_4$ and the modified materials containing $Bi_2S_3/Bi_2O_3$ and ZnS/ZnO. Looking at the pure g-$C_3N_4$ pattern (black curve), we can see two key features that tell us a lot about its structure.

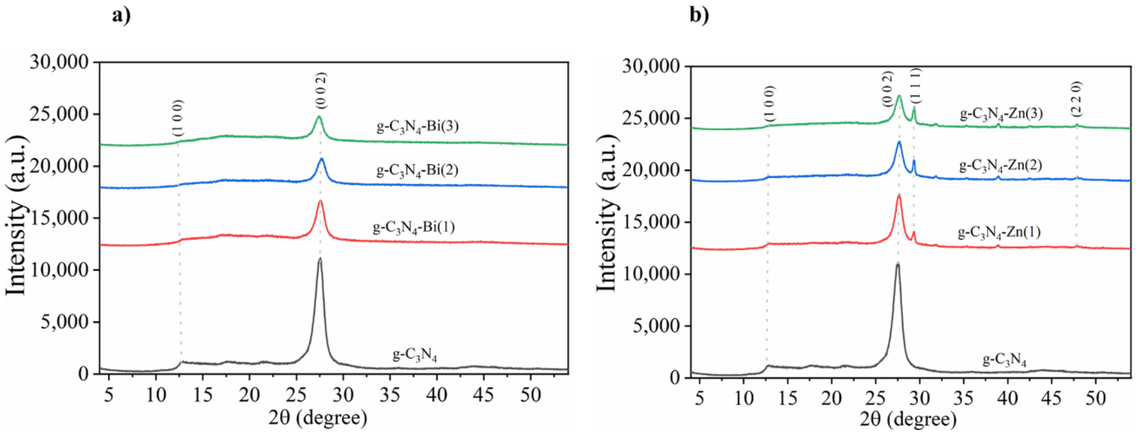

**Figure 5.19.** XRD spectra of parent g-$C_3N_4$ (550 °C) and modified ones (PDF card 00-066-0813). a) g-$C_3N_4$-Bi (b) g-$C_3N_4$-Zn.

The most prominent peak appears at around 27.4°, which corresponds to the (002) plane. This peak is like a fingerprint that confirms the carbon nitride sheets are stacked in layers, much like pages in a book or sheets of graphite. There is also a smaller, weaker peak at about 13.1° from the (100) plane, which tells us how the heptazine building blocks, the fundamental units of g-$C_3N_4$, are arranged within each individual layer [200]. Together, these two peaks confirm that our g-$C_3N_4$ has formed with the expected layered, well-organized structure.

In Figure 5.19/a, we observed that the positions and shapes of the main peaks remain unchanged even after incorporating $Bi_2S_3$ at various concentrations, as represented by the red, blue, and green curves for g-$C_3N_4$-Bi(1), g-$C_3N_4$-Bi(2), and g-$C_3N_4$-Bi(3), respectively. The lack of any noticeable shift or broadening in these key peaks indicates that the addition of $Bi_2S_3$/$Bi_2O_3$ does not significantly alter the crystalline structure of g-$C_3N_4$.

The data in the figure further reveal that as the concentration of $Bi_2S_3$/$Bi_2O_3$ increases, the intensity of the characteristic g-$C_3N_4$ peaks (around 13.1° and 27.4°) progressively decreases. This trend suggests that greater amounts of $Bi_2S_3$/$Bi_2O_3$ within the composite can partially mask the diffraction signals from g-$C_3N_4$, thereby reducing the observed peak intensities. Importantly, despite this decrease, the positions and shapes of the main peaks do not shift or broaden, indicating that the fundamental crystalline structure of g-$C_3N_4$ remains largely unaltered by the addition of $Bi_2S_3$/$Bi_2O_3$ [201]. These findings are in line with previous reports, confirming that $Bi_2S_3$/$Bi_2O_3$ incorporation does not significantly disrupt the structural integrity of g-$C_3N_4$.

Figure 5.19/b reveals the emergence of additional diffraction peaks at $2\theta = 28.5°$ and 47.5°, which match the (111) and (220) planes of cubic ZnS/ZnO (zinc blende phase). The sharpness and strength of these reflections show that ZnS/ZnO forms highly crystalline domains within the composite, without any distortion of its lattice [202]. At the same time, the characteristic peaks of g-$C_3N_4$ remain unchanged in width, confirming that both components coexist uniformly and that ZnS/ZnO nanoparticles retain their crystalline integrity after synthesis.

As the ZnS loading increases from g-$C_3N_4$-Zn(1) (red curve) through g-$C_3N_4$-Zn(2) (blue) to g-$C_3N_4$-Zn(3) (green), the intensity of the ZnS/ZnO peaks grows stronger. This trend indicates a larger fraction of well-ordered ZnS/ZnO in the material, which should enhance the interface between g-$C_3N_4$ and ZnS/ZnO and, consequently, improve the composite photocatalytic and electronic performance. The presence of starch during preparation helps distribute ZnS/ZnO particles evenly, reinforcing both structural stability and intimate contact at the heterojunction.

In the highest-loading samples (green curves in Figure 5.19/a, b), the main g-$C_3N_4$ reflections at 13.1° and 27.4° shift vary slightly toward lower angles. This small shift suggests a modest expansion of the interlayer spacing in g-$C_3N_4$, likely caused by lattice strain or interfacial tension where $Bi_2S_3$/$Bi_2O_3$ and ZnS/ZnO particles attach. Although the core layered structure of g-$C_3N_4$ remains intact, these slight changes in peak position and reduced peak intensity illustrate how increasing amounts of $Bi_2S_3$/$Bi_2O_3$ and ZnS/ZnO can subtly influence the stacking arrangement without disrupting the fundamental crystallinity of the carbon nitride framework.

The identified phase for g-$C_3N_4$ is shown to correspond to the PDF card 00-066-0813, ensuring accurate phase identification and supporting the assignment of crystalline phases in the composites. The amount of $Bi_2S_3$/$Bi_2O_3$ and ZnS/ZnO were too small to detect for XRD identification.

As seen in Figure 5.20/A(a, b), the SEM images reveal that g-$C_3N_4$ possesses a distinctive multi-layered, porous morphology. This structural arrangement significantly enhances the material's surface area and exposes more active sites, both of which are essential for achieving efficient photocatalytic performance. The combination of these features facilitates greater interaction between the catalyst and target molecules, thereby supporting its effectiveness in photocatalytic applications.

The low-magnification SEM image (Figure 5.20/A(a)) captures the typical layered, flake-like structure of g-$C_3N_4$, a hallmark of its graphitic nature that stems from the material's tendency to form stacked, sheet-like arrangements on the atomic scale [203]. Visibly, we observe loosely overlapping sheets with irregular edges and a somewhat uneven distribution, resulting in a highly textured surface. This structure not only confirms the expected morphology of graphitic carbon nitride but also supplies a relatively large surface area, which is highly beneficial for photocatalytic applications. The abundance of exposed sites facilitates efficient adsorption and interaction between reactants and the catalyst, thereby supporting enhanced photocatalytic activity.

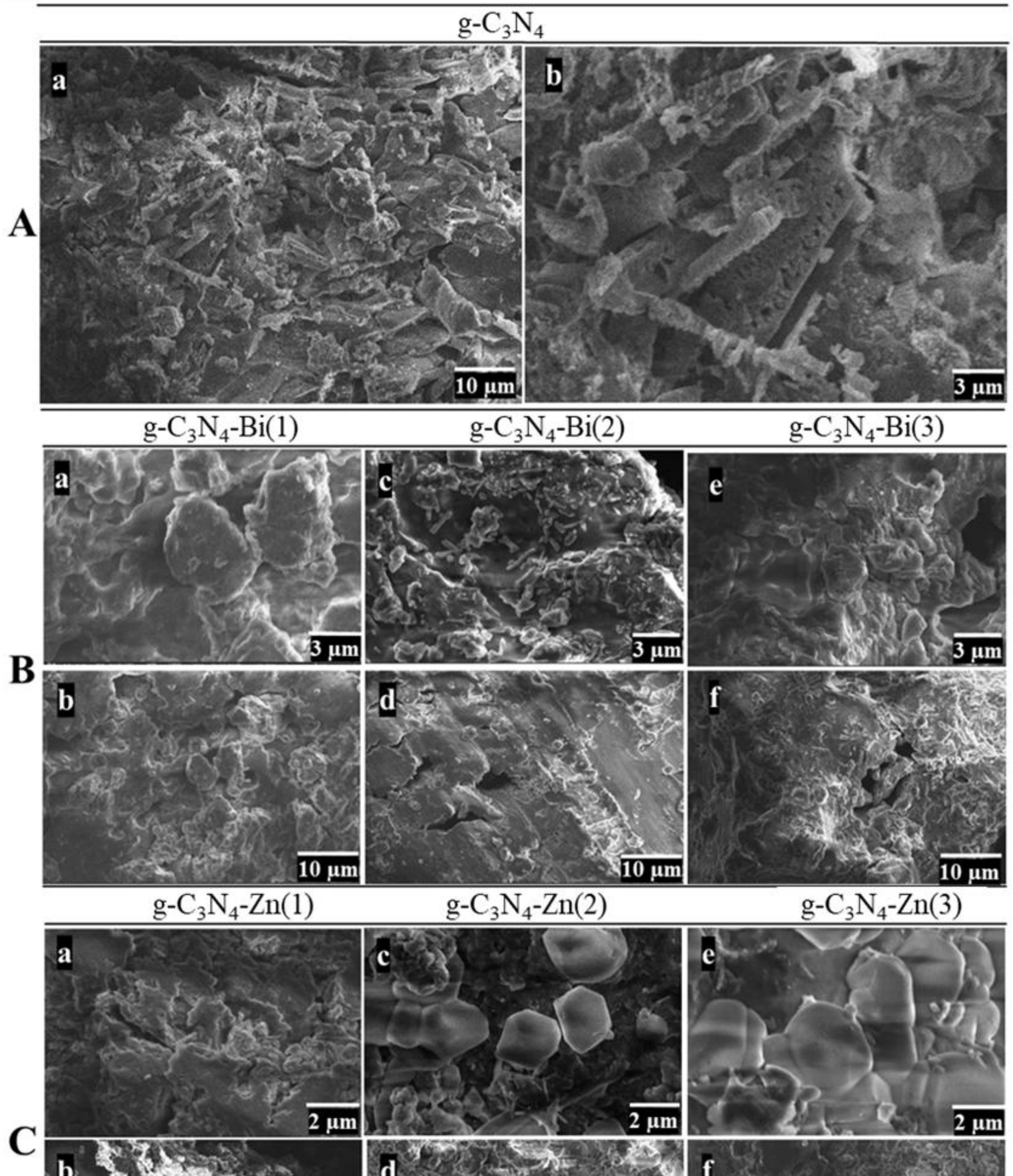

**Figure 5.20.** SEM images of

(A) g-$C_3N_4$ (a) at low (5000×) and (b) high (15,000×) magnification

(B) g-$C_3N_4$-Bi (b,d,f) at low (5000×) and (a,c,e) high (15,000×) magnification

(C) g-$C_3N_4$-Zn (b,d,f) at low (5000×) and (a,c,e) high (20,000×) magnification.

At higher magnification (Figure 5.20/A(b)), the detailed features of the g-$C_3N_4$ layers become more evident. The individual sheets are distinctly outlined, with noticeable gaps and cracks present throughout the structure, highlighting its layered and porous nature. The edges of these sheets appear irregular and somewhat frayed, which may contribute to enhanced photocatalytic activity by exposing additional active sites. This coarse, permeable morphology is advantageous for photocatalysis because it facilitates greater light penetration and improves contact between the catalyst surface and pollutant molecules, thereby potentially boosting the overall degradation efficiency.

The SEM images of the g-$C_3N_4$-Bi composites shown in Figure 5.20/B(a-f) demonstrate how different $Bi_2S_3$/$Bi_2O_3$ concentrations influence the surface morphology and structure of the material. In the sample with the lowest $Bi_2S_3$/$Bi_2O_3$ content, g-$C_3N_4$-Bi(1), the high-magnification image (Figure 5.20/B(a)) reveals an aggregated, granular texture composed of rounded particles without well-defined shapes. At lower magnification (Figure 5.20/B(b)), the surface appears relatively uniform, characterized by larger aggregates that likely correspond to the g-$C_3N_4$ matrix itself. This smooth and featureless morphology indicates that at this low $Bi_2S_3$/$Bi_2O_3$ concentration, the additive does not substantially modify the g-$C_3N_4$ structure, resulting in a dispersed or loosely clustered presence of $Bi_2S_3$/$Bi_2O_3$ without distinct morphological features.

A notable transformation is observed in the g-$C_3N_4$-Bi(2) sample, where the high-magnification SEM image (Figure 5.20/B(c)) reveals clear rod-like structures. These elongated formations suggest that the intermediate $Bi_2S_3$/$Bi_2O_3$ concentration encourages anisotropic growth, leading to the development of $Bi_2S_3$/$Bi_2O_3$ nanocrystals with a distinct rod-shaped morphology on the g-$C_3N_4$ surface. Such rod-like features are beneficial for photocatalytic performance, as they increase the available surface area and provide additional active sites for reactions. At lower magnification (Figure 5.20/B(d)), these rod-like structures appear more widely distributed throughout the sample, integrated within the g-$C_3N_4$ matrix. This distribution indicates enhanced interfacial contact between $Bi_2S_3$/$Bi_2O_3$ and g-$C_3N_4$ at this concentration, which likely contributes to improved photocatalytic efficiency.

In the g-$C_3N_4$-Bi(3) sample, a distinct morphological shift occurs compared to the previous intermediate concentration. The high-magnification SEM image (Figure 5.20/B(e)) reveals that the well-defined rod-like structures give way to densely packed clusters. This agglomeration likely results from the higher concentration of $Bi_2S_3$/$Bi_2O_3$, causing excessive coverage on the g-$C_3N_4$ surface, which may block active sites and reduce the overall accessible surface area. At lower magnification (Figure 5.20/B(f)), the material exhibits a compact and rough texture with limited discernible features, indicating that the increased $Bi_2S_3$/$Bi_2O_3$ loading oversaturates the surface and diminishes morphological clarity. Such structural changes are expected to negatively impact photocatalytic efficiency by restricting reactant access and decreasing the number of exposed catalytic sites crucial for effective pollutant degradation.

The SEM images of the g-$C_3N_4$-Zn composites shown in Figure 5.20/C(a-f) demonstrate how different concentrations of ZnS influence the surface morphology of the materials, specifically for g-$C_3N_4$-Zn(1), g-$C_3N_4$-Zn(2), and g-$C_3N_4$-Zn(3), which correspond to the addition of 25 $cm^3$, 45 $cm^3$, and 65 $cm^3$ of 10 mM ZnS, respectively. In the sample with the lowest ZnS/ZnO loading, g-$C_3N_4$-Zn(1), the high-magnification SEM image (Figure 5.20/C(a)) reveals a rough, irregular surface composed of small, aggregated particles dispersed throughout the g-$C_3N_4$ matrix. The corresponding low-magnification image (Figure 5.20/C(b)) shows a similarly coarse yet relatively porous structure, characterized by visible voids within the particle clusters. These features indicate a comparatively low ZnS/ZnO density on the surface of g-$C_3N_4$ in this sample.

In the g-$C_3N_4$-Zn(2) sample, where the ZnS/ZnO concentration is increased, the high-magnification SEM image (Figure 5.20/C(c)) reveals the development of larger, hexagonal-shaped ZnS clusters that are more distinctly defined within the g-$C_3N_4$ matrix. Compared to g-$C_3N_4$-Zn(1), these clusters exhibit a more extensive coverage of the surface, suggesting improved distribution and stronger interfacial interaction between ZnS/ZnO and g-$C_3N_4$. At lower magnification (Figure 5.20/C(d)), the composite maintains a porous overall structure while displaying a more homogeneous dispersion of ZnS/ZnO clusters across the surface. This enhanced uniformity likely contributes to an increased surface area and more accessible active sites, which are beneficial for boosting photocatalytic performance. The higher ZnS/ZnO loading thus results in a more consistent and comprehensive coating on the g-$C_3N_4$ substrate.

In the g-$C_3N_4$-Zn(3) sample, which features the highest ZnS/ZnO concentration, the high-magnification SEM image (Figure 5.20/C(e)) reveals densely packed ZnS/ZnO clusters forming extensive, plate-like structures that cover large portions of the g-$C_3N_4$ surface. This substantial ZnS/ZnO coverage suggests surface saturation, likely leading to a significant reduction in the exposed g-$C_3N_4$ surface area. Correspondingly, the low-magnification image (Figure 5.20/C(f)) shows a compact and less porous morphology compared to the samples with lower ZnS/ZnO loadings, characterized by a dense aggregation of ZnS/ZnO particles. Such extensive coverage may negatively impact photocatalytic efficiency by limiting light penetration and blocking active sites on the g-$C_3N_4$ surface, thereby restricting the catalyst's ability to interact effectively with pollutants. Overall, the images illustrate a clear progression from dispersed ZnS/ZnO clusters at low concentrations to more continuous and saturated ZnS/ZnO layers at high concentrations, with the best dispersion and potentially optimal photocatalytic performance observed at intermediate ZnS/ZnO loadings.

Transmission electron microscopy (TEM) analysis was performed on the selected optimal nanocomposites, specifically g-$C_3N_4$-Bi(2) and g-$C_3N_4$-Zn(2) (Figure 5.21). Figure 5.21/X presents a low-magnification scanning transmission electron microscopy (STEM) image of the $Bi_2S_3$/$Bi_2O_3$-modified graphitic carbon nitride. Both the high-angle annular dark-field (STEM-HAADF) image and the corresponding STEM energy-dispersive X-ray spectroscopy (STEM-EDS) elemental maps reveal the spatial distributions of carbon (green), nitrogen (blue), oxygen (orange), sulfur (purple), and bismuth (yellow).

In Figure 5.21/X, the maps indicate a uniform dispersion of bismuth and sulfur throughout the sample. Notably, larger bismuth-containing particles display a strong oxygen signal but a weak sulfur signal, suggesting the presence of bismuth oxide alongside bismuth sulfide. These observations are further supported by the EDS spectrum collected from the entire HAADF region, as shown in Figure 5.21/X(D).

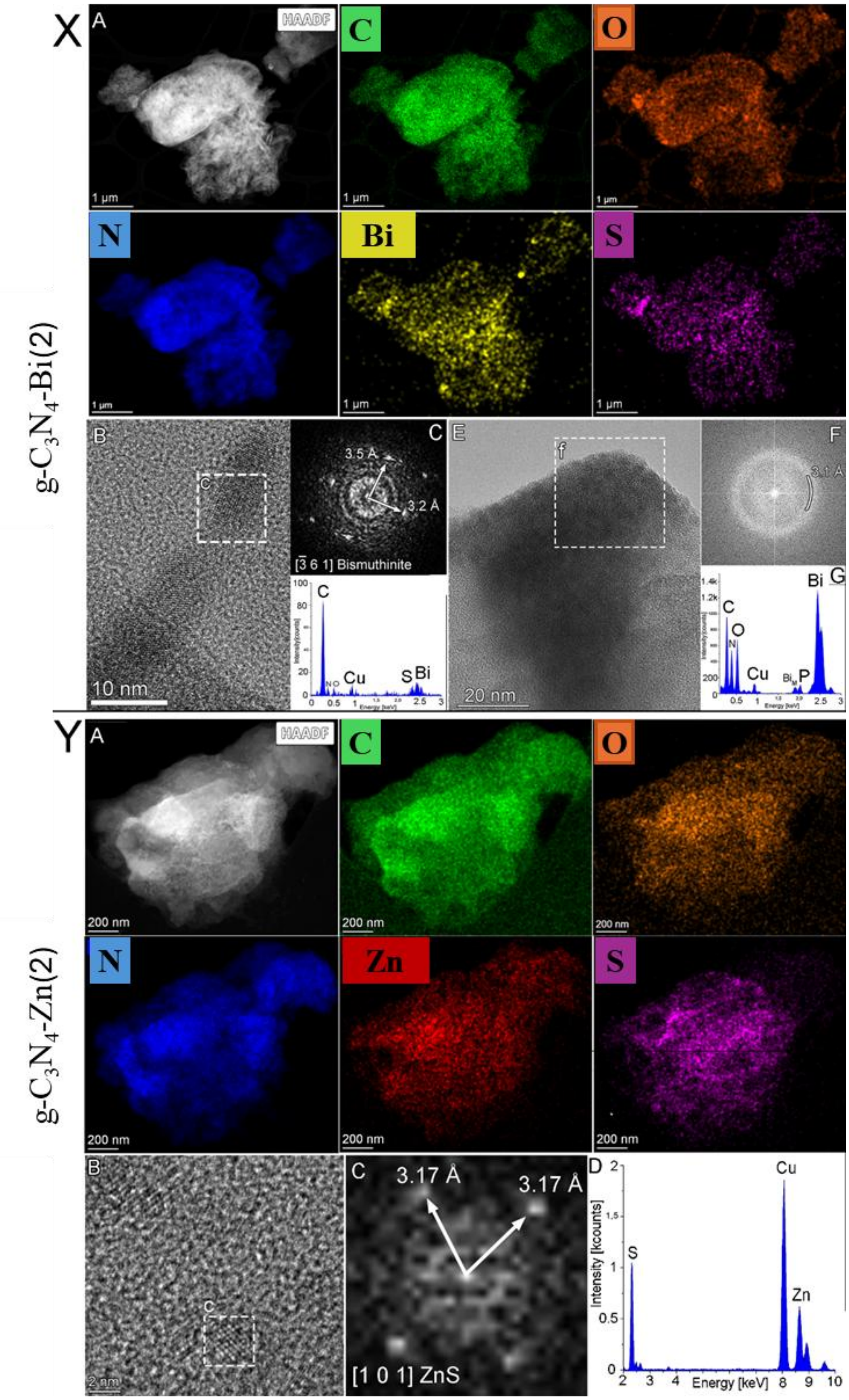

**Figure 5.21.** STEM-HAADF image and the STEM-EDS of (X) g-$C_3N_4$-Bi(2) nanocomposite (Y) g-$C_3N_4$-Zn(2) nanocomposite.

High-resolution transmission electron microscopy analysis of the $Bi_2S_3/Bi_2O_3$-modified graphitic carbon nitride sample was performed, as shown in Figure 5.21/X(E). The image reveals that the nanoparticles exhibit an amorphous structure, as evidenced by the lack of clear lattice fringes. Further examination of the selected region via fast Fourier transform (Figure 5.21/X(E/f)) displays a single diffraction ring with a radius of approximately 3.1 Å, characteristic of amorphous or poor crystalline material. The corresponding energy-dispersive X-ray spectroscopy spectrum collected from this region (Figure 5.21/X(G)) indicates that the nanoparticles are primarily composed of bismuth, along with notable amounts of oxygen and carbon, suggesting the particles are predominantly bismuth oxide rather than bismuth sulfide. It is important to note that copper signals detected in the EDS spectrum arise from the copper TEM grid used during analysis [204]. Control experiments using a gold grid confirmed the absence of copper contamination, verifying the source of copper signals.

The HRTEM image (Figure 5.21/X(B)) clearly depicts the crystalline structure of $Bi_2S_3/Bi_2O_3$ nanoparticles supported on the g-$C_3N_4$ substrate. The inset (Figure 5.21/X(B/c)) provides a detailed view of a single nanoparticle, whose fast Fourier transfor image (Figure 5.21/X(C)) confirms that the crystal structure corresponds to bismuthinite ($Bi_2S_3$). The electron beam during imaging was oriented parallel to the [-3 6 1] crystallographic direction, as verified by the FFT analysis.

Complementing this, the energy-dispersive X-ray spectroscopy spectrum (Figure 5.21/X(D)) of the same particle indicates a chemical composition consistent with $Bi_2S_3/Bi_2O_3$ but also reveals an elevated carbon content relative to the g-$C_3N_4$ carrier. This suggests the possible co-existence of carbon-containing species in the vicinity of the nanoparticle. Notably, the bismuth to oxygen atomic ratio derived from the spectrum is approximately 10:18, which aligns more closely with bismuth oxide ($Bi_2O_3$) than pure $Bi_2S_3$, implying partial surface oxidation of the bismuthinite particles.

Figure 5.21/Y presents the scanning transmission electron microscopy analysis of the optimized ZnS/ZnO-modified graphitic carbon nitride sample. The STEM-HAADF image (Figure 5.21/Y(A)) together with the corresponding STEM-EDS elemental maps (Figure 5.21/Y(D)) reveal the spatial distribution of key elements: carbon (green), nitrogen (blue), oxygen (orange), sulfur (purple), and zinc (red). The elemental mapping illustrates the uniform dispersion of zinc and sulfur within the carbon nitride matrix. Additionally, the EDS spectrum collected from the entire HAADF image confirms that the sample predominantly consists of carbon and nitrogen, consistent with the g-$C_3N_4$ substrate, along with appreciable amounts of zinc and sulfur, validating successful modification. It should be noted that the detected copper signal originates from the copper TEM grid used during the analysis, rather than the sample itself.

The HRTEM image in Figure 5.21/Y(B) reveals the crystalline nature of the zinc sulfide nanoparticles within the g-$C_3N_4$ composite. A specific region marked as (c) highlights a ZnS nanoparticle approximately 2 nm in size, situated on the carbon nitride support. The fast Fourier transform image of this nanoparticle (Figure 5.21/Y(B/c)) provides clear evidence that the crystal structure corresponds to sphalerite (ZnS). The measured lattice fringe spacing of 3.17 Å matches the characteristic (111)-type crystallographic planes, such as (111) and (1-1-1), observed along the (101) orientation. This confirms the successful incorporation of well-defined crystalline ZnS nanoparticles within the composite material [205].

The BET surface area plays a vital role in determining the photocatalytic performance of materials like g-$C_3N_4$ and its composites, as it directly affects the number of active sites available for light absorption and contaminant degradation. Pristine g-$C_3N_4$ exhibits a relatively high BET surface area of 27.9 $m^2/g$, which facilitates enhanced accessibility to reactive sites crucial for efficient photocatalysis. However, when composites are formed with $Bi_2S_3/Bi_2O_3$ and ZnS/ZnO using starch as a templating or modifying agent, a noticeable decrease in BET surface area is observed for both materials, as summarized in Table 5.9. This reduction can likely be attributed to surface coverage by the introduced phases, increased structural compactness, and the combined influence of the secondary components, which collectively limit the exposed surface area available for photocatalytic reactions.

The observed decrease in BET surface area for the starch-assisted synthesized g-$C_3N_4$-Bi and g-$C_3N_4$-Zn composites can be primarily attributed to the deposition of $Bi_2S_3/Bi_2O_3$ and ZnS/ZnO nanoparticles onto the g-$C_3N_4$ framework. This deposition may partially block or fill the intrinsic pores of g-$C_3N_4$, thereby limiting the accessibility of surface area during BET measurements. Additionally, starch used as a templating or modifying agent may undergo decomposition throughout the synthesis process, potentially leaving residual organic fragments or altering the composite microstructure.

**Table 5.9.** BET surface area of the catalyst samples.

| SN | Catalyst | $S_{BET}$ (m$^2$/g) | V (cm$^3$/g) | $D_{av}$ (nm) |
|---|---|---|---|---|
| **1** | g-$C_3N_4$ | 27.9 | 0.19479 | 24.3 |
| **2** | g-$C_3N_4$-Bi(1) | 12.9 | 0.09894 | 29.1 |
| **3** | g-$C_3N_4$-Bi(2) | 8.9 | 0.06227 | 25.0 |
| **4** | g-$C_3N_4$-Bi(3) | 6.9 | 0.05133 | 26.5 |
| **5** | g-$C_3N_4$-Zn(1) | 4.2 | 0.03735 | 35.1 |
| **6** | g-$C_3N_4$-Zn(2) | 2.6 | 0.02627 | 34.6 |
| **7** | g-$C_3N_4$-Zn(3) | 2.9 | 0.02752 | 37.2 |

Such changes can promote particle agglomeration or densification, resulting in reduced porosity and a decline in accessible surface sites. Furthermore, residual organic matter from starch degradation may occupy surface active sites, further contributing to the overall reduction in measured surface area. Together, these factors explain the notable decrease in BET surface area observed in these composites despite their enhanced photocatalytic functionalities.

Although the BET surface area decreases with the addition of starch in the synthesis of g-$C_3N_4$-Bi and g-$C_3N_4$-Zn composites, the presence of starch imparts synergistic benefits that enhance their photocatalytic performance. Starch plays a crucial role in facilitating the formation of effective heterojunctions between g-$C_3N_4$ and the metal sulfides, which promotes more efficient separation and transfer of photogenerated electrons and holes. This suppressed charge recombination results in improved generation of reactive oxygen species, such as $^{\bullet}OH$ and $O_2^{\bullet-}$ radicals, both of which are essential for the breakdown of pollutants. Additionally, the composites exhibit a reduced band gap, leading to a broader absorption spectrum that allows more effective utilization of visible light. These factors collectively compensate for the reduced surface area by enhancing light harvesting and charge-carrier dynamics, ultimately improving the overall photocatalytic efficiency of the materials.

The BET surface area noticeably decreased from 22 $m^2/g$ for pure g-$C_3N_4$ to 12.9, 6.9, and 8.9 $m^2/g$ for the g-$C_3N_4$-Bi composites (1, 2, and 3, respectively), and further dropped to 4.2, 2.6, and 2.6 $m^2/g$ for the g-$C_3N_4$-Zn composites synthesized using starch. This decline indicates a reduction in the number of accessible active sites on the catalyst surface. Nevertheless, despite the diminished surface area, the incorporation of starch plays a crucial role by promoting improved charge carrier separation, broadening light absorption, and fostering synergistic interactions within the composite materials. These effects significantly boost the photocatalytic performance, demonstrating that the interplay between surface area and enhanced functional properties is vital. Thus, starch serves as an essential component in engineering an effective photocatalytic system, where the formation of heterojunctions and functionalization mechanisms are key drivers for achieving superior catalytic efficiency.

XPS provides valuable insight into the synergistic interactions between g-$C_3N_4$ and $Bi_2S_3/Bi_2O_3$, as well as between g-$C_3N_4$ and ZnS/ZnO within the nanocomposite systems. As a surface-sensitive analytical technique, XPS enables us to probe the chemical composition and oxidation states of the constituent elements at the nanocomposite interface. Through detailed XPS analysis, we can not only determine how the various components are distributed on the surface but also assess any changes in chemical environment that may signal strong interfacial interactions or charge transfer. These inter-component effects reflected the shifts in binding energies or the appearance of new chemical states that help confirm the presence of synergistic phenomena that are often responsible for improved photocatalytic performance in these composites.

The XPS analysis presented in Figure 5.22 provides detailed insights into the valence states and chemical environments of the constituent elements within g-$C_3N_4$, g-$C_3N_4$-Bi, and g-$C_3N_4$-Zn nanocomposites. The comprehensive survey spectra (Figure 5.22/(a-e)) clearly reveal characteristic signals corresponding to C 1s, N 1s, O 1s, Bi 4f, Zn 2p, and S 2s, confirming the presence of these specific elements within the composites. Notably, the absence of additional peaks in the spectra indicates that only carbon, nitrogen, oxygen, sulfur, bismuth, and zinc are present in significant amounts within the g-$C_3N_4$-Bi and g-$C_3N_4$-Zn samples. This elemental composition reflects both the successful synthesis of the targeted nanocomposites and the chemical purity of the materials, as any potential contaminants are below the detectable limit of XPS.

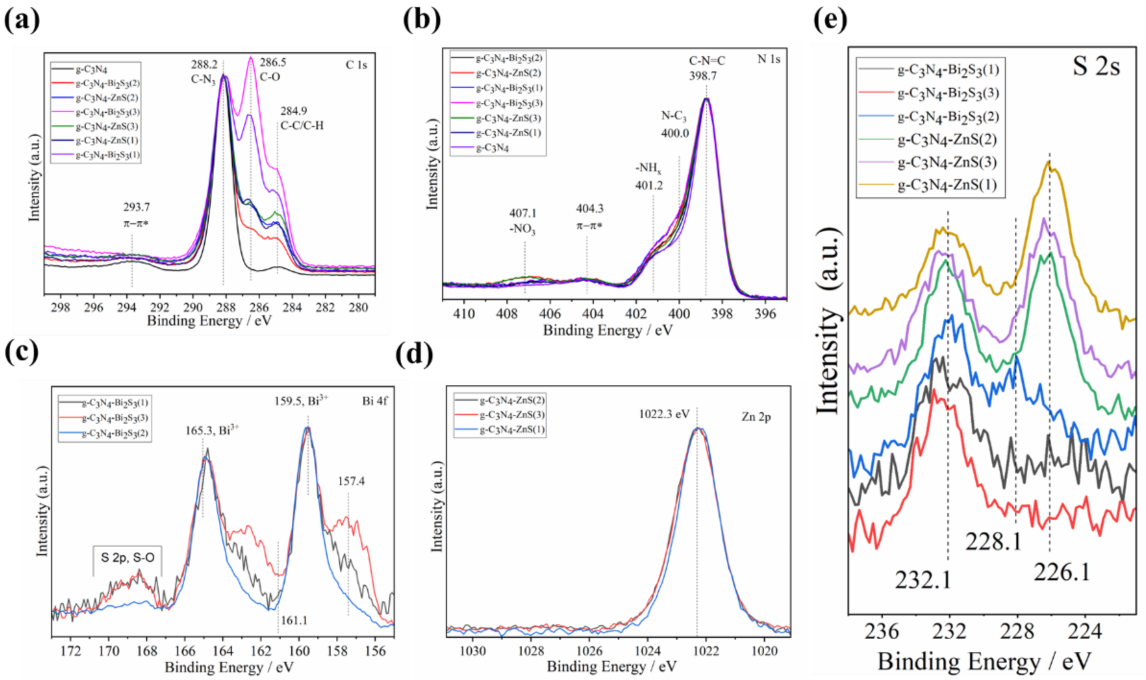

**Figure 5.22** Comprehensive XPS spectra of g-$C_3N_4$-Bi and g-$C_3N_4$-Zn nanocomposites. XPS spectra of (a) C 1s, (b) N 1s, (c) Bi 4f, (d) Zn 2p, and (e) S 2s.

The C 1s spectrum shown in Figure 5.22/a reveals that carbon atoms in the sample occupy a variety of chemical environments. For the g-$C_3N_4$ sample, depicted by the black curve, a minor C-C/C-H signal can be attributed to the presence of adventitious (surface-adsorbed) carbon. The high-resolution C 1s spectrum further displays three distinct peaks at binding energies of 288.2, 286.5, and 284.9 eV [146]. The peak at 288.2 eV is characteristic of the graphite-like C-$N_3$ structure found within the aromatic lattice of g-$C_3N_4$. Meanwhile, the peaks at 286.5 eV and 284.9 eV are associated with carbon-oxygen (C-O) and carbon-carbon/hydrogen (C-C/C-H) bonds, respectively, interactions that reflect the contribution from starch, which was used during synthesis as both a stabilizing and reducing agent. These observations collectively highlight how various carbon species are present due to both the intrinsic g-$C_3N_4$ framework and the influence of functional groups introduced by starch modification.

The high-resolution N 1s spectra shown in Figure 5.22/b display three prominent peaks that are characteristic of pyridine-like aromatic nitrogen structures. These peaks appear at binding energies of 398.7 eV, 400.0 eV, and 401.2 eV, corresponding respectively to C-N=C groups, tertiary nitrogen atoms ($N-(C)_3$), and terminal amino groups ($-NH_2$) within the $g-C_3N_4$ framework [206]. Additionally, a distinct peak at 407.1 eV can be attributed to the presence of nitrate species, arising from the use of metal nitrate salts during synthesis. The spectrum also features π→π* shake-up satellite peaks, observed at 293.7 eV in the C 1s region and at 404.3 eV in the N 1s region, which are indicative of the extended conjugated structure characteristic of graphitic carbon nitride. These spectral features collectively confirm the integrity of the $g-C_3N_4$ aromatic lattice while reflecting the chemical modifications introduced during composite formation.

The chemical states of bismuth and sulfur within the $Bi_2S_3$ nanoparticles were evaluated using high-resolution XPS analysis of the Bi 4f region, as illustrated in Figure 5.22/c. The characteristic binding energies for Bi $4f_{7/2}$ and Bi $4f_{5/2}$ were observed at 159.5 eV and 165.3 eV, respectively, consistent with the expected values for Bi in $Bi_2S_3$ [207]. Identification of sulfur within the nanocomposite presents some complexity, as the S $2p_{3/2}$ photoelectron signal typical of a sulfide environment in $Bi_2S_3$, expected near 161.1 eV, significantly overlaps with the Bi 4f doublet. As a result of this spectral overlap, only the S 2p doublet corresponding to S-O bonds, which shift by several electron volts and therefore do not coincide with Bi 4f, can be clearly seen in this region [208]. To more definitively confirm the presence of sulfur, we also examined the S 2s region (Figure 5.22/e), which provides an unobstructed measure of sulfur content and helps establish the chemical environment of sulfur within the composite. This approach allows us to differentiate sulfur species, despite the complexity introduced by the overlapping XPS features.

The Zn 2p core-level XPS spectra, as shown in Figure 5.22/d, display a prominent peak centered around 1022.3 eV, which corresponds to the Zn $2p_{3/2}$ orbital [209]. This distinct signal confirms the successful incorporation of zinc species within the sample. In the high-resolution S 2s spectra presented in Figure 5.22/e, the upper three spectra corresponding to the zinc-containing composites exhibit peaks at approximately 226.1 eV and 232.1 eV. These features can be attributed to zinc sulfide and sulfur species bound to oxygen, the latter likely arising from the starch used in the synthesis process. Meanwhile, the three lower spectra correspond to bismuth sulfide composites, characterized by a sulfur peak at around 228.1 eV, indicating the presence of $Bi_2S_3$.

Considering the elemental balance and the proximity of binding energies between sulfides and oxides, it is evident that, along with $Bi_2S_3$ and ZnS, oxidized forms such as $Bi_2O_3$ and ZnO are also likely present on the composite surfaces. This conclusion is supported by the overlapping binding energies of $Bi_2O_3$ and $Bi_2S_3$, as well as ZnO and ZnS, which can complicate spectral interpretation. Importantly, these XPS findings align well with supplementary inductively coupled plasma measurements, collectively confirming the coexistence of sulfide and oxide species in these photocatalytic nanocomposites.

Based on the Tauc-plot analysis (Figure A5.9 in the Attachment), the band-gap energies for all our nanocomposites were calculated, and these values are summarized in Table 5.10. If a semiconductor has a smaller band gap, it can absorb more photons and potentially work better as a photocatalyst.

**Table 5.10.** Band-gap energies of photocatalysts.

| Catalyst | Band gap energy (eV) |
|---|---|
| g-$C_3N_4$ | 2.88 |
| g-$C_3N_4$-Bi(1) | 2.86 |
| g-$C_3N_4$-Bi(2) | 2.84 |
| g-$C_3N_4$-Bi(3) | 2.88 |
| g-$C_3N_4$-Zn(1) | 2.84 |
| g-$C_3N_4$-Zn(2) | 2.81 |
| g-$C_3N_4$-Zn(3) | 2.86 |

Interestingly, we observed different behaviors between the two types of nanocomposites. For the $Bi_2S_3$/$Bi_2O_3$-modified materials, the band-gap changes did not seem to have a major impact on their photocatalytic activity. However, the ZnS/ZnO modified composites showed more promising results; their band gaps shifted further into the visible light range, which suggests they should be more effective at breaking down compounds like coumarin and para-nitrophenol when exposed to visible light. This makes the composites particularly attractive for practical applications where we want to use sunlight rather than UV lamps.

### *5.3.2. Comparison of atomic content by XPS and EDX analysis*

We compared the elemental compositions of all synthesized composites using both X-ray Photoelectron Spectroscopy and Energy-Dispersive X-ray Spectroscopy, with detailed results summarized in Table 5.11. These two analytical techniques differ fundamentally in their probing depths and sensitivities: EDX provides information on the bulk elemental makeup of the samples, while XPS offers a surface-sensitive analysis focused on the top few nanometers. Consequently, notable differences arise between their findings.

For pure g-$C_3N_4$, EDX detected a higher carbon content (47.39 %) compared to XPS (41.45 %), whereas XPS revealed greater nitrogen presence at the surface (57.76 %) than EDX did in bulk (43.9 %). This suggests that nitrogen is relatively enriched near the material's surface, while carbon is more uniformly distributed. Additionally, the elevated oxygen content observed by EDX (8.71 %) likely stems from oxygen species adsorbed within the bulk or from environmental exposure.

In the g-$C_3N_4$-Bi composites across all tested ratios, XPS consistently showed higher sulfur and bismuth concentrations compared to EDX, for instance, in g-$C_3N_4$-Bi(3), sulfur was 0.27 % (XPS) versus 0.11 % (EDX), and bismuth was 0.10 % (XPS) versus 0.06 % (EDX). This pattern strongly indicates that $Bi_2S_3$/$Bi_2O_3$ predominantly resides on the surface of these composites rather than being homogeneously distributed. Similarly, for the g-$C_3N_4$-Zn samples, XPS measurements revealed significantly elevated zinc and sulfur levels at the surface relative to the bulk values from EDX, such as zinc concentrations of 1.75 % (XPS) versus 0.16 % (EDX) in g-$C_3N_4$-Zn(1). These trends clearly demonstrate that ZnS/ZnO is surface enriched in the composites.

**Table 5.11.** Atomic weight % values determined by XPS and EDX measurements.

| **g-$C_3N_4$** | | | | | | | | |
|---|---|---|---|---|---|---|---|---|
| | C | N | O | S | Bi | Zn | Na | Si* |
| EDX | 47.39 | 43.9 | 8.71 | | | | | |
| XPS | 41.45 | 57.76 | 0.79 | | | | | |
| **g-$C_3N_4$-Bi(1)** | | | | | | | | |
| | C | N | O | S | Bi | Zn | Na | Si |
| EDX | 39.52 | 33.61 | 26.46 | 0.04 | 0.02 | | 0.28 | 0.07 |
| XPS | 49.97 | 26.77 | 22.79 | 0.14 | 0.03 | | 0.30 | |
| **g-$C_3N_4$-Bi(2)** | | | | | | | | |
| | C | N | O | S | Bi | Zn | Na | Si |
| EDX | 41.11 | 37.83 | 20.48 | 0.09 | 0.04 | | 0.44 | 0.01 |
| XPS | 44.02 | 44.67 | 10.62 | 0.27 | 0.13 | | 0.30 | |
| **g-$C_3N_4$-Bi(3)** | | | | | | | | |
| | C | N | O | S | Bi | Zn | Na | Si |
| EDX | 41.11 | 27.09 | 30.97 | 0.11 | 0.06 | | 0.59 | 0.06 |
| XPS | 51.98 | 19.22 | 27.08 | 0.27 | 0.1 | | 1.35 | |
| **g-$C_3N_4$-Zn(1)** | | | | | | | | |
| | C | N | O | S | Bi | Zn | Na | Si |
| EDX | 39.24 | 52.13 | 8.34 | 0.11 | | 0.16 | | 0.01 |
| XPS | 44.48 | 36.87 | 15.38 | 0.73 | | 1.75 | 0.79 | |
| **g-$C_3N_4$-Zn(2)** | | | | | | | | |
| | C | N | O | S | Bi | Zn | Na | Si |
| EDX | 36.55 | 39.63 | 22.87 | 0.35 | | 0.59 | | 0.02 |
| XPS | 41.70 | 36.82 | 16.21 | 0.97 | | 2.48 | 1.82 | |
| **g-$C_3N_4$-Zn(3)** | | | | | | | | |
| | C | N | O | S | Bi | Zn | Na | Si |
| EDX | 38.24 | 38.04 | 22.72 | 0.36 | | 0.61 | | 0.03 |
| XPS | 42.46 | 35.6 | 16.74 | 1.00 | | 2.40 | 1.81 | |

The presence of oxygen in both the EDX and the XPS data can be attributed not only to surface-adsorbed species but also to the formation of metal-oxygen species alongside the intended sulfides, meaning that mixed $Bi_2S_3/Bi_2O_3$ and ZnS/ZnO environments likely coexist in the g-$C_3N_4$-Bi and g-$C_3N_4$-Zn samples. This indicates that partial oxidation of $Bi_2S_3$ and ZnS occurred during synthesis or post-treatment, yielding oxide phases in addition to sulides, which is consistent with the significant O signal observed.

The detected Si* can reasonably be assigned to the sample holder or substrate rather than the photocatalyst itself, as Si is not a constituent of the designed compositions and appears at low levels compatible with background contribution from the support.

### *5.3.3. Photoactivity of g-$C_3N_4$-Bi and g-$C_3N_4$-Zn*

The photodegradation efficiency of coumarin and para-nitrophenol was investigated using several sulfide-based photocatalysts. Aqueous solutions containing each organic pollutant and the respective photocatalyst were exposed to both UV and visible light, with continuous air bubbling to maintain adequate oxygen levels. Before illumination, we ensured adsorption-desorption equilibrium by stirring the pollutant/catalyst suspensions in the dark for approximately 30 minutes. This step was conducted to distinguish true photocatalytic degradation from any reductions in pollutant concentration due to simple adsorption onto the photocatalyst surfaces.

**Photocatalytic degradation of coumarin**

The photocatalytic degradation kinetics of coumarin were comprehensively studied under UV and visible light illumination, employing pure g-$C_3N_4$ and a series of bismuth sulfide-modified composites: g-$C_3N_4$-Bi(1), g-$C_3N_4$-Bi(2), and g-$C_3N_4$-Bi(3), with each designation indicating successive increases in $Bi_2S_3/Bi_2O_3$ loading content. As depicted in Figure 5.23/a, the initial rate of coumarin degradation under UV light is highest for pure g-$C_3N_4$, highlighting its strong photocatalytic efficiency when exposed to UV radiation.

However, as the amount of $Bi_2S_3/Bi_2O_3$ incorporated into the g-$C_3N_4$ matrix increases, the degradation rate moderately decreases. For instance, the g-$C_3N_4$-Bi(1) ($1.21\times10^{-5}$ M h$^{-1}$) composite already shows a lower degradation rate compared to pure g-$C_3N_4$ ($3.0\times10^{-5}$ M h$^{-1}$), with further reductions observed in g-$C_3N_4$-Bi(2) and g-$C_3N_4$-Bi(3).

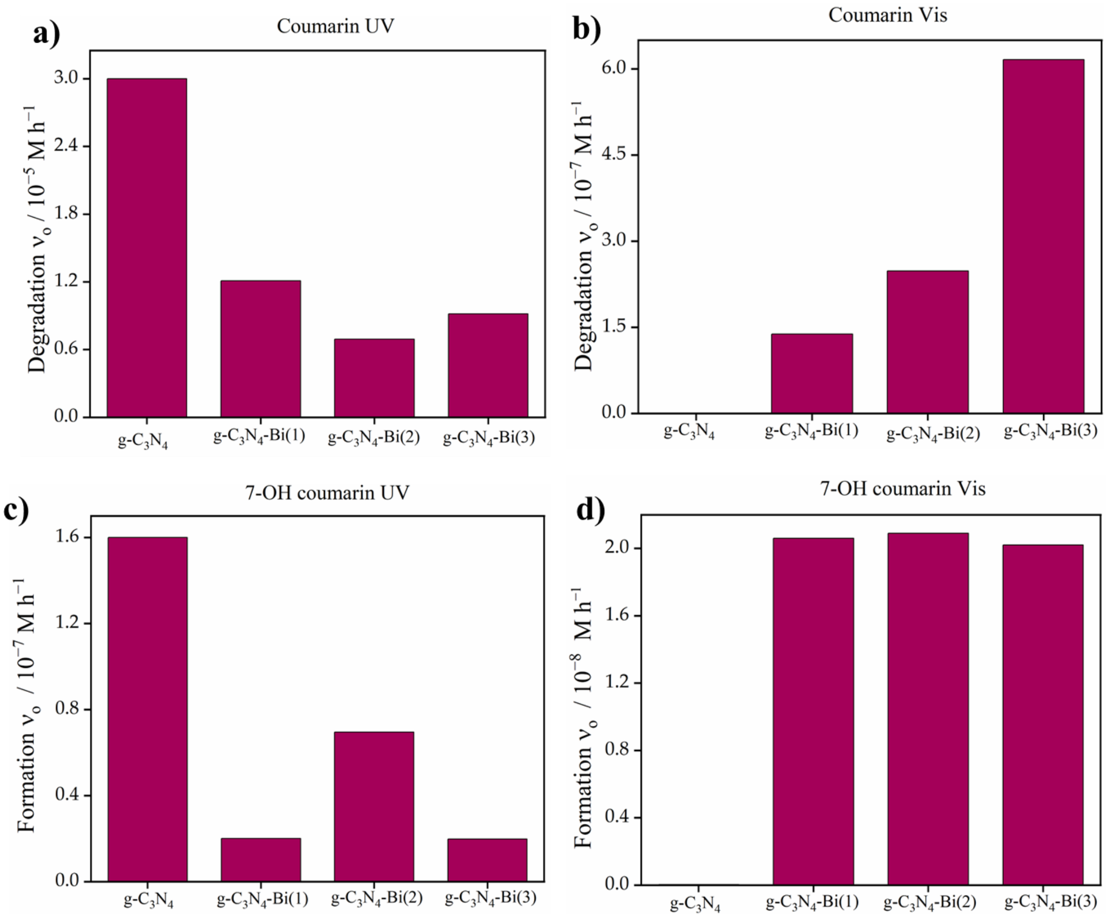

**Figure 5.23.** Initial rate of degradation of coumarin and formation of 7-OH coumarin under UV and visible light with g-$C_3N_4$ and g-$C_3N_4$-Bi nanocomposite.

Under UV light, the initial formation rate of 7-hydroxycoumarin (Figure 5.23/c), which directly reflects the production of hydroxyl radicals during photocatalysis, mirrors the trends observed for coumarin degradation. Pure g-$C_3N_4$ stands out, exhibiting the highest rate of 7-OH coumarin generation ($1.6\times10^{-7}$ M $h^{-1}$), signaling robust $^{\bullet}$OH radical formation. However, as the amount of $Bi_2S_3$/$Bi_2O_3$ incorporated into the catalyst increases, a pronounced decline in 7-OH coumarin production is evident, indicating a corresponding decrease in $^{\bullet}$OH radical generation. Notably, the lowest rate is seen for g-$C_3N_4$-Bi(3) ($1.98\times10^{-8}$ M $h^{-1}$), suggesting that excessive $Bi_2S_3$/$Bi_2O_3$ addition suppresses the ability of the composite to generate hydroxyl radicals under UV irradiation. This reduction is likely due to $Bi_2S_3$/$Bi_2O_3$ overshadowing the intrinsic UV photocatalytic activity of g-$C_3N_4$, thereby diminishing the overall efficiency of $^{\bullet}$OH radical production in these mixed catalysts.

As illustrated in Figure 5.23/b, the initial rate of coumarin degradation under visible light is negligible for unmodified g-$C_3N_4$, reflecting its limited efficiency in utilizing visible light due to a relatively wide bandgap. However, when $Bi_2S_3/Bi_2O_3$ is incorporated, the photocatalytic activity under visible light increases markedly. This improvement arises from the narrower band gap of $Bi_2S_3/Bi_2O_3$, which allows it to act as an effective photosensitizer. With higher $Bi_2S_3/Bi_2O_3$ content, the degradation rate continues to increase, reaching its peak with the g-$C_3N_4$-Bi(3) composite ($6.16\times10^{-7}$ M $h^{-1}$). This trend highlights the critical contribution of $Bi_2S_3/Bi_2O_3$ to extending the light absorption into the visible region and facilitating more efficient charge separation within the composite.

The initial rate of 7-OH coumarin formation under visible light, shown in Figure 5.23/d, is likewise negligible for pure g-$C_3N_4$ ($2.96\times10^{-11}$ M $h^{-1}$) but increases substantially upon $Bi_2S_3/Bi_2O_3$ incorporation. Interestingly, all three $Bi_2S_3/Bi_2O_3$-modified samples display similarly high rates of hydroxyl radical generation, indicating that even the lowest amount of $Bi_2S_3/Bi_2O_3$ is effective in enabling visible-light absorption and catalyzing the subsequent radical-producing reactions. The lack of any extra $^{\bullet}$OH production at higher $Bi_2S_3/Bi_2O_3$ loadings indicates that coumarin degradation is not driven only by hydroxyl radicals and that other reactive pathways are also involved.

This behaviour can be explained by the band alignment between g-$C_3N_4$ and $Bi_2S_3/Bi_2O_3$. The conduction band of $Bi_2S_3/Bi_2O_3$ (≈0.12–0.3 V vs NHE [210]) is much more positive than that of g-$C_3N_4$ (≈−1.3 or −1.1 V vs NHE [211]), while the valence band of g-$C_3N_4$ lies at about +1.5 or +1.6 V. Under illumination, electrons preferentially remain on the more negative g-$C_3N_4$ conduction band, where they can efficiently reduce dissolved oxygen to form superoxide radical and thus drive pollutant degradation, whereas the holes accumulate on the more positive $Bi_2S_3/Bi_2O_3$ valence band, which has sufficient potential to oxidize water to $^{\bullet}$OH. This spatial separation of electrons and holes across the two semiconductors promotes both superoxide and hydroxyl radical formation and helps explain the enhanced photocatalytic activity of the heterojunction.

The initial degradation rates of coumarin under both UV and visible light irradiation were also systematically evaluated using pure g-$C_3N_4$ and its zinc sulfide-modified nanocomposites: g-$C_3N_4$-Zn(1), g-$C_3N_4$-Zn(2), and g-$C_3N_4$-Zn(3), which correspond to increasing ZnS loadings. These results are specifically presented in Figure 5.24 for pure g-$C_3N_4$ ($3.0\times10^{-5}$ M $h^{-1}$) and for the ZnS composites. Regarding coumarin degradation under UV light, g-$C_3N_4$-Zn(2) demonstrates the highest initial degradation rate of $1.25\times10^{-5}$ M $h^{-1}$, followed by g-$C_3N_4$-Zn(3), with g-$C_3N_4$-Zn(1) showing the lowest rate, as illustrated in Figure 5.24/a.

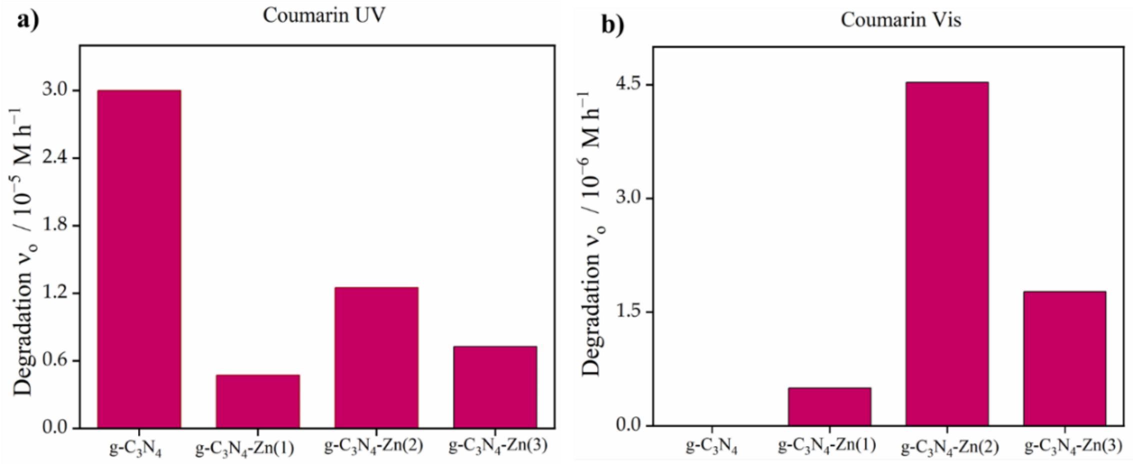

**Figure 5.24.** Photocatalytic degradation of coumarin (a) UV Source (b) Vis light source with photocatalyst g-$C_3N_4$-Zn(1), g-$C_3N_4$-Zn(2), and g-$C_3N_4$-Zn(3).

Under visible light irradiation, pure g-$C_3N_4$ exhibited negligible photocatalytic activity, and for g-$C_3N_4$-Zn, a similar trend is observed under visible light irradiation (Figure 5.24b), although the overall degradation rates are lower, likely due to the reduced intensity and energy of the visible light source.

In contrast, the g-$C_3N_4$-Zn composites demonstrated a modest improvement, with g-$C_3N_4$-Zn(2) achieving the highest activity among the series. This observation suggests that the incorporation of ZnS/ZnO enhances the material's ability to absorb visible light, thereby contributing to increased photocatalytic performance.

The superior photocatalytic activity of g-$C_3N_4$-Zn(2) under both UV and visible light for coumarin degradation is attributed to its optimal ZnS/ZnO content, which promotes efficient charge-carrier separation and enhances light-harvesting capability. Conversely, the diminished performance of g-$C_3N_4$-ZnS(3) may result from excessive ZnS/ZnO nanoparticles causing light scattering or blocking, thereby impeding effective irradiation of the composite. It is also important to note that ZnS/ZnO possesses a wider band gap compared to g-$C_3N_4$, which influences its photo-response characteristics.

In the g-$C_3N_4$-ZnS/ZnO composites, no 7-hydroxycoumarin was detected, indicating that hydroxyl radicals were not significantly formed. Coupling ZnS/ZnO to g-$C_3N_4$ narrows the band gap and makes the valence band less positive, so the photogenerated holes on g-$C_3N_4$ are no longer strong enough oxidants to convert water into $^{\bullet}OH$ efficiently. Instead, under these conditions, the holes oxidize the coumarin directly, while the electrons still reduce dissolved $O_2$ to $O_2^{\bullet-}$, meaning that coumarin degradation proceeds mainly via electron, direct hole, and superoxide pathways rather than via $^{\bullet}OH$.

In both cases, the presence of multiple reactive species introduces competition that suppresses the apparent coumarin degradation rate, but the pathways differ for g-$C_3N_4$-$Bi_2S_3/Bi_2O_3$ and g-$C_3N_4$-ZnS/ZnO.

In the g-$C_3N_4$-$Bi_2S_3/Bi_2O_3$ system, illumination generates electrons on g-$C_3N_4$, which can either reduce coumarin directly or react with dissolved $O_2$ to form $O_2^{\bullet-}$. At the same time, the band alignment favors accumulation of holes on the $Bi_2S_3/Bi_2O_3$ valence band, where they are sufficiently oxidizing to produce $^{\bullet}OH$ from water. As a result, three different species: electrons, $O_2^{\bullet-}$, and holes can all react with coumarin through parallel pathways. Because these routes compete for both the substrate and the photogenerated charges, none of them is used maximally, and the fraction of coumarin converted via any single, monitored pathway (e.g., via $^{\bullet}OH$ to 7-OHC) is reduced, giving a lower apparent degradation rate even though a rich set of ROS is present.

In contrast, the g-$C_3N_4$-ZnS/ZnO composites mainly generate electrons and superoxide, with negligible hole-driven $^{\bullet}OH$ formation. Under these conditions, coumarin is degraded predominantly by direct reduction with electrons and by attack with $O_2^{\bullet-}$, and these two reduction pathways now compete for coumarin and for the available electrons. This electron and $O_2^{\bullet-}$ competition again diminish the efficiency of any single route, leading to a suppressed overall coumarin degradation rate, but via a simpler set of species than in the Bi-modified system.

### Photocatalytic degradation of para-nitrophenol

The photocatalytic degradation kinetics of para-nitrophenol were thoroughly investigated under UV and visible light conditions using pristine g-$C_3N_4$ along with a range of bismuth sulfide-enhanced composites: g-$C_3N_4$-Bi(1), g-$C_3N_4$-Bi(2), and g-$C_3N_4$-Bi(3), where each label reflects progressively greater $Bi_2S_3$ incorporation levels.

Figure A5.10 in the Attachment presents the degradation efficiency of para-nitrophenol (expressed as $C/C_0$ versus time) by irradiation with g-$C_3N_4$-Bi under both (a) UV and (b) visible, comparing the performance of various photocatalysts. Under UV light, pure g-$C_3N_4$ shows moderate photocatalytic activity, which can be attributed to its strong UV absorption and effective generation of reactive species. Notably, the g-$C_3N_4$-Bi composites exhibit substantially improved degradation rates, with g-$C_3N_4$-Bi(2) achieving the highest performance by degrading approximately 90.86 % of para-nitrophenol within 8 hours (Figure A5.10a in the Attachment). This significant enhancement is primarily ascribed to the formation of a heterojunction between g-$C_3N_4$ and $Bi_2S_3$/$Bi_2O_3$, which promotes efficient charge-carrier separation and minimizes the recombination of photogenerated electrons and holes. Interestingly, pure $Bi_2S_3$ alone shows negligible photocatalytic activity under UV illumination, likely due to its limited responsiveness to UV light, underscoring the synergistic advantage of combining it with g-$C_3N_4$ for effective pollutant degradation.

Under visible-light irradiation (Figure A5.10/b in the Attachment), the g-$C_3N_4$-Bi composites exhibit superior photocatalytic activity compared to both pure g-$C_3N_4$ and $Bi_2S_3$ alone, underscoring the pivotal role of $Bi_2S_3$ in extending the material's light absorption capabilities into the visible spectrum. Among the composites tested, g-$C_3N_4$-Bi(3) stands out with the highest degradation efficiency, achieving 16.78 % removal of the target pollutant after 8 hours of Vis LED exposure. This enhanced performance is attributed to the higher $Bi_2S_3$/$Bi_2O_3$ loading, which not only improves visible light absorption but also facilitates more effective electron transfer within the heterojunction system. While pure g-$C_3N_4$ demonstrates significant photocatalytic activity under UV irradiation, its performance under visible light remains limited, and $Bi_2S_3$ by itself shows only minimal activity due to its poor visible light responsiveness. These results collectively highlight the synergistic interplay within the heterojunction composites, which significantly elevates photocatalytic efficiency under both UV and visible light conditions.

The results presented in Figure 5.25/a show that the introduction of $Bi_2S_3$/$Bi_2O_3$ into g-$C_3N_4$ substantially boosts the initial rate of para-nitrophenol degradation under UV illumination.

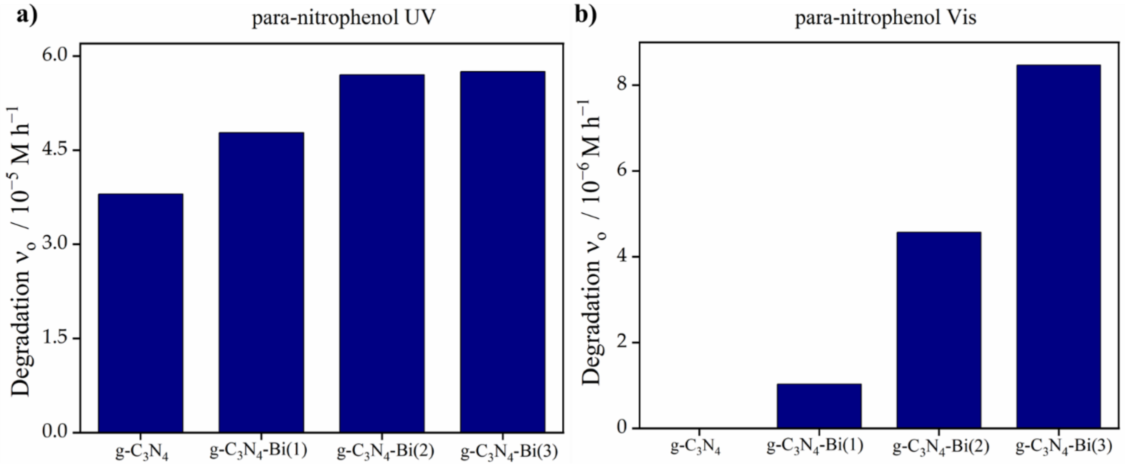

**Figure 5.25.** Initial rate of degradation of para-nitrophenol under (a) UV and (b) visible light.

While pure g-$C_3N_4$ alone demonstrates a relatively low photoactivity ($3.8\times10^{-5}$ M h$^{-1}$), even the lowest concentration of $Bi_2S_3/Bi_2O_3$ in the composite leads to a notable improvement, affirming the synergistic advantages gained by combining these materials. Among the modified catalysts, both g-$C_3N_4$-Bi(2) and g-$C_3N_4$-Bi(3) display comparable and slightly higher degradation rates than g-$C_3N_4$-Bi(1), suggesting that a moderate to high $Bi_2S_3/Bi_2O_3$ content creates an optimal balance between UV light absorption and charge separation. This enhanced performance is largely attributed to the $Bi_2S_3/Bi_2O_3$ role as an electron acceptor, which effectively promotes charge-carrier separation and reduces electron-hole recombination.

Notably, the incorporation of $Bi_2S_3/Bi_2O_3$ does not suppress photocatalytic activity for para-nitrophenol under UV light, as observed with coumarin degradation (Figure 5.25/a). This contrast implies that different degradation pathways or reactive intermediates may be at play, allowing the $Bi_2S_3/Bi_2O_3$ modified composites to efficiently degrade para-nitrophenol through mechanisms that remain active or are even enhanced under UV irradiation. This observation underscores the importance of considering both the nature of the target pollutant and the photocatalyst composition when designing effective photocatalytic systems.

Under visible light irradiation, pure g-$C_3N_4$ shows negligible para-nitrophenol degradation (**Figure 5.25/b**), primarily due to its limited absorption in the visible spectrum and a high rate of charge-carrier recombination. However, the introduction of $Bi_2S_3/Bi_2O_3$ markedly enhances photocatalytic activity, with degradation rates increasing progressively as the $Bi_2S_3/Bi_2O_3$ content rises. The highest degradation rate is observed with the g-$C_3N_4$-Bi(3) composite ($8.47\times10^{-6}$ M $h^{-1}$), followed by g-$C_3N_4$-Bi(2) ($4.57\times10^{-6}$ M $h^{-1}$) and g-$C_3N_4$-Bi(1) ($1.03\times10^{-6}$ M $h^{-1}$). This trend underscores the crucial role of $Bi_2S_3/Bi_2O_3$ as an effective visible light photosensitizer. By absorbing visible photons, $Bi_2S_3/Bi_2O_3$ facilitates the generation of reactive oxidizing species that drive para-nitrophenol degradation. Moreover, the interface between g-$C_3N_4$ and $Bi_2S_3/Bi_2O_3$ promotes efficient separation of photoinduced electron-hole pairs by trapping charge carriers, thereby suppressing recombination and significantly boosting photocatalytic efficiency under visible light conditions.

The above results demonstrated that para-nitrophenol is degraded efficiently when g-$C_3N_4$ is optimally modified with $Bi_2S_3/Bi_2O_3$ nanoparticles and irradiated by either UV or visible light. The composite managed charge recombination more effectively and generated larger amounts of reactive species. The combined action of these reactive species (photogenerated holes, electrons, and superoxide radicals) played an essential role in the efficient degradation of para-nitrophenol, as each species contributes to breaking down the pollutant through direct oxidation or indirect radical-mediated pathways.

The initial degradation rates of para-nitrophenol were also systematically evaluated under both UV and visible light, using the same set of photocatalysts: pure g-$C_3N_4$, and the nanocomposites g-$C_3N_4$-Zn(1), g-$C_3N_4$-Zn(2), and g-$C_3N_4$-Zn(3).

Figure A5.11 in the Attachment depicts the degradation efficiency of para-nitrophenol (expressed as $C/C_0$ versus time) by irradiation with g-$C_3N_4$-Zn (a) UV and (b) visible LEDs. The g-$C_3N_4$-Zn (Figure A5.11/a in the Attachment) composites exhibit significantly enhanced degradation rates. Among these, g-$C_3N_4$-Zn(2) achieves the best performance, completely degrading para-nitrophenol within 8 hours. This marked improvement is primarily ascribed to the formation of an effective heterojunction between g-$C_3N_4$ and ZnS/ZnO, which facilitates the separation of photogenerated electron-hole pairs and suppresses their recombination, thereby enhancing catalytic efficiency. This highlights the synergistic advantage of combining ZnS/ZnO with g-$C_3N_4$ to optimize photocatalytic degradation of pollutants.

Under visible light irradiation (Figure A5.11/b in the Attachment), the g-$C_3N_4$-Zn composites outperform both pure g-$C_3N_4$ and ZnS alone, highlighting the significant role of ZnS in extending light absorption into the visible spectrum. Among the composites tested, g-$C_3N_4$-Zn(2), with an optimal ZnS/ZnO concentration, exhibits the highest degradation efficiency, achieving 15.1 % pollutant removal after 8 hours under Vis LED illumination. This improved performance is attributed to enhanced electron transport and more effective harvesting of visible light. In contrast, pure g-$C_3N_4$ shows limited activity, while ZnS alone demonstrates negligible photocatalytic behavior under visible light. These results emphasize the synergistic effect arising from heterojunction formation, which boosts photocatalytic efficiency across both UV and visible light conditions. The relevant results of the degradation efficiency of para-nitrophenol under UV light and visible light have been shown in Figure 5.26.

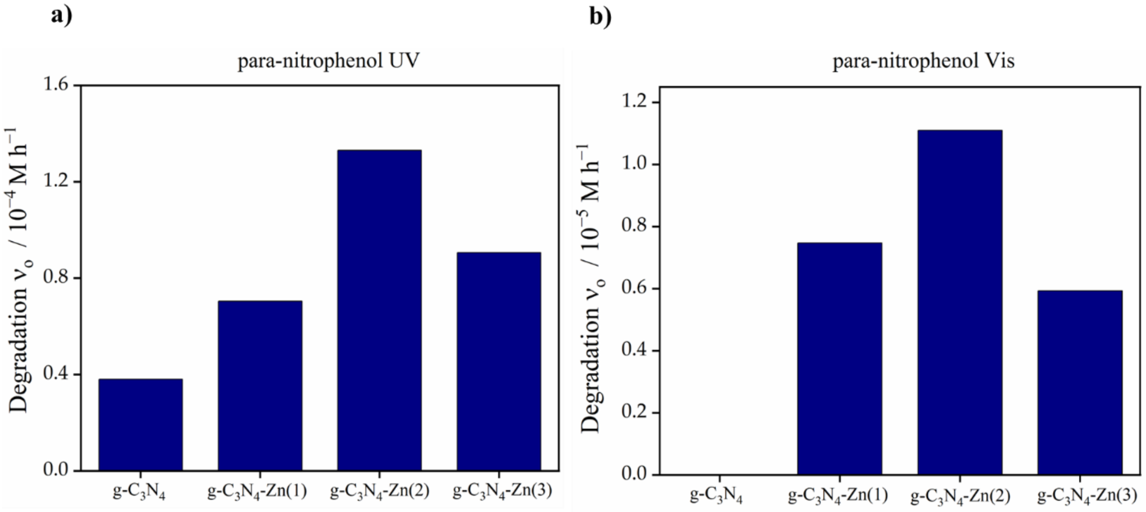

**Figure 5.26.** Photocatalytic degradation of para-nitrophenol (a) UV light (b) visible light with g-$C_3N_4$-ZnS photocatalyst.

The g-$C_3N_4$-Zn nanocomposites exhibit significantly enhanced photocatalytic performance, with g-$C_3N_4$-Zn(2) achieving the highest initial degradation rate of $1.33\times10^{-4}$ M $h^{-1}$ under UV light, followed by g-$C_3N_4$-Zn(3) and g-$C_3N_4$-Zn(1) (Figure 5.26/a). This enhancement is attributed to the effective formation of heterojunctions between ZnS/ZnO and g-$C_3N_4$, which facilitates efficient charge-carrier separation, thereby increasing the generation and availability of reactive species essential for para-nitrophenol breakdown.

Under visible light irradiation, pure g-$C_3N_4$ demonstrates negligible photocatalytic activity, in agreement with Figure 5.26/b, due to its limited visible light absorption and rapid charge recombination. In contrast, the g-$C_3N_4$-Zn composites show moderate photocatalytic performance, with g-$C_3N_4$-Zn(2) again proving to be the most effective, achieving an initial degradation rate of $1.11\times10^{-5}$ M $h^{-1}$ (Figure 5.26/b**)**. This improvement results from the ZnS/ZnO modification, which broadens the light absorption range into the visible spectrum and enhances charge-transfer processes, thereby promoting the degradation of para-nitrophenol under visible light.

The initial degradation rates of para-nitrophenol are significantly higher than those observed for coumarin under both UV and visible light irradiations. Thus, faster degradation of para-nitrophenol can be attributed to its stronger reactivity with the photogenerated reactive species other than hydroxyl radicals, such as electron or superoxide radical.

Since the second-order rate constant for the reaction between para-nitrophenol and electrons is $4.4\times10^{10}$ $M^{-1}$ $s^{-1}$, while that for the competing reaction between electrons and dissolved oxygen is $2.3\times10^{10}$ $M^{-1}$ $s^{-1}$ [193], besides, the concentrations are $4.5\times10^{-4}$ M and $2.6\times10^{-4}$ M [212], respectively, electrons react more than 3 times as fast with para-nitrophenol as they do with oxygen. This implies that, when electrons are generated on the photocatalyst surface, para-nitrophenol is kinetically the preferred sink, so direct electron transfer to para-nitrophenol is a very efficient degradation pathway. At the same time, a fraction of the electrons also still reduce oxygen to form superoxide radicals, which can further attack para-nitrophenol and its intermediates, meaning that both the direct electron-driven route and the indirect superoxide-mediated route contribute to its overall degradation.

The photocatalytic degradation of para-nitrophenol under UV and visible light was systematically assessed using bismuth sulfide- and zinc sulfide-modified catalysts, with the corresponding results presented in Table 5.12 and Figures A5.12 and A5.14 (in the Attachment). The reaction kinetics were further examined through a pseudo-first-order model, as shown in Figures A5.13 and A5.15 (in the Attachment). The kinetic fittings exhibited strong consistency with the experimental data, thereby confirming the model's reliability in describing the degradation process. This analysis underscores the applicability of the pseudo-first-order model for effectively comparing degradation efficiencies and rate constants across different photocatalysts and irradiation conditions.

**Table 5.12.** Percentage and rate constant of para-nitrophenol degradation of bismuth and zinc sulfide catalysts with UV and visible light sources.

| **Catalyst** | **% Degradation (8 h)** | | **k ($h^{-1}$)** | |
|---|---|---|---|---|
| | **Irradiation with** | | | |
| | **UV** | **Vis** | **UV** | **Vis** |
| g-$C_3N_4$ | 59 | 0 | 0.11 | 0 |
| g-$C_3N_4$-Bi(1) | 88.1 | 7.4 | 0.26 | $9.8\times10^{-3}$ |
| g-$C_3N_4$-Bi(2) | 90.8 | 11.7 | 0.29 | $1.6\times10^{-2}$ |
| g-$C_3N_4$-Bi(3) | 87.4 | 16.7 | 0.25 | $2.2\times10^{-2}$ |
| g-$C_3N_4$-Zn(1) | 95.5 | 12.7 | 0.37 | $1.6\times10^{-2}$ |
| g-$C_3N_4$-Zn(2) | 100 | 15.1 | 0.57 | $1.8\times10^{-2}$ |
| g-$C_3N_4$-Zn(3) | 94.5 | 9.9 | 0.37 | $1.3\times10^{-2}$ |

This comparison allows for a straightforward evaluation of the effects that different amounts of $Bi_2S_3/Bi_2O_3$ and ZnS/ZnO have on the photocatalytic performance in degrading these model pollutants under various light conditions. The findings emphasize how adding $Bi_2S_3/Bi_2O_3$ and ZnS/ZnO improves light absorption, charge-carrier behavior, and the production of reactive species, all of which are key factors determining the photocatalytic efficiency for breaking down both coumarin and para-nitrophenol under UV and visible light.

### *5.3.4. Photoactivity of combined nanocomposites*

The synergistic effect of the optimally selected catalysts, g-$C_3N_4$-Bi(2) and g-$C_3N_4$-Zn(2), was evaluated during the photodegradation of para-nitrophenol under both UV and visible light irradiation. A total catalyst concentration of 1 g $dm^{-3}$ was maintained throughout the experiments. Various composite ratios of g-$C_3N_4$-Bi to g-$C_3N_4$-Zn were tested, specifically 1:0, 3:1, 1:1, 1:3, and 0:1 by weight, to determine the optimal blend for enhanced photocatalytic activity. The degradation efficiencies and reaction kinetics corresponding to these compositions are summarized and illustrated in Figure 5.28.

This systematic variation allowed the investigation of how the relative proportions of $Bi_2S_3$/$Bi_2O_3$ and ZnS/ZnO-modified g-$C_3N_4$ influenced the overall photocatalytic performance, considering their distinct optical and charge-transfer properties. The results from Figure 5.27 reveal the interplay between these components under different irradiation conditions, highlighting any synergistic enhancements in para-nitrophenol degradation attributable to combination effects.

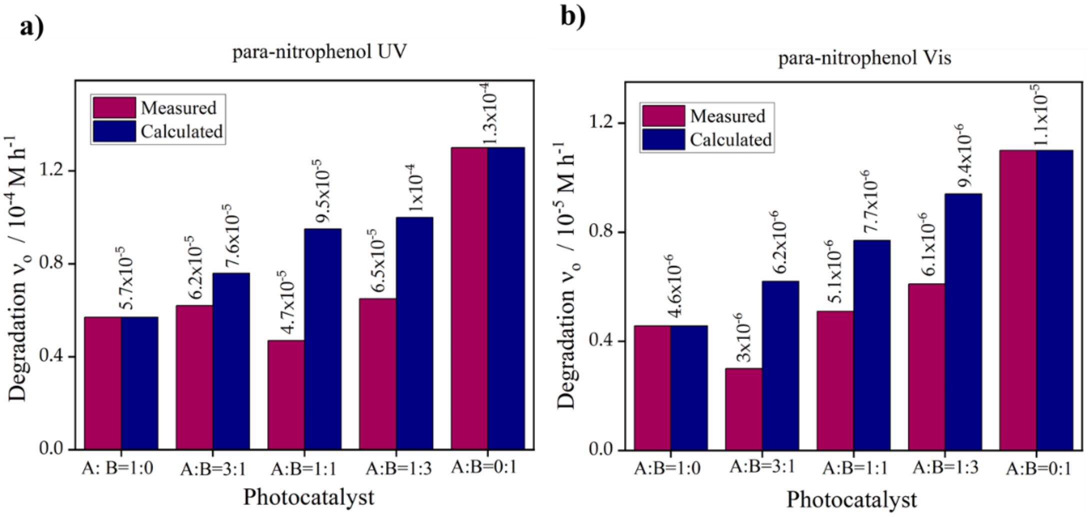

**Figure 5.27.** Photocatalytic degradation of para-nitrophenol (a) UV light (b) visible light with combined effect of photocatalysts A: g-$C_3N_4$-Bi(2) and B: g-$C_3N_4$-Zn(2).

First, the measured degradation rates were obtained by tracking the concentration of para-nitrophenol as a function of time with different photocatalyst combinations and light sources (UV and visible). The experimental data were plotted (concentration vs. time), and the initial degradation rates ($v_0$) were extracted based on the slope or polynomial fit of the kinetic curves for each system.

For calculated rates, a weighted average formula was used to model the theoretical degradation rate for each binary photocatalyst mixture. Here, component A represents g-$C_3N_4$-Bi(2) and component B represents g-$C_3N_4$-Zn(3). Their respective individual initial degradation rates ($v_{01}$ for A, $v_{02}$ for B) under the same conditions were multiplied by the proportion of each photocatalyst in the mix. For example, at a mass ratio (A: B) of 1:3, the calculated rate is given by: (0.25×$v_{01}$) + (0.75×$v_{02}$).

This calculation was performed for each ratio, including 1:0, 3:1, 1:1, 1:3, and 0:1. The same methodology was applied for both UV and visible light conditions, allowing direct comparison between the measured experimental values and the calculated theoretical values. Any observed synergy or deviation between these values highlights interactions between the two photocatalysts in mixed systems. This approach provides a quantitative evaluation of combined photocatalyst performance versus their individual contributions.

The initial degradation rates of para-nitrophenol under UV and visible light were evaluated using the photocatalysts g-$C_3N_4$-Bi(2) (denoted as A), g-$C_3N_4$-Zn(2) (denoted as B), and their mixtures at various mass ratios: A:B = 1:0, 3:1, 1:1, 1:3, and 0:1. Notably, the sample with ratio A:B = 0:1, corresponding to pure B, exhibited the highest degradation rate under UV light, highlighting ZnS/ZnO exceptional photocatalytic activity in the UV region, which is attributed to its favourable band gap. Additionally, composite ratios such as A:B = 1:3 and 3:1 surpassed the performance of pure A, indicating a synergistic effect resulting from the interaction between A and B. This synergy likely enhances charge-carrier separation and reduces electron-hole recombination losses, thereby improving the overall photocatalytic efficiency. The observed trend of increasing activity with higher ZnS/ZnO concentration emphasizes the critical role of ZnS/ZnO in driving the photocatalytic process under UV illumination.

The highest photocatalytic activity under visible light is observed for the sample with a composition of A:B = 0:1 (pure B), indicating that ZnS/ZnO exhibits superior photocatalytic performance in the visible spectrum. This outcome highlights the material's strong ability to effectively harness visible light, likely due to enhanced surface properties and improved charge-carrier dynamics. Additionally, composite ratios such as A:B = 1:3 and 1:1 also show significant activity, suggesting complementary interactions between g-$C_3N_4$-Bi(A) and g-$C_3N_4$-Zn(B). By synergistically combining the strengths of both materials, mixtures outperform pure A (A:B = 1:0), which alone contributes less effectively but aids overall performance when paired with B. Although pure B consistently leads in photocatalytic efficiency under both visible and UV light, the interaction between

$Bi_2S_3/Bi_2O_3$ and ZnS/ZnO enhances the mixed composites, resulting in more efficient para-nitrophenol degradation through improved light absorption and charge separation.

### *5.3.5. Reusability*

A critical aspect of practical photocatalytic applications is the reliability and reusability of the photocatalyst materials. The stability and reusability of g-$C_3N_4$-Bi and g-$C_3N_4$-Zn nanocomposites were evaluated via cyclic photocatalytic degradation of para-nitrophenol (Figure 5.28). After each cycle, the catalyst was recovered by centrifugation, washed, and dried before reuse. Minor catalyst loss occurred due to handling. The degradation efficiency remained mostly stable over two cycles (~16 hours), with only slight decreases mainly caused by physical catalyst loss rather than loss of activity. These results demonstrate the satisfactory stability and reusability of the nanocomposite photocatalysts.

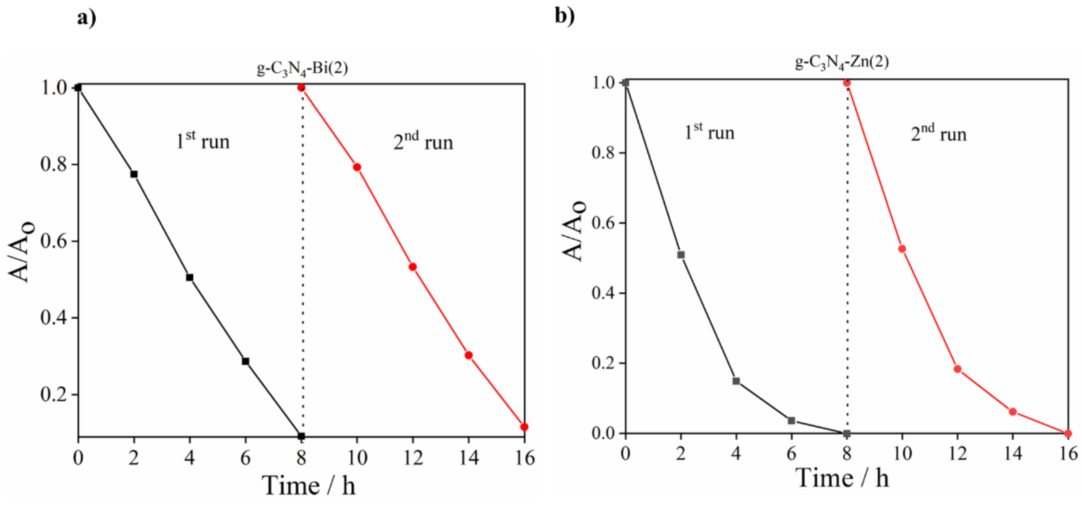

**Figure 5.28.** Reusability of catalysts (a) g-$C_3N_4$-Bi(2) and (b) g-$C_3N_4$-Zn(2).

### *5.3.6. Conclusions*

The g-$C_3N_4$-Bi and g-$C_3N_4$-Zn nanocomposites were successfully synthesized via a starch-assisted method, which facilitated the uniform distribution and strong attachment of $Bi_2S_3/Bi_2O_3$ and ZnS/ZnO nanoparticles onto the g-$C_3N_4$ surface, effectively reducing agglomeration due to starch's stabilizing role. UV-Vis diffuse reflectance spectroscopy confirmed that the composites absorb both UV and visible light, broadening their photo response. Photocatalytic degradation tests revealed that the enhanced activity of these composites stems predominantly from improved photogenerated charge-carrier separation and transfer processes. Notably, although surface oxides of bismuth and zinc were present, the sulfide phases were principally responsible for boosting photocatalytic efficiency. This highlights the pivotal role of starch in promoting heterojunction formation, which underpins the observed photocatalytic improvements. Overall, this work advances sustainable, green synthesis strategies for photoactive nanocomposites and provides valuable insights into the efficient photocatalytic degradation of para-nitrophenol, with promising implications for environmental pollution remediation.

# 6. Summary

Water contamination by persistent organic pollutants has become a global problem, driven by industrial and agricultural discharges. Traditional water treatment methods often fail to degrade colorless yet toxic molecules such as para-nitrophenol and coumarin. Photocatalysis, particularly using visible-light-responsive materials, offers an eco-friendly route for the degradation of recalcitrant pollutants. Graphitic carbon nitride stands out for its stability, visible light absorption, low cost, and metal-free composition. However, its real-world applicability is hampered by the rapid recombination of photogenerated carriers and limited active sites.

Several approaches to enhance g-$C_3N_4$ photocatalytic efficacy are presented in this thesis, which show different modification strategies aiming for improved charge separation, broader light absorption, and greater photocatalytic activity. Through a direct thermal polymerization route, g-$C_3N_4$ is produced from melamine and urea under different atmospheric and temperature conditions. Melamine is superior to urea, delivering higher yield, more ordered structures, and competitive photocatalytic performance.

Environmentally benign synthesis of silver nanoparticles is achieved with cardamom seed extract, acting as a green reducing and capping agent. The resulting Ag NPs are deposited on g-$C_3N_4$, producing nanocomposites with enhanced light absorption and charge-carrier separation. g-$C_3N_4$ is also modified with $Bi_2S_3/Bi_2O_3$ and ZnS/ZnO nanoparticles, using starch as an eco-friendly dispersing template. These modifications improve visible light activity and facilitate a more homogeneous distribution of metal sulfides on the g-$C_3N_4$ surface.

The structural and functional properties of the modified g-$C_3N_4$ photocatalysts were thoroughly analyzed using various techniques. FTIR and XRD confirmed the stability of the g-$C_3N_4$ framework after doping, with peak shifts and broadenings indicating surface effects and heterojunction formation. SEM and TEM showed clear morphological changes and strong interfacial contact between nanosheets and metal-based nanoparticles, with elemental mapping revealing a uniform distribution of metals. Although the BET surface area decreased due to pore coverage by dopants, photocatalytic efficiency improved, highlighting the importance of enhanced charge separation. XPS and EDX analysis revealed surface enrichment of metal phases and minor oxidation, with surface-sensitive

XPS showing more localized dopant concentration than bulk-sensitive EDX, emphasizing the key role of surface chemistry in boosting photocatalytic activity.

The photocatalytic performance of g-$C_3N_4$ modified with both silver and metal sulfide/oxide shows significant enhancement in degrading pollutants like coumarin and para-nitrophenol under UV and visible light compared to pure g-$C_3N_4$. Optimal doping levels are essential, as excessive loading can block active sites, while moderate amounts improve charge transfer and visible light absorption. Mechanistic studies reveal that under light irradiation, electrons and holes generated in g-$C_3N_4$ drive redox reactions producing reactive radicals such as superoxide and hydroxyl species. All the nanoparticles, Ag and $Bi_2S_3$/$Bi_2O_3$ and ZnS/ZnO, enhance electron-hole separation and reduce the band gap, thus boosting activity, especially under visible light due to plasmonic and band alignment effects. Furthermore, the modified catalysts exhibit strong stability and retain photocatalytic activity over multiple cycles, with only minor performance loss attributed to handling and recovery.

Nanocomposites with moderate loadings of Ag or $Bi_2S_3$/$Bi_2O_3$ and ZnS/ZnO achieve an optimal balance between surface coverage, electron trapping, and pollutant access, leading to enhanced photocatalytic activity. Green synthesis methods, particularly for silver nanoparticles, improve catalytic efficiency under visible light and support scalable, sustainable production. The choice of precursor and calcination conditions for g-$C_3N_4$ synthesis also significantly affects its structural order, electronic properties, and overall photocatalytic performance. Overall, these studies confirm that using green, scalable methods to modify g-$C_3N_4$ with Ag NPs, $Bi_2S_3$/$Bi_2O_3$, or ZnS/ZnO produces highly effective visible-light-responsive photocatalysts capable of efficiently degrading stubborn organic pollutants, offering promising paths towards practical water treatment applications.

These nanocomposites, Ag-g-$C_3N_4$, g-$C_3N_4$-Bi, and g-$C_3N_4$-Zn, distinctly stand out as superior in the photocatalytic degradation of para-nitrophenol compared to other reported studies listed in Table 3.5, owing to a combination of synthesis strategy, structural features, and photocatalytic performance.

In conclusion, this work with Ag-g-$C_3N_4$, g-$C_3N_4$-Bi, and g-$C_3N_4$-Zn nanocomposites not only matches or outperforms many leading modified g-$C_3N_4$ photocatalysts but does so with greener, facile, and scalable synthesis methods. The integration of bio-inspired and starch-assisted techniques, combined with demonstrated high photocatalytic rates and efficiencies, clearly establishes the composites as superior and highly promising materials for para-nitrophenol degradation and sustainable water treatment.

This work fits well within the broader literature landscape on modified g-$C_3N_4$ photocatalysts, where metal and metal sulfide nanocomposites (e.g., g-$C_3N_4$-Bi and g-$C_3N_4$-Zn), heterojunction systems (e.g., NiO/g-$C_3N_4$, CdS/g-$C_3N_4$), and metal nanoparticle decorations (Ag, Au) have all demonstrated improvements in para-nitrophenol degradation efficiencies by enhancing charge dynamics and light absorption.

# 7. Thesis points of PhD dissertation

I. **I systematically investigated the synthesis of well-structured g-$C_3N_4$, using melamine as a precursor, achieving high product yield and improved structural ordering. I developed two eco-friendly modification strategies: bio-inspired incorporation of silver nanoparticles by using cardamom extract and adsorption impregnation, and starch-assisted incorporation of metal sulfides ($Bi_2S_3/Bi_2O_3$ or ZnS/ZnO).**

- I quantified that melamine thermal polymerization at 500 °C yields approximately ten times more product and produces more ordered g-$C_3N_4$ (sharper and better-defined XRD peaks) than urea, consistent with literature but reaffirmed under my synthesis conditions.
- The synthesis was performed in two different atmospheres; air and nitrogen, where melamine with the air atmosphere was preferred due to high photocatalytic efficiency.
- I verified that cardamom extract-assisted green synthesis enabled homogeneous Ag nanoparticle distribution, enhancing photocatalytic performance through natural reducing and capping agents.
- I demonstrated that starch-assisted green synthesis promoted stable $Bi_2S_3/Bi_2O_3$ and ZnS/ZnO nanoparticle dispersion, further improving photocatalytic efficiency by preventing agglomeration.

Mukhtar, S., Szabó-Bárdos, E., Horváth, O., Makó, E., Juzsakova, T., & Molnár, Z. (2025). Bio-inspired synthesis of Ag-g-$C_3N_4$ nanocomposites and their application for photocatalytic degradation of para-nitrophenol. *Colloids and Surfaces A: Physicochemical and Engineering Aspects*, *705*, 135739. (https://doi.org/10.1016/j.colsurfa.2024.135739)

Mukhtar, S., Szabó-Bárdos, E., Őze, C., Juzsakova, T., Rácz, K., Németh, M., & Horváth, O. (2025). g-$C_3N_4$ Modified with Metal Sulfides for Visible-Light-Driven Photocatalytic

Degradation of Organic Pollutants. *Molecules*, *30*(2), 253.
(https://doi.org/10.3390/molecules30020253).

II. **I systematically investigated the effect of Ag, $Bi_2S_3/Bi_2O_3$, and ZnS/ZnO nanoparticle modification on graphitic carbon nitride (g-$C_3N_4$) and revealed that the interaction between the nanoparticles and the g-$C_3N_4$ matrix is predominantly weak and physical in nature, leading to a notable decrease in the specific surface area.**

- XRD and FTIR analyses confirmed the preservation of the g-$C_3N_4$ framework, with only minor peak shifts indicating weak bonding.
- SEM and TEM observations revealed morphological changes and uniform dispersion of ~2–20 nm nanoparticles on the g-$C_3N_4$ surface.
- The BET surface area decreased markedly due to nanoparticle deposition.
- XPS analysis demonstrated compositional stability of the hybrid materials.

Mukhtar, S., Szabó-Bárdos, E., Horváth, O., Makó, E., Juzsakova, T., & Molnár, Z. (2025). Bio-inspired synthesis of Ag-g-$C_3N_4$ nanocomposites and their application for photocatalytic degradation of para-nitrophenol. *Colloids and Surfaces A: Physicochemical and Engineering Aspects*, *705*, 135739.
(https://doi.org/10.1016/j.colsurfa.2024.135739)

Mukhtar, S., Szabó-Bárdos, E., Őze, C., Juzsakova, T., Rácz, K., Németh, M., & Horváth, O. (2025). g-$C_3N_4$ Modified with Metal Sulfides for Visible-Light-Driven Photocatalytic Degradation of Organic Pollutants. *Molecules*, *30*(2), 253.
(https://doi.org/10.3390/molecules30020253).

III. **I demonstrated that incorporating Ag, $Bi_2S_3/Bi_2O_3$, and ZnS/ZnO nanoparticles into graphitic carbon nitride significantly reduces the efficiency of the photocatalytic degradation of coumarin by Ag-loaded g-$C_3N_4$ and moderately reduces it by Ag-, $Bi_2S_3/Bi_2O_3$-, and ZnS/ZnO-loaded g-$C_3N_4$ under UV irradiation.**

- I showed that pristine g-$C_3N_4$ produces both $^\bullet OH$ and $O_2^{\bullet -}$ radicals under UV light irradiation and that, in the coumarin degradation, the reactions of hydroxyl radicals play considerable roles.
- I observed that Ag, $Bi_2S_3$/$Bi_2O_3$, and ZnS/ZnO nanoparticles doping reduces the band gap of g-$C_3N_4$, which lowers the oxidation potential of the valence band holes ($h^+_{VB}$), making them less effective at oxidizing adsorbed $H_2O$ or $OH^-$ ions and generating hydroxyl radicals under UV irradiation, decreasing the efficiency of coumarin degradation.
- I noticed that excessive nanoparticle loading blocks active sites, which ultimately reduces photocatalytic activity.

Mukhtar, S., Szabó-Bárdos, E., Horváth, O., Makó, E., Juzsakova, T., & Molnár, Z. (2025). Bio-inspired synthesis of Ag-g-$C_3N_4$ nanocomposites and their application for photocatalytic degradation of para-nitrophenol. *Colloids and Surfaces A: Physicochemical and Engineering Aspects*, *705*, 135739.
(https://doi.org/10.1016/j.colsurfa.2024.135739)

Mukhtar, S., Szabó-Bárdos, E., Őze, C., Juzsakova, T., Rácz, K., Németh, M., & Horváth, O. (2025). g-$C_3N_4$ Modified with Metal Sulfides for Visible-Light-Driven Photocatalytic Degradation of Organic Pollutants. *Molecules*, *30*(2), 253.
(https://doi.org/10.3390/molecules30020253).

**IV. I demonstrated that $Bi_2S_3$/$Bi_2O_3$ and ZnS/ZnO modification of g-$C_3N_4$ promotes the degradation of coumarin under visible light irradiation.**

- The pristine g-$C_3N_4$ cannot degrade coumarin at all under visible light irradiation.
- Although no or very slight formation of hydroxyl radicals was observed in the case of $Bi_2S_3$/$Bi_2O_3$ and ZnS/ZnO modified g-$C_3N_4$, a considerable increase in the efficiency of coumarin degradation occurred under visible light irradiation.
- The enhanced efficiency of coumarin degradation can be attributed to the reactions of other photogenerated reactants, such as electron and/or superoxide radical.

Mukhtar, S., Szabó-Bárdos, E., Őze, C., Juzsakova, T., Rácz, K., Németh, M., & Horváth, O. (2025). g-$C_3N_4$ Modified with Metal Sulfides for Visible-Light-Driven Photocatalytic Degradation of Organic Pollutants. *Molecules*, *30*(2), 253. (https://doi.org/10.3390/molecules30020253).

**V. I demonstrated that the degradation efficiency of a colorless pollutant (para-nitrophenol) under UV and visible light is significantly enhanced by optimal modification of g-$C_3N_4$ with Ag, $Bi_2S_3/Bi_2O_3$, and ZnS/ZnO nanoparticles.**

- I showed that under UV irradiation, Ag, $Bi_2S_3/Bi_2O_3$, and ZnS/ZnO modifications achieved high degradation efficiencies of 82-100 % (within 6-8 hours).
- I revealed that under visible light, the best-performing composites achieved pollutant degradation efficiencies of 15-27 % (within 6-8 hours), whereas pristine g-$C_3N_4$ was ineffective.
- I attributed enhanced photocatalytic performance to improved charge separation and thus increased generation of reactive species other than hydroxyl radicals (electron and/or superoxide radical).
- I demonstrated catalyst stability with minor activity loss after 5 cycles of photocatalytic degradation of para-nitrophenol, indicating potential for practical wastewater treatment applications.

Mukhtar, S., Szabó-Bárdos, E., Horváth, O., Makó, E., Juzsakova, T., & Molnár, Z. (2025). Bio-inspired synthesis of Ag-g-$C_3N_4$ nanocomposites and their application for photocatalytic degradation of para-nitrophenol. *Colloids and Surfaces A: Physicochemical and Engineering Aspects*, *705*, 135739. (https://doi.org/10.1016/j.colsurfa.2024.135739)

Mukhtar, S., Szabó-Bárdos, E., Őze, C., Juzsakova, T., Rácz, K., Németh, M., & Horváth, O. (2025). g-$C_3N_4$ Modified with Metal Sulfides for Visible-Light-Driven Photocatalytic Degradation of Organic Pollutants. *Molecules*, *30*(2), 253. (https://doi.org/10.3390/molecules30020253).

# 8. References

[1] S. L. Postel, “Entering an era of water scarcity: The challenges ahead,” *Ecological Applications*, vol. 10, no. 4, pp. 941–948, 2000 doi: 10.1890/1051-0761(2000)010[0941: EAEOWS]2.0.CO;2.

[2] B. A. Alotaibi, M. B. Baig, M. M. M. Najim, A. A. Shah, and Y. A. Alamri, “Water scarcity management to ensure food scarcity through sustainable water resources management in Saudi Arabia,” *Sustainability (Switzerland)*, vol. 15, no. 13, 2023, doi: 10.3390/su151310648.

[3] M. J. Keyhanpour, S. H. Musavi Jahromi, and H. Ebrahimi, “System dynamics model of sustainable water resources management using the Nexus Water-Food-Energy approach,” *Ain Shams Engineering Journal*, vol. 12, no. 2, 2021, doi: 10.1016/j.asej.2020.07.029.

[4] C. Y. Zhang and T. Oki, “Water pricing reform for sustainable water resources management in China’s agricultural sector,” *Agricultural Water Management*, vol. 275, 2023, art. no. 108045, doi: 10.1016/j.agwat.2022.108045.

[5] P. H. Gleick, “Water in crisis: Paths to sustainable water use,” *Ecological Applications*, vol. 8, no. 3, 1998, doi: 10.1890/1051-0761(1998)008[0571: WICPTS]2.0.CO;2.

[6] A. J. B. Zehnder, H. Yang, and R. Schertenleib, “Water issues: The need for action at different levels,” *Environment, Development and Sustainability*, 2003, doi: 10.1007/s000270300000.

[7] N. K. Dulvy *et al.*, “Extinction risk and conservation of the world’s sharks and rays,” *Elife*, vol. 2014, no. 3, 2014, doi: 10.7554/elife.00590.

[8] S. Jahan and A. Singh, “Causes and impact of industrial effluents on receiving water bodies: A review,” *Malaysian Journal of Science and Advanced Technology*, vol. 3, no. 2, pp. 111–121, 2023, doi: 10.56532/mjsat.v3i2.144.

[9] S. Sarna, “Convention for the prevention of pollution from ships,” in *Berkshire Encyclopedia of Sustainability 3/10*, 2023, doi: 10.2307/jj.9561408.23.

[10] P. Rajasulochana and P. Vijay, “Comparison on efficiency of various techniques in treatment of waste and sewage water – A comprehensive review,” *Resource-Efficient Technologies*, no. 4, 2016, doi: 10.18799/24056529/2016/4/63.

[11] T. Rajabloo, W. De Ceuninck, L. Van Wortswinkel, M. Rezakazemi, and T. Aminabhavi, “Environmental management of industrial decarbonization with focus on chemical sectors: A review,” *Journal of Environmental Management*, vol. 302, 2022, art. no. 114055,
doi: 10.1016/j.jenvman.2021.114055.

[12] J. Jefry and A. Djazuli, “The effect of inflation, interest rates and exchange rates on stock prices of manufacturing companies in basic and chemical industrial sectors on the indonesia stock exchange (IDX),” *International Journal of Business, Management & Economics Research*, vol. 1, no. 1, 2020,
doi: 10.47747/ijbmer.v1i1.49.

[13] M. Syafrudin, R. Kristanti, A. Yuniarto, T. Hadibarata, J. Rhee, W. Al-onazi, T. Algarni, A. Almarri and A. Al-Mohaimeed “Pesticides in drinking water-a review,” *International Journal of Environmental Research and Public Health*, vol. 18, no. 2, art. no. 468, 2021,
doi: 10.3390/ijerph18020468.

[14] B. Mansfield, M. Werner, C. Berndt, A. Shattuck, R. Galt, B. Williams, L. Argüelles, “A new critical social science research agenda on pesticides,” *Agriculture and Human Values*, vol. 41, no. 2, 2024,
doi: 10.1007/s10460-023-10492-w.

[15] A. Santamaría, P. Linares, and P. Pintos, “The effects of carbon prices and anti-leakage policies on selected industrial sectors in spain - Cement, steel and oil refining,” *Energy Policy*, vol. 65, 2014,
doi: 10.1016/j.enpol.2013.10.031.

[16] S. Griffiths, B. K. Sovacool, J. Kim, M. Bazilian, and J. M. Uratani, “Decarbonizing the oil refining industry: A systematic review of sociotechnical systems, technological innovations, and policy options,” *Energy Research and Social Science*, 2022,
doi: 10.1016/j.erss.2022.102542.

[17] Energy Information Administration, “Oil and petroleum products explained use of oil,” *EIA*.

[18] N. Kosaric, “Biosurfactants in industry,” *Pure and Applied Chemistry*, vol. 64, no. 11, 1992,
doi: 10.1351/pac199264111731.

[19] A. Pohar, “A review of computational fluid dynamics (CFD) simulations of mixing in the pharmaceutical industry,” *Biomedical Journal of Scientific & Technical Research,* vol. 27, no. 3, 2020,
doi: 10.26717/bjstr.2020.27.004494.

[20] E. Książek, “Citric Acid: properties, microbial production, and applications in industries,” *Molecules*, 2024, doi: 10.3390/molecules29010022.

[21] W. Gwenzi and N. Chaukura, “Organic contaminants in African aquatic systems: Current knowledge, health risks, and future research directions,” *Science of The Total Environment*, vol. 619–620, pp. 1493–1514, 2018, 2018, doi: 10.1016/j.scitotenv.2017.11.121.

[22] B. Streit, “Bioaccumulation processes in ecosystems,” *Experientia,* vol. 48, no. 10, pp. 955–970, 1992, doi: 10.1007/BF01919142.

[23] R. Zait, D. Fighir, B. Sluser, O. Plavan, and C. Teodosiu, “Priority pollutants effects on aquatic ecosystems evaluated through ecotoxicity, impact, and risk assessments,” *Water (Switzerland)*, vol. 14, no. 20, 2022, doi: 10.3390/w14203237.

[24] F. A. Huntingford, C. Adams, V. A. Braithwaite, S. Kadri, T. G. Pottinger, P. Sandøe, and J. F. Turnbull, “Current issues in fish welfare,” *Journal of Fish Biology*, vol. 68, no. 2, pp. 332–372, 2006, doi: 10.1111/j.0022-1112.2006.001046.

[25] R. Mithuna, R. Tharanyalakshmi, Ishan Jain, Shivangi Singhal, Divyanshu Sikarwar, Sovik Das, J. Ranjitha, Devanita Ghosh, Mohammad Mahmudur Rahman, and Bhaskar Das, “Emergence of antibiotic resistance due to the excessive use of antibiotics in medicines and feed additives: A global scenario with emphasis on the Indian perspective,” *Emerging Contaminants*, vol. 10, no. 4, p. 100389, Dec. 2024, doi: 10.1016/J.EMCON.2024.100389.

[26] M. Farhan Hanafi and N. Sapawe, “A review on the water problem associate with organic pollutants derived from phenol, methyl orange, and remazol brilliant blue dyes,” *Materials Today: Proceedings*, vol. 31, pp. A141–A150, Jan. 2020, doi: 10.1016/J.MATPR.2021.01.258.

[27] L. Lin, H. Yang, and X. Xu, “Effects of Water Pollution on Human Health and Disease Heterogeneity: A Review,” Frontiers in Environmental Science, vol. 10, p. 880246, Jun. 30, 2022, doi: 10.3389/fenvs.2022.880246.

[28] V. Camel and A. Bermond, “The use of ozone and associated oxidation processes in drinking water treatment,” *Water Research*, vol. 32, no. 11, pp. 3208–3222, 1998, doi: 10.1016/S0043-1354(98)00130-4.

[29] G. Zhu, H. Zheng, Z. Zhang, T. Tshukudu, P. Zhang, and X. Xiang, “Characterization and coagulation-flocculation behavior of polymeric aluminum ferric sulfate (PAFS),” *Chemical Engineering Journal*, vol. 178, 2011, doi: 10.1016/j.cej.2011.10.008.

[30] C. P. Huang, C. Dong, and Z. Tang, “Advanced chemical oxidation: Its present role and potential future in hazardous waste treatment,” *Waste Management*, vol. 13, no. 5–7, pp. 361–377, 1993, doi: 10.1016/0956-053X(93)90070-D.

[31] W. C. Koskinen, K. E. Sellung, J. M. Baker, B. L. Barber, and R. H. Dowdy, “Ultrasonic decomposition of atrazine and alachlor in water.,” *Journal of Environmental Science and Health, Part B*, vol. 29, no. 3, pp. 581–590, Jan. 1994, doi: 10.1080/03601239409372895.

[32] J. Ma, F. Yu, L. Zhou, L. Jin, M. Yang, J. Luan, Y. Tang, H. Fan, Z. Yuan, and J. Chen, “Enhanced adsorptive removal of methyl orange and methylene blue from aqueous solution by alkali-activated multiwalled carbon nanotubes,” *ACS Applied Materials & Interfaces*, vol. 4, no. 11, 2012, doi: 10.1021/am301053m.

[33] L.N. Ukiwe, S.I. Ibeneme, C.E. Duru, B.N. Okolue, G.O. Onyedika and C.A. Nweze “Chemical and electro-coagulation techniques in coagulation-floccculation in water and wastewater treatment- A Review,” *Journal of Advances in Chemistry*, vol. 9, no. 3, 2013, doi: 10.24297/jac.v9i3.1006.

[34] A. W. Mohammad, Y. H. Teow, W. L. Ang, Y. T. Chung, D. L. Oatley-Radcliffe, and N. Hilal, “Nanofiltration membranes review: Recent advances and future prospects,” *Desalination*, 2015. doi: 10.1016/j.desal.2014.10.043.

[35] M. Coha, G. Farinelli, A. Tiraferri, M. Minella, and D. Vione, “Advanced oxidation processes in the removal of organic substances from produced water: Potential, configurations, and research needs,” *Chemical Engineering Journal*, vol. 414, p. 128668, Jun. 2021, doi: 10.1016/J.CEJ.2021.128668.

[36] A. Noor, I. Khan, M. Asif, M. Khan, M. Arslan, F. Ali, and M. Bilal, “Treatment innovation using biological methods in combination with physical treatment methods,” *The Treatment of Pharmaceutical Wastewater: Innovative Technologies and the Adaptation of Treatment Systems*, pp. 217–245, Jan. 2023, doi: 10.1016/B978-0-323-99160-5.00010-2.

[37] M. B. Ahmed, J. L. Zhou, H. H. Ngo, W. Guo, N. S. Thomaidis, and J. Xu, “Progress in the biological and chemical treatment technologies for emerging contaminant

removal from wastewater: A critical review," *Journal of Hazardous Materials*, vol. 323, pp. 274–298, Feb. 2017,
doi: 10.1016/J.JHAZMAT.2016.04.045.

[38] S. F. Ahmed, M. Mofijur, S. Nuzhat, A. Chowdhury, N. Rafa, Md. Uddin, A. Inayat, T. M. I. Mahlia, H. Ong, W. Chia, P. Show, "Recent developments in physical, biological, chemical, and hybrid treatment techniques for removing emerging contaminants from wastewater," *Journal of Hazardous Materials*, vol. 416, p. 125912, Aug. 2021,
doi: 10.1016/J.JHAZMAT.2021.125912.

[39] I. Naz, I. Ahmad, R. W. Aslam, A. Quddoos, and A. Yaseen, "Integrated assessment and geostatistical evaluation of groundwater quality through water quality indices," *Water (Switzerland)*, vol. 16, no. 1, 2024,
doi: 10.3390/w16010063.

[40] A. Pistocchi, H. R. Andersen, G. Bertanza, A. Brander, J. M. Choubert, M. Cimbritz, J. E. Drewes, C. Koehler, J. Krampe, M. Launay, P. H. Nielsen, N. Obermaier, S. Stanev, and D. Thornberg, "Treatment of micropollutants in wastewater: Balancing effectiveness, costs and implications," *Science of The Total Environment*, vol. 850, p. 157593, Dec. 2022,
doi: 10.1016/J.SCITOTENV.2022.157593.

[41] A. Saravanan, P. Senthil Kumar, S. Jeevanantham, R. Karthikeyan, M. Dhanapal, and S. Palanivelu, "Effective water/wastewater treatment methodologies for toxic pollutants removal: Processes and applications towards sustainable development," *Chemosphere*, vol. 280, p. 130595, Oct. 2021,
doi: 10.1016/J.CHEMOSPHERE.2021.130595.

[42] G. Crini and E. Lichtfouse, "Advantages and disadvantages of techniques used for wastewater treatment," *Environmental Chemistry Letters.* vol. 17, no. 1, pp. 145–155, 2019.
doi: 10.1007/s10311-018-0785-9.

[43] A. Sonune and R. Ghate, "Developments in wastewater treatment methods," D*esalination*, vol. 167, no. 1–3, pp. 55–63, Aug. 2004,
doi: 10.1016/J.DESAL.2004.06.113.

[44] G. Rodriguez-Garcia, M. Molinos-Senante, A. Hospido, F. Hernández-Sancho, M. T. Moreira, and G. Feijoo, "Environmental and economic profile of six typologies of wastewater treatment plants," *Water Research*, vol. 45, no. 18, pp. 5997–6010, Nov. 2011,
doi: 10.1016/J.WATRES.2011.08.053.

[45] K. Sathya, K. Nagarajan, G. Carlin Geor Malar, S. Rajalakshmi, and P. Raja Lakshmi, "A comprehensive review on comparison among effluent treatment methods and modern methods of treatment of industrial wastewater effluent from

different sources," *Environmental Science and Pollution Research,* vol. 29, no. 25, pp. 37647–37670, 2022,
doi: 10.1007/s13201-022-01594-7.

[46] D. P. Zagklis and G. Bampos, "Tertiary wastewater treatment technologies: A review of technical, economic, and life cycle aspects," *Processes,* vol. 10, no. 11, art. no. 2304, 2022,
doi: 10.3390/pr10112304.

[47] R. J. E. Martins, "Quarterly progress in environmental development," *Waste water Treatment (primary treatment)*, in *Quarterly Progress in Environmental Development*, 2023,2023,
doi: 10.36599/qped-978-65-5376-205-3.

[48] F. Tatiana, P. Paula, B. Vivian, P. Rigoberto, O. Jannet, and A. Paola, "Life cycle assessment to identify environmental improvements in an aerobic wastewater treatment plant," *Chemical Engineering Transactions*, vol.49,2016,
doi: 10.3303/CET1649083.

[49] T. P. Wong, R. W. Babcock, B. Hu, J. Schneider, and S. Milan, "High rate biological contactor system using waste activated sludge from trickling filter/solids contact process," *Water Science and Technology*, vol. 81, no. 10, 2020,
doi: 10.2166/wst.2020.288.

[50] L. Postacchini, K. M. Lamichhane, D. Furukawa, R. W. Babcock, F. E. Ciarapica, and M. J. Cooney, "Life cycle assessment comparison of activated sludge, trickling filter, and high-rate anaerobic-aerobic digestion (HRAAD)," *Water Science and Technology*, vol. 73, no. 10, 2016,
doi: 10.2166/wst.2016.087.

[51] D. Jolis, R. Hirano, and P. Pitt, "Tertiary treatment using microfiltration and UV disinfection for water reclamation," *Water Environment Research*, vol. 71, no. 2, 1999,
doi: 10.2175/106143098x121789.

[52] D. Pelayo, M. J. Rivero, G. Santos, P. Gómez, and I. Ortiz, "Techno-economic evaluation of UV light technologies in water remediation," *Science of the Total Environment*, vol. 868, 2023,
doi: 10.1016/j.scitotenv.2022.161376.

[53] N. Collado, H. Pérez, J. Rodriquez-Mozaz, and D Barceló, "Pharmaceuticals occurrence in a WWTP with significant industrial contribution and its input into the river system," *Environmental Pollution*, vol. 185, 2014,
doi: 10.1016/j.envpol.2013.10.040.

[54] M. F. Hamoda, I. Al-Ghusain, and N. Z. AL-Mutairi, “Sand filtration of wastewater for tertiary treatment and water reuse,” *Desalination*, vol. 164, no. 3, 2004, doi: 10.1016/S0011-9164(04)00189-4.

[55] G. Pérez, A. R. Fernández-Alba, A. M. Urtiaga, and I. Ortiz, “Electro-oxidation of reverse osmosis concentrates generated in tertiary water treatment,” *Water Research*, vol. 44, no. 9, 2010,
doi: 10.1016/j.watres.2010.02.017.

[56] M. U. Masood, M. Rashid, S. Haider, I. Naz, C. B. Pande, S. Heddam, F. Alshehri, I. Elkhrachy, A. Ahsan, and S. S. Sammen, “Exploring Groundwater Quality Assessment: A Geostatistical and Integrated Water Quality Indices Perspective,” *Water*, vol. 16, no. 1, p. 138, 2024,
doi: 10.3390/w16010138.

[57] M. A. Al-Nuaim, A. A. Alwasiti, and Z. Y. Shnain, “The photocatalytic process in the treatment of polluted water,” *Applied Chemistry and Biotechnology*, vol. 77, no. 2, pp. 677–701, 2023,
doi: 10.1007/s11696-022-02468-7.

[58] F. Mohamadpour and A. M. Amani, “Photocatalytic systems: reactions, mechanism, and applications,” *RSC Advances*, vol. 14, no. 29, pp. 20609–20645, 2024,
doi: 10.1039/D4RA03259D.

[59] R. S. Dhamorikar, V. G. Lade, P. V. Kewalramani, and A. B. Bindwal, “Review on integrated advanced oxidation processes for water and wastewater treatment,” *Journal of Industrial and Engineering Chemistry*, vol. 138, pp. 104–122, Oct. 2024,
doi: 10.1016/J.JIEC.2024.04.037.

[60] S. Jiménez, M. Andreozzi, M. M. Micó, M. G. Álvarez, and S. Contreras, “Produced water treatment by advanced oxidation processes,” *Science of The Total Environment*, vol. 666, pp. 12–21, May 2019,
doi: 10.1016/J.SCITOTENV.2019.02.128.

[61] I. A. Ricardo, R. Busquets, M. Waisman, G. Carvalho, J. Zuin, and F. Souza, “A critical review on microplastics, interaction with organic and inorganic pollutants, impacts and effectiveness of advanced oxidation processes applied for their removal from aqueous matrices,” *Chemical Engineering Journal*, vol. 424, p. 130282, Nov. 2021,
doi: 10.1016/J.CEJ.2021.130282.

[62] N. A. Sacco, F. M. Zoppas, A. Devard, M. del P. González Muñoz, G. García, and F. A. Marchesini, “Recent advances in microplastics removal from water with special attention given to photocatalytic degradation: Review of scientific research,” *Microplastics*, vol. 2, no. 3, 2023,
doi: 10.3390/microplastics2030023.

[63] Z. Bi, Z. Yu, Z. Sun, L. He, X. Meng, G. Zeng, Y. Yang, Y. Deng, and Q. Zhang, "The generation and transformation mechanisms of reactive oxygen species in the environment and their implications for pollution control processes: A review," *Environmental Research*,vol. 260, p. 119592, Nov. 2024,
doi: 10.1016/J.ENVRES.2024.119592.

[64] Y. Yang, J. J. Pignatello, J. Ma, and W. A. Mitch, "Comparison of halide impacts on the efficiency of contaminant degradation by sulfate and hydroxyl radical-based advanced oxidation processes (AOPs)," *Environmental Science & Technology*, vol. 48, no. 4, 2014,
doi: 10.1021/es404118q.

[65] A. Babu, M. Garg, R. Gabriel, R. Raj, M. Ghangrekar, A. Nema, and S. Das, "Advanced oxidation process (AOP) combined biological process for wastewater treatment: A review on advancements, feasibility and practicability of combined techniques," *Environmental Research*, vol. 237, p. 116944, Nov. 2023,
doi: 10.1016/J.ENVRES.2023.116944.

[66] D. Peramune, D. C. Manatunga, R. S. Dassanayake, V. Premalal, R. N. Liyanage, C. A. Gunathilake, and N. Abid, "Recent advances in biopolymer-based advanced oxidation processes for dye removal applications: A review," *Environmental Research*, vol. 215, p. 114242, Dec. 2022,
doi: 10.1016/J.ENVRES.2022.114242.

[67] U. Černigoj, U. L. Štangar, and P. Trebše, "Degradation of neonicotinoid insecticides by different advanced oxidation processes and studying the effect of ozone on $TiO_2$ photocatalysis," *Applied Catalysis B: Environmental*, vol. 75, no. 3–4, pp. 229–238, Sep. 2007,
doi: 10.1016/J.APCATB.2007.04.014.

[68] O. Gimeno, M. Carbajo, F. J. Beltrán, and F. J. Rivas, "Phenol and substituted phenols AOPs remediation," *Journal of Hazardous Materials*, vol. 119, no. 1–3, pp. 99–108, Mar. 2005,
doi: 10.1016/J.JHAZMAT.2004.11.024.

[69] M. Klavarioti, D. Mantzavinos, and D. Kassinos, "Removal of residual pharmaceuticals from aqueous systems by advanced oxidation processes," *Environmental International*, vol. 35, no. 2, pp. 402–417, Feb. 2009,
doi: 10.1016/J.ENVINT.2008.07.009.

[70] M. P. Rayaroth, M. Marchel, and G. Boczkaj, "Advanced oxidation processes for the removal of mono and polycyclic aromatic hydrocarbons – A review," *Science of The Total Environment*, vol. 857, p. 159043, Jan. 2023,
doi: 10.1016/J.SCITOTENV.2022.159043.

[71] L. Liu, Z. Chen, J. Zhang, D. Shan, Y. Wu, L. Bai, and B. Wang, "Treatment of industrial dye wastewater and pharmaceutical residue wastewater by advanced

oxidation processes and its combination with nanocatalysts: A review," *Journal of Water Process Engineering*, vol. 42, p. 102122, Aug. 2021, doi: 10.1016/J.JWPE.2021.102122.

[72] K. Paździor, L. Bilińska, and S. Ledakowicz, "A review of the existing and emerging technologies in the combination of AOPs and biological processes in industrial textile wastewater treatment," *Chemical Engineering Journal*, vol. 376, p. 120597, Nov. 2019, doi: 10.1016/J.CEJ.2018.12.057.

[73] F. C. Moreira, V. J. P. Vilar, A. C. C. Ferreira, M. A. Sousa, C. Gonçalves, M. F. Alpendurada, and R. A. R. Boaventura, "Treatment of a pesticide-containing wastewater using combined biological and solar-driven AOPs at pilot scale," *Chemical Engineering Journal*, vol. 209, pp. 429–441, Oct. 2012, doi: 10.1016/J.CEJ.2012.08.009.

[74] C. Amor, L. Marchão, M. S. Lucas, and J. A. Peres, "Application of advanced oxidation processes for the treatment of recalcitrant agro-industrial wastewater: A review," *Water (Switzerland)*, vol. 11, no. 2, 2019, doi: 10.3390/w11020205.

[75] V. S. Solanki, B. Pare, P. Gupta, S. B. Jonnalagadda, and R. Shrivastava, "A review on advanced oxidation processes (AOPs) for wastewater remediation," Asian Journal of Chemistry, vol. 32, no. 11, pp. 2677-2684, Nov. 01, 2020, Asian Publication Corporation, doi: 10.14233/ajchem.2020.22806.

[76] J. H. Carey, J. Lawrence, and H. M. Tosine, "Photodechlorination of PCB's in the presence of titanium dioxide in aqueous suspensions," *Bulletin of Environmental Contamination and Toxicology*, vol. 16, no. 6, 1976, doi: 10.1007/BF01685575.

[77] F. Wang, J. Xu, Z. Wang, Y. Lou, C. Pan, and Y. Zhu, "Unprecedentedly efficient mineralization performance of photocatalysis-self-Fenton system towards organic pollutants over oxygen-doped porous g-$C_3N_4$ nanosheets," *Applied Catalysis B: Environmental*, vol. 312, p. 121438, Sep. 2022, doi: 10.1016/J.APCATB.2022.121438.

[78] R. V. Prihod'ko and N. M. Soboleva, "Photocatalysis: Oxidative processes in water treatment," *Journal of Chemistry*, vol. 2013, art. no. 168701, 2013, doi: 10.1155/2013/168701.

[79] Y. Liu, X. Zeng, X. Hu, Y. Xia, and X. Zhang, "Solar-driven photocatalytic disinfection over 2D semiconductors: The generation and effects of reactive oxygen species," *Solar RRL*, vol. 5, no. 6, art. no. 2000594, 2021, doi: 10.1002/solr.202000594.

[80] Z. H. Xie, C. He, H. Zhou, L. Li, Y. Liu, Y. Du, W. Liu, Y. Mu, and B. Lai, "Effects of molecular structure on organic contaminants' degradation efficiency and dominant ROS in the advanced oxidation process with multiple ROS," *Environmental Science & Technology*, vol. 56, no. 12, 2022, doi: 10.1021/acs.est.2c00464.

[81] M. Antonopoulou, "Homogeneous and heterogeneous photocatalysis for the treatment of pharmaceutical industry wastewaters: A Review," *Toxics*, vol. 10, no. 9, art. no. 539, 2022, doi: 10.3390/toxics10090539.

[82] D. Binding and F. Steinbach, "Homogeneous photocatalysis by organic dyes in the liquid phase," *Nature*, vol. 227, no. 5260, 1970, doi: 10.1038/227832a0.

[83] P. Cieśla, P. Kocot, P. Mytych, and Z. Stasicka, "Homogeneous photocatalysis by transition metal complexes in the environment," *Journal of Molecular Catalysis A: Chemical*, 2004, doi: 10.1016/j.molcata.2004.08.043.

[84] S. Loaiza-Ambuludi, M. Panizza, N. Oturan, and M. A. Oturan, "Removal of the anti-inflammatory drug ibuprofen from water using homogeneous photocatalysis," *Catalysis Today*, vol. 224, pp. 29–33, 2014, doi: 10.1016/j.cattod.2013.12.018.

[85] M. Muruganandham, R. P. S. Suri, S. Jafari, M. Sillanpää, G. J. Lee, J. J. Wu, and M. Swaminathan, "Recent developments in homogeneous advanced oxidation processes for water and wastewater treatment," *International Journal of Photoenergy*, art. no. 821674, 2014, doi: 10.1155/2014/821674.

[86] E. Issaka, E. Danso-Boateng, and J. Baffoe, "Harnessing the power of heterogeneous photocatalytic process for sustainable pharmaceutical contaminant remediation in water environments," *Desalination and Water Treatment*, vol. 319, p. 100574, Jul. 2024, doi: 10.1016/J.DWT.2024.100574.

[87] S. N. Ahmed and W. Haider, "Heterogeneous photocatalysis and its potential applications in water and wastewater treatment: A review," *Nanotechnology*, vol. 29, no. 34, art. no. 342001, 2018, doi: 10.1088/1361-6528/aac6ea.

[88] M. Náfrádi, G. Veréb, D. S. Firak, and T. Alapi, "Photocatalysis: Introduction, Mechanism, and Effective Parameters," in *Advances in Photocatalysis, Cham: Springer,* pp. 3–31, 2022 doi: 10.1007/978-3-030-77371-7_1.

[89] H. Wang, M. Wang, X. Zhang, Y. Gong, and W. Wang, “A review on heterogeneous photocatalysis for environmental remediation: From semiconductors to modification strategies,” *Journal of Environmental Chemical Engineering*, vol. 10, no. 6, p. 108605, 2022, doi: 10.1016/S1872-2067(21)63910-4.

[90] M. N. Alikulov, “Auger Recombination in Semiconductors,” *International Journal of Development and Public Policy*, vol. 1, no. 3, pp. 1–4, 2021.

[91] T. Goudon, V. Miljanović, and C. Schmeiser, “On the Shockley–Read–Hall model: Generation–recombination in semiconductors,” *SIAM Journal on Applied Mathematics*, vol. 67, no. 4, pp. 1183–1201, 2007.

[92] P. Laurent and L. Titarchuk, “Electron–Positron Pair Creation Close to a Black Hole Horizon: Redshifted Annihilation Line in the Emergent X-Ray Spectra of a Black Hole. I.,” *Astrophys J*, vol. 859, no. 2, 2018, doi: 10.3847/1538-4357/aac090.

[93] P. K. Pandis, G. O. Kakavogiannis, E. A. Kouli, and A. Kalogirou, “Key Points of Advanced Oxidation Processes (AOPs) for Wastewater, Organic Pollutants and Pharmaceutical Waste Treatment: A Mini Review,” *Chemical Engineering*, vol. 6, no. 1, p. 8, 2022, doi: 10.3390/chemengineering6010008.

[94] L. Zhou, Z. Q. Zhang, M. M. Li, Q. Wang, J. N. Gao, K. B. Li, and L. Lei, “Graphitic carbon nitride (g-$C_3N_4$) as a sustainable heterogeneous photocatalyst for metal free and oxygen-tolerant photo-atom transfer radical polymerization (photo-ATRP),” *Green Chemistry*, vol. 23, no. 23, 2021, doi: 10.1039/d1gc03604a.

[95] E. Issaka, E. Danso-Boateng, and J. Baffoe, “Harnessing the power of heterogeneous photocatalytic process for sustainable pharmaceutical contaminant remediation in water environments,” *Desalination and Water Treatment*, vol. 319, p. 100574, Jul. 2024, doi: 10.1016/J.DWT.2024.100574.

[96] D. Teng, J. Qu, P. Li, P. Jin, J. Zhang, Y. Zhang, and Y. Cao, “Heterostructured α-$Bi_2O_3$/BiOCl nanosheet for photocatalytic applications,” *Nanomaterials*, vol. 12, no. 20, 2022, doi: 10.3390/nano12203631.

[97] J. A. Rengifo-Herrera and C. Pulgarin, “Why five decades of massive research on heterogeneous photocatalysis, especially on $TiO_2$, has not yet driven to water disinfection and detoxification applications? Critical review of drawbacks and challenges,” *Chemical Engineering Journal*, vol. 477, p. 146875, Dec. 2023, doi: 10.1016/J.CEJ.2023.146875

[98] X. Yuan, L. Jiang, X. Chen, L. Leng, H. Wang, and S. Wu, “Highly efficient Visible-light-induced photoactivity of Z-scheme $Ag_2CO_3$/Ag/$WO_3$ photocatalysts for organic pollutant degradation,” *Environmental Science: Nano*, vol. 4, no. 11, 2017, doi: 10.1039/c7en00713b.

[99] C. Dong, M. Xing, and J. Zhang, “Recent progress of photocatalytic Fenton-like process for environmental remediation,” *Frontiers in Environmental Chemistry*, vol. 1, art. no. 8, 2020,
doi: 10.3389/fenvc.2020.00008.

[100] A. Khan, Z. Valicsek, and O. Horváth, “Photocatalytic degradation of Rhodamine B in heterogeneous and homogeneous systems,” *Hungarian Journal of Industry and Chemistry*, vol. 49, no. 1, pp. 9–16, Sep. 2021,
doi: 10.33927/hjic-2021-02.

[101] W. H. Brock, “Justus von Liebig. Gatekeeper of chemistry,” *Chemical Society Reviews*, vol. 24, no. 6, 1995,
doi: 10.1039/cs9952400383.

[102] Y. Zheng, J. Liu, J. Liang, M. Jaroniec, and S. Z. Qiao, “Graphitic carbon nitride materials: Controllable synthesis and applications in fuel cells and photocatalysis,” *Energy & Environmental Science*, vol. 5, no. 5, pp. 6717–6731, 2012,
doi: 10.1039/c2ee03479d.

[103] A. Y. Liu and M. L. Cohen, “Prediction of new low compressibility solids,” *Science (1979)*, vol. 245, no. 4920, 1989,
doi: 10.1126/science.245.4920.841.

[104] D. M. Teter and R. J. Hemley, “Low-compressibility carbon nitrides,” *Science (1979)*, vol. 271, no. 5245, pp. 53–55, 1996,
doi: 10.1126/science.271.5245.53.

[105] X. Wang, K. Maeda, A. Thomas, K. Takanabe, G. Xin, J. M. Carlsson, K. Domen, and M. Antonietti, “A metal-free polymeric photocatalyst for hydrogen production from water under Visible light,” *Nature Materials*, vol. 8, no. 1, pp. 76–80, 2009,
doi: 10.1038/nmat2317.

[106] L. Sun, Y. Chen, Z. Sun, H. Zhu, J. Zhang, and S. Wang, “Enhanced Visible-light photocatalytic activity of g-$C_3N_4$-$ZnWO_4$ by fabricating a heterojunction: Investigation based on experimental and theoretical studies,” *Journal of Materials Chemistry*, vol. 22, no. 44, 2012,
doi: 10.1039/c2jm34965e.

[107] A. Alaghmandfard and K. Ghandi, “A Comprehensive Review of Graphitic Carbon Nitride (g-$C_3N_4$)–Metal Oxide-Based Nanocomposites: Potential for Photocatalysis and Sensing,” Nanomaterials, vol. 12, no. 2, p. 294, Jan. 01, 2022, *MDPI*,
doi: 10.3390/nano12020294.

[108] A. Basso Peressut, M. Cristiani, S. Besco, C. Minero, and L. Getti, "Reduced Graphene Oxide/Waste-Derived $TiO_2$ Composite Membranes: Preliminary Study of a New Material for Hybrid Wastewater Treatment," *Nanomaterials*, vol. 13, no. 6, p. 1043, 2023,
doi: 10.3390/nano13061043.

[109] J. Fu, J. Yu, C. Jiang, and B. Cheng, "g-$C_3N_4$-Based Heterostructured Photocatalysts," Advanced Energy Materials, *Advanced Energy Material*, vol. 8, no. 3, art. no. 1701503, 2018,
doi: 10.1002/aenm.201701503.

[110] O. M. Bankole, T. D. Olorunsola, and A. S. Ogunlaja, "Photocatalytic decontamination of toxic hexavalent chromium in water over graphitic carbon nitride supported sulfur nanoparticles," *Journal of Photochemistry and Photobiology A: Chemistry*, vol. 405, 2021,
doi: 10.1016/j.jphotochem.2020.112934.

[111] Y. Zhang, T. Mori, J. Ye, and M. Antonietti, "Phosphorus-doped carbon nitride solid: Enhanced electrical conductivity and photocurrent generation," *Journal of the American Chemical Society*, vol. 132, no. 18, 2010,
doi: 10.1021/ja101749y.

[112] Y. Gao, Y. Zhu, L. Lyu, Q. Zeng, X. Xing, and C. Hu, "Electronic structure modulation of graphitic carbon nitride by oxygen doping for enhanced catalytic degradation of organic pollutants through peroxymonosulfate activation," *Environmental Science & Technology*, vol. 52, no. 24, 2018,
doi: 10.1021/acs.est.8b05246.

[113] P. Zandi, A. Phani, and S. Kim, "High-performance P-N junction heterostructure with carbon quantum dot and nitrogen self-doped graphitic carbon nitride for Visible light photodetection," *Advanced Optical Materials*, vol. 12, no. 21, art. no. 2401317, Oct. 2024,
doi: 10.1002/adom.202401317.

[114] P. Kyokunzire, G. Jeong, S. Y. Shin, H. J. Cheon, E. Wi, M. Woo, and T. T. Vu, "Enhanced nitric oxide sensing performance of conjugated polymer films through incorporation of graphitic carbon nitride," *International Journal of Molecular Sciences*, vol. 24, no. 2, 2023,
doi: 10.3390/ijms24021158.

[115] A. Manohar, S. Chandrasekar, R. Kumaravel, V. Raghavan, S. Meenakshi, and S. Ramar, "Multifunctional g-$C_3N_4$/NixMg1-x$Fe_2O_4$ nanocomposites: Advanced materials for electrochemical energy storage and biocompatibility," *Colloids and Surfaces A: Physicochemical and Engineering Aspects*, vol. 715, p. 136618, Jun. 2025,
doi: 10.1016/J.COLSURFA.2025.136618.

[116] A. Ghaffar Rana, "Modification of Graphitic Carbon Nitride (g-$C_3N_4$) for Photocatalytic Redox Reactions," PhD thesis, Technical University of Munich, 2023.

[117] S. Soni, S. Teli, P. Teli, and S. Agarwal, "Empowering sustainability: Charting the seven years of progress in g-$C_3N_4$ based materials and their crucial role in building a greener future," *Sustainable Chemistry and Pharmacy*, vol. 41, p. 101693, Oct. 2024,
doi: 10.1016/J.SCP.2024.101693.

[118] H. Sun, X. Zhou, H. Zhang, and W. Tu, "An efficient exfoliation method to obtain graphitic carbon nitride nanosheets with superior Visible-light photocatalytic activity," *International Journal of Hydrogen Energy*, vol. 42, no. 12, 2017,
doi: 10.1016/j.ijhydene.2016.12.080.

[119] A. Shahpal, "Harnessing palladium-decorated g-$C_3N_4$ nanosheets for selective catalytic benzyl alcohol synthesis," *Molecular Catalysis*, vol. 567, p. 114453, Oct. 2024,
doi: 10.1016/J.MCAT.2024.114453.

[120] B. Lin, M. Xia, B. Xu, B. Chong, Z. Chen, and G. Yang, "Bio-inspired nanostructured g-$C_3N_4$-based photocatalysts: A comprehensive review," *Chinese Journal of Catalysis*, vol. 43, no. 8, pp. 2141–2172, Aug. 2022,
doi: 10.1016/S1872-2067(22)64110-X.

[121] G. Zhang, Z. A. Lan, and X. Wang, "Conjugated Polymers: Catalysts for photocatalytic hydrogen evolution," *Angewandte Chemie International Edition*, vol. 55, no. 51, pp. 15712–15727, 2016,
doi: 10.1002/anie.201607375.

[122] D. Bokov, A. Turki Jalil, S. Chupradit, W. Suksatan, M. Javed Ansari, I. H. Valiev, G. H. Gabdrakhman, and E. Kianfar, "Nanomaterial by sol-gel method: Synthesis and application," *Advances in Materials Science and Engineering*, 2021,
doi: 10.1155/2021/5102014.

[123] D. Bhanderi, P. Lakhani, and C. K. Modi, "Graphitic carbon nitride (g-$C_3N_4$) as an emerging photocatalyst for sustainable environmental applications: a comprehensive review," vol. 4, no. 2, pp. 499–543, 2024, *Royal Society of Chemistry*.
doi: 10.1039/d3su00382e.

[124] T. Wang, T. Wan, W. Di, and J. Li, "Facile fabrication of graphitic carbon nitride by solvothermal method with hierarchical structure and high Visible light photocatalytic activity," *Journal of the Taiwan Institute of Chemical Engineers*, vol. 145, 2023,
doi: 10.1016/j.jtice.2023.104773.

[125] P. A. Nguyen, T. K. A. Nguyen, D. Q. Dao, and E. W. Shin, "Ethanol Solvothermal Treatment on Graphitic Carbon Nitride Materials for Enhancing Photocatalytic Hydrogen Evolution Performance," *Nanomaterials*, vol. 12, no. 2, p. 179, Jan. 2022, doi: 10.3390/nano12020179.

[126] H. Li, D. Li, M. Long, X. Bai, Q. Wen, and F. Song, "Solvothermal synthesis of MIL-53Fe@g-$C_3N_4$ for peroxymonosulfate activation towards enhanced photocatalytic performance," *Colloids and Surfaces A: Physicochemical and Engineering Aspects*, vol. 658, p. 130646, Feb. 2023, doi: 10.1016/J.COLSURFA.2022.130646.

[127] M. T. Abdullahi, M. Ali, W. Farooq, M. Khan, M. Younas, and M. N. Tahir, "Solvothermal synthesis of carbon nitride (g-$C_3N_4$): bandgap engineering for improved photocatalytic performance," *Sustainable Energy & Fuels*, vol. 9, no. 4, pp. 1109–1119, 2025, doi: 10.1039/D4SE01646G.

[128] Q. Zhang, J. Chen, J. Zhou, H. Li, and X. Wang, "Construction of g-$C_3N_4$/$Bi_4O_5I_2$ heterojunction via the solvothermal method for the purification of eutrophic water," *Catalysis Communications*, vol. 149, p. 106200, Jan. 2021, doi: 10.1016/J.CATCOM.2020.106200.

[129] N. A. Nordin, M. A. Mohamed, M. S. Mastuli, S. F. Mohd Yusoff, T. Sugiura, and K. Manseki, "Revealing the impact of different precursors and solvents for supramolecular complex formation and in-situ C-doping in g-$C_3N_4$ with enhanced photocatalytic $H_2O_2$ production," *Journal of Industrial and Engineering Chemistry*, vol. 135, pp. 197–212, Jul. 2024, doi: 10.1016/J.JIEC.2024.01.032.

[130] E. N. Ermakova, E. A. Maksimovskii, I. V. Yushina, and M. L. Kosinova, "CVD synthesis of graphitic carbon nitride films from melamine," *Russian Journal of Inorganic Chemistry*, vol. 68, no. 2, 2023, doi: 10.1134/S0036023622602252.

[131] E. B. Chubenko, N. G. Kovalchuk, I. V. Komissarov, and V. E. Borisenko, "Chemical Vapor Deposition of 2D Crystallized g-$C_3N_4$ Layered Films," *Journal of Physical Chemistry C*, vol. 126, no. 9, pp. 4710–4714, Mar. 2022, doi: 10.1021/acs.jpcc.1c10561.

[132] Y. Fukasawa, K. Takanabe, A. Shimojima, M. Antonietti, K. Domen, and T. Okubo, "Synthesis of ordered porous graphitic-$C_3N_4$ and regularly arranged $Ta_3N_5$ nanoparticles by using self-assembled silica nanospheres as a primary template," *Chemistry - An Asian Journal*, vol. 6, no. 1, 2011, doi: 10.1002/asia.201000523.

[133] X. Wang, H. Yu, H. Zhang, X. Zhang, and Y. Zhang, "Novel fumed silica/g-$C_3N_4$ composites for highly efficient removal of rhodamine B under visible light emitting

diodes light irradiation," *Environmental Progress & Sustainable Energy*, vol. 41, no. 1, Jan. 2022,
doi: 10.1002/ep.13714.

[134] W. Jiang, J. Li, X. Yang, J. Wang, J. Zhang, and L. Zhang, "Template/surfactant free and UV light irradiation assisted fabrication of Mn-Co oxides composite nanorings: Structure and synthesis mechanism," *Progress in Natural Science: Materials International*, vol. 29, no. 2, pp. 163–169, Apr. 2019,
doi: 10.1016/J.PNSC.2019.02.002.

[135] G. Gianola, C. Monti, F. Cecchini, C. Locatelli, A. Vaccari, and D. Tonelli, "Effect of silica leaching treatment during template-assisted synthesis on the performance of FeNC catalysts for oxygen reduction reaction," *Electrochimica Acta*, vol. 525, p. 146085, Jun. 2025,
doi: 10.1016/J.ELECTACTA.2025.146085.

[136] M. Mirhosseyni, G. Mohammadi Ziarani, and A. Badiei, "Catalytic development of boron and sulphur-doped g-$C_3N_4$ supported Cu-MOF composite for nitroarenes reduction reaction," *Journal of Molecular Structure*, vol. 1321, p. 139763, Feb. 2025,
doi: 10.1016/J.MOLSTRUC.2024.139763.

[137] W. Luo, W. Huang, X. Feng, Y. Huang, X. Song, H. Lin, S. Wang, and G. Mailhot, "The utilization of Fe-doped g-$C_3N_4$ in a heterogeneous photo-Fenton-like catalytic system: The effect of different parameters and a system mechanism investigation," *RSC Advances*, vol. 10, no. 37, pp. 21799–21808, 2020,
doi: 10.1039/d0ra00993h.

[138] T. N. Xuan, N. T. K. Dat, T. T. T. Huyen, and N. H. Dat, "Effect of Ruthenium Modification of g-$C_3N_4$ in the Visible-Light-Driven Photocatalytic Reduction of Cr(VI)," *Catalysts*, vol. 13, no. 6, p. 964, Jun. 2023,
doi: 10.3390/catal13060964.

[139] R. Kumar, S. Ali, M. Abbas, and S. Mohammad, "Optimal synthesis of Ag modified g-$C_3N_4$ for improved visible light photocatalytic performance and self-cleaning applications," *Diamond and Related Materials*, vol. 144, 2024,
doi: 10.1016/j.diamond.2024.110974.

[140] M. Michalska, M. Bajkacz, P. Kosobucki, and M. Gajewska, "Comparative study of photocatalysis with bulk and nanosheet graphitic carbon nitrides enhanced with silver," *Scientific Reports*, vol. 14, no. 1, Dec. 2024,
doi: 10.1038/s41598-024-62291-w.

[141] M. E. Khan, T. H. Han, M. M. Khan, M. R. Karim, and M. H. Cho, "Environmentally sustainable fabrication of Ag@g-$C_3N_4$ nanostructures and their multifunctional efficacy as antibacterial agents and photocatalysts," *ACS Applied Nano Materials*, vol. 1, no. 6, pp. 2912–2922, Jun. 2018,

doi: 10.1021/acsanm.8b00548.

[142] L. A. Luu Thi, T. T. Nguyen, T. V. Pham, and T. T. N. Nguyen, “Environmentally friendly fabrication of Ag nanoparticles decorated on g-$C_3N_4$ for enhancing the photodegradation of RhB,” *Nanoscale Advances*, vol. 7, no. 17, 2025, doi: 10.1039/d5na00552c.

[143] I. Idrees, M. A. Qamar, M. A. Khan, M. Muneer, and M. S. Javed, “Silver (Ag) doped graphitic carbon nitride (g-$C_3N_4$) photocatalyst for enhanced degradation of ciprofloxacin (CIP) under visible light irradiation,” *Arabian Journal of Chemistry*, vol. 17, no. 3, Mar. 2024, doi: 10.1016/j.arabjc.2024.105615.

[144] K. Qi, Y. Sun, X. Li, and J. Yu, “Ag loading enhanced photocatalytic activity of g-$C_3N_4$ porous nanosheets for decomposition of organic pollutants,” *Frontiers in Chemistry*, vol. 7, Apr. 2019, doi: 10.3389/fchem.2019.00091.

[145] R. Liu, Q. Zhang, Y. Xu, and H. Li, “Ag-modified g-$C_3N_4$ prepared by a one-step calcination method for enhanced catalytic efficiency and stability,” *ACS Omega*, vol. 5, no. 31, pp. 19615–19624, Aug. 2020, doi: 10.1021/acsomega.0c02161.

[146] R. Rajendran, S. J. Daisy, and S. Ravichandran, “Design and fabrication of g-$C_3N_4$/$Bi_2S_3$ heterojunction photocatalysts for efficient organic pollutant degradation and antibacterial activity,” *Journal of Alloys and Compounds*, vol. 976, 2024, doi: 10.1016/j.jallcom.2023.173116.

[147] K. Yang, X. Wang, Y. Zhang, and H. Liu, “Controlled synthesis of g-$C_3N_4$/$Bi_2S_3$ nanosheets for efficient degradation of rhodamine B and reduction of Cr(VI) under visible light,” *Surfaces and Interfaces*, vol. 52, Sep. 2024, doi: 10.1016/j.surfin.2024.104885.

[148] A. C. Swathi and M. Chandran, “Visible light responsive MWCNT decorated g-$C_3N_4$/$Bi_2S_3$ photocatalyst for malachite green dye degradation,” *Journal of Applied Physics*, vol. 133, no. 20, 2023, doi: 10.1063/5.0145796.

[149] M. Mateen, G. Chen, N. Guo, and W. S. Chin, “In situ interfacial engineering of 1D g-$C_3N_4$/2D $Bi_2S_3$ heterostructure for antibiotics degradation in aqueous media via light mediated peroxymonosulfate activation,” *Nanoscale Horizons*, 2025, doi: 10.1039/D5NH00265F.

[150] Q. Jing, Y. Zhang, L. Chen, and X. Li, “Constructing an ultrathin g-$C_3N_4$/BiOI/$Bi_2S_3$ multiphase heterojunction system for effectively enhanced photocatalytic performance,” preprint, *SSRN*, 2024,

doi: 10.2139/ssrn.5025940preprint,

[151] J. Hao, X. Sun, Y. Liu, and F. Wang, "S-type g-$C_3N_4$/$Bi_2O_3$ heterojunction as a visible photocatalytic substance: enhanced effective interfacial charge transfer in heterojunction," preprint*, SSRN*, 2023, doi: 10.2139/ssrn.4646207.preprint,

[152] L. Kang, Y. Wang, R. Du, J. Zhang, and C. Kang, "Construction of S/g-$C_3N_4$@β-$Bi_2O_3$ heterojunction and its photocatalytic degradation of toluene in the gas phase," *Environmental Science and Pollution Research*, vol. 31, no. 43, pp. 55836–55849, Sep. 2024, doi: 10.1007/s11356-024-34840-3.

[153] D. Chen, L. Li, L. Zhuang, Y. Liu, B. Zhang, and Z. Jia, "Highly efficient CoFe LDO/α-$Bi_2O_3$/g-$C_3N_4$ heterojunction for photocatalytic elimination of antibiotic pollutants," *Applied Catalysis O*: Open, vol. 194, 2024, doi: 10.1016/j.apcato.2024.206992.

[154] G. M. Manoj, H. Shankar, D. K. Patel, and N. Arumugam, "Direct Z-scheme ZnS@g-$C_3N_4$ heterojunction photocatalysts synthesized via a single-step method for sunlight-assisted degradation of organic pollutants," *Journal of Water Process Engineering*, vol. 79, p. 108845, Nov. 2025, doi: 10.1016/j.jwpe.2025.108845.

[155] M. Danish and M. Muneer, "Facile synthesis of highly efficient Co@ZnSQDs/ g-$C_3N_4$/MWCNT nanocomposites and their photocatalytic potential for the degradation of RhB dye: Efficiency, degradation kinetics, and mechanism pathway," *Ceramics International*, vol. 47, no. 9, pp. 13043–13056, May 2021, doi: 10.1016/j.ceramint.2021.01.168.

[156] Y. R. Girish, K. H. Shivakumar, S. C. Prashanth, and B. M. Nagabhushana, "Rapid and facile synthesis of Z-scheme ZnO/g-$C_3N_4$ heterostructure as efficient visible light-driven photocatalysts for dye degradation and hydrogen evolution reaction," *Journal of Hazardous Materials Advances*, vol. 9, Feb. 2023, doi: 10.1016/j.hazadv.2023.100230.

[157] I. L. Ouriques Brasileiro, V. S. Madeira, A. L. Lopes-Moriyama, and M. L. Rodrigues de Almeida Ramalho, "Addition of g-$C_3N_4$ to ZnO and $ZnFe_2O_4$ to improve photocatalytic degradation of emerging organic pollutants," *Ceramics International*, vol. 49, no. 3, pp. 4449–4459, Feb. 2023, doi: 10.1016/j.ceramint.2022.09.331.

[158] M. H. Suhag, A. Khatun, I. Tateishi, M. Furukawa, H. Katsumata, and S. Kaneco, "One-step fabrication of the ZnO/g-$C_3N_4$ composite for visible light-responsive photocatalytic degradation of bisphenol E in aqueous solution," *ACS Omega*, vol. 8, no. 13, pp. 11824–11836, Apr. 2023, doi: 10.1021/acsomega.2c06678.

[159] A. Zholdas, A. K. Yedilbayev, A. K. Kudaibergenov, and A. E. Yerkinbekova, “Solid-state in situ synthesis of g-$C_3N_4$/ZnO nanocomposites for photocatalytic water cleaning,” *RSC Advances*, vol. 15, no. 46, pp. 38532–38546, 2025, doi: 10.1039/D5RA06422H.

[160] Y. Wang, Q. an Qiao, H. Cai, J. Jin, H. Gao, and Y. Xu, “Experimental and first-principles investigations on g-$C_3N_4$/ZnS heterostructures with enhanced photocatalyst capability,” *Micro & Nano Letters*, vol. 17, no. 11, 2022, doi: 10.1049/mna2.12131.

[161] Y. Sun, X. Zhang, L. Li, and J. Wang, “Efficient organic contaminant degradation by visible-light-driven Z-scheme g-$C_3N_4$/$Bi_2S_3$ heterojunction under the experimental and natural environment,” *Journal of Molecular Structure*, vol. 1318, 2024, doi: 10.1016/j.molstruc.2024.139247.

[162] Z. Abbasi, E. I. García-López, G. Marcì, A. Farrokhnia, and M. Z. Shoushtari, “Photocatalytic degradation of 4-Nitrophenol by g-$C_3N_4$-MCy: Mechanism study and kinetic modeling,” *Journal of Photochemistry and Photobiology A: Chemistry*, vol. 407, 2021, doi: 10.1016/j.jphotochem.2020.113004.

[163] M. Zarei, J. Bahrami, and M. Zarei, “Zirconia nanoparticle-modified graphitic carbon nitride nanosheets for effective photocatalytic degradation of 4-nitrophenol in water,” *Applied Water Science*, vol. 9, no. 8, 2019, doi: 10.1007/s13201-019-1076-8.

[164] R. Liu, H. Li, H. Ma, C. Ma, and L. Cao, “Ag-Modified g-$C_3N_4$ prepared by a one-step calcination method for enhanced catalytic efficiency and stability,” *ACS Omega*, vol. 5, no. 31, 2020, doi: 10.1021/acsomega.0c02161.

[165] M. Ismael, “Facile synthesis of NiO-loaded g-$C_3N_4$ heterojunction photocatalyst for efficient photocatalytic degradation of 4-nitrophenol under Visible light irradiation,” *Journal of Photochemistry and Photobiology A: Chemistry*, vol. 439, 2023, doi: 10.1016/j.jphotochem.2023.114576.

[166] M. Saad, S. Mukhtar, A. Khan, R. S. R. Kumar, and M. Imran, “Development of stable S-scheme 2D–2D g-$C_3N_4$/CdS nanoheterojunction arrays for enhanced Visible light photomineralisation of nitrophenol priority water pollutants,” *Scientific Reports*, vol. 14, no. 1, 2024, doi: 10.1038/s41598-024-52950-3.

[167] T. N. Xuan, D. T. Nguyen, Q. T. Thuong, and T. N. Ngoc, “Effect of copper-modification of g-$C_3N_4$ on the Visible-light-driven photocatalytic oxidation of nitrophenols,” *Molecules*, vol. 28, no. 23, 2023, doi: 10.3390/molecules28237810.

[168] V. Leandri, J. M. Gardner, and M. Jonsson, “Reply to ‘comment on coumarin as a quantitative probe for hydroxyl radical formation in heterogeneous photocatalysis’’, *The Journal of Physical Chemistry C*, vol. 123, no. 33, pp. 20471–20472, 2019, doi: 10.1021/acs.jpcc.9b06021.

[169] Y. Nosaka and A. Y. Nosaka, “Comment on coumarin as a quantitative probe for hydroxyl radical formation in heterogeneous photocatalysis,” *The Journal of Physical Chemistry C*, *vol. 123, no. 33, pp. 20469–20470, 2019,* doi: 10.1021/acs.jpcc.9b04190.

[170] W. J. McCormick, C. Rice, D. McCrudden, N. Skillen, and P. K. J. Robertson, “Enhanced monitoring of photocatalytic reactive oxygen species: Using electrochemistry for rapid sensing of hydroxyl radicals formed during the degradation of coumarin,” *Journal of Physical Chemistry A*, vol. 127, no. 23, 2023, doi: 10.1021/acs.jpca.3c00741.

[171] F. Ducrozet, A. Sebastian, C. J. Garcia Villavicencio, S. Ptasinska, and C. Sicard-Roselli, “Quantifying hydroxyl radicals generated by a low-temperature plasma using coumarin: methodology and precautions,” *Physical Chemistry Chemical Physics*, vol. 26, no. 11, 2024, doi: 10.1039/d4cp00040d.

[172] A. Wafi, E. Szabó-Bárdos, O. Horváth, É. Makó, M. Jakab, and B. Zsirka, “Coumarin-based quantification of hydroxyl radicals and other reactive species generated on excited nitrogen-doped $TiO_2$,” *Journal of Photochemistry and Photobiology A: Chemistry*, vol. 404, 2021, doi: 10.1016/j.jphotochem.2020.112913.

[173] P. Geng, J. Lv, L. Zhao, and Y. Wang, “Online chemiluminescence determination of the hydroxyl radical using coumarin as a probe,” *Analytical Methods*, vol. 15, no. 39, 2023, doi: 10.1039/d3ay01476b.

[174] G. Žerjav, A. Albreht, I. Vovk, and A. Pintar, “Revisiting terephthalic acid and coumarin as probes for photoluminescent determination of hydroxyl radical formation rate in heterogeneous photocatalysis,” *Applied Catalysis A*: General, vol. 598, p. 117566, May 2020, doi: 10.1016/J.APCATA.2020.117566.

[175] O. Fónagy, E. Szabó-Bárdos, and O. Horváth, “1,4-Benzoquinone and 1,4-hydroquinone based determination of electron and superoxide radical formed in heterogeneous photocatalytic systems,” *Journal of Photochemistry and Photobiology A: Chemistry*, vol. 407, 2021, doi: 10.1016/j.jphotochem.2020.113057.

[176] S. M. Hosseini, S. Asadpour, M. Ghasemi, and M. Shirani, "Efficient photocatalytic activity of ZnO/GO/CuO nanocomposite with solar light for reduction of hexavalent chromium," *Scientific Reports*, vol. 15, no. 1, Dec. 2025, doi: 10.1038/s41598-025-05790-8.

[177] S. McMichael, A. Tolosana-Moranchel, M. A. L. R. M. Cortes, J. W. J. Hamilton, P. Fernandez-Ibanez, and J. A. Byrne, "An investigation of photoelectrocatalytic disinfection of water using titania nanotube photoanodes with carbon cathodes and determination of the radicals produced," *Applied Catalysis B: Environmental*, vol. 311, 2022, doi: 10.1016/j.apcatb.2022.121339.

[178] J. Zhang, W. Wang, S. Huang, Y. Lv, L. Li, Z. Huang, and L. Chen, "Metal-free photocatalyst with reduced graphene oxide-doped graphitic carbon nitride homojunctions for efficient antibacterial applications," *RSC Advances*, vol. 15, no. 4, pp. 2444–2451, Jan. 2025, doi: 10.1039/d4ra07829b.

[179] I. Itskou, S. C. Sageer, D. M. Dawson, A. Kafizas, I. Nevjestic, C. M. McGilvery, M. Daboczi, G. Kerherve, S. Eslava, S. Heutz, S. E. Ashbrook, and C. Petit, "Boron-functionalized graphitic carbon nitride materials for photocatalytic applications: Effects on chemical, adsorptive, optoelectronic, and photocatalytic properties," *ACS Materials Au*, vol. 5, no. 4, pp. 656–674, Jul. 2025, doi: 10.1021/acsmaterialsau.5c00007.

[180] S. E. Huang, K. H. Tan, R. S. Sahu, T. A. Geleta, A. Miri, C. Lin, Y. Shih, and W. L. Chen, "Facile synthesis and optimization of graphitic carbon nitride nanoparticles to effectively photodegrade tetracycline under Visible light in water," *ACS Agricultural Science and Technology*, vol. 5, no. 2, pp. 235–245, Feb. 2025, doi: 10.1021/acsagscitech.4c00637.

[181] J. Wang and S. Wang, "A critical review on graphitic carbon nitride (g-$C_3N_4$)-based materials: Preparation, modification and environmental application," *Chemical Communications Reviews*, vol. 128, pp. 1–26, 2022, doi: 10.1016/j.ccr.2021.214338.

[182] S. B. R. Gupta, S. Singh, S. Kumar, R. J. Kalathil, and A. Kumar, "Green-synthesized cardamom-modified iron oxide nanoparticles with potent antibacterial, antioxidant, anti-inflammatory, and anticancer activities," *RSC Advances*, vol. 15, no. 49, pp. 41381–41399, 2025, doi: 10.1039/D5RA06699A.

[183] G. Gnanajobitha, G. Annadurai, and C. Kannan, "Green synthesis of silver nanoparticles using Elettaria cardamomum and assessment of its antimicrobial activity". *International Journal of Pharma Sciences and Research (IJPSR)*, vol. 3, no. 3, pp. 323–330, March 2012, ISSN: 0975-9492.

[184] I. Uddin, S. Mukhtar, O. Horváth, and M. Pósfai, “Room-temperature synthesis of rGO/Ag nanocomposite as a photocatalyst for the degradation of organic pollutants in wastewater,” *Materialia*, vol. 36, p. 102179, 2024, doi: 10.1016/j.mtla.2024.102179.

[185] I. Uddin, M. Ahmad, G. Sebők, and M. Pósfai, “Starch-Assisted Synthesis of $Bi_2S_3$ Nanoparticles for Enhanced Dielectric and Antibacterial Applications,” *ACS Omega,* vol. 7, no. 46, pp. 42438–42445, Nov. 2022, doi: 10.1021/acsomega.2c05593.

[186] Ö. B. Mergen and E. Arda, “Determination of optical band gap energies of CS/MWCNT bio-nanocomposites by Tauc and ASF Methods,” *Synthetic Metals*, vol. 269, 2020, doi: 10.1016/j.synthmet.2020.116539.

[187] O. O. Akintunde, L. Yu, J. Hu, M. G. Kibria, and G. Achari, “Visible-light driven photocatalytic degradation of 4-chlorophenol using graphitic carbon nitride-based nanocomposites,” *Catalysts*, vol. 12, no. 3, 2022, doi: 10.3390/catal12030281.

[188] X. Li, J. Zhang, Y. Gong, L. Chen, H. Zhang, and W. Wu, “Preparation and characterization of graphitic carbon nitride through pyrolysis of melamine,” *Applied Physics A: Materials Science & Processing*, vol. 94, no. 2, 2009, doi: 10.1007/s00339-008-4816-4.

[189] F. Fina, S. K. Callear, G. M. Carins, and J. T. S. Irvine, “Structural investigation of graphitic carbon nitride via XRD and neutron diffraction,” *Chemistry of Materials*, vol. 27, no. 7, pp. 2612–2618, Apr. 2015, doi: 10.1021/acs.chemmater.5b00411.

[190] M. S. Nasir, S. Zhang, Z. Pan, G. Lv, and L. Wang, “Recent development in graphitic carbon nitride based photocatalysis for hydrogen generation,” *Applied Catalysis B: Environmental*, 2019, doi: 10.1016/j.apcatb.2019.117855.

[191] X. Mao, R. Guo, Q. Chen, H. Zhu, H. Li, and Z. Yan, “Recent advances in graphitic carbon nitride based electro-catalysts for $CO_2$ reduction reactions,” *Molecules*, vol. 28, no. 8, p. 3292, 2023, doi: 10.3390/molecules28083292.

[192] A. A. Frimer, G. Aljadeff, and P. Gilinsky-Sharon, “Reaction of coumarins with superoxide anion radical ($O_2$): Facile entry to o-coumarinic acid systems,” *Israel Journal of Chemistry*, vol. 27, no. 1, 1986, doi: 10.1002/ijch.198600007.

[193] G. V. Buxton, C. L. Greenstock, W. P. Helman, and A. B. Ross, “Critical review of rate constants for reactions of hydrated electrons, hydrogen atoms and hydroxyl

radicals ($^{\cdot}$OH/$^{\cdot}$O$^{-}$) in aqueous solution," *J. Phys. Chem. Ref.* Data, vol. 17, no. 2, pp. 513–886, 1988,
doi: 10.1063/1.555805.

[194] J. H. Shen, J. J. Horng, Y. S. Wang, and Y. R. Zeng, "The use of reactive index of hydroxyl radicals to investigate the degradation of acid orange 7 by Fenton process," *Chemosphere*, vol. 182, 2017,
doi: 10.1016/j.chemosphere.2017.05.043.

[195] G. Louit, S. Foley, J. Cabillic, H. Coffigny, F. Taran, A. Valleix, J. P. Renault, and S. Pin, "The reaction of coumarin with the OH radical revisited: Hydroxylation product analysis determined by fluorescence and chromatography," *Radiation Physics and Chemistry*, vol. 72, no. 2–3, 2005,
doi: 10.1016/j.radphyschem.2004.09.007.

[196] S. Ganesan, T. Kokulnathan, S. Sumathi, and A. Palaniappan, "Efficient photocatalytic degradation of textile dye pollutants using thermally exfoliated graphitic carbon nitride (TE-g-C$_3$N$_4$)," *Scientific Reports*, vol. 14, no. 1, Dec. 2024,
doi: 10.1038/s41598-024-52688-y.

[197] O. J. Achadu, I. Uddin, and T. Nyokong, "The interaction between graphene quantum dots grafted with polyethyleneimine and Au@Ag nanoparticles: Application as a fluorescence 'turn-on' nanoprobe," *Journal of Photochemistry and Photobiology A: Chemistry*, vol. 324, 2016,
doi: 10.1016/j.jphotochem.2016.03.016.

[198] M. Michalska, K. Matuszewska, and W. Lisowski, "A facile approach for fabricating g-C$_3$N$_4$-based materials as metal-free photocatalysts," *Results in Engineering*, vol. 24, p. 103109, Dec. 2024,
doi: 10.1016/J.RINENG.2024.103109

[199] S. M. Abdel-Moniem, M. A. El-Liethy, H. S. Ibrahim, and M. E. M. Ali, "Innovative green/non-toxic Bi$_2$S$_3$@g-C$_3$N$_4$ nanosheets for dark antimicrobial activity and photocatalytic depollution: Turnover assessment," *Ecotoxicology and Environmental*, vol. 226, 2021,
doi: 10.1016/j.ecoenv.2021.112808.

[200] G. J. Hutchings, P. R. Davies, S. Pattisson, T. E. Davies, D. J. Morgan, and M. W. Dlamini, "Facile synthesis of a porous 3D g-C$_3$N$_4$ photocatalyst for the degradation of organics in shale gas brines," *Catalysis Communications*, vol. 169, p. 106480, Sep. 2022,
doi: 10.1016/J.CATCOM.2022.106480.

[201] M. Danish and M. Muneer, "Excellent Visible-light-driven Ni-ZnS/g-C$_3$N$_4$ photocatalyst for enhanced pollutants degradation performance: Insight into the photocatalytic mechanism and adsorption isotherm," *Applied Surface Science*, vol. 563, 2021,

doi: 10.1016/j.apsusc.2021.150262.

[202] T. Suter, P. Kunzmann, P. Amade, F. P. Gabb, and H.-P. Steinrück, "Synthesis, structure and electronic properties of graphitic carbon nitride films," *Journal of Physical Chemistry C*, vol. 122, no. 44, 2018, doi: 10.1021/acs.jpcc.8b07972.

[203] S. A. Saah, N. O. Boadi, and J. A. M. Awudza, "Facile synthesis of PbS, $Bi_2S_3$ and Bi-doped PbS nanoparticles from metal piperidine dithiocarbamates complexes," *Results in Chemistry*, vol. 4, 2022, doi: 10.1016/j.rechem.2022.100618.

[204] J. Ganesamurthi, R. Shanmugam, S. M. Chen, and P. Veerakumar, "Bismuth sulfide/zinc-doped graphitic carbon nitride nanocomposite for electrochemical detection of hazardous nitric oxide," *Journal of Electroanalytical Chemistry*, vol. 910, 2022, doi: 10.1016/j.jelechem.2022.116174.

[205] K. Liu, W. Song, Y. Xu, J. Li, and Z. Wang, "Study on the phase and bath electrochemical properties in electrodeposition of ZnS film," *Journal of Ceramic Processing Research*, vol. 19, no. 2, 2018.

[206] J. R. Zhang, L. J. Wan, and W. F. Fu, "Accurate K-edge X-ray photoelectron and absorption spectra of g-$C_3N_4$ nanosheets by first-principles simulations and reinterpretations," *Physical Chemistry Chemical Physics*, vol. 21, no. 41, 2019, doi: 10.1039/c9cp04573b.

[207] X. Liu, W. Wang, Y. Liu, B. Huang, and Y. Dai, "In situ synthesis of $Bi_2S_3$/$Bi_2SiO_5$ heterojunction photocatalysts with enhanced Visible light photocatalytic activity," *RSC Advances*, vol. 5, no. 69, 2015, doi: 10.1039/c5ra09070a.

[208] Y. Shi, X. Xiong, S. Ding, X. Liu, Q. Jiang, and J. Hu, "In-situ topotactic synthesis and photocatalytic activity of plate-like BiOCl/2D networks $Bi_2S_3$ heterostructures," *Applied Catalysis B: Environmental*, vol. 220, 2018, doi: 10.1016/j.apcatb.2017.08.074.

[209] G. Lakshminarayana, M. Kawa, S. Baki, K. M. Kaky, and A. Rammah, "X-ray photoelectron spectroscopy (XPS) and radiation shielding parameters investigations for zinc molybdenum borotellurite glasses containing different network modifiers," *Journal of Materials Science*, vol. 52, no. 12, 2017, doi: 10.1007/s10853-017-0974-0.

[210] Y. Jin, Z. Xing, Y. Li, J. Han, H. Lorenz, and J. Chen, "Synthetic BiOBr/$Bi_2S_3$/Cds crystalline material and its degradation of dye under Visible light," *Crystals (Basel)*, vol. 11, no. 8, 2021, doi: 10.3390/cryst11080899.

[211] S. Yang, K. Wang, Q. Chen, and Y. Wu, "Enhanced photocatalytic hydrogen production of S-scheme $TiO_2$/g-$C_3N_4$ heterojunction loaded with single-atom Ni," *Journal of Materials Science & Technology*, vol. 175, 2024, doi: 10.1016/j.jmst.2023.07.044.

[212] W. Xing, M. Yin, Q. Lv, Y. Hu, C. Liu, and J. Zhang, "Oxygen solubility, diffusion coefficient, and solution viscosity," in Rotating Electrode Methods and Oxygen Reduction Electrocatalysts, 1st ed., *Elsevier*, 2014, pp. 1–31, doi: 10.1016/B978-0-444-63278-4.00001-X.

# 9. Attachment figures

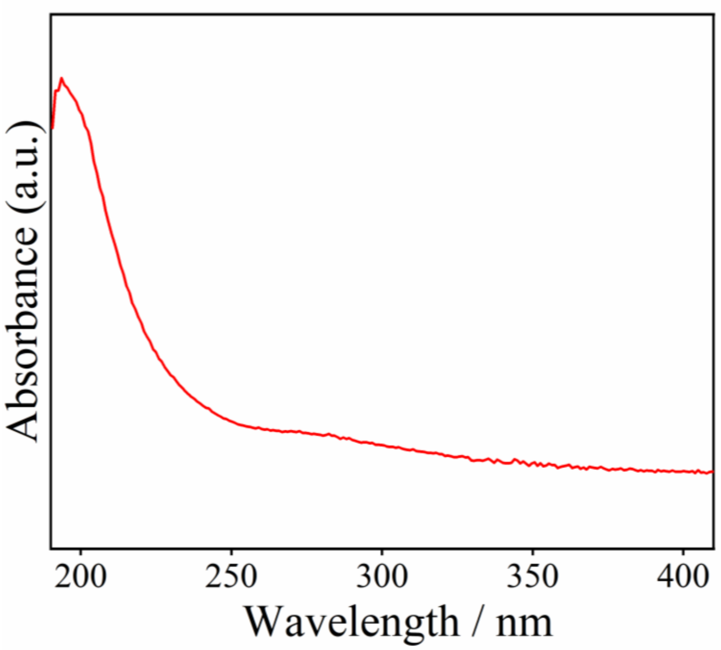

**Figure A4.1.** Absorbance spectrum of cardamom extract.

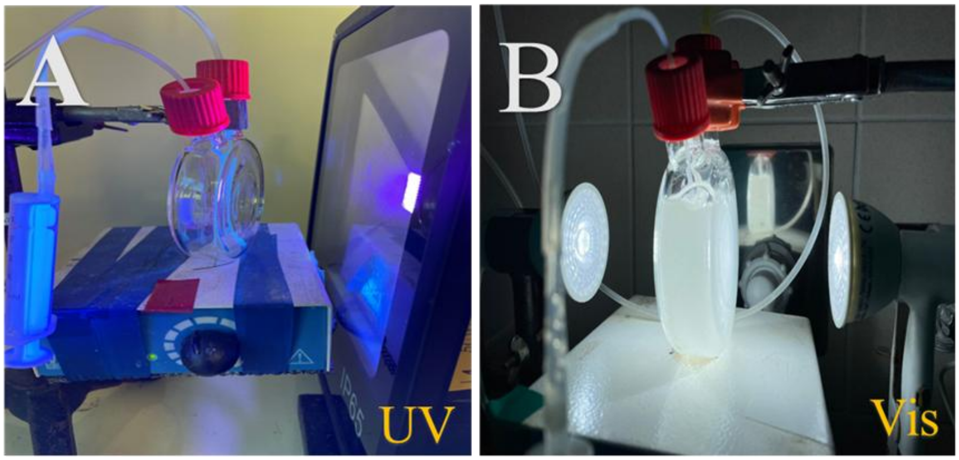

**Figure A4.2.** Lab-scale quartz glass reactors and their arrangement in the setup for photocatalytic experiments under (A) UV and (B) Visible light.

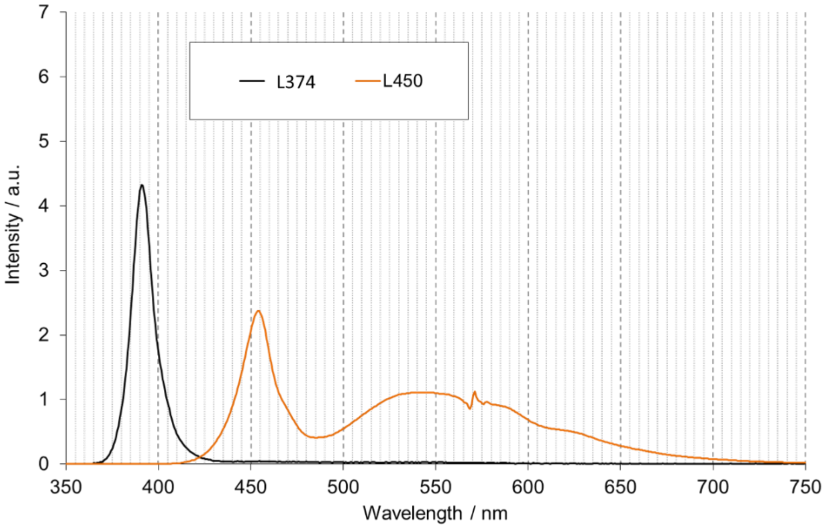

**Figure A4.3.** Emission spectra of UV (black) and Vis (red) light sources applied.

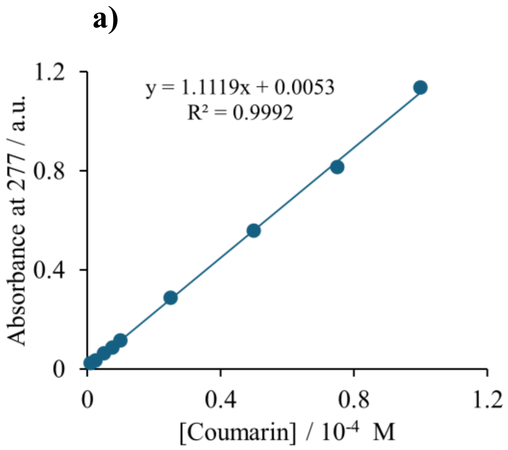

**Figure A4.4.a** Calibration curve of coumarin

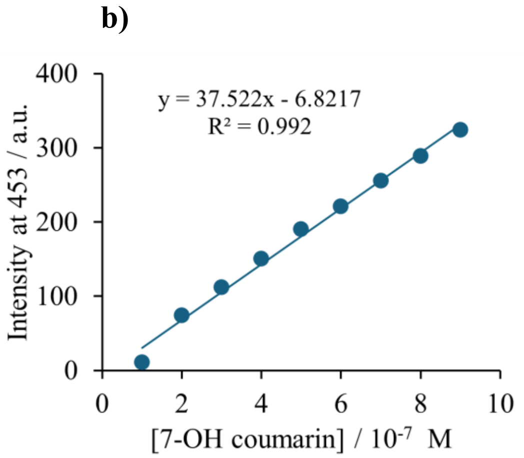

**Figure A4.4.b** Calibration curve of 7-OH coumarin.

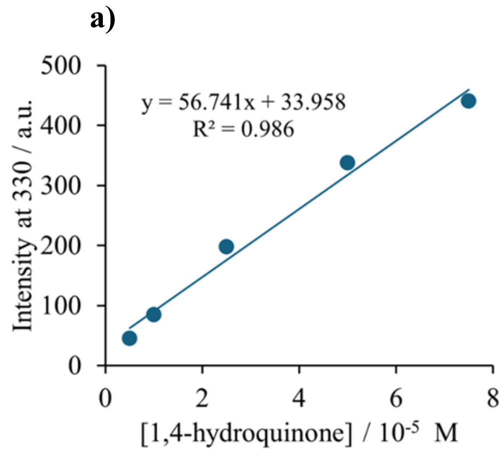

**Figure A4.5.** Calibration curve of $H_2Q$.

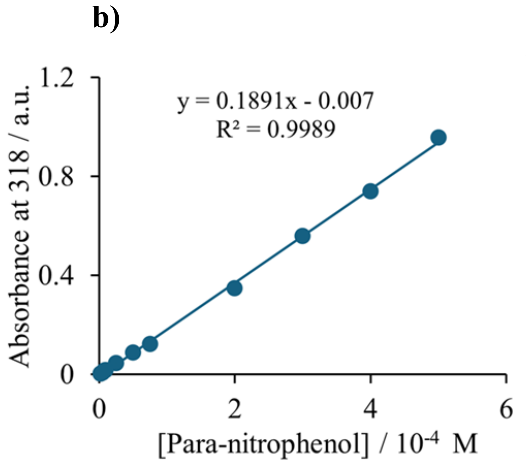

**Figure A4.6.** Calibration curve of para-nitrophenol.

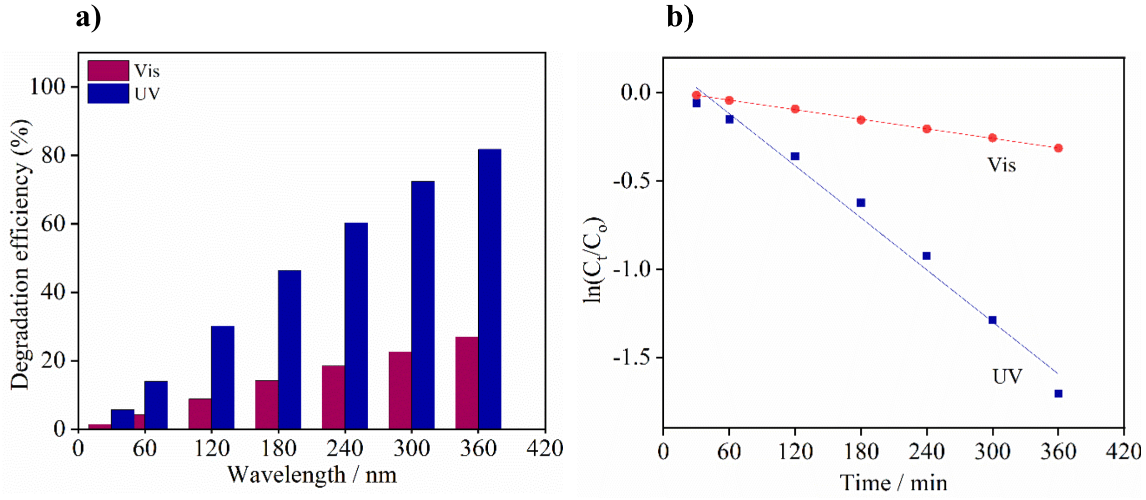

**Figure A5.1.** Photocatalytic degradation of para-nitrophenol with Ag(2)-g-$C_3N_4$ synthesized using cardamom extract.

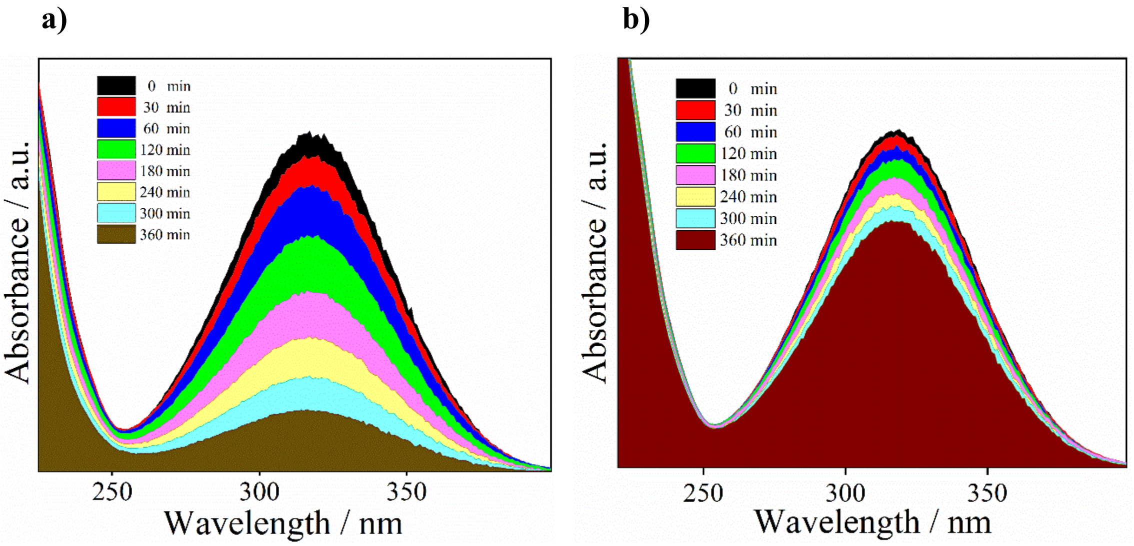

**Figure A5.2.** Photocatalytic degradation of 4-nitrophenol using cardamom Ag(2)-g-$C_3N_4$ nanocomposite under (a) UV and (b) Visible light.

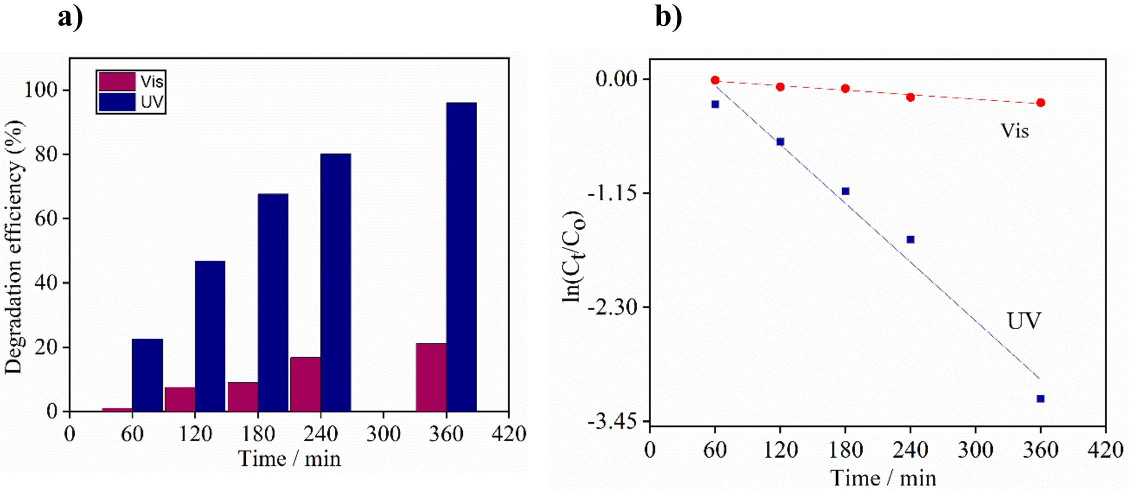

**Figure A5.3.** Photocatalytic degradation of para-nitrophenol with Ag(4)-g-$C_3N_4$ synthesized without using extract.

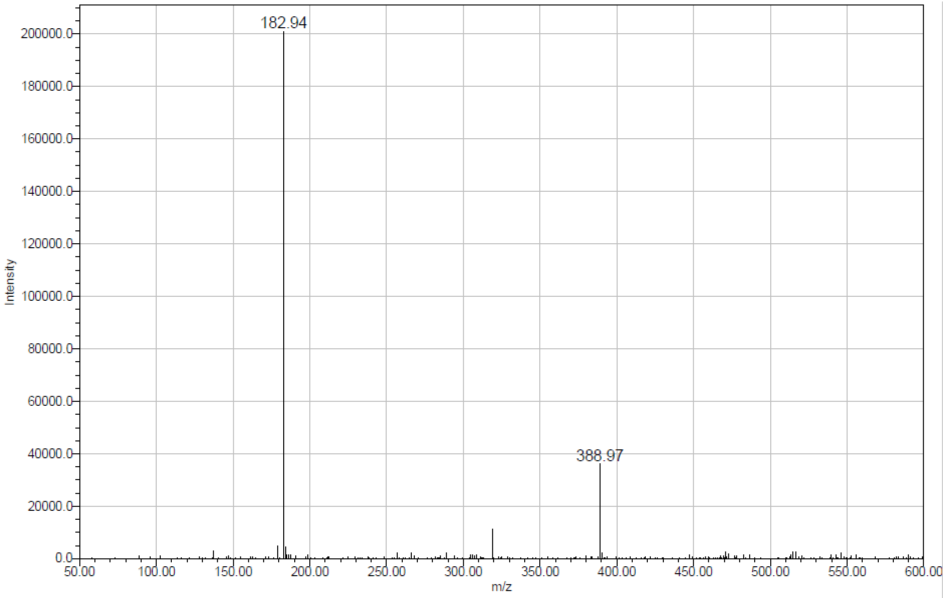

**Figure A5.4.** The mass spectrum for the intermediate.

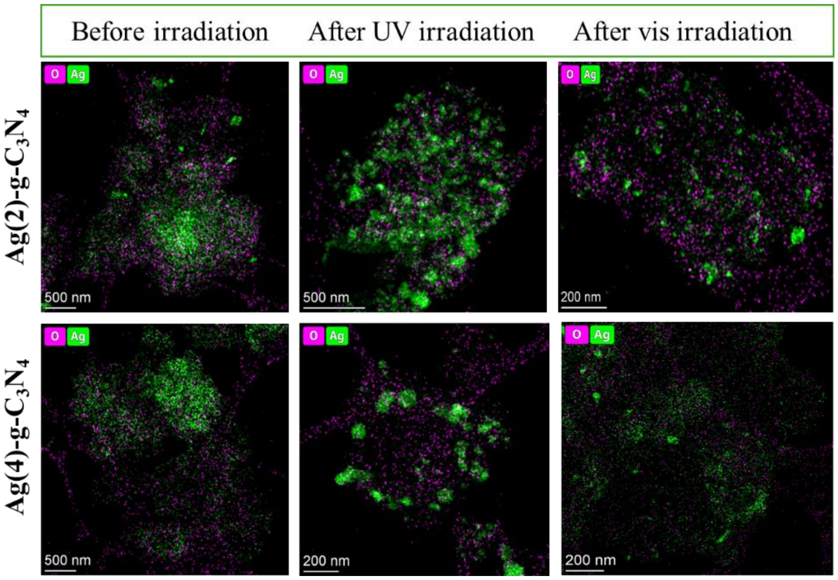

**Figure A5.5.** Oxygen-silver elemental maps for the Ag(2)-g-$C_3N_4$ (bio-inspired route) and Ag(4)-g-$C_3N_4$ (Impregnation method).

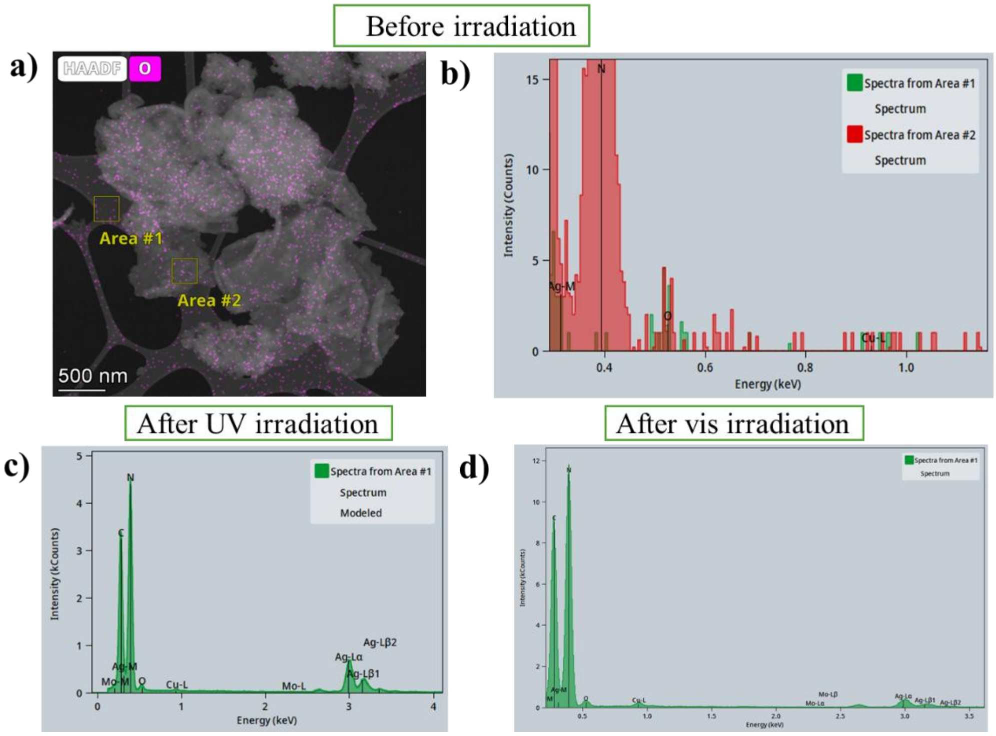

Before irradiation, the HAADF image and elemental maps show a uniform (a), low oxygen signal spread over both the catalyst flakes and the surrounding carbon support, while Ag appears as larger, uneven aggregates.

The EDX spectra (b) collected from (a) area #1 (on the support) and area #2 (on the Ag-containing region) exhibit essentially the same, very small oxygen contribution, indicating that the detected oxygen mainly originates from background sources such as the support film, adsorbed moisture or surface functional groups, rather than from silver oxide associated specifically with the nanoparticles.

After UV (c) and visible (d) irradiation, the spectra are dominated by C and N from g-$C_3N_4$ and clear Ag peaks, while the oxygen contribution remains negligible and does not increase at the Ag-rich regions. Together, the oxygen maps for Ag(2)-g-$C_3N_4$ and Ag(4)-g-$C_3N_4$ and the EDX analysis for Ag(4)-g-$C_3N_4$ support the conclusion that light irradiation mainly restructures metallic Ag nanocrystals on g-$C_3N_4$, with no detectable formation of a separate Ag and oxygen phase within the sensitivity of TEM–EDX.

**Figure A5.6.** EDX spectra for Ag(4)-g-$C_3N_4$.

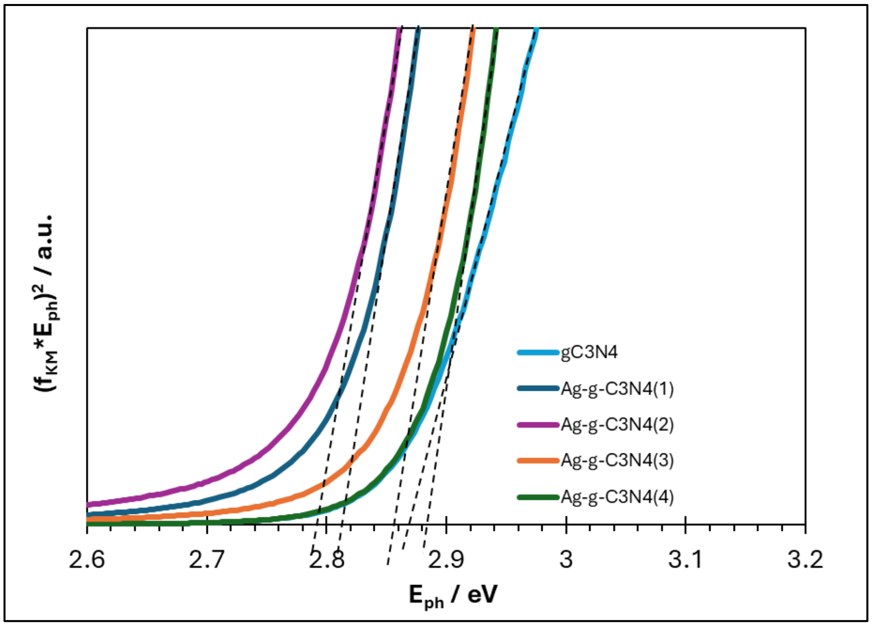

**Figure 5.7.** Tauc plots for the determination of band-gap energy.

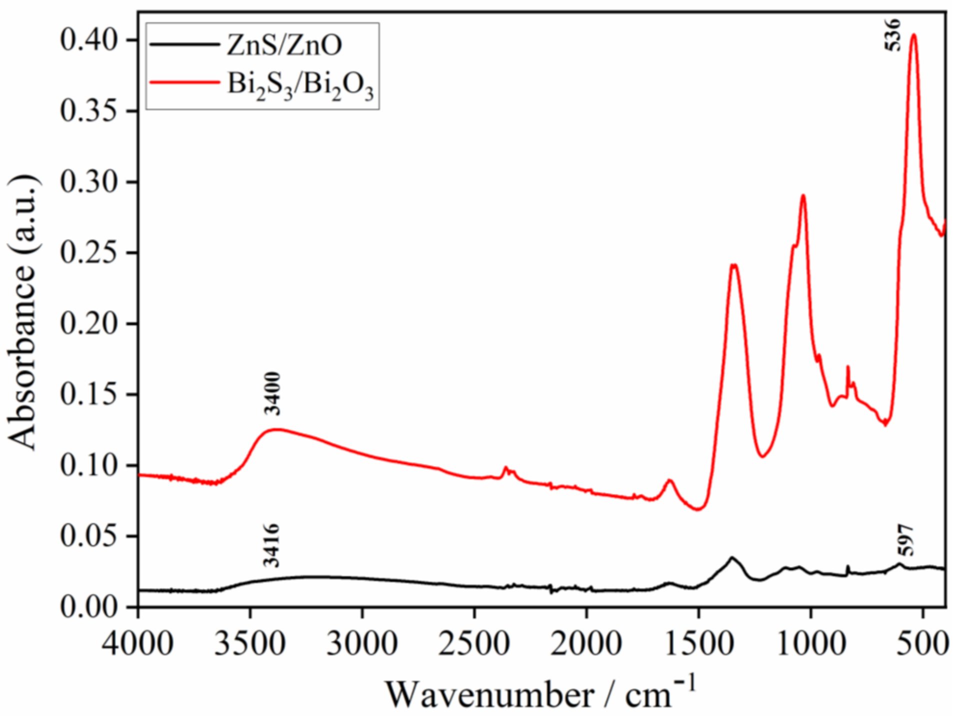

**Figure A5.8.** FTIR spectra of ZnS/ZnO and $Bi_2S_3/Bi_2O_3$.

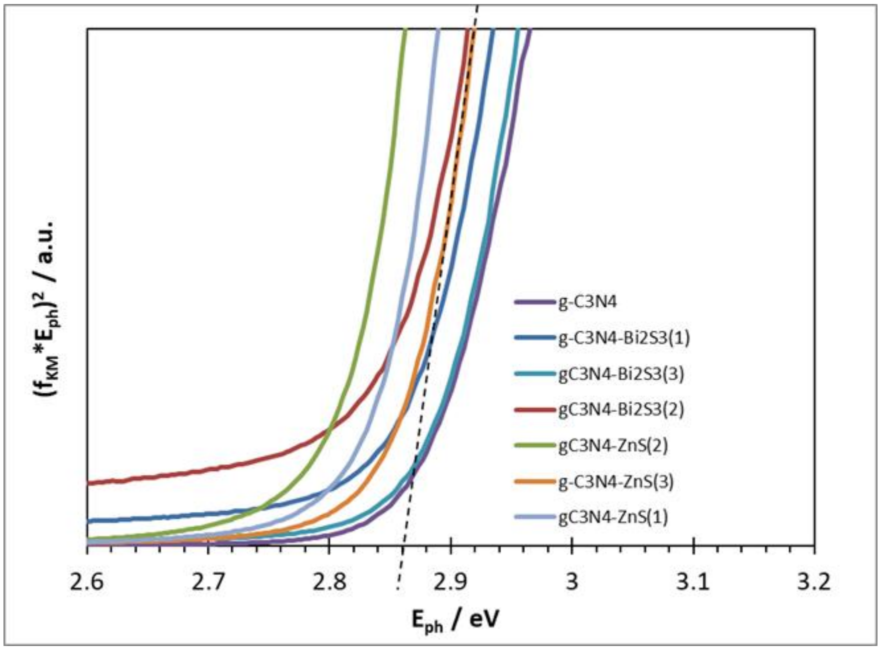

**Figure 5.9.** Tauc plots for the determination of band-gap energy.

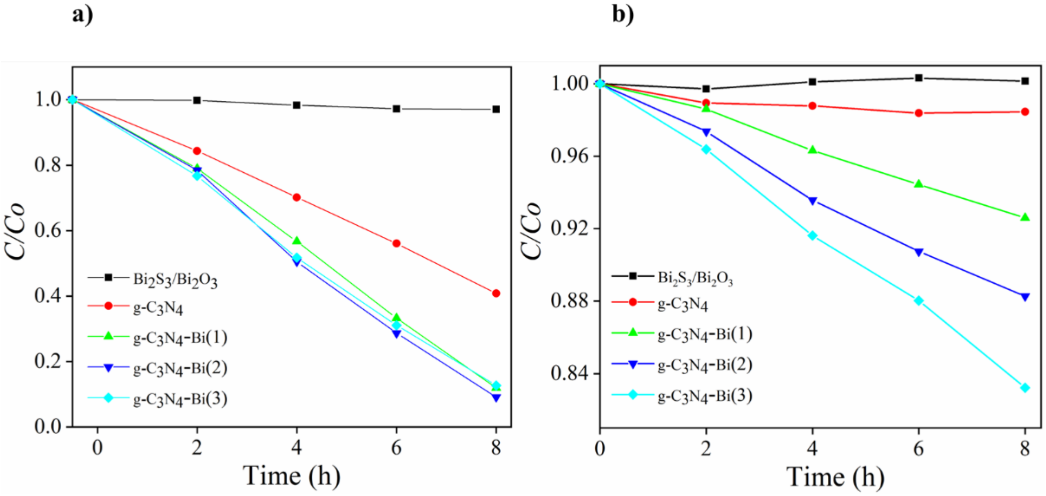

**Figure A5.10.** C/$C_0$ curves for para-nitrophenol degradation by irradiation with g-$C_3N_4$-Bi (a) UV and (b) Visible LEDs.

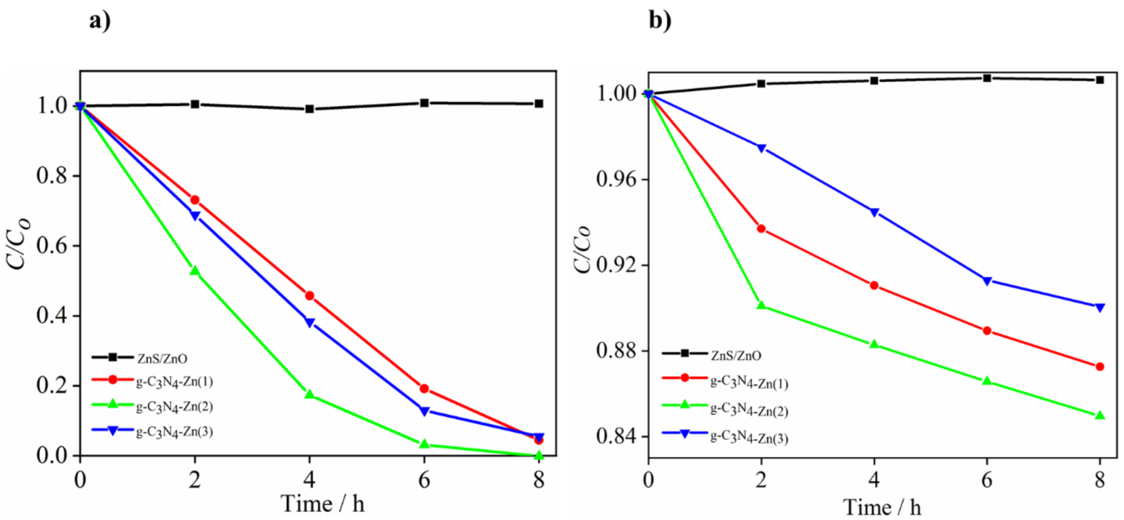

**Figure A5.11.** $C/C_0$ curves for para-nitrophenol degradation by irradiations with $g$-$C_3N_4$-Zn (a) UV and (b) Visible LEDs.

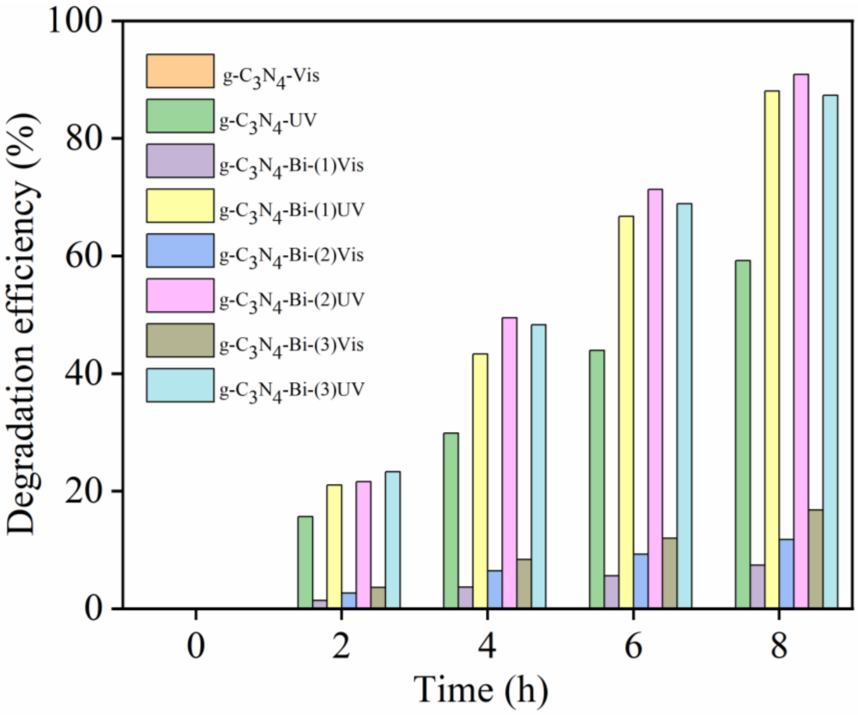

**Figure A5.12.** Degradation efficiency of $Bi_2S_3/Bi_2O_3$-modified catalyst under UV and Vis LED irradiation.

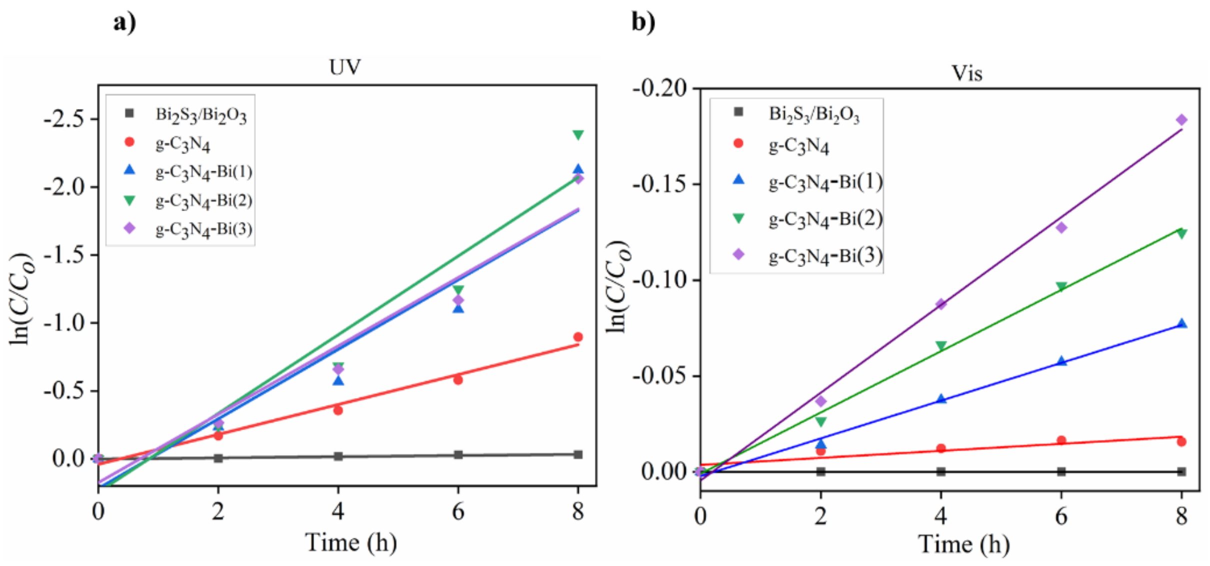

**Figure A5.13.** Pseudo-first-order kinetic model for the $Bi_2S_3/Bi_2O_3$-modified catalyst under (a) UV and (b) Vis LED irradiation.

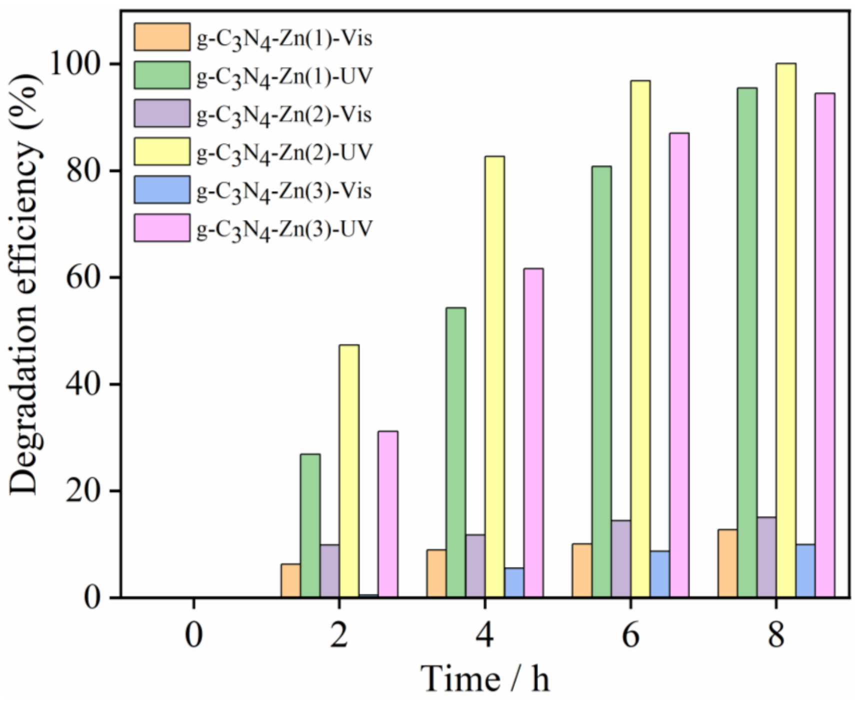

**Figure A5.14.** Degradation efficiency of ZnS/ZnO modified catalyst under UV and Vis LED irradiation.

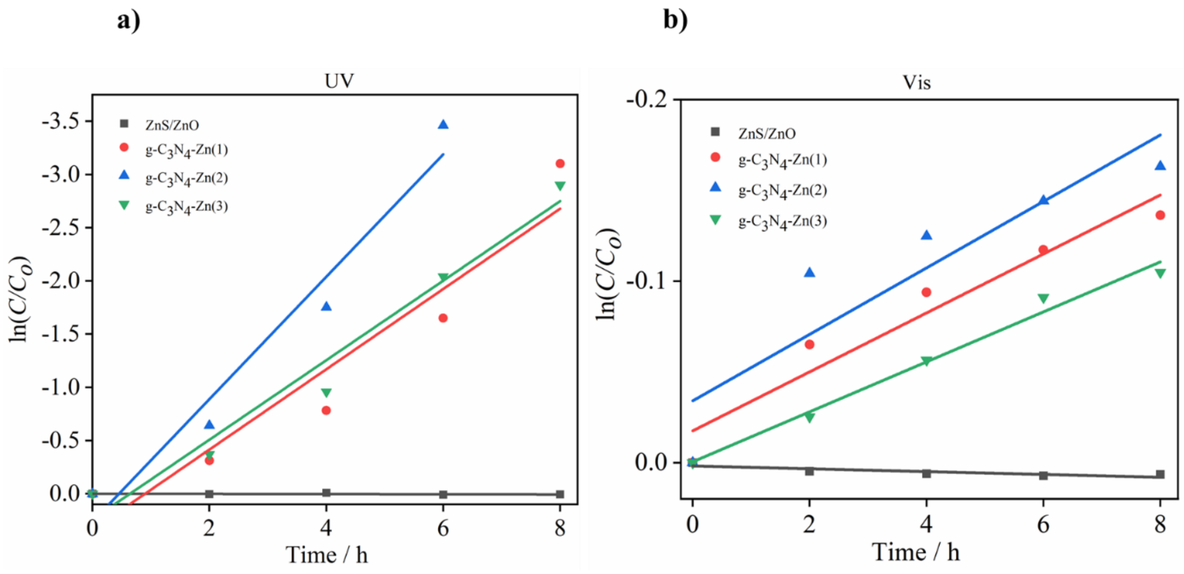

**Figure A5.15.** Pseudo-first-order kinetic model for the ZnS/ZnO modified catalyst under (a) UV and (b) Vis LED irradiation.

# 10. Attachment tables

**Table AT4.1:** List of samples for physiochemical characterization.

| Catalyst | Physicochemical characterisation | | | | | | |
|---|---|---|---|---|---|---|---|
| | **XRD** | **SEM** | **TEM** | **FTIR** | **XPS** | **BET** | **UV-vis DRS** |
| g-$C_3N_4$-melamine 500 °C (2h) (air, nitrogen) | ☑ | ☑ | | | | | |
| g-$C_3N_4$-urea 500 °C (2h) (air, nitrogen) | ☑ | ☑ | | | | | |
| g-$C_3N_4$-melamine 550 °C (4h) (air, nitrogen) | ☑ | ☑ | ☑ | ☑ | ☑ | ☑ | ☑ |
| Ag(1)-g-$C_3N_4$ | ☑ | ☑ | ☑ | ☑ | ☑ | ☑ | ☑ |
| Ag(2)-g-$C_3N_4$ | ☑ | ☑ | ☑ | ☑ | ☑ | ☑ | ☑ |
| Ag(3)-g-$C_3N_4$ | ☑ | ☑ | ☑ | ☑ | ☑ | ☑ | ☑ |
| Ag(3)-g-$C_3N_4$ | ☑ | ☑ | ☑ | ☑ | ☑ | ☑ | ☑ |
| g-$C_3N_4$-Bi(1) | ☑ | ☑ | ☑ | ☑ | ☑ | ☑ | ☑ |
| g-$C_3N_4$-Bi(2) | ☑ | ☑ | ☑ | ☑ | ☑ | ☑ | ☑ |
| g-$C_3N_4$-Bi(3) | ☑ | ☑ | ☑ | ☑ | ☑ | ☑ | ☑ |
| g-$C_3N_4$-Zn(1) | ☑ | ☑ | ☑ | ☑ | ☑ | ☑ | ☑ |
| g-$C_3N_4$-Zn(2) | ☑ | ☑ | ☑ | ☑ | ☑ | ☑ | ☑ |
| g-$C_3N_4$-Zn(3) | ☑ | ☑ | ☑ | ☑ | ☑ | ☑ | ☑ |

**Table AT5.1.** Total pore volume (V) and micropore volume ($V_{micro}$).

| **SN** | **Catalyst** | **V ($cm^3/g$)** | **$V_{micro}$ ($cm^3/g$)** |
|---|---|---|---|
| **1** | g-$C_3N_4$ | 0.21994 | 0.001894 |
| **2** | Ag(2)-g-$C_3N_4$_b_irr | 0.26765 | 0.002409 |
| **3** | Ag(2)-g-$C_3N_4$_aUV_irr | 0.24898 | 0.003245 |
| **4** | Ag(2)-g-$C_3N_4$_aVIS_irr | 0.26968 | 0.003973 |
| **5** | Ag(4)-g-$C_3N_4$_b_irr | 0.19399 | 0.003203 |
| **6** | Ag(4)-g-$C_3N_4$_aUV_irr | 0.25038 | 0.002355 |
| **7** | Ag(4)-g-$C_3N_4$_aVIS_irr | 0.20886 | 0.002194 |

(Abbreviations: b_irr: before irradiation, a_irr: after irradiation.)

# 11. Acknowledgement

Completing this doctoral thesis would not have been achievable without the help and encouragement of many individuals. I would like to use this moment to express my heartfelt thanks to everyone who contributed to making this PhD work a reality.

First and foremost, I wish to express my profound appreciation to my supervisors, Dr. Ottó Horváth, DSc., and Dr. Erzsébet Szabó-Bárdos, PhD, for their unwavering guidance, patience, and mentorship throughout this journey. Their expertise and dedication kept my research on track and made my time in Hungary both intellectually stimulating and personally rewarding.

I am sincerely grateful to my colleagues who provided essential technical support and valuable insights that greatly enhanced my research. Special thanks to Zsombor Molnár and Kornél Rácz for conducting TEM analysis; Dr. Éva Makó and Csilla Öze for performing XRD measurements; Dr. Tatjana Juzsakova for carrying out BET and ICP analysis; Miklós Jakab for assistance with SEM-EDS; Miklós Németh for XPS analysis; Veronika Vágvölgyi for FTIR analysis and Edina Ring-Nyári for TOC analyses. Their collaboration and professionalism significantly enriched my research experience.

I gratefully acknowledge the financial support provided by the Stipendium Hungaricum Program for my doctoral scholarship, National Research, Development, and Innovation Office of Hungary in the frame of the bilateral Hungarian-Vietnamese S&T Cooperation Program (project code 2019–2.1.12-TET_VN-2020–00009 and NĐT/HU/22/21) as well as the Ministry for Innovation and Technology of Hungary, whose funding via the National Research, Development and Innovation Fund, under the 2021 Thematic Excellence Program (TKP2021-NKTA-21), enabled essential aspects of my research.

I would like to extend my heartfelt appreciation to my dear friends Dr. Imran Uddin, Abid Ali, Mohammad Umar, Sabica Naz, Asmae Ghoumit and Saad Mehmood for their unwavering support and friendship throughout this doctoral journey. Their constant encouragement helped me overcome the most difficult moments.

I am also deeply indebted to my family, whose unconditional support, motivation, and love have carried me through every stage of my research career. To my parents, siblings, and extended family, your faith in me has been an enduring source of strength.

Finally, I express my heartfelt gratitude for the blessings and grace that have guided me throughout this work, and I remain truly thankful for every person who played a role, big or small, in the successful completion of my thesis.